ISTANBUL TECHNICAL UNIVERSITY ★ GRADUATE SCHOOL OF SCIENCE ENGINEERING AND TECHNOLOGY

SYNTHESIS, DEVELOPMENT AND CHARACTERIZATION OF SOME RARE-EARTH METAL HEXABORIDE POWDERS AND THEIR SINTERED PRODUCTS

Ph.D. THESIS

Duygu AĞAOĞULLARI

Department of Materials Science and Engineering

Materials Science and Engineering Program

FEBRUARY 2014

ISTANBUL TECHNICAL UNIVERSITY ★ GRADUATE SCHOOL OF SCIENCE ENGINEERING AND TECHNOLOGY

SYNTHESIS, DEVELOPMENT AND CHARACTERIZATION OF SOME RARE-EARTH METAL HEXABORIDE POWDERS AND THEIR SINTERED PRODUCTS

Ph.D. THESIS

Duygu AĞAOĞULLARI
(521072006)

Department of Materials Science and Engineering

Materials Science and Engineering Program

Thesis Advisor: Prof. Dr. İsmail DUMAN

FEBRUARY 2014

İSTANBUL TEKNİK ÜNİVERSİTESİ ★ FEN BİLİMLERİ ENSTİTÜSÜ

BAZI NADİR TOPRAK METAL HEKZABORÜR TOZLARININ VE SİNTER ÜRÜNLERİNİN SENTEZLENMESİ, GELİŞTİRİLMESİ VE KARAKTERİZASYONU

DOKTORA TEZİ

Duygu AĞAOĞULLARI
(521072006)

Malzeme Bilimi ve Mühendisliği Anabilim Dalı

Malzeme Bilimi ve Mühendisliği Programı

Tez Danışmanı: Prof. Dr. İsmail DUMAN

ŞUBAT 2014

Duygu AĞAOĞULLARI, a **Ph.D.** student of ITU **Graduate School of Science, Engineering and Technology** student ID 521072006, successfully defended the **dissertation** entitled "**SYNTHESIS, DEVELOPMENT AND CHARACTERIZATION OF SOME RARE-EARTH METAL HEXABORIDE POWDERS AND THEIR SINTERED PRODUCTS**", which she prepared after fulfilling the requirements specified in the associated legislations, before the jury whose signatures are below.

Thesis Advisor :	**Prof. Dr. İsmail DUMAN** Istanbul Technical University	.....
Jury Members :	**Prof. Dr. M. Lütfi ÖVEÇOĞLU** Istanbul Technical University	.....
	Prof. Dr. Hüseyin ÇİMENOĞLU Istanbul Technical University	.....
	Prof. Dr. Müzeyyen MARŞOĞLU Yıldız Technical University	.....
	Prof. Dr. Gökhan ORHAN Istanbul University	.....

Date of Submission : 24 January 2014
Date of Defense : 18 February 2014

To my Angel - my Dad and

to my family,

FOREWORD

I would like to express my sincere gratitude and appreciation to many people who have made this dissertation possible. Amongst them, I would like to express the most profound and sincere gratitude to my advisor Prof. Dr. İsmail Duman for his priceless mentorship, knowledge, support and motivation throughout this dissertation work and my academic life. I would like to thank Prof. Dr. M. Lütfi Öveçoğlu for introducing me the mechanical alloying and mechanochemical synthesis techniques, for teaching me a new concept of scientific research, for guiding and encouraging me during my academic life.

I would also like to acknowledge Prof. Dr. Cüneyt Arslan, Prof. Dr. Hüseyin Çimenoğlu and Prof. Dr. Eyüp Sabri Kayalı for motivating me during the dissertation work of this Ph.D. thesis and for helping me in analyses and mechanical tests.

I would like to thank special people associated with this dissertation who deserve appreciation: Özge Balcı (M.Sc.), Nazlı Akçamlı (M.Sc.), Didem Ovalı (M.Sc.). I would also thank to all the precious members of the Particulate Materials Laboratories and in particular to Hasan Gökçe (Ph.D.), Ceren İmer (M.Sc.), Şeyma Duman (M.Sc.), Umut Söyler (M.Sc.), Meltem Bolluk and Emre Tekoğlu for their help during the experiments. I am also thankful to Faiz Muhaffel (M.Sc.), Onur Tazegül (M.Sc.) and Yakup Yürektürk (M.Sc.) for their support and assistance.

This dissertation was supported by "The Scientific and Technological Research Council of Turkey (TÜBİTAK)" with the project title of "Synthesis of Lanthanum, Cerium and Samarium Borides by Solid-State Reaction at Room Temperature" and the project number of 109M364. It was also funded by "Istanbul Technical University Scientific Research Projects" with the project title of "Mechanochemical Synthesis and Characterization of Some Rare-Earth Metal Borides" and the project number of 33549.

Finally, I would like to convey my deep appreciation and gratitude to my beloved husband Kubilay, to my dearest daughter Azra and to my parents for their support, motivation, guidance and encouragement at all times. My dad has always been and is always in my heart with every accomplishment or failure during my pursuit of this degree.

January 2014

Duygu AĞAOĞULLARI

M.Sc. Metallurgical and
Materials Engineer

TABLE OF CONTENTS

page

ABBREVIATIONS

A : Ampere
Å : Ångstrom
AAS : Atomic absorption spectrometer
ab : As-blended
ATR : Attenuated total reflection
BET : Brunauer-Emmett-Teller
BF : Bright-field
BPR : Ball-to-powder weight ratio
CP : Cold pressing
CR : Charge ratio
CS : Combustion synthesis
CTE : Coefficient of thermal expansion
CVD : Chemical vapor deposition
D : Diameter
DC : Direct current
DDAA : Diodecyl dimethyl ammonium acetate
DDAB : Didocyl dimethyl ammonium bromide
DF : Dark-field
DSC : Differential scanning calorimeter
EDS : Energy dispersive spectroscopy
emu : Electromagnetic unit
eV : Electron volt
FEAs : Field emitter arrays
FTIR : Fourier transform infrared spectroscopy
g : Gram
h : Hour
HV : Vickers hardness
ICDD : International center for diffraction data®
kg : Kilogram
kJ : Kilojoule
l : Liter
M : Molarity
MA : Mechanical alloying
MCP : Mechanochemical process
min : Minute
µm : Micrometer
MMC : Metal matrix composite
N : Newton
nm : Nanometer
ODS : Oxide dispersion strengthened
Oe : Oersted
OM : Optical microscope

Pa : Pascal
PCA : Process control agent
PLD : Pulsed laser deposition
PM : Powder metallurgy
ppm : Part per million
PRMMC : Particulate reinforced metal matrix composite
PSA : Particle size analyzer
PVD : Physical vapor deposition
RAPET : Reaction under autogenic pressure at elevated temperature
RE : Rare-earth metals
REB_6 : Rare-earth hexaborides
RF : Radio frequency
RM : Reaction milling
rpm : Rotation per minute
sec : Second
SADP : Selected area diffraction pattern
SEM : Scanning electron microscope
SHS : Self-propagating high-temperature synthesis
SM : Stereomicroscope
SPS : Spark plasma sintering
t_{ig} : Ignition time
T_{ig} : Ignition temperature
T_M : Melting temperature
TM : Trademark
TEM : Transmission electron microscope
V : Volt
VLS : Vapor-liquid-solid
VSM : Vibrating sample magnetometer
W : Watt
WVL : Wear volume loss
XRD : X-ray diffractometer
YAG : Yttrium aluminium garnet

LIST OF TABLES

Page

LIST OF FIGURES

Page

LIST OF SYMBOLS

a, b, c	**:** Lattice parameters
°C	**:** Degree Celsius
°K	**:** Degree Kelvin
ΔG	**:** Gibbs free energy change
ΔG°	**:** Standard Gibbs free energy change
ΔH	**:** Enthalpy change
ΔS	**:** Entropy change
I	**:** Current
λ	**:** Wavelength
Ω	**:** Ohm
ρ	**:** Electrical resistivity
s	**:** Typical probe spacing
T	**:** Temperature
θ	**:** Diffraction angle
~	**:** Approximation

SYNTHESIS, DEVELOPMENT AND CHARACTERIZATION OF SOME RARE-EARTH METAL HEXABORIDE POWDERS AND THEIR SINTERED PRODUCTS

SUMMARY

Lanthanum hexaboride (LaB_6), cerium hexaboride (CeB_6) and samarium hexaboride (SmB_6) have attracted significant interest in the last 60 years amongst transition metal borides and rare-earth metal borides. They are refractory ceramic materials characterized by high melting point, high strength, high rigidity, high chemical and thermal stability, low vapor pressure (at high temperatures), low electronic work function, low resistivity, low expansion coefficient (in some temperature ranges), high transmission stability, high current and voltage capability and high neutron absorbability. All these superior properties make these hexaborides suitable for use as components of high-energy optical systems, sensors for high resolution detectors, electrical coatings for resistors, coatings for high-current hot cathodes, decorative coatings, thermionic materials and to use in nuclear technology. LaB_6 and CeB_6 are the most widely used thermionic emitters (electron guns) which can offer about 10 to 15 times higher brightness, lower energy spread and longer service life than the tungsten cathodes utilized in a large variety of devices such as high-resolution electron microscope, electron beam writing unit, microwave tubes, free electron lasers and X-ray tubes. SmB_6 is a classical fluctuating-valence semiconductor and a Kondo insulator, having a relatively low work function which enables it for use as a potential thermionic emission material.

Many diverse processes or methods have been applied in the preparation of rare-earth borides up to now. Traditionally, rare-earth hexaborides were synthesized by using high temperature processess such as direct solid-phase reaction of the corresponding elements/compounds with elemental boron, as carbothermal reduction of the rare-earth oxides with boron and boron oxide or as reaction of the rare-earth oxides with boron carbide. Besides, carbothermal reduction and boron carbide methods have been widely used in the industrial-scale productions due to their low costs and simple equipments. Floating zone and electrosynthesis methods have been also developed conventionally in order to obtain the crystal forms of the rare-earth hexaborides. Since many years, researchers have been trying to obtain rare-earth hexaborides in different forms such as particles, whiskers, wires, rods, tubes, cubes or obelisks using various fabrication techniques. Recently, nano-scale or submicron structures (nano-cubes, nano-rods, etc.) of rare-earth hexaboride powders have been obtained by using low temperature synthesis methods in an autoclave and self-propagating high-temperature synthesis (SHS) methods under atmospheric conditions. Furthermore, rare-earth hexaborides in the form of whiskers, wires, rods, tubes, cubes and obelisks in nano- or micro-scales have been produced by conventional or modified chemical vapor deposition (CVD) techniques. It has been also reported that bulk rare-earth hexaborides can not be prepared easily via

conventional pressing and sintering methods with high relative densities due to their high plastic yield stress. In generel, spark plasma sintering (SPS) method is used to obtain highly dense rare-earth hexaboride sintered bodies. Although the development of bulk density is essential, sintering process of rare-earth hexaborides has not been comprehensively investigated in the literature. Consequently, it is very important to develop an efficient method for the preparation of technologically important hexaboride powders in high purity and with fine particles having various morphologies and hence it is significant to improve an effective method for the preparation of their corresponding sintered bodies. It has been attracting more attention to find new synthesis procedures from easy to handle raw materials with low reaction temperature, low reaction duration, simple process control, less equipment requirements and low cost.

Apart from the above mentioned powder production techniques, an alternative method has been utilized and developed in this dissertation for the production of pure fine-grained hexaboride powders at room temperature. This method involves solid-state reactions performed by high-energy ball milling and named as mechanochemical synthesis. This novel route enables rapid preparation for oxide dispersion strengthened alloys, amorphous materials, solid solution alloys, non-equilibrium alloys, intermetallics, nanocomposites, ceramics and advanced materials which are hard or impossible to be obtained by conventional production techniques. The mechanism of the process is based on repeated welding, fracturing and rewelding of the raw materials. It has been controlled by several factors such as type of mill, material of milling media, size and size distribution of milling media, milling speed, milling time, ball-to-powder weight ratio (BPR), extent of filling the milling chamber, milling atmosphere, process control agent and temperature of milling.

In this dissertation, LaB_6, CeB_6 and SmB_6 powders were synthesized by mechanochemical synthesis process carried out at room temperature for the first time in the literature. The synthesis of these rare-earth hexaborides were originated from their oxide powders such as La_2O_3, CeO_2, and Sm_2O_3. B_2O_3 powders were used as a native boron source for the formations of hexaboride phases. Mg powders were used in the experiments as a strong metallic reducing agent. Ca granules were alternatively utilized as a reductant in order to examine its influence on the formation of LaB_6. Mechanochemical synthesis parameters of milling duration, ball-to-powder weight ratio, type of mill and process control agent were used to reveal the ideal production conditions of LaB_6 powders. Mechanochemical synthesis of CeB_6 and SmB_6 were carried out with the optimum process parameters determined during the synthesis of LaB_6. Mechanochemically synthesized LaB_6, CeB_6 and SmB_6 powders were subjected to selective HCl leaching to obtain hexaboride powders in high purity. After mechanochemical synthesis and leaching treatments, optimized conditions of obtaining pure LaB_6, CeB_6 and SmB_6 powders were determined: polycrystalline LaB_6, CeB_6 and SmB_6 powders were achieved with average particle sizes ranging between 50-90 nm with a minimum purity value of 99.99 %. These laboratory-synthesized LaB_6, CeB_6 and SmB_6 powders were compared with each other and their commercial ones in terms of microstructural, physical (density and surface area) and magnetic properties. Following to that, LaB_6, CeB_6 and SmB_6 powders obtained with a high quality after mechanochemical synthesis and leaching treatments were prepared in bulk forms via cold pressing and pressureless sintering processes. The bulk properties, in terms of microstructure, density, electrical resistivity, roughness,

friction coefficient, hardness and relative wear volume loss, of the sintered LaB_6, CeB_6 and SmB_6 samples originated from the laboratory-synthesized powders were elaborated and compared with each other and those of commercial ones.

Furthermore, it is a necessity to research the possibilities of obtaining high-technology boron products since Turkey owns about 72 % of the world's boron mine reserves. There is not still any mass production of high-technology boron products, but it is possible to overcome this situation by supporting the laboratory studies concerning improvement of crude and refined boron products towards advanced boron products. Besides, Turkey has a small amount of lanthanide group mine reserves. Consequently, the present dissertation also aims the creation of added value, by using the native boron source and by introducing the idea of using native lanthanide group metals after their purification, for the production of high-technology boron materials.

BAZI NADİR TOPRAK METAL HEKZABORÜR TOZLARININ VE SİNTER ÜRÜNLERİNİN SENTEZLENMESİ, GELİŞTİRİLMESİ VE KARAKTERİZASYONU

ÖZET

Lantan hekzaborür (LaB_6), seryum hekzaborür (CeB_6) ve samaryum hekzaborür (SmB_6) özellikle geçiş metali borürleri ve nadir toprak metal borürleri arasından, son 60 yıldır oldukça yoğun ilgi görmektedir. Bu refrakter seramik malzemeler, yüksek ergime noktası, yüksek dayanım, yüksek rijitlik, yüksek kimyasal ve termal kararlılık, düşük buhar basıncı (yüksek sıcaklıklarda), düşük elektronik iş fonksiyonu, düşük elektriksel direnç, düşük termal genleşme katsayısı (bazı sıcaklık aralıklarında), yüksek iletim kararlılığı, yüksek akım ve gerilim kapasitesi ve yüksek nötron absorpsiyon kapasitesi ile karakterize edilirler. Bu hekzaborürler, tüm bu üstün özellikleri sayesinde, örneğin yüksek enerjili optik sistemlerde bileşen olarak, yüksek çözümlemeli dedektörlerde sensör olarak, dekoratif amaçlı kaplamalar olarak, yüksek-gerilim sıcak katotlarında ve rezistörlerde elektriksel kaplamalar olarak, termiyonik malzemeler olarak ve nükleer teknoloji alanlarında kullanılmaktadırlar. LaB_6 ve CeB_6 örneğin yüksek çözünürlüklü elektron mikroskopları, elektron demeti ile damgalama üniteleri, mikrodalga tüpleri, serbest elektron lazerleri, X-ışını tüpleri gibi oldukça çeşitli cihazlarda kullanılan tungsten katotlardan yaklaşık 10-15 kat daha fazla parlaklık, düşük enerji dağılımı ve kullanım ömrü sağlayabilmeleri nedeniyle en sık kullanılan termiyonik emisyon malzemeleridir (elektron tabancaları). Bunun yanında, SmB_6 oldukça düşük iş fonksiyonuna sahip olması sayesinde termiyonik emisyon malzemesi olarak kullanıma aday bir klasik geçişli-valans banta sahip bir yarıiletken ve bir Kondo yalıtkandır.

Bugüne kadar nadir toprak borürlerinin üretiminde oldukça çeşitli prosesler ve metotlar kullanılmıştır. Nadir toprak hekzaborürleri, geleneksel olarak ilgili element/bileşiklerin elementel bor ile direkt katı-faz reaksiyonu, nadir toprak metal oksitlerinin bor ve bor oksit ile karbotermal redüksiyonu ya da nadir toprak metal oksitlerinin bor karbür ile reaksiyonu gibi yüksek sıcaklık prosesleri kullanılarak sentezlenmiştir. Ayrıca, karbotermal redüksiyon ve bor karbür yöntemleri düşük maliyetleri ve ekipman kolaylığı nedeniyle endüstriyel ölçekteki üretimlerde geniş ölçüde tercih edilmektedir. Aynı zamanda, nadir toprak hekzaborürlerinin kristal formlarının sentezlenmesi için yine geleneksel yöntemler olarak zon ergitme yöntemi ve elektrolitik yöntemler de geliştirilmiştir. Araştırmacılar, nadir toprak hekzaborürlerini partikül, tel, tüp, çubuk, küp ya da sütun gibi farklı yapılarda elde etmek üzere farklı üretim teknikleri üzerinde uzun yıllardır çalışmaktadır. Son yıllarda, nano-ölçekli ya da mikron altı küp ve çubuksu yapıya sahip nadir toprak hekzaborür tozları, otoklavda düşük sıcaklıkta sentezleme ve atmosferik koşullar altında kendiliğinden ilerleyen yüksek-sıcaklık sentezleme (SHS) yöntemleri kullanılarak üretilmişlerdir. Bunun yanında, tel, çubuk, tüp, küp yada sütun

formlarındaki nano- ve mikro-boyutlardaki nadir toprak hekzaborürleri geleneksel yada modifiye edilmiş kimyasal buhar biriktirme (CVD) teknikleri ile üretilmiştir. Ayrıca, sinter ürün haline getirilmiş nadir toprak hekzaborürlerinin yüksek plastik akma gerilmesine sahip olmaları nedeniyle, klasik presleme ve sinterleme yöntemleri ile yüksek relatif yoğunluklarda kolayca elde edilemediği belirtilmiştir. Genel olarak, yüksek yoğunluklu, sinterlenmiş nadir toprak hekzaborürlerini elde etmek için spark plasma sintering (SPS) yöntemi kullanılmıştır. Buna rağmen, nadir toprak hekzaborürlerinin sinter ürün haline getirilmiş yoğunluklarının geliştirilmesi gerekmektedir ve sinterleme prosesi literatürde detaylı olarak incelenmemiştir. Sonuç olarak, teknolojik önem arz eden bu tozları yüksek safiyette, ince partiküller halinde ve çeşitli morfolojilerde elde etmek ve bununla birlikte bu tozlara ait sinterlenmiş parçaları hazırlamak üzere etkin yöntemlerin geliştirilmesi oldukça önemlidir. Özellikle kolay ulaşılabilir hammaddelerden yola çıkan, düşük reaksiyon sıcaklığı ve süresi gerektiren, daha az ekipman kullanan, düşük maliyetli yeni sentezleme prosesleri giderek daha ilgi çekici hale gelmektedir.

Bu tez çalışmasında, yukarıda bahsedilen toz üretim tekniklerinden farklı olarak, saf ince taneli hekzaborür tozlarının oda sıcaklığında üretimi için alternatif bir yöntem kullanılmış ve geliştirilmiştir. Bu yöntem yüksek enerjili bilyalı değirmenlerde gerçekleşen katı-hal reaksiyonlarını içermektedir ve mekanokimyasal sentezleme olarak isimlendirilmektedir. Mekanokimyasal sentezleme, klasik üretim teknikleri ile elde edilmeleri oldukça zor ya da imkansız olan oksit dağılımıyla mukavemetlendirilmiş alaşımlar, amorf malzemeler, katı çözelti alaşımları, denge koşulları dışındaki alaşımlar, intermetalik bileşikler, nanokompozitler, seramikler ve ileri teknoloji malzemelerinin hızlı üretimini mümkün kılmaktadır. Prosesin temel mekanizması ham maddelerin tekrarlı olarak kaynaklanma, kopma ve tekrar kaynaklanma olaylarına dayanmaktadır. Bu yöntem, öğütücü tipi, öğütme ortamının malzemesi, öğütücü bilyaların boyut ve boyut dağılımları, öğütme hızı, bilya-toz ağırlık oranı, öğütme kabının doluluk oranı, öğütme atmosferi, kullanılan proses kontrol ajanları ve öğütme sıcaklığı gibi çeşitli faktörler ile kontrol edilir.

Bu doktora tezi ile LaB_6, CeB_6 ve SmB_6 tozları literatürde ilk kez olarak oda sıcaklığında yürütülen mekanokimyasal sentezleme prosesi ile sentezlenmiştir. Bu nadir toprak hekzaborürlerinin sentezlenmesi için lantan, seryum ve samaryum metallerinin La_2O_3, CeO_2 ve Sm_2O_3 gibi oksitlerinden yola çıkılmıştır. Hekzaborür fazlarının oluşumu için yerli bir bor kaynağı olan B_2O_3 tozları kullanılmıştır. Deneylerde kullanılan Mg tozları kuvvetli bir metalik indirgeyici ajandır. İndirgeyici ajan etkisini gözlemlemek adına indirgeyici ajan alternatifi olarak Ca granülleri kullanılmış ve LaB_6 oluşumu üzerindeki etkisi belirlenmiştir. LaB_6 tozlarının ideal üretim koşullarını ortaya koymak için mekanokimyasal sentezleme parametreleri olarak öğütme süresi, bilya-toz ağırlık oranı, öğütücü tipi ve proses kontrol ajanı üzerinde durulmuştur. CeB_6 ve SmB_6 tozlarının mekanokimyasal sentezi, LaB_6 tozlarının sentezlenmesi sırasında belirlenen optimum proses parametreleri kullanılarak gerçekleştirilmiştir. Mekanokimyasal olarak sentezlenmiş LaB_6, CeB_6 ve SmB_6 tozları, yüksek saflıkta hekzaborür tozlarının elde edilmesi için selektif HCl liçine tabi tutulmuştur. Mekanokimyasal sentezleme ve liç işlemlerinin ardından, saf LaB_6, CeB_6 ve SmB_6 tozları sentezi için optimum koşullar saptanmıştır: Polikristalin LaB_6, CeB_6 ve SmB_6 tozlarının 50-90 nm arasında değişen partikül boyutları ile minimum % 99,99 safiyette eldesi başarılmıştır. Laboratuvar ortamında sentezlenmiş bu tozlar birbirleri ve piyasada satılan ticari tozlar ile mikroyapısal, fiziksel

(yoğunluk ve yüzey alanı) ve manyetik özellikler açısından karşılaştırılmıştır. Bunu takiben, mekanokimyasal sentezleme ve liç işlemlerinden sonra yüksek kalitede elde edilen LaB_6, CeB_6 ve SmB_6 tozları soğuk presleme ve basınçsız sinterleme prosesleri ile sinterlenmiştir. Sinterlenmiş LaB_6, CeB_6 ve SmB_6 numunelerinin; mikroyapı, yoğunluk, elektriksel direnç, yüzey pürüzlülüğü, sürtünme katsayısı, sertlik ve aşınmadan kaynaklanan relatif hacim kaybı özellikleri araştırılmış ve birbirleri ve ticari eşdeğerleri ile karşılaştırılmıştır.

Ayrıca bu tez kapsamında Türkiye'nin sahip olduğu zengin bor kaynaklarının (yaklaşık dünya bor rezervlerinin % 72'si), ileri teknoloji bor ürünlerine dönüştürülmesinin olanakları araştırılmıştır. Ülkemizde henüz hiçbir ileri teknoloji bor ürünün kitlesel üretimi bulunmamaktadır. Bu durumun aşılması, ham ve rafine bor ürünlerinin ileri teknoloji bor ürünlerine doğru geliştirilmesini konu edinen laboratuvar çalışmalarının desteklenmesi ile mümkündür. Bununla birlikte, Türkiye çeşitli ayrıştırma ve saflaştırma işlemleri gerektiren sınırlı miktarda lantanit grubu rezervlerine de sahiptir. Sonuç olarak, bu tez çalışması yerli bor kaynaklarından ve yerli lantanit grubu kaynaklarından yola çıkma fikrini ortaya atarak ülke için katma değer yaratabilecek yüksek teknoloji bor malzemelerinin üretimini amaç edinmiştir.

1. INTRODUCTION

Materials based on boron compounds have been explored since 1950s because of their superior properties in respect to chemical bonding, crystal structure and phonon and electron conduction. Especially, rare-earth metal hexaborides have numerous useful physical and chemical characteristics which make them important to investigate (Post et al, 1956; Futamoto et al, 1980; Otani and Ishizawa, 1996; Balakrishnan et al, 2004; Selvan et al, 2008; Wang et al, 2010; Ji et al, 2011; Brewer et al, 2011; Aprea et al, 2013). Lanthanum hexaboride (LaB_6), cerium hexaboride (CeB_6) and samarium hexaboride (SmB_6) have attracted significant interest amongst transition metal borides and rare-earth metal borides (Samsonov et al, 1963; Paderno et al, 1979; Mitterer et al, 1996; Chen et al, 2004; Baranovskiy et al, 2007; Brewer et al, 2007; Loboda et al, 2009; Petrosyan et al, 2012; Xu et al, 2012; Dou et al, 2012). They are refractory ceramic materials characterized by high melting point, high strength, high rigidity, high chemical and thermal stability (insoluble in water and HCl), low vapor pressure (at high temperature), low electronic work function, low resistivity, low expansion coefficient (in some temperature ranges), high transmission stability, high current and voltage capability and high neutron absorbability (Gao et al, 2005; Xu et al, 2006; Zhang et al, 2008a; Selvan et al, 2008). LaB_6, CeB_6 and SmB_6 have the cubic CsCl structure with a space group of *Pm3m* symmetry, in which rare-earth metal ions and boron atoms occupy the Cs site and the octahedral sites, respectively (Perkins et al, 1999; Kanakala, 2008). The structure of these borides is built from B_6 type (octahedrons in cubic hexaborides) which boron sublattice is electron-deficient and requires electron transfer from the metal atoms in order to be stabilized (Swanson and McNeely, 1979; Mitterer et al, 1996). Furthermore, these boron octahedrons are united by very strong covalent bonds giving the crystals their characteristic hardness (Ji et al, 2011). LaB_6 and CeB_6 are defined as dense Kondo materials which show several interesting phases such as antiferro-quadrupolar ordered phase and antiferromagnetic ordered phase in the effect of magnetic field and temperature (Tanaka et al, 2004; Carlsson et al, 2005;

Jha et al, 2012a). SmB_6 is defined as a classic fluctuating-valence semiconductor which has an intermediate valence state and as a Kondo insulator (Ji et al, 2011).

All the superior properties of LaB_6, CeB_6 and SmB_6 make them candidates for several applications such as high-energy optical systems, sensors for high resolution detectors, electrical coatings for resistors (Balakrishnan et al, 2004; Bao et al, 2011b). Moreover, rare-earth nanomaterials are candidates to motivate the new designs of nanoscale electronic devices operated at high temperatures with the need of enhanced electron collection and injection properties (Brewer et al, 2011). Single crystalline rare-earth metal hexaboride nanowires are used as electron emitter for electron emission cathode in electron gun due to the fact that the single crystal possesses excellent emission current stability (Qin et al, 2010; Bao et al, 2011b). Rare-earth hexaborides are also used in electronic devices that require high performance electron sources (Qin et al, 2010). The rare-earth hexaborides have exceptional thermoelectric properties at low temperatures providing their usage in solid-state cryocooling, thermoelectric refrigerators, generators and single-photon detectors operating at temperatures near to the boiling point of liquid helium which serve in technical applications including quantum computing, quantum cryptography, homeland security, defect control in microchips, astronomy, chemical analysis and particle physics (Carlsson et al, 2005; Petrosyan et al, 2012; Jha et al, 2012a).

Many production techniques have been applied in the preparation of rare-earth borides. Traditionally, rare-earth borides are synthesized by high temperature reaction processes such as direct solid-phase reaction of the corresponding elements/compounds, carbothermal reaction of the rare-earth oxides and B or boron carbide (B_4C) method (Post et al, 1956). In industry, carbothermal reduction and boron carbide method are widely used due to their low cost and simple equipment (Dou et al, 2011c; Hasan et al, 2013). However, disadvantages in these methods such as high content of carbon or high processing temperature limit the possibility of preparing boride powders with high purity and small particle sizes (Dou et al, 2012). Moreover, powders prepared by these conventional methods have generally poor sintering property (Dou et al, 2012). Floating zone method and electrosynthesis have been also developed conventionally in order to obtain crystal structures of rare-earth hexaborides (Verhoeven et al, 1976). Essentially, floating zone method is carried out to produce single crystals of hexaborides by using laser or RF heating (Otani and

Ishizawa, 1996; Otani et al, 2000). Electrosynthesis of hexaboride crystals is applied by molten salt technique from an electrolyte consisting of respective chlorides/oxides, boron sources (B_2O_3, $Li_2B_4O_7$, etc.) and chloride/fluoride agents (LiCl, LiF, etc.) (Amalajyothi et al, 2008; Amalajyothi et al, 2011). For a number of years, researchers have been trying to obtain rare-earth hexaborides in different forms such as particles, whiskers, rods or cubes using various fabrication techniques. Recently, nano-scaled (nanocubes and nanorods) or submicron rare-earth hexaboride powders were obtained by using low temperature synthesis in an autoclave and self-propagating high-temperature synthesis (SHS) methods (Ji et al 2011; Dou et al, 2012). Autoclave systems provide an alternative route for obtaining borides at lower temperatures than used in traditional methods (Wang et al, 2010). SHS methods have high reaction speed, simple equipment and low energy consumption but after ignition, the reaction process becomes uncontrolled which results in the occurence of intermediate phases in the reaction products (Dou et al, 2011c). Rare-earth hexaboride whiskers, wires, tubes and obelisks in nano or micro-scales were produced by chemical vapor deposition technique (CVD) (Motojima et al, 1978; Zhang et al, 2006). CVD methods include self-catalyst or metal-catalyst (Au, Pt, etc.) growth of hexaborides on a substrate based on the catalytic reaction of rare-earth element/compound containing powders and boron (BCl_3, $B_{10}H_{14}$, etc.), hydrogen and argon containing gas mixtures (Ji et al, 2011).

Therefore, it is significant to develop an efficient method of preparing technologically important hexaboride powders with high purity, small particle size and various morphologies. It has been attracting more attentions to find new synthesis strategies with low reaction temperature, easy to handle precursors, simple process control, less equipment requirements and low cost (Selvan et al, 2008).

Apart from the above-mentioned production techniques, mechanochemical synthesis is a novel, simple and room temperature process which enables a great degree of controlling the product microstructure (content, shape, size, etc.) and obtaining highly pure materials (Suryanarayana, 2001). To the best of our knowledge, there is recently one report involved ball milling process on the fabrication of CeB_6 powders (Liu et al, 2010; Akgun et al, 2013). It has been also reported that rare-earth haxaborides in the bulk forms can not be prepared easily via conventional hot-pressing method with high density due to their high plastic yield stress (Bao et al,

2011a). Although the development of bulk density is essential, sintering process of rare-earth hexaborides has not been comprehensively investigated in the literature. In generel, spark plasma sintering (SPS) method is used to obtain high density sintered bodies (Zhou et al, 2009; Bao et al, 2011a).

In this dissertation, mechanochemical synthesis process will be carried out for the production of LaB_6, CeB_6 and SmB_6 powders for the first time in the literature. Although mechanochemical synthesis method was established in 1970s, the production studies of the mentioned lanthanide group hexaborides have been started in 1956 and have become intense after 2000s. However, literature findings prove that the production of the mentioned hexaborides has not been performed by mechanochemical synthesis yet. This dissertation will introduce a novel, simple and room temperature process for the production of LaB_6, CeB_6 and SmB_6 powders and consequently it will contribute the first results of the mechanochemically synthesized LaB_6, CeB_6 and SmB_6 powders to the archival literature. This novel and simple process will be conducted on the stoichiometric La_2O_3-B_2O_3-Mg, La_2O_3-B_2O_3-Ca, CeO_2-B_2O_3-Mg and Sm_2O_3-B_2O_3-Mg powder blends. After mechanochemical synthesis, a subsequent purification process, selective HCl leaching, will be utilized for the obtainment of LaB_6, CeB_6 and SmB_6 powders in high purity. So, the synthesis of LaB_6, CeB_6 and SmB_6 powders in high purity will contain a two step route containing mechanochemical synthesis and HCl leaching. The mechanochemical process parameters such as milling duration, ball-to-powder weight ratio, type of mill and process control agent will be tested on the synthesis of LaB_6 powders. The latter syntheses of CeB_6 and SmB_6 powders will be carried out in the light of the optimized parameters determined in the synthesis of LaB_6. Besides, experimental results will be evaluated according to the thermodynamical interpretations. After all powder production experiments will be completed, some yielded products will be selected as the ideal laboratory-synthesized powders. After that, laboratory-synthesized LaB_6, CeB_6 and SmB_6 powders will be compared with each other and their commercial ones in terms of microstructural, physical (density and surface area) and magnetic properties. Conventional consolidation process including cold pressing and pressureless sintering will be conducted on the selected laboratory-synthesized LaB_6, CeB_6 and SmB_6 powders. Finally, the bulk properties of the sintered LaB_6, CeB_6 and SmB_6 originated from the laboratory-synthesized powders will be elaborated in terms

of microstructure, density, electrical resistivity, roughness, friction coefficients, hardness and relative wear volume loss and will be compared with each other and those of commercial ones.

2. LITERATURE REVIEW

2.1 Lanthanum, Cerium and Samarium Hexaborides

Lanthanum hexaboride (LaB_6), cerium hexaboride (CeB_6) and samarium hexaboride (SmB_6) which are refractory ceramic materials have taken considerable interest amongst transition metal borides and rare-earth metal borides due to their superior properties. They are characterized by high melting point, high strength, high rigidity, high chemical and thermal stability such as insolubility in water and HCl, low vapor pressure at high temperature, low electronic work function, low resistivity, low expansion coefficient in some temperature ranges, high transmission stability, high current and voltage capability and high neutron absorbability (Gao et al, 2005; Xu et al, 2006; Zhang et al, 2008a; Selvan et al, 2008).

All these excellent properties make these hexaborides suitable to use as component of high-energy optical systems, sensors for high resolution detectors, electrical coatings for resistors, coatings for high-current hot cathodes, decorative coatings, thermionic materials and to use in nuclear technology (Xu et al, 2006; Xu et al, 2008a; Zhang et al, 2008b).

2.1.1 Physical and chemical properties

Rare-earth metal hexaborides are refractory ceramic materials which are stable in vacuum having the highest electron emissivity known up to now. Rare-earth metal borides have non-stoichiometric composition ranges (Otani and Ishizawa, 1996). The rare-earth metals (RE) and boron form several compounds with B/RE molar ratio varying between 1:4 and 66:1 which its higher values result in the exceptional self-binding ability of boron atoms occuring as isolated atoms, pairs, chains, two-dimensional networks or three-dimensional frameworks in the compounds (Meschel and Kleppa, 1995). In a detailed study of both equilibrium and non-equilibrium vaporization of LaB_6, it was stated that the vaporization rate was dependent on the variations in the bulk stoichiometry of La and B and the minimum vaporization rate

of LaB_6 was obtained at the stoichiometry of B/La≅6.1 (Swanson and McNeely, 1979). Unlikely, in a study on the thermionic emission properties of boron-rich LaB_6 and CeB_6 crystal cathodes, it was reported that the evaporation rates of LaB_6 and CeB_6 decreased with the increase in the boron content which provide two to four times longer lifetime to the boron-rich cathodes than the stoichiometric commercial cathodes, independent from the emission properties (Otani and Ishizawa, 1996).

The binary phase diagrams of La-B, Ce-B and Sm-B systems respectively given in Figure 2.1(a)-(c) illustrate the stable (LaB_6, LaB_4, CeB_6, CeB_4, SmB_6, SmB_4, SmB_{65}) and unstable (LaB_9, Sm_2B_5) boride phases that can be formed during the proposed experimental procedure (Massalski et al, 1990; Schlesinger et al, 1999). The phase diagram of the La-B system shows one congruently melting compound LaB_6 (at 2715°C), a peritectic phase LaB_4 (at 1800°C) and an unstable phase LaB_9 (at ~2007°C). The phase diagram of the Ce-B system shows one congruently melting compound CeB_6 (at 2550°C) and a peritectic phase CeB_4 (at 2380°C). The phase diagram of the Sm-B system shows one congruently melting compound SmB_6 (at 2580°C), peritectic phases SmB_4 and SmB_{65} (respectively at ~2400 and 2150°C) and an unstable compound Sm_2B_5 (owning undefined melting point) (Massalski et al, 1990).

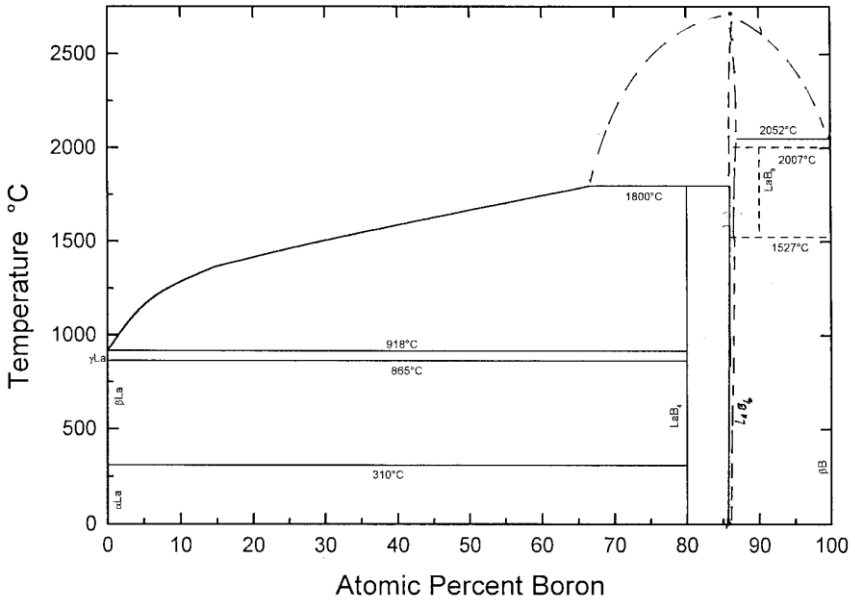

Figure 2.1 : Binary phase diagrams of rare-earth metal-boron systems: (a) La-B, (b) Ce-B and (c) Sm-B, adapted from Massalski et al (1990) and Schlesinger et al (1999).

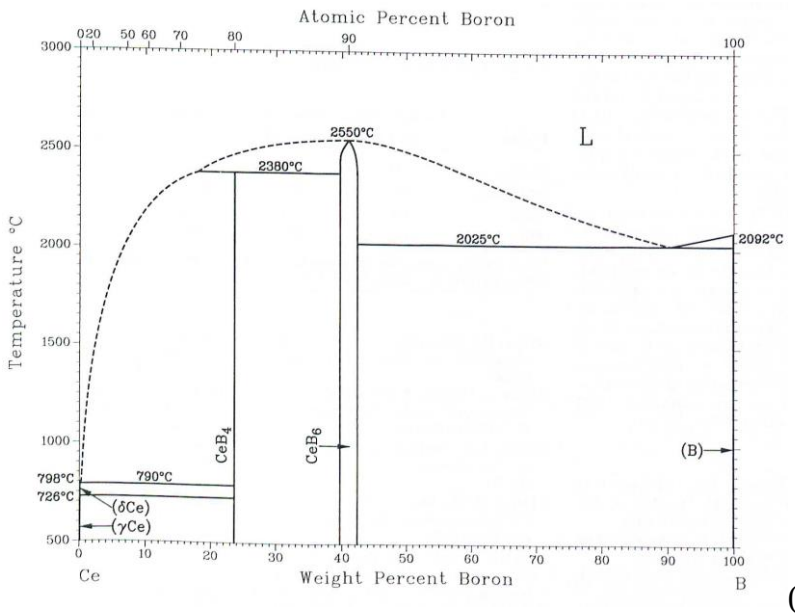

(b)

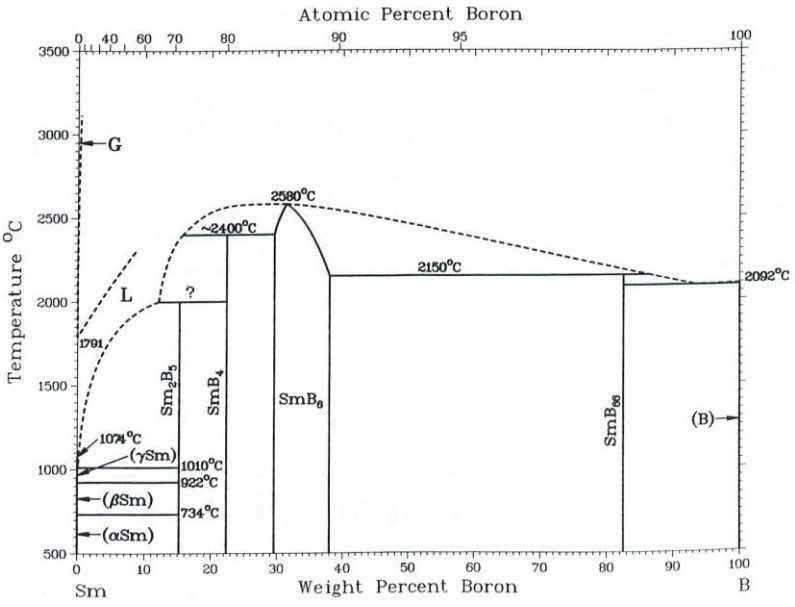

(c)

Figure 2.1 (continued) : Binary phase diagrams of rare-earth metal-boron systems: (a) La-B, (b) Ce-B and (c) Sm-B, adapted from Massalski et al (1990) and Schlesinger et al (1999).

LaB_6, CeB_6 and SmB_6 have the cubic CsCl structure with a space group of *Pm3m* symmetry, in which rare-earth metal ions and boron atoms occupy the Cs site and octahedral site, respectively (Perkins et al, 1999; Kanakala, 2008). A schematic representation of the crystal structure of REB_6 type compounds is given in Figure 2.2 (Kanakala, 2008). The boron atoms have a size and an electronic structure allowing them to form direct boron-boron bonds (Swanson and McNeely, 1979; Jha et al, 2012b). The structure of these borides is built from B_6 type (octahedrons in cubic

hexaborides) which boron sublattice is electron-deficient and requires electron transfer from the metal atoms in order to be stabilized (Swanson and McNeely, 1979; Mitterer et al, 1996). Furthermore, these boron octahedrons are united by very strong covalent bonds giving the crystals their characteristic hardness (Ji et al, 2011). Thus, they are very hard due to the strong covalent bonds of boron atoms in the structure (Ji et al, 2011).

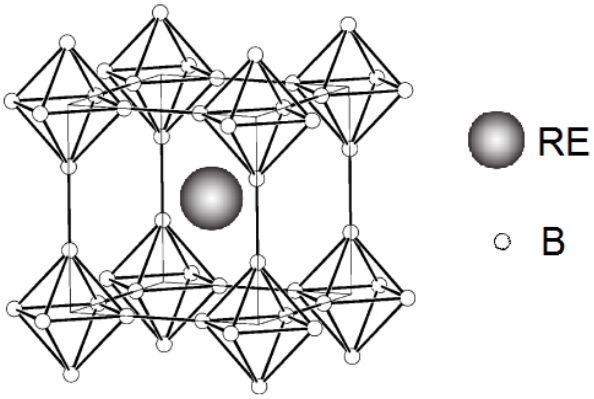

Figure 2.2 : Crystal structure of REB_6 type compounds, adapted from Kanakala (2008).

As an approximation, the octahedron can be thought as a pseudomolecule, $B^* \equiv B_6$, which the bonds between each pseudomolecule and the six neighboring octahedra form a three-dimensional boron sublattice (Popov et al, 2007). It was stated in an article relating the thermal conductivity of LaB_6 and CeB_6 that each metal atom in the SmB_6 is surrounded by such octahedra and by 24 equidistant boron atoms (Popov et al, 2007). The three-dimensional boron-framework positively contributes to the properties of SmB_6. In other words, the covalent bonding within the boron polyhedral is responsible for the stability, hardness and high melting point (Berchmans et al, 2010). However, in earlier studies carried out on the structure refinements of SmB_6, there was a contradiction about which site (metal or boron site) contains the occurence of vacancies and the complete occupancy (Trunov et al, 1991; Trunov et al, 1993).

LaB_6 and CeB_6 have been defined as dense Kondo materials which show several interesting phases such as antiferro-quadrupolar ordered phase and antiferromagnetic ordered phase in the effect of magnetic field and temperature (Tanaka et al, 2004; Carlsson et al, 2005; Jha et al, 2012a). On the other hand, SmB_6 has been defined as a classic fluctuating-valence semiconductor which has an intermediate valence state

and as a Kondo insulator (Ji et al, 2011). SmB_6 is a typical intermediate-valence material characterized by an energy gap near the Fermi level like a semiconductor (Trunov et al, 1993; Popov et al, 2007). It is also named as a classical fluctuating-valence semiconductor or heavy electron (fermion) semiconductor and a Kondo insulator (Macedo and Souza, 2002; Xu et al, 2008a). In a study related with the thermodynamic properties of SmB_6, it was reported that the valence fluctuation phenomena occured in SmB_6 leads to instabilities of the charge configuration and of the magnetic moment (Macedo and Souza, 2002). As known by the physicists for a long time, Kondo insulators are fermion materials where the local magnetic moments are screened by the itinerant electrons and the hybridisation of these conduction electrons with the magnetic moments under a certain temperature results in an energy gap formation in the density of states (Hatnean et al, 2013). Currently, SmB_6 is predicted to be a topological Kondo insulator which exhibits topological surface properties (Hatnean et al, 2013). SmB_6 behaves as an insulator to metal transition at around -223°C which coincides with the opening of the gap in accordance with the Kondo behavior and the resistivity shows a saturation behavior at low temperatures (-268°C) unlike the most insulators in which the resistivity continues to increase (Menth et al, 1969; Allen et al, 1979; Cooley et al, 1995; Hatnean et al, 2013). Furthermore, when SmB_6 is subjected to an ambient pressure, it becomes a mixed valence material showing antiferromagnetic correlations without magnetic ordering. Under increasing pressures, SmB_6 starts to have a metallic and magnetically ordered state (Barla et al, 2005; Miyazaki et al, 2012).

General properties of LaB_6, CeB_6 and SmB_6 are summarized in Table 2.1 (Landolt, 1984; Chen et al, 2003; Popov et al, 2007; Zhang et al, 2010a; Bakr et al, 2011; Bao et al, 2012; Url-1; Url-2; Url-3; Url-4; Url-5; Url-6; Url-7). As seen from Table 2.1, LaB_6, CeB_6 and SmB_6 have high melting point, high hardness, high thermal conductivity and high young modulus. LaB_6 and CeB_6 possess very low work functions which are lower than any other known materials except YB_6 (2.22 eV). SmB_6 has a relatively lower work function (3.11-4.4 eV) which can make it a candidate for applications such as thermionic emission, field-induced emission and thermal field-induced emission materials (Xu et al, 2008a; Xu et al, 2009). Therefore, in the current literature, the low work function property of rare-earth hexaborides (especially for SmB_6) has attracted great interest by physicists.

Table 2.1 : General properties of LaB_6, CeB_6 and SmB_6, adapted from Landolt (1984), Chen et al (2003), Popov et al (2007), Zhang et al (2010a), Bakr et al (2011), Bao et al (2012), Url-1, Url-2, Url-3, Url-4, Url-5, Url-6, Url-7.

Properties	**LaB_6**	**CeB_6**	**SmB_6**
Theoretical density (g/cm^3)	4.7	4.79	5.07
Melting point (°C)	2483-2715	2463-2580	2550
Work function (eV)	2.6	~2.5	~3.11-4.4
Hardness (HV)	2070-2825	~2530	2450-2500
Electrical resistivity (μΩ.cm)	8.9 - 50	~29-65	150-300
Thermal conductivity (W/m.K)	110-147	33-124	13.8-19.6
Thermal expansion coefficient (10^{-6}/K)	5.6-6.4	6.8-7.8	6.5-6.8
Young modulus (GPa/mm^2)	392-470	379	-

As generally known, surfaces exhibiting low work function values own low vaporization heat with respect to one or more of the surface constituents (Swanson and McNeely, 1979). Otherwise, high volatility of the surface constituents causes undesirable contamination of a neighboring electrode surface or limited cathode life (Swanson and McNeely, 1979). Thus, rare-earth hexaborides are useful in developing high brightness cathodes due to their unusual combination of metallic-like electrical and thermal conductivities with a low surface work function, high melting point and low volatility (Swanson and McNeely, 1979). Amongst the rare-earth hexaborides, the order of increasing work function was determined as $CeB_6<LaB_6<SmB_6$ that surfaces having low work function were correlated with low B/RE ratios (Swanson and McNeely, 1979).

Earlier measurements carried out on the work function of polycrystalline LaB_6 revealed that they ranged from 2.4 to a maximum value of 3.2 eV. The desorption of an oxide layer through volatilization of B_2O_3 and LaO could cause change in the surface stoichiometry and hence cause variation in the work function of LaB_6 (Swanson and McNeely, 1979). The variation in the work functions of the crystals could be attributed to the shift of the conduction band edge relative to the Fermi level, suggesting the probability of work function adjustment by stoichiometric variation or impurity doping (Swanson and McNeely, 1979).

Some changes present in the order from SmB_6 to LaB_6 can be established as the increase in the length of metal-metal and metal-boron bonds which results in weakening of their metallic characters, the increase in the transfer of electrons from the metal atoms to the boron atoms, the increase in the tendency of boron atoms to

form a stable sp^3 electron state, the decrease in the microelasticity of the hexaborides, the decrease in the resistance to the formation of the cracks and hence the increase in the fragility of the compounds (Paderno et al, 1979; Trunov et al, 1993). The brittleness of the rare-earth hexaborides limits the surface treatment conditions which is neccessary for eliminating surface microcracks (Paderno et al, 1979).

SmB_6 can resist a greater degree of deformation without destruction than the rest of hexaborides. This is due to the identical crystallographic positions of Sm atoms in the simple cubic sublattice and due to the existence of Sm ions in various valence states (Paderno et al, 1979; Trunov et al, 1993).

Thermal conductivity of the LaB_6 crystals prepared by floating-zone method was an order of magnitude higher than that of semiconductor SmB_6 crystals synthesized with the same method up to 27°C (Popov et al, 2007). It was also stated that low temperature thermal and electrical conductivities of LaB_6 and SmB_6 were very sensitive to their structural perfection (Popov et al, 2007).

2.1.2 Application areas

All superior properties of LaB_6, CeB_6 and SmB_6 make them candidates for several applications such as high-energy optical systems, sensors for high resolution detectors, electrical coatings for resistors (Balakrishnan et al, 2004; Bao et al, 2011b). Moreover, rare-earth nanomaterials are candidates to motivate the new designs of nanoscale electronic devices operated at high temperatures with the need of enhanced electron collection and injection properties (Brewer et al, 2011). Single crystalline rare-earth metal hexaboride nanowires are used as electron emitters for electron emission cathode in electron gun due to the fact that the single crystal possesses excellent emission current stability (Bao et al, 2011b; Qin et al, 2010).

Rare-earth hexaborides are also used in electronic devices that require high performance electron sources (Qin et al, 2010). Thus, they can be utilized for direct thermal-to-electrical converters, analytical instrumentation, electron beam lithographic system, focused ion beam system, electron beam welding, transmission electron microscope (TEM), scanning electron microscope (SEM), microwave tubes, computed tomography, flat panel displays, digital fluoroscopy, radiography and portable X-ray machine (Qin et al, 2010; Xu et al, 2012).

The rare-earth hexaborides have exceptional thermoelectric properties at low temperatures providing their usage in solid-state cryocooling, thermoelectric refrigerators, generators and single-photon detectors operating at temperatures near the boiling point of liquid helium which serve in technical applications including quantum computing, quantum cryptography, homeland security, defect control in microchips, astronomy, chemical analysis and particle physics (Carlsson et al, 2005; Petrosyan et al, 2012; Jha et al, 2012a). A CeB_6-based thermoelectric detector whose operational temperature is above 4 K can record a single photon with high spectral resolution and high counting rate, implying that it reduces the cost and simplifies the application compared with the superconducting detectors (Petrosyan et al, 2012).

The crystal structure of rare-earth hexaborides which consists of rare-earth metal atoms embedded inside a stable boron octahedron network provides the advantage of using them as thermionic cathode materials (Zhang et al, 2005). This atomic arrangement results in a unique combination of all the desired properties for the utilization in electron beam applications.

High-quality rare-earth hexaboride targets in the form of billets or rods for evaporation and plates for sputtering are generally fabricated by powder metallurgy methods such as sintering or hot pressing with 70-85 % of their theoretical density (Mitterer et al, 1996). Furthermore, it was also reported that the conventional solid phase hot-pressing method is difficult to prepare highly densified rare-earth hexaborides due to their high plastic yield stresses (Bao et al, 2011a).

Rare-earth hexaborides can be used in wear and corrosion resistant hard coatings for decoration of consumer products such as eye-glass frames and wristwatch casings (Mitterer et al, 1996; Selvan et al, 2008). It was stated that they were easily deposited in the amorphous form or fine-grained structure by physical vapor deposition (PVD) method thanks to the strong directionality of the covalent boron-boron bonds (Mitterer et al, 1996).

Field emission current density should be high for the cathode materials designed to be used in field-induced electron emission applications, which offer 100 or more times higher brigthness than a thermionic electron source (Zhang et al, 2005). Brewer et al (2007) reported that electron emitters made of materials with high aspect ratio tips and low work function enhanced field emission current with low

applied voltage. It was also stated that geometric factors of the electron emitters such as shapes and aspect ratios extremely affected the local electric field at the tips and field emission current in various nanomaterials systems though the difficulty in producing nanomaterials with different geometric tip shapes and diameters was well known (Brewer et al, 2007). Thus, the development of field emission cathodes depends on making sharp tips from rare-earth hexaborides having convenient morphological, physical and mechanical properties to the sequential shaping processes.

LaB_6 is one of the most widely used thermionic emitter which offers better performance (higher emission current density, higher brightness, higher emission stability, lower energy spread and longer service life) than tungsten cathodes in a large variety of devices such as high-resolution electron microscopes, electron beam writing units, vacuum electron beam welding machines, electron beam surface reforming and lithography devices, microwave tubes, free electron lasers and X-ray tubes (Ahmed et al, 1975; Perkins et al, 1999; Chen et al, 2004; Wen et al, 2004; Zhang et al, 2006; Zhang et al, 2007; Zhang et al, 2008a; Wang et al, 2009). It has the highest electronic emissivity of any known material and its performance is unaffected by the presence of nitrogen (N_2) or oxygen (O_2) up to 700ºC (Xu et al, 2006, Wen et al, 2004; Futamoto et al, 1980). Recently, LaB_6 nanoparticles have been proved as effective materials in near-infrared absorption enabling application in reduction of solar heat gain (Yuan et al, 2011). Additionally, LaB_6 was considered as a potential grain refining agent in Al alloys due to its act as an effective, stable and reliable nucleation substrate for Al during the solidification process (Li et al, 2012).

The LaB_6 nanowires with a 140 nm diameter was found to have an emission current density in the same order of magnitude as that of carbon nanotubes having 10-50 times smaller diameter (Brewer et al, 2007). Thinner LaB_6 wires were predicted to provide better stability and field emission performance considering that the structurally robust materials with smaller tip diameters are less susceptible to thermal vibrations and mechanical stresses (Brewer et al, 2007).

In a study related with the thermionic emission properties of hexaborides, LaB_6 was reported to have the highest emission current density amongst other single crystal hexaborides as CeB_6, PrB_6, NdB_6, SmB_6 and EuB_6 and amongst LaB_6-based mixed

hexaborides as $(La,Sr)B_6$, $(La,Ba)B_6$, $(La,Ce)B_6$, $(La,Pr)B_6$, $(La,Sm)B_6$ and $(La,Dy)B_6$ in the temperature range between 1250 and 1700°C due to its relatively slow evaporation rate (Futamoto et al, 1980). However, in different investigations on rare-earth hexaborides, it was reported that CeB_6 has a lower work function (~2.5 eV) than that of LaB_6 (~2.72 eV) which means a higher brightness, a smaller optical size, a higher monoenergetic electron character, a lower volatility, lower operation temperature, longer service life and higher electrical resistance when used as a thermionic electron emitter (Zhang et al, 2009; Zhang et al, 2005; Selvan et al, 2008). Besides, CeB_6 cathodes have one and half of the LaB_6 cathodes' lifetime due to their higher resistance to the carbon contamination (Swanson and McNeely, 1979).

Polycrystalline and single crystalline CeB_6 can be utilized to fabricate various devices such as field emitter arrays (FEAs) because of their larger sizes, low cost, simple preparation and superior field or thermionic emission properties, compared with the nanowires, nanorods, nanotubes and films (Bao et al, 2011a; Bao et al, 2011b).

According to a study on the thermionic emission property of CeB_6, single crystalline CeB_6 which its all diffraction spots were independent of the high axial symmetry had two times larger emission current density than that of polycrystalline one at temperatures between 1400 and 1600°C (Bao et al, 2011b). This can be explained with the obstruction of the electron transport by the grain boundaries of polycrystalline materials which it leads to an increase in the work function of the polycrystalline one (2.6 eV) compared to that of the single crystalline (2.44 eV) (Bao et al, 2011b).

High quality CeB_6 thin films were deposited by direct evaporation (which is based on the simple physical vapor deposition process) of micron-sized CeB_6 powders placed in a BN crucible in a vertical induction furnace operated at a temperature of 1700°C and at a pressure of 70 Pa for 3 h (Xu et al, 2012).

Fully densified polycrystalline CeB_6 cathode material was prepared by spark plasma sintering (SPS) method starting from CeB_6 nanopowders ball milled to result in average sizes of 50 nm, less than 3 h with a rotation speed of 500 rpm and with a BPR of 20:1 using stainless steel balls, in an oxygen free system at 1550°C under 50 MPa (Bao et al, 2011a).

2.2 Production Techniques

Many production techniques have been applied in the preparation of rare-earth borides (Post et al, 1956; Samsonov et al, 1963; Paderno et al, 1979; Futamoto et al, 1980; Mitterer et al, 1996; Otani and Ishizawa, 1996; Balakrishnan et al, 2004; Chen et al, 2004; Baranovskiy et al, 2007; Brewer et al, 2007; Selvan et al, 2008; Loboda et al, 2009; Wang et al, 2010; Ji et al, 2011; Brewer et al, 2011; Dou et al, 2012; Petrosyan et al, 2012; Xu et al, 2012; Aprea et al, 2013). Traditionally, rare-earth borides are synthesized by high temperature reaction processes such as direct solid-phase reaction of the corresponding elements/compounds, carbothermal reaction of the rare-earth oxides and B or boron carbide method (B_4C method) (Post et al, 1956). In industry, carbothermal reduction and boron carbide methods are widely used due to their low cost and simple equipment (Dou et al, 2011c; Hasan et al, 2013). However, disadvantages in these methods such as high content of carbon or high processing temperature limits the possibility of preparing boride powders with high purity and small particle sizes (Dou et al, 2012). Moreover, powders prepared by these conventional methods have generally poor sinterability (Dou et al, 2012).

Floating zone method and electrosynthesis have also been developed conventionally in order to obtain crystal structures of rare-earth borides (Verhoeven et al, 1976). Essentially, floating zone method is carried out to produce single crystals of hexaborides by using laser or RF heating (Otani and Ishizawa, 2000). Electrosynthesis of hexaboride crystals is applied by molten salt technique from an electrolyte consisting of respective chlorides/oxides, boron sources (B_2O_3, $Li_2B_4O_7$, etc.) and chloride/fluoride agents (LiCl, LiF, etc.) (Amalajyothi et al, 2008; Amalajyothi et al, 2011).

For a number of years, researchers have been trying to obtain rare-earth borides in different forms such as particles, whiskers, rods or cubes using various fabrication techniques (Motojima et al, 1978; Zhang et al, 2006; Wang et al, 2010; Dou et al, 2011c; Ji et al, 2011; Dou et al, 2012). Recently, nano-scale or submicron, nano-cubes and nano-rods of rare-earth boride powders were obtained by using low temperature synthesis in an autoclave and self-propagating high-temperature synthesis (SHS) methods (Ji et al, 2011; Dou et al, 2012). Autoclave systems provide an alternative route for obtaining borides at lower temperatures than used in

traditional methods (Wang et al, 2010). SHS method provides high reaction speed, simple equipment and low energy consumption but after ignition, the reaction process becomes un-controlled which results in the occurence of intermediate phases in the reaction product (Dou et al, 2011c).

Rare-earth boride whiskers, wires, tubes and obelisks in nano or micro-scales were produced by chemical vapor deposition technique (CVD) (Motojima et al, 1978; Zhang et al, 2006). CVD method includes self-catalyst or metal-catalyst (Au, Pt, etc.) growth of borides based on the catalytic reaction of rare-earth element/compound powders and boron (BCl_3, $B_{10}H_{14}$ etc.), hydrogen and argon containing gas mixture on a substrate (Ji et al, 2011).

Consequently, it is significant to develop an efficient method of preparing technologically important hexaboride powders with high purity and with small particle size in various morphologies. To find new synthesis strategies with low reaction temperature, easy to handle precursors, simple process control, less equipment requirements and low cost has been attracting more attentions (Selvan et al, 2008).

A summary of production techniques of La, Ce and Sm hexaborides obtained from current literature are given in Table 2.2. As seen from Table 2.2, there are so many investigations on the production of La, Ce and Sm hexaborides in different shapes and sizes. Apart from the above-mentioned production techniques, mechanochemical synthesis is a novel, simple and room temperature process which enables a great degree of controlling the product microstructure (content, shape, size, etc.) and obtaining high purity materials (Suryanarayana, 2001). To the best of our knowledge, there is recently one report involved ball milling process on the fabrication of CeB_6 powders (Liu et al, 2010).

It has been reported that bulk rare-earth haxaborides can not been prepared easily via conventional hot-pressing method with high density due to their high plastic yield stresses (Bao et al, 2011a). Although the development of bulk density is essential, sintering process of rare-earth borides has not been comprehensively investigated in the literature. In general, the SPS method is used to obtain high density hexaboride sintered bodies (Bao et al, 2011a; Zhou et al, 2009).

Table 2.2 : Summary of the production techniques of La, Ce and Sm hexaborides.

Production techniques	**Materials**	**References**
Direct solid-phase reaction of the corresponding elements/compounds at high temperature	LaB_6 powders	Shiota et al, 1980
	LaB_6 nanocrystals	Yuan et al, 2011
Carbothermal reaction of rare-earth oxides and B or boron carbide method (B_4C method)	LaB_6, CeB_6, SmB_6	Samsonov et al, 1963
	$La_xCe_{1-x}B_6$ whiskers	Carlsson et al, 2005
	LaB_6 powders	Wenyuan et al, 2007
		Zheng et al, 2001
		Hasan et al, 2013
Borothermal and aluminothermal reduction of rare-earth elements or oxides	LaB_6, CeB_6, SmB_6	Iltis and Maestro, 1991, 1993
	LaB_6 nanopowders	Szépvölgyi et al, 2008
	$La_{1-x}Ce_xB_6$ polycrystals	Jha et al, 2012a
	CeB_6	Bliznakov and Peshev, 1964
	CeB_6 nanorods	Jha et al, 2012b
	SmB_6	Trunov et al, 1991, 1993
Floating zone method	LaB_6 crystals	Curtis and Graffenberger, 1966
		Tanaka et al, 1975
		Verhoeven et al, 1976
		Takagi and Ishii, 1977
		Otani et al, 1993a, 1993b, 1993c
	LaB_6 and CeB_6 crystals	Otani and Ishiziwa, 1996
	LaB_6, CeB_6, SmB_6 crystals	Otani et al, 2000
	CeB_6 crystals	Balakrishnan et al, 2004
		Bao et al, 2011b
		Petrosyan et al, 2012
Electrosynthesis in molten salts	LaB_6 crystals	Zubeck et al, 1976
		Kamaludeen et al, 1998
	CeB_6 crystals	Amalajyothi et al, 2008
		Arockiam et al, 2009
		Amalajyothi et al, 2011
		Abazova et al, 2012
	SmB_6 crystals	Berchmans et al, 2010
Low temperature synthesis in an autoclave or in a reactor	LaB_6 nanoparticles and nanocubes	Zhang et al, 2008b
		Wang et al, 2010
	LaB_6, CeB_6, SmB_6 cubes	Chen et al, 2012
		Selvan et al, 2008
	LaB_6, CeB_6, SmB_6 nanopowders	Qian et al, 2011
	CeB_6 nanocubes and nanoparticles	Zhang et al, 2009
	CeB_6 and SmB_6 powders	Aprea et al, 2013
	SmB_6 submicron cubes and rods	Zhang et al, 2010b
Self-propagating high-temperature synthesis (SHS)	LaB_6 and $Sm_{0.8}B_6$ nanocubes	Kanakala et al, 2010
	CeB_6 nanoparticles	Dou et al, 2011a, 2011b, 2011c, 2012
	CeB_6 powders	Akgun et al, 2013

Table 2.2 (continued) : Summary of the production techniques of La, Ce and Sm hexaborides.

Production Techniques	Materials	References
Ball milling	CeB_6 nanopowders	Liu et al, 2010 Akgun et al, 2013
Physical vapor deposition (PVD)	CeB_6 thin film	Xu et al, 2012
Chemical vapor deposition (CVD)	LaB_6 whiskers	Motojima et al, 1978 Givargizov and Obolenskaya, 1981, 1986
	LaB_6 nanowires and nanotubes	Xu et al, 2006 Zhang et al, 2006
	LaB_6 nanowires	Xu et al, 2008b Fan et al, 2013
	LaB_6 nanoobelisks	Brewer et al, 2007
	LaB_6, CeB_6, SmB_6 nanowires	Qin et al, 2010 Brewer et al, 2011
	CeB_6 nanowires	Zhang et al, 2005 Zou et al, 2006
	CeB_6	Wang et al, 2010
	SmB_6 nanowires	Xu et al, 2008b Xu et al, 2009
Pulsed laser deposition (PLD)	LaB_6 thin film	Late et al, 2008 Late et al, 2009

2.2.1 Production techniques of LaB_6

LaB_6 powders and nanocrystals have been produced by direct solid-phase reaction of the corresponding elements/compounds at high temperatures. Shiota et al (1980) reported the synthesis of LaB_6 from the powder mixtures of boron nitride (BN) and lanthanum-citrate-hydrate ($La(C_6H_5O_7)(H_2O)_2$). Synthesis of LaB_6 powders was carried out in a BN crucible placed in an induction furnace at a reaction temperature of 1550°C (Shiota et al, 1980). Yuan et al (2011) investigated a solid state reaction route of $LaCl_3.nH_2O$ and $NaBH_4$ in order to prepare LaB_6 nanocrystals. Experiments were carried out using a graphite crucible placed in a vacuum resistance furnace and the powder mixtures were heated to the temperatures between 900 and 1200°C, then they were kept for 1 h in vacuum. Pertinent investigations showed that reaction temperature, molar ratio of the reactants and heat preservation time had great effects on the properties of final products (Yuan et al, 2011). Higher reaction temperature, higher amount of $NaBH_4$ reactant and longer heat preservation time provided less agglomeration, less impurities and helped LaB_6 grains to form regular shapes. So,

cubic LaB_6 particles with sizes ranging from 20 to 100 nm were obtained. Based on this study, optimized working conditions for preparing nanocrystalline LaB_6 in vacuum were achieved from the reaction between $LaCl_3$ and $NaBH_4$ with a molar ratio of 1:2 using a reaction temperature of 1200°C during 2 h (Yuan et al, 2011).

Other high temperature techniques for preparing LaB_6 are carbothermal, borothermal and aluminothermal reductions of rare earth elements or oxides and also boron carbide (B_4C) method. Samsonov et al (1963) reported the formation of some hexaborides by the reactions of metal oxides with boron carbide, boron and a mixture of boron and carbon in a vacuum according to the reactions (2.1) through (2.3), respectively.

$$Me_2O_3 + 3B_4C \rightarrow 2MeB_6 + 3CO \quad \textbf{(2.1)}$$

$$Me_2O_3 + 15B \rightarrow 2MeB_6 + 3BO \quad \textbf{(2.2)}$$

$$Me_2O_3 + 12B + 3C \rightarrow 2MeB_6 + 3CO \quad \textbf{(2.3)}$$

The studies were conducted in the temperature range between 1000 and 2000°C and LaB_6 was formed at 1650°C during 60 min in the case of using B_4C as reductant. On the other hand, the reaction of lanthanum oxide (La_2O_3) with boron takes place at slightly higher temperatures than with B_4C and in this case, boride and volatile boron oxides were formed. During the reaction of La_2O_3 with a mixture of boron and carbon, metallic lanthanum (La) formed as a reaction product. Results of this study showed that B_4C is the sufficient reducing agent for preparing carbon-free hexaboride products. Furthermore, the purity of the starting materials had no effect on the purity of the resultant product because impurities present in the starting oxides are removed during the evacuation of the gaseous reaction products (CO, BO) (Samsonov et al, 1963). Carlsson et al (2005) fabricated $La_xCe_{1-x}B_6$ whiskers by the carbothermal vapor-liquid-solid (VLS) growth mechanism using La_2O_3, CeO_2, B_2O_3, C, NaCl and Ni as starting materials. La_2O_3, CeO_2, B_2O_3 were used as sources for La, Ce and B whereas C was used as a reducing agent and Ni was used as a catalyst metal. NaCl was added for generating chlorides and oxychlorides. Starting powder mixtures were placed in a graphite furnace and heated in flowing Ar using various reaction temperatures in the range 1200-1800°C with a holding time between 1.5 and 3 h. In the temperature range of 1500-1650°C, in addition to (La, Ce)B_6; B_4C, La_2CO_5, $LaBO_3$ and La_2C_3 were formed as well. (La, Ce)B_6 whiskers in length of

10-2000 μm and in diameter of 0.2-10 μm were produced in the temperature region 1650-1800°C (Carlsson et al, 2005). Wenyuan et al (2007) studied a carbothermal process based on the high temperature chemical reactions (800-1500°C) of La_2O_3 in the H_3BO_3-C system. The powder mixtures were prepared according to the molar ratio of La_2O_3:H_3BO_3:C=1:12:21, pressed into the disk and then roasted in the tube furnace under Ar atmosphere.

At the temperature of 980°C, the reaction products were LaB_3O_6, $LaBO_3$, B_4C and LaB_2C_2, which occured in regard of the reactions (2.4a) through (2.4d). B_2O_3 was formed due to the dehydration of H_3BO_3 at temperatures above 287°C.

$$La_2O_3 + 3B_2O_3 \rightarrow 2LaB_3O_6 \quad \textbf{(2.4a)}$$

$$LaB_3O_6 + La_2O_3 \rightarrow 3LaBO_3 \quad \textbf{(2.4b)}$$

$$La_2O_3 + B_2O_3 + 8C \rightarrow LaB_2C_2 + 6CO \quad \textbf{(2.4c)}$$

$$La_2O_3 + 3B_2O_3 + 7C \rightarrow 2LaBO_3 + B_4C + 6CO \quad \textbf{(2.4d)}$$

The products synthesized at 1130°C did not include LaB_2C_2 because LaB_2C_2 reacted with LaB_3O_6 at this temperature according to the reaction (2.4e).

$$14La_2B_2C_2 + 19LaB_3O_6 \rightarrow 33LaBO_3 + 13B_4C + 15CO \quad \textbf{(2.4e)}$$

LaB_4 and LaB_6 phases formed at temperatures of 1450 and 1500°C according to the reactions (2.4f) and (2.4g). However, the products synthesized at 1450°C still contained a small amount of $LaBO_3$. These reactions showed that the undesired product $LaBO_3$ was completely reduced by B_4C at 1500°C during 2 h and the final products contained the LaB_4, LaB_6, B_4C and B phases.

$$LaBO_3 + 3B_4C \rightarrow LaB_4 + 9B + 3CO \quad \textbf{(2.4f)}$$

$$LaB_4 + 2B \rightarrow LaB_6 \quad \textbf{(2.4g)}$$

It was claimed that prolonging heating time from 2 to 6 h at 1500°C caused the completion of the reactions (2.4f) and (2.4g) and only the LaB_6 phase was obtained (Wenyuan et al, 2007). Hasan et al (2013) investigated carbothermal reduction using La_2O_3-B-C and boron carbide reduction using La_2O_3-B_4C powder blends. For the carbothermal route, powder blends containing stoichiometric amounts of dry reactants were mixed by milling for 30 min in a high energy ball mill on the basis of reaction (2.5).

$$La_2O_3 + 12B + 3C \rightarrow 2LaB_6 + 3CO \quad \textbf{(2.5)}$$

For the boron carbide reduction route, graphite was added in excess of the stoichiometric ratio by 16-19 % and powders were mixed by milling for 20 min in a high energy ball mill using the reaction (2.6).

$$La_2O_3 + 3B_4C \rightarrow 2LaB_6 + 3CO \quad \textbf{(2.6)}$$

Both types of milled powders were pressed into cylindrical pellets and these pellets were annealed in a horizontal furnace at different temperatures in the range 1250-1500°C for 4 or 8 h. At low temperatures between 1250 and 1350°C, final products contained certain amounts of $LaBO_3$ in both cases and some amount of B_4C in the case of using the B_4C method. As the temperature increased to 1400°C, undesired products disappeared completely and high-purity LaB_6 powders were obtained. Several researchers asserted that milling may play a role in the reduced synthesis temperature (lower temperatures than previously reported) for both methods to prepare pure LaB_6 because of the formation of very fine nanostructured reactants (Wenyuan et al, 2007; Hasan et al, 2013). Particle sizes of LaB_6 obtained by the B_4C method (220 nm) were smaller than particle sizes of LaB_6 obtained by the carbothermal route (600 nm) (Hasan et al, 2013). Jha et al (2012a) reported a borothermal route for the synthesis of lanthanum cerium hexaborides and field emmision properties of their films fabricated by spin coating. The nanostructured (in the form of cubes, rods and pyramids) lanthanum-cerium borides were synthesized from the $La_{1-x}Ce_x(OH)_3$ (x=0.1, 0.2, 0.3 and 0.5) and B containing powder blends using a weight ratio of 1:1.5 by a sequential annealing process at 800 and 1300°C for 6 h under Ar atmosphere. Fabrication of boride films were made by spin coating on a Si substrate using a suspension of borides dispersed in a mixture of ethanol and ethylene glycol. Different precursors annealing with B at 1300°C led to the formation of $La_{0.9}Ce_{0.1}B_6$, $La_{0.8}Ce_{0.2}B_6$, $La_{0.7}Ce_{0.3}B_6$ and $La_{0.5}Ce_{0.5}B_6$ phases. The results showed that the morphology of the final products depended on the La/Ce ratio in the borides. Films fabricated by spin coating gave high field enhancement factor depending on the La/Ce ratio in the boride and at the La/Ce ratio of unity. It is observed that nanopyramids of $La_{0.5}Ce_{0.5}B_6$ displayed excellent field emission characteristics with highest field enhancement factor among all specimens (Jha et al, 2012a). Another synthesis method for obtaining LaB_6 nanopowders (10-50 nm)

based on a borothermal route was conducted in a radiofrequency (RF) thermal plasma reactor using the solid mixture of La_2O_3 and amorphous B (Szépvölgyi et al, 2008). It has been stated that in the case of using high concentrations of He and/or H_2 as plasma and/or carrier gases, conversion yield of La_2O_3 to LaB_6 increased due to the high thermal conductivity of these gases which resulted in improvement of the heat transfer between the plasma frame and the solid particles. Surfaces of LaB_6 particles were oxidized due to the contact with ambient air which was covered with a $LaBO_3$ and B_2O_3 and then a CH_x layer (Szépvölgyi et al, 2008).

Floating zone technique was developed conventionally for preparing LaB_6 single crystals using various heating methods (Curtis and Graffenberger, 1966; Tanaka et al, 1975; Verhoeven et al, 1976; Takagi and Ishii, 1977). Curtis and Graffenberger (1966) obtained LaB_6 in single crystal form with interesting optical properties which may have applications as an electron emitter. Tanaka et al (1975) reported the growth of high purtiy LaB_6 single crystals by multi-float zone passage using a pressurized atmosphere to prevent vaporization and dissociation of LaB_6. The purity of the crystals after three passes has higher than the crystals obtained after one zone pass (Tanaka et al, 1975). Verhoeven et al (1976) prepared LaB_6 single crystals by using an arc floating zone technique, whereas Takagi and Ishii (1977) performed a laser heated floating zone method. Otani et al (1993a), Otani et al (1993b) and Otani et al (1993c) reported the preparation of LaB_6 single crystals by using RF heating. By increasing the boron content in the molten zone, the growth temperature was decreased (Otani et al, 1993c). Single crystals of rare-earth hexaborides were also prepared by floating zone method using RF heating under Ar atmosphere (Otani and Ishizawa 1996; Otani et al, 2000). Figure 2.3(a) and (b) reveal the mechanism of the traveling solvent floating zone method which shows the melting of LaB_6 phase and the formation of high quality crystals without boundaries. As seen from Figure 2.3(a), LaB_6 melts congruently at 2715°C and the crystals prepared at this composition contained subgrain boundaries. Authors claimed that a decrease by 200°C in the growth temperature caused a suppression on the formation of the boundaries due to controlling the zone composition. Thus, excess amounts of La or B in the overall composition enabled to obtain high quality crystals without boundaries (Otani et al, 2000).

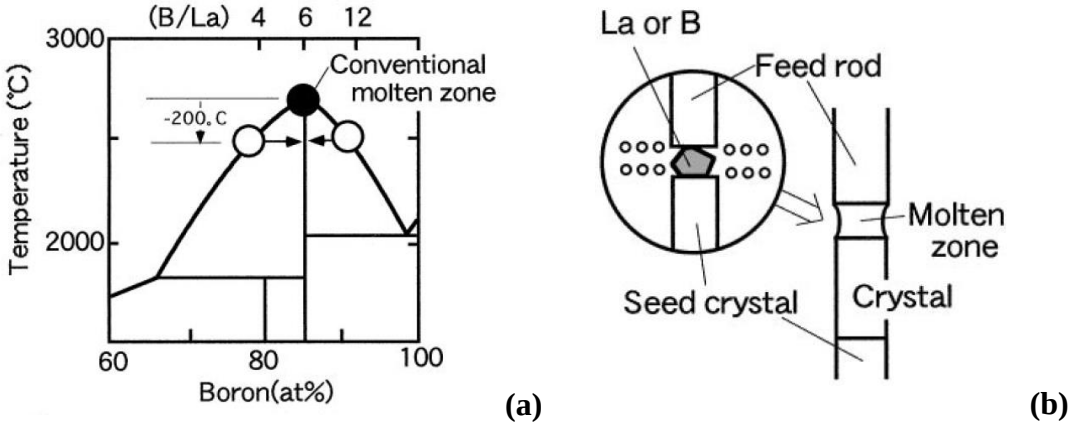

Figure 2.3 : The mechanism of the traveling solvent floating zone method: (a) phase diagram of the La-B system showing the melting of LaB_6 phase, (b) high quality crystals without boundaries, adapted from Otani et al (2000).

Crystals of LaB_6 were produced by molten salt electrolysis from oxyfloride baths (Zubeck et al, 1976; Kamaludeen et al, 1998). Zubeck et al (1976) prepared large crystals of LaB_6 by electrodeposition (1.87 to 2.1 V) at 800°C in He atmosphere in a period of 300 h. Kamaludeen et al (1998) obtained purple crystals of LaB_6 by electrodeposition from a melt consisting of La_2O_3-B_2O_3-LiF-Li_2O under N_2 atmosphere.

LaB_6 particles and rare-earth hexaborides have been synthesized by low temperature reaction processes under pressure (Zhang et al, 2008b; Selvan et al, 2008). Zhang et al (2008b) studied a low temperature route for the fabrication of nanocrystalline LaB_6 using an autoclave at 400 and 500°C for 4 h. LaB_6 nanoparticles with mean size of 30 nm were obtained starting from appropriate amounts of $LaCl_3.7H_2O$, excessive $NaBH_4$ and excessive Mg according to the reaction (2.7). Experiments were performed in a stainless steel autoclave of 25 ml capacity at 400°C under a pressure of 110 atm for 4 h.

$$LaCl_3.7H_2O + 6NaBH_4 + 4Mg \rightarrow LaB_6 + 3NaCl + 4MgO + 3NaOH + 17.5H_2 \quad \textbf{(2.7)}$$

For the preparation of LaB_6 nanocubes with a mean size of 200 nm, B_2O_3 was used instead of $NaBH_4$ as boron source based on the reaction (2.8). Experiments were performed in a stainless steel autoclave of 25 ml capacity at 500°C under a pressure of 55 atm for 4 h.

$$LaCl_3.7H_2O + 3B_2O_3 + 17.5Mg \rightarrow LaB_6 + 1.5MgCl_2 + 16MgO + 7H_2 \quad \textbf{(2.8)}$$

Two types of products were washed respectively with dilute HCl and distilled water in order to remove MgO, $MgCl_2$ and other impurities. It was stated that the reaction temperature and duration play significant roles on the formation of LaB_6. Nanoparticles and nanocubes could not be obtained below 350 and 400°C, respectively. The optimum reaction temperatures were 400 and 500°C, respectively for preparing LaB_6 nanoparticles and LaB_6 nanocubes. On the other hand, reaction times shorter than 2 h were not sufficient for completing the boride formation. The crystallinity or morphology for two types of LaB_6 were not significantly affected by varying the reaction time between 4 and 12 h. Authors emphasized that the formation of LaB_6 was achieved at relatively low temperatures because of the high pressure in the autoclave created due to the H_2 gas in reactions (2.7) and (2.8) (Zhang et al, 2008b). LaB_6, CeB_6 and SmB_6 having a cubic morphology with submicron-sized crystals were obtained from related metal acetates and $NaBH_4$ by the single-step synthesis of the reaction under an autogenic pressure at elevated temperature (RAPET) technique in a 5 ml stainless steel closed-cell kept at 900°C for 3 h in regard of the reactions (2.9a) through (2.9d), without observation of B, B_2O_3 and $NaBH_4$ impurities (Selvan et al, 2008).

$$2RE(CH_3COO)_3 \rightarrow RE_2O(CO_3)_2 + 3(CH_3COCH_3) + O_2 \quad \textbf{(2.9a)}$$

$$RE_2O(CO_3) \rightarrow RE_2O_3 + 2CO_2 \quad \textbf{(2.9b)}$$

$$NaBH_4 \rightarrow NaH + BH_3 \quad \textbf{(2.9c)}$$

$$RE_2O_3 + 4NaH + 12BH_3 \rightarrow 2REB_{6(s)} + 2Na_2O_{(s)} + 20H_{2(g)} \quad \textbf{(2.9d)}$$

All the rare-earth metal acetates were thermally decomposed into metal carbonates and oxygen at 700°C in regard of the reaction (2.9a). Similarly, $NaBH_4$ decomposed into NaH and BH_3 at 500°C as given in the reaction (2.9c). Above 700°C, the as-formed RE_2O_3 was reacted with NaH and BH_3 to form REB_6 according to the reaction (2.9d). Reaction mechanism for the formation of rare-earth hexaborides of RAPET technique is given in Figure 2.4 which explains the crystal growth during the process. At 800°C, the agglomerated particles were surrounded by a carbon layer and this amorphous product acted as the nucleation center for the formation of boride cubes. It was converted into small crystalline primary particles at 850°C and final products with submicron sized cubic crystals were obtained at 900°C.

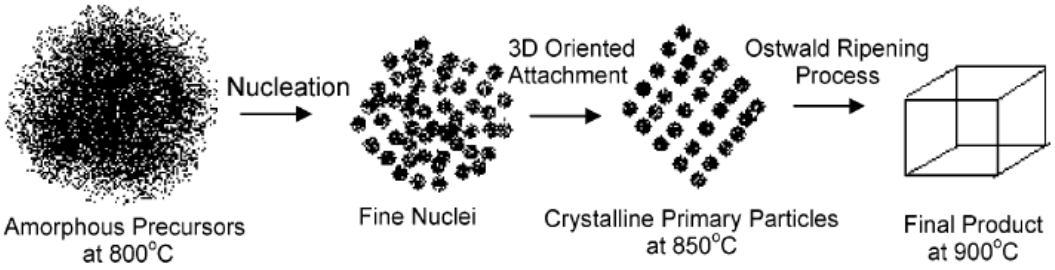

Figure 2.4 : Reaction mechanism of RAPET technique for the formation of rare-earth hexaborides, adapted from Selvan et al (2008).

Synthesized powders were washed with dilute HCl, then with distilled water in order to remove Na_2O generated from the reaction (2.9d) and C, H, N and S impurities remained from acetate reactant. However, after washing, carbon and hydrogen impurities were observed in final products and the purity of all rare-earth hexaborides could be reached to 95 % (Selvan et al, 2008). Some rare-earth and alkaline-earth hexaborides were fabricated in an autoclave at mild temperatures (Wang et al, 2010). For the preparation of LaB_6, CeB_6 and SmB_6, the mixture of related oxides (respectively La_2O_3, CeO_2 and Sm_2O_3), H_3BO_3, Mg and I_2 were placed into an autoclave of 20 ml capacity. Produced powders were leached with distilled water and hot HCl in order to remove the impurities of borates, MgI_2 and MgO. For the comparison, B_2O_3 was also used as boron source to prepare LaB_6 in regard of the reaction (2.10).

$$La_2O_3 + 27Mg + 6I_2 + 6B_2O_3 \rightarrow 2LaB_6 + 21MgO + 6MgI_2 \qquad \textbf{(2.10)}$$

The reaction temperature was the most important parameter during the process and the temperatures below 170°C were not sufficient to obtain rare-earth hexaborides. High yields of cube-like hexaborides could be obtained at 250°C for 12 h. However, in the case of using B_2O_3 as boron source, the optimum temperature for the preparation of LaB_6 was increased to 500°C. It was claimed that I_2 played significant role during this process since the intermediates such as LaI_3, LaOI, etc. may play a quasi-catalytic role in the synthesis of hexaborides. Thus, if I_2 was not used as starting material, LaB_6 could not be detected even at 650°C both case of using H_3BO_3 and B_2O_3 as boron sources. Moreover, the molar ratio of La_2O_3 to I_2 affected the morphology of LaB_6. Eventually, cube-like LaB_6, CeB_6 and SmB_6 were obtained with average particle sizes ranging from 360 nm to 1.65 μm (Wang et al, 2010). Chen et al (2012) developed an additive-assisted synthesis method for the

preparation of boride, carbide and nitride micro/nanocrystals. LaB_6, CeB_6 and SmB_6 were fabricated in an autoclave at 150°C under a pressure of 80 MPa for 2 h from related oxides, amorphous boron/active carbon/NaN_3 with the assistance of metallic Na and elemental S. Once the autoclave was heated to 100°C, the temperature increased rapidly from 100 to 850°C, which was attributed to the intense exothermic reaction between the additives, Na and S. This reaction produced Na_2S which gave a large quantity of heat and the actual temperature inside the autoclave assisted the formation of boride phases. LaB_6, CeB_6 and SmB_6 cubes were fabricated with average sizes of 1 μm, 300 nm and 300 nm, respectively (Chen et al, 2012).

For obtaining nanocubes and ultrafine powders of LaB_6, self-propagating high-temperature synthesis (SHS) method was employed by various researchers. In the scope of the PhD thesis written by Kanakala (2008), the synthesis of hexaborides was investigated using easy-handle chemicals and low processing temperatures via SHS method. Various precursors were used in order to determine the effects of different fuels (carbohydrazide, hydrazine, glycine and urea), different sources of metal ions (LaCl and $La(NO_3)_3.6H_2O$) and different sources of boron (rhombohedral B, cubic B and H_3BO_3) on the final properties of the hexaboride powders. Kanakala et al (2010) also reported the preparation of LaB_6 and $Sm_{0.8}B_6$ nanocubes via combustion synthesis method. LaB_6 and $Sm_{0.8}B_6$ nanocubes in high purity were prepared by low-temperature combustion synthesis using $La(NO_3)_3.6H_2O$ or $Sm(NO_3)_3.6H_2O$, $CO(NHNH_2)_2$ and B powders, in regard of reaction (2.11), at 320°C which was lower than the typical temperature values used in combustion method originated from oxides.

$$Ln(NO_3)_3 + 6B + X(H_2NNH)_2C{=}O \rightarrow LnB_6 + xN_2 + yH_2O + zCO_2 + \text{other gases (Ln=La or Sm)} \quad \textbf{(2.11)}$$

After mixing the reactants, the blend containing fuel-to-oxidizer ratio of 0.08 was spread as a thin layer at the bottom of a ceramic crystallization dish and placed into a muffle furnace heated up to 320°C. Reaction products were also subjected to repeated cleaning/washing and centrifuging processes using diluted HCl, deionized water and diluted H_2SO_4 and lastly they were dried. Cleaning with HCl was required in order to remove the unwanted borate phases ($LaBO_3$ and $SmBO_3$) that formed during combustion. Subsequent cleaning with H_2SO_4 was applied to remove the unreacted boron and obtain a nano-scale cubic morphology for application in

electron emission. After leaching processes, LaB_6 powders were free of impurity phases and consisted of cuboids of single crystals with cube sizes around 500 nm. Although combustion synthesis was thought as an unfeasible method for preparing borides, Kanakala et al (2010) represented its effectiveness by synthesizing high purity powders with a unique cubic morphology, in which the corners of the cubes can be used as point sources for efficient electron emission. The advantages of this method were reported as low process temperature, fast heating rate, short reaction time, easy handling of reactants, easy scale-up and no requirement of an inert atmosphere. Besides, it was especially mentioned that this process was not a conventional SHS method since an exothermic reaction took place in a furnace and mixture of nitrate salts and an organic fuel in the form of a slurry resulted in the occurance of homogeneous products (Kanakala et al, 2010). Dou et al (2011c) reported the fabrication of ultra fine LaB_6 powder via combustion synthesis by using the raw materials of La_2O_3, B_2O_3 and Mg prepared stoichiometrically according to the reaction (2.12).

$$La_2O_3 + 6B_2O_3 + 21Mg \rightarrow 2LaB_6 + 21MgO \qquad \textbf{(2.12)}$$

The powders were mixed by milling for 24 h, then the mixtures were pressed into cylinders under pressures of 5-20 MPa and then the cylinders were placed in an open equipment to perform combustion synthesis. Combustion products consisted of LaB_6, MgO and $Mg_3B_2O_6$ which occured because of the reactions (2.12) and (2.13).

$$3MgO + B_2O_3 \rightarrow Mg_3B_2O_6 \qquad \textbf{(2.13)}$$

Authors claimed that the amount of $Mg_3B_2O_6$ in final products decreased with increasing Mg reductant ratio in reaction (2.12). The optimum yield of LaB_6 was determined if a Mg ratio of 10 % excess than the stoichiometric amount was used. Combustion products were leached by HCl to remove $Mg_3B_2O_6$ by-product and to obtain pure LaB_6. Finally, cubic LaB_6 particles with size in range of 1.92-3 μm were obtained with a purity higher than 99 % (Dou et al, 2011c).

LaB_6 in various morphologies such as whisker, wire, tube, obelisk, etc. were obtained by using chemical vapor deposition (CVD) technique including metal-catalyzed or catalyst-free CVD (Ji et al, 2011). LaB_6 whiskers of 1-20 μm thick and 2-5 mm long were prepared using the gas mixture of $LaCl_3$, BCl_3, H_2 and Ar on a graphite substrate at 1150°C after 1 h of growth (Motojima et al, 1978). LaB_6

whiskers were grown on LaB_6 crystal substrates using BBr_3-H_2 gas mixtures by means of the vapor-liquid-solid mechanism (Givargizov and Obolenskaya, 1981; 1986). Xu et al (2006) reported the fabrication of LaB_6 nanowires and nanotubes with self-catalyst method using La and BCl_3 gas mixed with H_2 and Ar. LaB_6 nanowires having a diameter of 20-200 nm were synthesized on a Si substrate with La powders in a quartz tube at 1070°C for 60 min based on the reaction (2.14).

$$La_{(s)} + 6BCl_{3(g)} + 9H_2 \rightarrow LaB_{6(s)} + 18HCl_{(g)} \quad \textbf{(2.14)}$$

A model sketched in Figure 2.5 explains the self-catalyst growth process of LaB_6 nanowire. During the reaction process, La started to melt at its melting point and subsequently pyrolyzed B^{3+} from BCl_3 was absorbed by the melting La at the surface which resulted in the formation of some LaB_6 nanoclusters. These clusters served as nuclei for the nanowire and the growth of boride nanowires continued until appropriate amounts of B^{3+} and the source of metal reactans were still present. Thus, the melting metal La played the role of reactant and catalyst at the same time which was the reason of calling this process as "self-catalytic" growth (Xu et al, 2006).

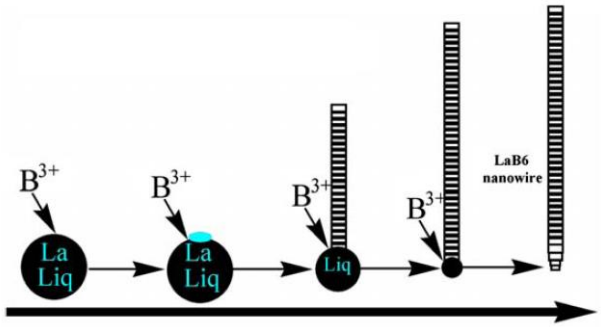

Figure 2.5 : The mechanism of self-catalyst growth process of LaB_6 nanowire, adapted from Xu et al (2006).

Similarly, Xu et al (2008b) reported the preparation of LaB_6 nanowires by self-catalyst method based on the reaction (2.14) at 1100°C. Another study for preparing LaB_6 nanowires via CVD method were conducted in a tube furnace at 1150°C using $LaCl_3$ powders and BCl_3/H_2 gas mixtures according to the reaction (2.15) (Zhang et al, 2006). Single crystalline nanowires with widths ranging from 15 nm to more than 100 nm were obtained with a small amount of amorphous boron impurity (Zhang et al, 2006).

$$2LaCl_{3(s)} + 12BCl_{3(g)} + 21H_2 \rightarrow 2LaB_{6(s)} + 42HCl_{(g)} \quad \textbf{(2.15)}$$

Fan et al (2013) investigated the synthesis of LaB_6 nanowires by Au catalyst method using the starting materials of La powders and $BCl_3/H_2/Ar$ gas mixtures based on the reaction (2.14). LaB_6 nanowires with lengths of 10 μm were obtained on a gold-coated Si substrate at 1070°C (Fan et al, 2013). LaB_6 nanoobelisks were prepared via CVD method in a tube furnace at 1000°C using a pressure of 160 mTorr for 13 min from $LaCl_3$ powders and $B_{10}H_{14}$ gas according to the reaction (2.16) (Brewer et al, 2007).

$$10LaCl_{3(s)} + 6B_{10}H_{14(g)} \rightarrow 10LaB_{6(s)} + 30HCl_{(g)} + 27H_{2(g)} \quad \textbf{(2.16)}$$

Single crystalline rare-earth hexaboride (LaB_6, CeB_6 and SmB_6) nanowires with diameters of about 50 nm and lengths of several micrometers were deposited on a Si wafer substrate or on single-side polished MgO single-crystals in high purity and in correct stoichiometry using Pd nanoparticle-assisted CVD via the VLS mechanism, starting from $RECl_3$ powders loaded in a quartz boat placed in a quartz tube and $B_{10}H_{14}$ (with a flow rate of 0.75 ml/min) and Ar (with a flow rate of 20 ml/min) gas mixtures fed into the quartz tube placed in a horizontal tube furnace at 1000°C (Brewer et al, 2011). To use Pd catalyst instead of Pt which was utilized in several studies provides higher solubility of boron and lower growth temperature of hexaborides. It was reported that a catalyst particle occured at the tip of a nanowire after the reaction and no Pd diffusion was detected beyond 2 nm from the nanowire-catalyst nanoparticle interface, indicating that the synthesis method was based on the VLS growth model. Moreover, similar nanowire growth results were obtained with MgO substrates, indicating that Si substrates are not necessary for REB_6 nanowire growth (Brewer et al, 2011).

Additionally, there is few amount of patents relating to the preparation of rare-earth borides using the techniques of borothermal reduction in a tube furnace, low temperature synthesis in a reactor, electrosynthesis and CVD (Iltis and Maestro, 1991; 1993; Qian et al, 2011; Arockiam et al, 2009; Qin et al, 2010). Rare-earth hexaborides ranging in size between 4 and 40 μm were produced at temperatures around 1000-1400°C for 1-4 h under H_2 and/or Ar atmosphere by reacting a rare-earth halide (chloride or fluoride, referred as X) with elemental boron (amorphous or crystalline form) in the presence and absence of a reducing amount of Al metal in regard of reactions (2.17) and (2.18), using conventional apparatus such as a boat or

crucible placed in a furnace with alumina or aluminosilicate refractory lining (Iltis and Maestro, 1991; 1993). A considerable advantage of this process was that there was no need for final product purification and hence rare-earth hexaborides were directly obtained after washing by water, filtrating, settling and drying treatments since AlX_3 and BX_3 (X=Cl or F) secondary compounds were volatile under the reaction conditions. Moreover, the use of Al made it possible to lower the reaction temperature by 100-200°C and to reduce the amount of B introduced into the reaction as a starting material (Iltis and Maestro, 1991; 1993).

$$REX_3 + 6B + Al \rightarrow REB_6 + AlX_3 \quad \textbf{(2.17)}$$

$$REX_3 + 7B \rightarrow REB_6 + BX_3 \quad \textbf{(2.18)}$$

According to a patent by Qian et al (2011), LaB_6, SmB_6 and CeB_6 nanopowders were obtained from the reaction of a metal source raw material (oxide, chloride or oxychloride of RE or their mixtures), a boron source raw material (H_3BO_3, B_2O_3, B or $Na_2B_4O_7$) and a reducing agent carried out at 500-650°C for 30 min to 72 h, requiring post treatments of the primary products as stirring in 1-6 M HCl at 95°C, filtering, washing and drying. According to a patent by Arockiam et al (2009), fine and pure crystals of LaB_6, SmB_6 and CeB_6 were electrolytically prepared at 850-950°C using oxyfluoride melt with current density range of 0.5-2 A/cm^2 and cell voltage range of 2-7 V, which eliminated engineering complexities, reduced electrolysis duration and provided a single stage process for the synthesis of rare-earth hexaboride crystals with predetermined colors (Arockiam et al, 2009). According to another patent, single crystalline rare-earth metal hexaboride nanowires were manufactured by delivering a gas mixture containing rare-earth metal trichloride, boron trichloride, hydrogen and nitrogen on a coated (gold, iron, nickel, cobalt and platinum) substrate made of silicon, doped silicon, metal, metal alloy, glass, graphite, diamond or ceramic (Qin et al, 2010).

In the current literature, there exists only one study about the mechanochemical route of La_2O_3, B_2O_3 and Mg powder blends for obtaining LaB_6 fine powders which is within the scope of the present dissertation (Ağaoğulları et al, 2012).

Beside the above-mentioned powder production techniques, LaB_6 thin films were developed by using pulsed laser deposition method (Late et al, 2008; Late et al, 2009). LaB_6 thin films were deposited by the pulsed laser deposition technique at

850ºC and LaB_6 micro/nano structures were synthesized by picosecond neodymium-doped yttrium aluminium garnet (Nd:YAG) laser (Late et al, 2009).

Bulk LaB_6 cathode materials were prepared by using spark plasma sintering (SPS) method in the temperature range between 1000 and 1300°C with a pressure of 70 MPa without holding time (Bao et al, 2010). The starting precursor nanopowders (50 nm) were prepared by using a high-energy ball mill with a rotation speed of 500 rpm and milling times of 8, 15 and 20 h. It was claimed that relative density and grain size of sintered LaB_6 bulks strongly depended on the sintering temperatures (Bao et al, 2010). If the temperature increased from 1000 to 1200°C, relative densities of the bulks increased from 78 to 92 % and grain sizes of them increased from 50 nm to 1 μm. Nanopowders were fully densified at 1300°C and LaB_6 bulk materials with grain size of 3 μm were obtained (Bao et al, 2010). According to a patent belonging to Knoch et al (1987), LaB_6 sintered bodies were manufactured via pressureless sintering at 2150-2200°C with dwell times of 5 to 60 min using the green bodies of the powder mixtures comprising LaB_6, B_4C and B prepared by pressing with 100 to 500 MPa.

2.2.2 Production techniques of CeB_6

One of the conventional synthesis method for preparing CeB_6 is based on the borothermal reduction of cerium oxide (CeO_2) or cerium (Ce) at high temperatures. Bliznakov and Peshev (1964) reported the synthesis of CeB_6 via borothermal reduction of cerium oxide. Amorphous boron was used as a boron source and the stoichiometric materials were obtained at the reaction temperatures of 1700-1800°C according to the reaction (2.19).

$$Me_mO_n + (6m+n)B \rightarrow mMeB_6 + nBO \qquad \textbf{(2.19)}$$

CeB_6 nanorods with diameters in the range between 30 and 200 nm were manufactured via borothermal reduction process at 1300°C using the starting materials of Ce and B (Jha et al, 2012b).

Floating zone technique was developed conventionally for preparing CeB_6 single crystals using various heating methods (Balakrishnan et al, 2004; Bao et al, 2011b; Petrosyan et al, 2012). Large and high quality LaB_6 and CeB_6 single crystals without any inclusions or contaminations were grown up to 1 cm^3 in volume by the floating

zone technique using a high-power image furnace equipped with four mirrors and 3 kW Xenon arc lamps, which was described as an ideal route for applications requiring large volumes of single crystals (Balakrishnan et al, 2004). Bao et al (2011b) investigated the growth of CeB_6 single crystals via optical floating zone method using four 3 kW Xenon lamps with a maximum heating temperature of 3000°C which was carried out in an enclosed quartz tube under Ar gas with a pressure of 0.7 MPa. Seed and feed rods aligned in the furnace were rotated to obtain an efficient mixing and uniform temperature distribution in the molten zone. It was stated that the relative density of the feed rods significantly affected the quality of the grown crystal (Bao et al, 2011b). Petrosyan et al (2012) investigated the floating zone and flux methods for obtaining CeB_6 crystals. It was reported that surfaces of the CeB_6 crystals grown by flux and floating zone methods were considerably different: The roughness amplitudes of the samples obtained by floating zone method were higher than those of obtained by flux method (Petrosyan et al, 2012). It was found that the resistivity of the crystals obtained by the flux method was higher than that of floating zone method due to the deviation in the stoichiometric value of B/Ce and the presence of uncontrolled Al impurity and higher oxygen content (Petrosyan et al, 2012).

Another conventional method for preparing CeB_6 crystals is electrosynthesis in molten salts. Bluish-black CeB_6 crystals with a single CeB_4 impurity were electrochemically synthesized by molten salt technique in which stoichiometric quantities of $CeCl_3$, B_2O_3 and lithium fluoride (LiF) containing molten electrolyte was used at different current densities (0.5, 1, 1.5 and 2 A/cm^2) at 900°C (Amalajyothi et al, 2008). Schematic representation of electrosynthesis cell is given in Figure 2.6. After cleaning in dilute HCl solution, this pure CeB_6 with a degree of impurity has a decreasing tendency in the resistivity value (from 0.0053 to 0.0023 Ω.cm) up to a temperature of 200°C and it was found as paramagnetic material demonstrating the dense Kondo system (Amalajyothi et al, 2008). Moreover, the presence of a lower valence CeB_4 phase and of minor C, H, N and S impurities in addition to the CeB_6 with a particle size value up to 1 μm was reported after carrying out molten salt electrolysis in the cerium chloride ($CeCl_3$), lithium tetraborate ($Li_2B_4O_7$) and lithium chloride (LiCl) containing electrolyte at 900°C (Amalajyothi et al, 2011).

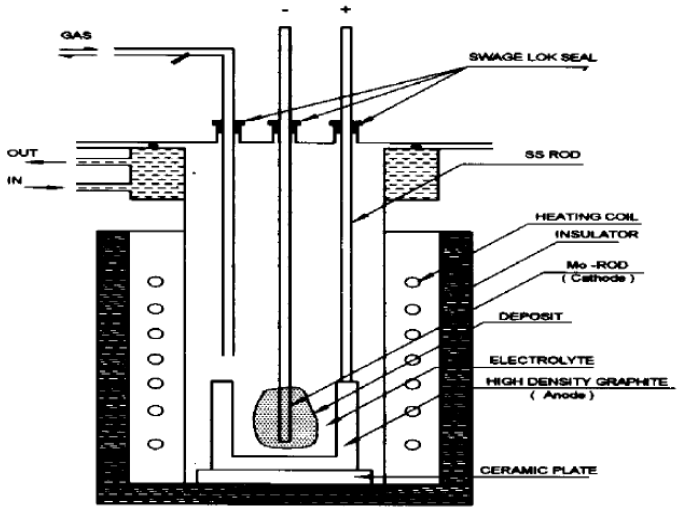

Figure 2.6 : Schematic representation of electrosynthesis cell, adapted from Amalajyothi et al (2011).

CeB_6 nanocubes and nanoparticles have been produced via low temperature synthesis method using an autoclave or a furnace (Zhang et al, 2009; Aprea et al, 2013). Single crystalline CeB_6 nanocubes with an average size of 200 nm were fabricated at 500°C for 12 h in a stainless steel autoclave (with a capacity of 25 ml) from $CeCl_3.6H_2O$, B_2O_3 and Mg containing powder blends whereas nanoflakes and nanoparticles of CeB_6 with an average size of 30 nm could be obtained about 400°C for 48 h using $NaBH_4$ as boron source (Zhang et al, 2009). The reactions (2.20a) and (2.20b) which were difficult to monitor after sealing in the autoclave were thermodynamically spontaneous and exothermic although the reaction temperature was not very high source (Zhang et al, 2009).

$$RECl_3.6H_2O_{(s)} + 3B_2O_{3(s)} + 16.5\ Mg_{(s)} \rightarrow REB_{6(s)} + 1.5\ MgCl_{2(s)} + 15MgO_{(s)} + 6H_{2(g)} \quad \textbf{(2.20a)}$$

$$RECl_3.6H_2O_{(s)} + 6NaBH_{4(s)} + 3Mg_{(s)} \rightarrow REB_{6(s)} + 3NaCl_{(s)} + 3MgO_{(s)} + 3NaOH_{(s)} + 16.5H_{2(g)} \quad \textbf{(2.20b)}$$

Aprea et al (2013) reported the low temperature synthesis of CeB_6 and SmB_6 in a horizontal furnace in vacuum or under Ar atmosphere. Some unwanted by-products such as cerium or samarium oxychlorides (CeOCl and SmOCl), reduced samarium chloride ($SmCl_2$), MgO and $MgCl_2$ were detected after a metathesis reaction, starting from a mixture of a hydrated cerium or samarium trichloride ($CeCl_3.6H_2O$ or $SmCl_3.6H_2O$) and MgB_2 in a molar ratio of 1:3, proceeding at 650°C for 1 h under vacuum, in regard of reaction (2.21). The analytically pure nanosized CeB_6 and

SmB_6 products with average crystallite sizes down to a few nanometers were recovered after the treatment in a hot 5 M HCl solution (Aprea et al, 2013).

$$RECl_3.6H_2O + 3MgB_2 \rightarrow REB_6 + \text{other by-products} \quad \textbf{(2.21)}$$

Self-propagating high-temperature synthesis (SHS) technique has been employed to obtain CeB_6 nanoparticles and powders. According to a reported study on the synthesis of high purity (> 99 %), homogeneous and nanometer-sized (< 150 nm) CeB_6 powders by SHS and subsequent acid leaching from the stoichiometric CeO_2, B_2O_3 and Mg powder blends (reaction (2.22)), combustion products consisted MgO and $Mg_3B_2O_6$ unwanted phases in addition to the CeB_6 whose content and density could be increased with excessive amount of Mg (Dou et al, 2011a; 2011b; 2012). The high reaction temperature during the SHS process induced the formation of $Mg_3B_2O_6$ arising from the reaction between MgO and remaining B_2O_3 (Dou et al, 2011a; 2011b; 2012).

$$CeO_2 + 3B_2O_3 + 11Mg \rightarrow CeB_6 + 11MgO \quad \textbf{(2.22)}$$

Due to the fact that high reaction temperature of SHS method causes the volatilization loss of Mg with low melting and boiling points, using excess amount (5, 10 and 25 wt. %) of Mg ensured both the reducing effect on the reaction and the CeB_6 conversion (Dou et al, 2012). Increasing the proportioning ratio of Mg significantly enhanced the diffraction peaks of CeB_6 and MgO phases and gradually decreased those of $Mg_3B_2O_6$ due to the more favored reaction of boride formation rather than borate. A CeB_6 production yield of 68.68 % was merely obtained using SHS process even when the excess amount of Mg reached to 25 wt. % (Dou et al, 2012). CeB_6 powders were obtained from CeO_2, B_2O_3 and Mg containing powder blends with a yield of 68.6 % in the presence of MgO and $Mg_3B_2O_6$ phases by SHS method in which reactants were ignited in a preheated pot furnace under Ar atmosphere (Akgun et al, 2013). In the same study, mechanochemical processing of CeO_2, B_2O_3 and Mg containing powder blends were reported as well. CeB_6 powders with a yield of 84.4 % in the presence of MgO and small amount of Fe phases were obtained by using a planetary ball mill with a rotation speed of 300 rpm and with a milling duration of 30 h in a stainless steel vial (Akgun et al, 2013).

Various CVD techniques including vapor-liquid-solid process (VLS) and self-catalyst metal-gas reaction method have been developed to prepare CeB_6 nanowires.

The single crystalline CeB_6 nanowires with a lateral dimension about 50 nm and a length more than several micrometers were deposited on a Pt coated Si substrate by a vapor-liquid-solid process in which $CeCl_3$ powders (T_M: 817°C) and BCl_3/H_2 gas mixtures were introduced to the reaction zone in a tube furnace operated at 1125°C according to the reaction (2.23) (Zhang et al, 2005).

$$2CeCl_{3(g)} + 12BCl_{3(g)} + 21H_{2(g)} \rightarrow 2CeB_{6(s)} + 42HCl_{(g)} \quad \textbf{(2.23)}$$

Large-scale CeB_6 nanowires having a diameter around 20-100 nm and a length up to several micrometers were fabricated over a single crystalline Si(111) substrate in a tube furnace at 1125ºC by a self-catalyst metal-gas reaction method from Ce powders and BCl_3 (at a rate of 40 ml/min) under a gas mixture of H_2 and Ar (at a rate of 60 ml/min), in regard of the reaction (2.24) (Zou et al, 2006).

$$Ce_{(s)} + 6BCl_{3(g)} + 9H_{2(g)} \rightarrow CeB_{6(s)} + 18HCl_{(g)} \quad \textbf{(2.24)}$$

Large commercial scale production of CeB_6 is not possible with these above-mentioned two methods due to the usage of $CeCl_3$ as reactant which is a hygroscopic solid rapidly absorbing moisture to form a hydrate, due to the utilization of BCl_3 as the boron source which easily absorbs water to form H_3BO_3 and prevents further reaction, due to the application of Pt coating over the catalyst and due to the difficult control of the product stoichiometry considering gaseous raw materials (Zou et al, 2006; Zhang et al, 2005; Bao et al, 2010).

In a related study, single crystalline cube-like rare-earth hexaborides with mean sizes ranging from 450 to 700 nm were synthesized through the co-reduction of rare-earth oxides and boric acid by Mg with the assistance of I_2 at temperatures between 170 and 250°C (Wang et al, 2010).

In addition to the above mentioned techniques, CeB_6 thin films were obtained by using physical vapor deposition (PVD) process whose schematic illustration is given in Figure 2.7 (Xu et al, 2012). CeB_6 thin films in high quality were deposited by direct evaporation (which is based on the simple PVD process) of micron-sized CeB_6 powders placed in a BN crucible in a vertical induction furnace operated at a temperature of 1700°C and at a pressure of 70 Pa for 3 h (Xu et al, 2012).

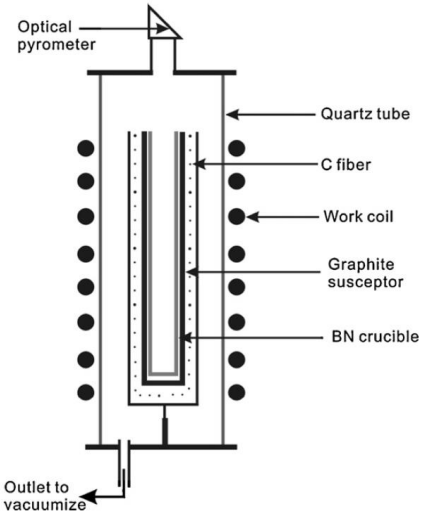

Figure 2.7 : Schematic illustration of the PVD process for CeB_6 thin films, adapted from Xu et al (2012).

There is few amount of patents relating to the preparation of CeB_6 using the techniques of ball milling and electrosynthesis (Liu et al, 2010; Abazova et al, 2012). According to a patent by Liu et al (2010), the preparation of CeB_6 nanopowders with purities more than 99.5 % and in granularity between 50 and 400 nm involved mixing of CeO_2, B_2O_3 and Mg powders with a weight ratio of 100:110-130:160-185, ball milling of blends, pressing of ball milled blends at 40-70 MPa, directly heating of the green compacts at 680-900°C in air until self-propagating reaction occurred, leaching of the intermediate products comprising CeB_6 diffused in MgO using diluted H_2SO_4 at 50-80°C for 24-40 h, filtering of the leach solution, washing of the filter residue with water until the solution was neutral and drying of it in vacuum at 80-150°C for 24 h (Liu et al, 2010). Ultrafine CeB_6 powders were synthesized via electrolysis from an eutectic melt of KCl-NaCl-CsCl containing 1-4 wt.% anhydrous $CeCl_3$ and 1-3 wt.% potassium fluoroborate (KBF_4), enabling to reduce power consumption by decreasing reaction temperature and enabling to obtain a pure end product owing to good solubility of the eutectic electrolyte in water (Abazova et al, 2012).

Polycrystalline bulk CeB_6 cathodes were fabricated by spark plasma reactive liquid phase sintering method from the nano-CeH_x and micron boron containing powder mixtures with a pressure of 50 MPa, a temperature of 1500°C and a holding time of 5 min (Zhou et al, 2009). Bulk CeB_6 cathodes had a relative density of 99.61 % and a hardness value of 2051 kg/mm^2 (Zhou et al, 2009). Fully densified polycrystalline

CeB_6 cathode material was prepared by SPS method starting from CeB_6 nanopowders ball milled down to 50 nm, less than 3 h with a rotation speed of 500 rpm and with a BPR of 20:1 using stainless steel balls, in an oxygen free system at 1550°C under 50 MPa (Bao et al, 2011a).

2.2.3 Production techniques of SmB_6

There are few amounts of researches on the preparation of SmB_6 in the current literature. Single crystals of SmB_6 were prepared by the high-temperature solution growth method in an alumina crucible heated up to 1500°C under Ar atmosphere using Al as a solvent and Sm_2O_3 and B as initial materials. Following the growth, SmB_6 crystals were seperated by dissolving the Al ingot in diluted HCl (Trunov et al, 1991).

Fine crystals of SmB_6 (72-83 nm) exhibiting irregular morphology were produced by molten salt electrolysis performed at 900°C in Ar atmosphere at various current densities ranging from 1 to 2.3 A/cm^2, from Sm_2O_3, $Na_2B_4O_7$ (sodium tetraborate) and LiF (lithium fluoride) raw materials with the Sm/B molar ratio of 1:6-1:12 (Berchmans et al, 2010). The electrolytic cell which was made from a high density graphite crucible and placed in an Inconel reactor played both the role of electrode container and reaction anode whereas 1 cm molybdenum (Mo) rod was used as the cathode. The reason for utilizing LiF was to increase the ionic conductivity and fluidity of the electrolyte and to enhance the mobility of electroactive species. The mechanism of SmB_6 formation was explained by the joint deposition or adherence of electrochemically dissociated B and Sm ions on the Mo cathode, according to the total reaction (2.25) in which B_2O_3 originated from the decomposition of $Na_2B_4O_7$.

$$Sm_2O_3 + 6B_2O_3 \rightarrow 2SmB_6 + 10.5O_2 \qquad \textbf{(2.25)}$$

It was reported that the color of the final product changed from light shiny black to dark black color depending on the cathode current density and the maximum yield of SmB_6 (80-82 %) was obtained at 1.8 A/cm^2 with a Sm/B molar ratio of 1:10. Moreover, the SmB_6 deposit was in the form of fine powders at lower current densities up to 1.5 A/cm^2 and it became coarser at higher current densities above 1.65 A/cm^2. It was stated that the formation of pure SmB_6 was favored at current densities between 1.65 and 1.8 A/cm^2 due to the dissappearance of Sm_2O_3, $SmBO_3$

and B_2O_3 impurities detected at lower current densities up to 1.5 A/cm^2 (Berchmans et al, 2010).

Submicron-sized SmB_6 in high purity and high crystallinity were prepared by a one-step solid state reaction of $SmCl_3.6H_2O$, B_2O_3 and Mg powders in an autoclave at 500°C for 12 h, in regard of the reactions (2.26a) through (2.26d) (Zhang et al, 2010b). Although the reaction (2.26a) shows the total reaction, the reaction began with the melting of B_2O_3 at 450°C and proceeded with the obtainment of B via Mg reduction of B_2O_3, as given in the reaction (2.26b). Meanwhile, Sm obtained from the reduction of $SmCl_3$ by Mg reacted with free B and formed SmB_6, according to the reaction (2.26c) and (2.26d). Besides, the use of high pressure environment arising from the H_2 produced during the reaction could be responsible for the growth of highly crystalline SmB_6. The structure of SmB_6 particles varied from cube to rod-like and needle-like structures by controlling the reaction conditions especially the reaction duration: The reaction was incomplete and the crystallinity of the products was poor if the reaction was shorter than 4 h. Exceeding the reaction time results in the highly crystalline submicron-sized cubes after 12 h, the short rod-like structures after 24 h, the long rod-like structures after 36 h and the needle-like structures after 48 h. The primary formation of perfect submicron cubes after 12 h was correlated with the Ostwald ripening process in which large particles grew at the side of the small ones through the diffusion of ions, atoms or molecules within a cluster of crystallites (Zhang et al, 2010b).

$$SmCl_3.6H_2O_{(s)} + 3B_2O_{3(s)} + 16.5Mg_{(s)} \rightarrow SmB_{6(s)} + 1.5MgCl_{2(s)} + 15MgO_{(s)} + 6H_{2(g)} \quad \textbf{(2.26a)}$$

$$B_2O_{3(s)} + 3Mg_{(s)} \rightarrow 2B_{(s)} + 3MgO_{(s)} \quad \textbf{(2.26b)}$$

$$2SmCl_{3(s)} + 3Mg_{(s)} \rightarrow 2Sm_{(s)} + 3MgCl_{2(s)} \quad \textbf{(2.26c)}$$

$$Sm_{(s)} + 6B_{(s)} \rightarrow SmB_{6(s)} \quad \textbf{(2.26d)}$$

As already mentioned in the 2.2.1 section of this dissertation (titled as "production techniques of LaB_6"), Kanakala et al (2010) reported the preparation of LaB_6 and $Sm_{0.8}B_6$ nanocubes via combustion synthesis method. As-synthesized powders contained $Sm_{0.8}B_6$, high-temperature $SmBO_3$ and unreacted B phases whose borate and boron contents were respectively removed with diluted HCl and H_2SO_4. After

cleaning/washing process, $Sm_{0.8}B_6$ powders obtained in the presence of a small $SmBO_3$ residue with a process yield of 10 % (Kanakala et al, 2010).

Single crystalline SmB_6 nanowires, with lateral dimensions from tens of nanometers to more than 100 nm and lengths extending to more than a few micrometers, were fabricated in a conventional tube furnace with a horizontal quartz tube at 1120, 1130 and 1140°C for 20-30 min using self-catalyst one-step CVD method by the direct reaction of Sm powders with BCl_3 gas (with a flow rate of 10, 20 and 30 ml/min) and H_2/Ar gas mixtures (with a flow rate of 120 ml/min) on Si substrates without utilizing catalysts throughout the whole growth process, in regard of the reaction (2.27) (Xu et al, 2008a; Xu et al, 2009).

$$Sm_{(s)} + 6BCl_{3(g)} + 9H_{2(g)} \rightarrow SmB_{6(s)} + 18HCl_{(g)} \qquad \textbf{(2.27)}$$

No catalyst particles were found on the tips of the nanowires, which implies that a no-catalyst growth process was involved. In other words, the nanowires were not grown by the conventional VLS mechanism in which a transition metal particle is capped at the tip of the nanowire and serves as an active catalytic site (Xu et al, 2008a; Xu et al, 2009). According to this method, Sm melts at 1072°C, which is below the process temperature, and plays both the role of a reactant and a catalyst over the Si substrate. It was also reported the change in the growth temperature and in the BCl_3 flow rate affected the morphology of the nanowires: In other words, the increase in the BCl_3 flow rate increases the lenghts of nanowires whereas the increase in the temperature thickens their diameters (Xu et al, 2008a). Moreover, the effect of temperature on the field enhancement factor, current density and work function were investigated and the results were found as hopeful for the usage in electronic devices requiring high performance electron sources (Xu et al, 2009).

2.3 Mechanical Alloying and Mechanochemistry

2.3.1 Historical perspective

Mechanochemical process (MCP) uses mechanical energy to induce a wide variety of chemical reactions by promoting chemical and physico-chemical changes. This route is very old which dates back to the early history of mankind, since first attempts by man to obtain fire by friction and more recent data on the ignition of

certain solid state reactions which initiate by mechanical means (Mccormick and Froes, 1998; Boldyrev, 1986).

The first document about mechanochemistry of sulphides was written by Theophrastus of Ephesus (371-286 B.C.), a student of Aristotle, in "De Lapidibus" or "On stones". In this book, it was stated that "native cinnabar was rubbed with vinegar in a copper mortar with a copper pestle yielding the liquid metal. This mechanochemical reaction can be shown by the reaction (2.28) (Balaz, 2008).

$$HgS + Cu \rightarrow Hg + CuS \qquad \textbf{(2.28)}$$

In the 19th century, Faraday (1827) wrote a chapter relating with mortars and comminution: He noticed an acceleration of the dehydration of crystalline hydrates when mechanically treated. Also, a direct reference of mechanochemical reaction applying "mortar milling" was shown in his book by the reaction (2.29).

$$2AgCl + Zn \rightarrow 2Ag + ZnCl_2 \qquad \textbf{(2.29)}$$

Faraday described the reduction of silver chloride (AgCl) by zinc (Zn) as fast and highly exothermic (Takacs, 2002; 2007; Balaz, 2008). The effect of mechanical action to initiate chemical reactions was published by Ostwald (1887) and Carey Lea (1893) at the end of the 19th century. Carey Lea (1893) studied the decomposition of Ag, Hg, Pt and Au halides to halogens and metal during fine grinding in a mortar. Ostwald introduced the term of mechanochemistry in 1891 just before Carey Lea's paper was published (Balaz, 2008). A much later definition was made by Heinicke (1984) for mechanochemistry as "branch of chemistry which is concerned with chemical and physicochemical transformations of substances in all states of aggregation produced by the effect of mechanical energy".

The first applications of mechanochemical treatment were seen in the field of extractive metallurgy, where the process was used before leaching and extraction as a pretreatment step. Afterwards, the industrial necessity to develop a nickel-base superalloys was intended for gas turbine applications, which combined oxide-dispersion strengthening (ODS) with γ'-precipitation hardening in a nickel-base superalloys drove this rather simple technique to manufacturing advanced materials (Balaz, 2008). Benjamin (1970) showed that mechanical alloying (MA) is needed when ordinary dispersion of oxide particles in liquid metal is not possible. Moreover,

a paper and a Ph.D thesis related with the development of dispersion strengthened Al-Fe-Ce alloy produced by MA and rapid solidification were published (Öveçoğlu and Nix, 1986; Öveçoğlu, 1987). The further investigations on ODS superalloys for aerospace industry was conducted by the INCO laboratories (Ivanov and Suryanarayana, 2000). The commercial production of nickel or iron-based alloys for handling in temperatures higher than 1300ºC in carburizing or sulphidizing atmospheres was the major user of the MA process (Benjamin, 1970). Also during the Desert Storm Operation by the USA in 1996, the intensive usage of mechanically alloyed Mg and Fe powders as heaters of MRE (meal, ready-to-eat) gave birth to another commercial application of MA (Ivanov and Suryanarayana, 2000).

In the subsequent studies, a nickel-chromium-aluminium-titanium alloy containing a thoria (ThO_2) dispersoid was produced by the MA process. The equipment used in this study was also first successfully produced small high-speed mixer-mill. Following to that, MA started to use as a method to produce oxide dispersion strengthened (ODS) alloys in an industrial scale (Suryanarayana, 2001).

Mechanical alloying is accepted as a potential non-equilibrium processing technique when the formation of amorphous phases observed by mechanical grinding of Y-Co intermetallic compound in 1981 and ball milling of blended elemental Ni-Nb powder mixture in 1983 (Ermakov et al, 1981; Koch et al, 1983; Suryanarayana, 2001). Also at this time period, in the former USSR, intensive studies on the application of mechanochemical processes were conducted and some practical results such as the treatment of tungsten-containing ore were obtained (Boldyrev and Tkacova, 2000; Sopicka-Lizer, 2010). Since 1980s, syntheses of a variety of stable and metastable phases and amorphous alloys by using mechanochemical processes have been investigated. Moreover, it has been shown that it is possible to produce pure metals, nanocomposites and a variety of commercial materials at room temperatures or much lower temperatures by the effect of mechanical activation (Suryanarayana, 2001).

The great developments in the technique itself and in the area of milling equipment have broadened the applications and research areas. In recent years, more than 1500 scientific papers have been published every year in the field of mechanochemistry (Sopicka-Lizer, 2010).

Similarly, also in recent years, the field of mechanochemistry has attracted a growing interest for the synthesis of advanced materials. Mechanochemical methods show some promise for the synthesis of different materials such as lithium ion batteries, hydrogen storage materials, photocatalysts, etc. Mechanochemistry is frequently investigated in the area of hydrogen chemistry and hydrogen storage materials, such as metallic or complex hydrides (Maltseva et al, 2001; Huot et al, 2013). Also, during the past decade, mechanochemical synthesis has become one of the most utilized preparation methods for nanostructured electrode materials for Li-ion batteries. The method includes fast formation of amorphous or low crystalline precursors during MA and subsequently their transformation into nanostructured products under soft heating conditions (lower temperatures and shorter treatment times) (Ninga et al, 2004; Yang et al, 2010). Moreover, surface modifications and preparing of photocatalysts by mechanical doping are in the interest of research areas of mechanochemical process (Kim et al, 2005; Komarov et al, 2010; Yin et al, 2010).

2.3.2 Mechanical alloying

Mechanical alloying (MA) can be defined as a method for producing composite metallic powders from elemental powders with a controlled fine microstructure by milling for prolonged time (German, 2005). The process involves loading of powder mixtures to a grinding medium which is a container sealed under a protective argon atmosphere to avoid oxidation during milling and milling for a fixed time. MA occurs by repeated deformation, fracturing and cold welding of particles in a highly energetic stirred ball mill. The particles become homogeneous at the atomic level after a time period. Figure 2.8 illustrates a schematic diagram of an attritor mill, a high intensity ball mill, and the progressive homogenization of the ingredients (German, 1994).

During MA, powders are exposed to intense plastic deformation as a result of compression between colliding and grinding balls. This motion ruptures the adsorbed surface contaminant layers on each powder particles and new metal surface layers are emerged. Metallurgical bonds between particles are formed by continual collision leading to particle growth and hence formation of composite particles takes place (Benjamin, 1992). The process involves at least one ductile metal to act as a host or

binder and other components such as ductile metals, brittle metals and intermetallic compounds or non-metals and refractory compounds (Benjamin, 1992).

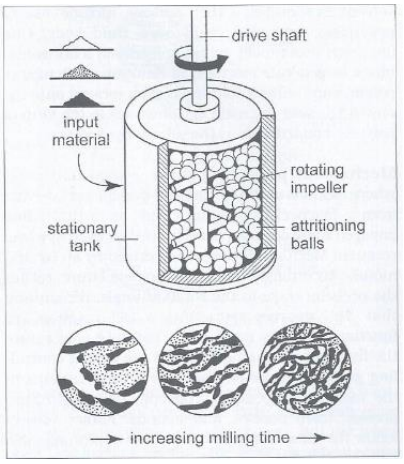

Figure 2.8 : MA process for creating alloys from blended particles, adapted from German (1994).

A metastable, nanoscale (grain size below 100 nm) or even amorphous powder is obtained under certain conditions (German and Park, 2008). Generally, a ball-to-powder weight ratio (BPR) ranging from 3:1 to 50:1 is applied (Benjamin, 1992). Generally, grinding elements and the container are made from the same material for reducing the powder contaminations to a minimum level (German, 1994).

2.3.2.1 Alloying mills

Amongst the different high-energy milling equipment for MA, the types of mills generally used are SPEX mixer/mills, planetary ball mills and attritor-type ball mills. The main differences of these mills are their capacity, speed of operation, efficiency of milling and the functions for controlling the milling temperature and contamination of powders (Balaz, 2008).

SPEX mixer/mill

SPEX mixer/mills generally mill roughly 10-20 g powder per time and commonly used for exploratory purposes (Suryanarayana, 2001). SPEX mills consist of one vial or two vials, containing the powders and milling balls, make back and forth motion several thousands per minute. This shaking motion works together with lateral movements of the ends of vial, so the vial looks like figuring out infinity sign as it moves. When the vial moves, the balls impact against sample and the bottom of the vial hence the sample are both mixed and milled. In SPEX mills, the ball velocities

are high (in the order of 5 m/s) due to the amplitude (about 5 cm) and speed (about 1200 rpm) of the clamp motion, therefore the impact force of balls is substantially great. Different type of vial materials are available including hardened steel, alumina, tungsten carbide, zirconia, stainless steel, silicon nitride, agate, plastic and methacrylate. An example of SPEX^{TM} mixer/mill is given in the Figure 2.9 (Suryanarayana, 2001).

Figure 2.9 : SPEX^{TM} 8000D Dual Mixer/Mill.

Planetary ball mill

Planetary ball mills (Figure 2.10) or attritors are used to produce larger quantities of milled powders. The mechanics of this mill are characterized by the planet-like movements of its vials. Centrifugal acceleration principle is used in planetary mills instead of gravitational acceleration. The charge is exposed to two relative motions: a rotary motion around the mill axis and a planetary motion around the vial axis (Avvakumov et al, 2001; Balaz, 2008).

Figure 2.10 : Planetary ball mill, Fritsch^{TM} Pulverisette.

The vials travel around their own axes through a special drive mechanism. The vials and support disk produce centrifugal force which affects the milling charge. Due to the opposite directions of supporting disc and the vial, the centrifugal forces alternatively act in parallel and opposite directions. This causes to friction effect by running down motion of grinding balls and to impact effect by powder and grinding ball's lifting off and travelling freely through the inner chamber of the vial and colliding against the opposing inside wall, as schematically presented in Figure 2.11 (Avvakumov et al, 2001; El-Eskandarany, 2001). The linear velocity of the balls in planetary ball mills is higher than that in the SPEX^{TM} mills but the frequency of impacts is much more in the SPEX^{TM} mills. For this reason, in comparison to SPEX^{TM} mills, this type of mills can be accepted as lower energy mills (Suryanarayana, 2001). According to Russian scientists who used planetary mills for mechanical activation, these mills provide high mechanical activation after short milling times (Balaz, 2008).

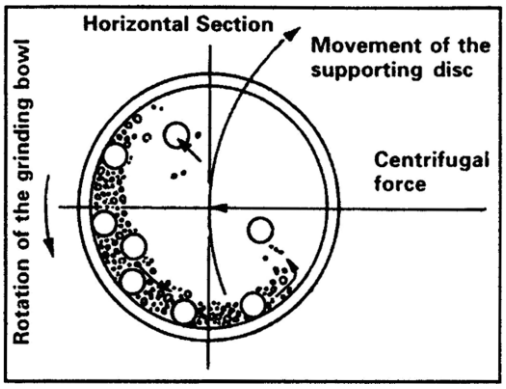

Figure 2.11 : Movements of working parts and balls in a planetary mill, adapted from El-Eskandarany (2001).

Attritor mill

An attritor mill consists of a cylindrical grinding chamber with a centrally mounted vertical shaft having horizontal arms radiating from it and the grinding media (Soni, 2001). When the agitator shaft rotates, the arms crush to the grinding balls and energize them and powder size reduction takes place because of impact between balls, between balls and container wall and between balls, agitator shaft and arms (El-Eskandarany, 2001; Upadhyaya, 2002). A diagrammatic illustration of an attritor is given in Figure 2.12. Some of the size reduction occurs by interparticle collision and by ball sliding. The mixture is agitated by this vertical shaft at a speed of an

approximately 250 rpm (El-Eskandarany, 2001). The powders are exposed to both shearing and impact forces, however less efficient than either SPEX or planetary ball mill. The vessel is usually made from gas-tight rubber seals, especially when a controlled atmosphere is required to be maintained (Suryanarayana, 2001).

Various types of attritors are available for wet or dry grinding processing conditions using the batch, circulation and continuous mode (Balaz, 2008). They can be used with different sizes and capacities. Large amounts of powders (from 0.5 to 40 kg) can be milled by attritor mills at a time. The velocity of the grinding medium is much lower than other types of grinding mills therefore the energy of attritors is low (Suryanarayana, 2001).

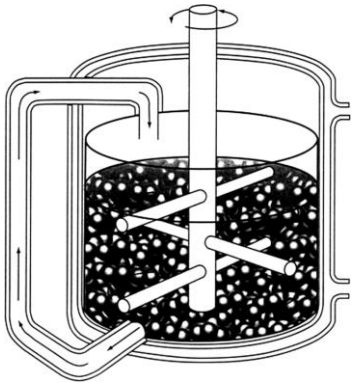

Figure 2.12 : Diagrammatic view of the attritor, adapted from Balaz (2008).

2.3.2.2 Process parameters

MA process is highly affected by a number of processing parameters. Hence, optimization of these variables is needed to obtain the desired product phase and/or microstructure. Some of the important parameters are (Suryanarayana, 2001):

- type of mill,
- material of milling media,
- milling speed,
- milling time,
- ball-to-powder weight ratio,
- extent of filling the milling chamber,
- milling atmosphere,
- process control agent,
- temperature of milling

Type of mills

As described previously, a number of different types of mills are available for MA. These mills have different properties such as capacity, speed and temperature of milling and extent of contamination. Typical capacities of the different types of mills are given in Table 2.3. A suitable mill can be chosen by taking into consideration the type and quantity of powders and the final constitution required. Nevertheless, SPEX^{TM} mills are the most common mill type for alloy screening. Moreover, planetary ball mills or attritors are used for milling larger amount of powders. Usually, specially designed mills are applied for specific purposes (Suryanarayana, 2001).

Table 2.3 : Typical capacities of the different types of mills, adapted from Suryanarayana (2001).

Mill type	Sample weight
Mixer mills	Up to 2 x 20 g
Planetary mills	Up to 4 x 250 g
Attritors	0.5-100 kg
Uni-ball mill	Up to 4 x 2000 g

Materials of milling media

The impact of the milling balls on the inner walls of the milling chamber is affected by the material used for milling media (milling chamber, vial and balls). The material of grinding medium can be dislodged and get mixed into the powder. This causes contamination or alters the chemistry of the powder. For this reason, if it is possible, the grinding vessel and the grinding medium should be made of the same material as the powder to prevent cross contamination. Various steels (stainless, tool, hardened chromium, tempered, bearing steel and tungsten carbide lined), tungsten carbide, zirconia, agate, alumina and silicon nitride are the most common types of materials. Some specific materials are also used for special purposes (Suryanarayana, 2001).

The shape of the container, especially the inner design, can be important. It is stated that for SPEX mills, the alloying rates in the flat-ended vial is found to be much higher than in the rounded-ended containers (Suryanarayana, 2001).

At the same time, the density of the balls plays an important role; their density should be higher than the materials to be milled (Balaz, 2008). In general, more

impact energy is transferred to the powder particles by high density or larger weight of grinding medium. Additionally, the size of the grinding medium has an influence on the final constitution of the powder. It has also been reported that soft milling conditions (small ball sizes, lower energies and lower ball-to-powder weight ratios) appear to promote amorphization or metastable phase formation (Guo et al, 1994).

In some studies, different sized balls have been used instead of one size of the milling media in the same milling (El-Eskandarany, 2001; Suryanarayana, 2001). It has been predicted that the highest collision energy can be obtained if balls with different diameters are used (Suryanarayana, 2001). Usage of same size milling balls gives rise producing tracks and following a well-defined way instead of hitting the end surfaces randomly. Therefore, it can be better to use a combination of smaller and larger balls to randomize the motion of the balls (Suryanarayana 2001; Rhodes 2008).

Milling speed

The milling speed can have an important influence but there are certain limitations to the maximum speed depending on the design of the mill. Above a critical speed, the balls do not exert any impact force on the powder because of pinning of the balls to the inner walls of the chamber. Thus, to obtain the maximum collision energy, the maximum speed should be adjusted to just below this critical value for allowing the balls to fall down from the maximum height (Suryanarayana, 2001).

On the other hand, the temperature of the vial may raise to a high value with the high speed. In the situations where diffusion encourages homogenization or alloying, it can be desirable. However, the increased temperature brings about the decomposition of supersaturated solid solutions or other metastable phases formed during milling through acceleration of the transformation process. It has also been stated that during the nano crystal formation, due to the enhanced dynamical recrystallization at higher milling intensities, the average crystal size increases and the internal strain decreases. The maximum speed varies widely for different types of mills (Suryanarayana, 2001).

Milling time

The time of milling is one of the most important parameters. The necessity to obtain a steady state between the fracturing and cold welding of the powder particles should be taken into account while processing time is being determined. The time required can alter together with other parameters such as the intensity of milling, the ball-to-powder weight ratio, temperature and likewise the type of milling. However, the level of contamination will increase and undesirable phases form when milling time is too long (Suryanarayana, 2001; Balaz, 2008).

Ball-to-powder weight ratio

The weight ratio of the balls to powder (BPR) or charge ratio (CR) has been used in different studies from 1:1 to 220:1 (Kis-Varga and Beke, 1996; Chin and Perng, 1997). Generally, in small capacity mills such as SPEX^{TM} mills, a ratio of 10:1 is mostly used, besides when milling is carried out in a larger capacity mill, like an attritor, a higher ratio of up to 50:1 or even 100:1 can be applied (Suryanarayana, 2001).

The mean free path of the motion reduces with increasing ball-to-powder weight ratio, whilst a low BPR causes lower collision frequency. Thus, impact frequency and total energy consumption per second rise with increasing BPR (Soni, 2001).

The BPR affects considerably the time needed to have a particular phase; shorter times are required with higher BPR. The rate of amorphization is accelerated by the increasing BPR, which is explained by the increase in the weight proportion of the balls and so the increase in the number of collisions per unit, thus more energy is transferred to the powder particles and alloying occurs faster (Suryanarayana, 2001).

Extent of filling the vial

The impact forces exerted on particles enable the alloying process to take place. Therefore, enough space should be given to the balls and the powder particles to move around freely in the milling container. If the quantities of the balls and powders are not enough, the production rate reduces considerably. However, when the quantity is over, the balls can not move adequately and collisions do not have enough impact energy. Hence, the vial should not overfill and generally about 50 % of the vial space is left empty (Suryanarayana, 2001; Balaz, 2008).

Milling atmosphere

During milling, as the powders are getting finer, their surface areas become relatively large, thus they are highly reactive to oxygen and other gases (El-Eskandarany, 2001). Therefore, the milling containers can be evacuated or filled with an inert gas such as argon or helium. High purity argon is the most commonly used milling atmosphere to avoid oxidation and/or contamination of the powders (Suryanarayana, 2001).

Loading is carried out inside atmosphere controlled glove boxes to prevent oxidation of powders while charging into vial. Recurring evacuation and refilling are applied to these glove boxes with the argon gas (Suryanarayana, 2001). Other atmospheres can also be used during milling for specific purposes. Nitrogen (N_2) or ammonia (NH_3) atmospheres have been used to produce nitrides, similarly for obtaining hydrides; hydrogen atmosphere has been applied (Calka and Radlinski, 1991; Ogino et al, 1993).

Process control agents

MA is difficult to apply in brittle-brittle systems because of excessive cold-welding. Process control agents (PCA) preferentially adsorb onto the interfaces and they minimize the cold welding by lubricating effect. A balance between cold welding and fracturing is achieved by PCAs and thereby inhibits the agglomeration and process yield rise (Soni, 2001; Chen and Chen, 2006; Machio et al, 2011).

Stearic acid ($C_{18}H_{36}O_2$), oxalic acid ($C_2H_2O_4$), hexane (C_6H_{14}), methanol (CH_3OH) and ethanol (C_2H_5OH) are the most common PCAs. They are added to powder mixtures at a level of 1-5 wt.%. Other types of PCAs such as sodium-1,2-bis-(dodecyl carbonyl)ethane-1-sulfonate, lithium-1,2-bis-dodecylloxy carbonyl sulfasuccinate, diodecyl dimethyl ammonium acetate (DDAA), didocyldimethyl ammonium bromide (DDAB), trichlorotrifluoroethane and others such as polyethylene glycol, dodecane, ethyl acetate, boric acid, borax, alumina and aluminium nitrate have also been used. The use of organic PCAs contaminates the resulting powders by residual species or gives rise to formation of inclusions and/or dispersoids. Carbon and/or oxygen from these compounds are likely to cause the formation of carbides and oxides which are uniformly dispersed in the matrix. These

are not always undesired in the system since they can provide dispersion strengthening to the material. The hydrogen leaves the system as a gas or is absorbed into the metal lattice during annealing or sintering (Suryanarayana, 2001; Balaz, 2008).

A large amount of surfactant may cover the whole surface area of the particles and particle size can be reduced further (Nouri and Wen, 2014). It is stated that a more homogeneous particle size distribution can be achieved with a liquid PCA (e.g., ethyl acetate) than in case of a solid PCA (e.g., stearic acid) (Suryanarayana, 2001).

The quantity of the PCA varies depending on the (a) cold welding characteristics of the powder particles, (b) chemical and thermal stabilities of PCA and (c) amount of the powder and grinding medium used (Suryanarayana, 2001). Excessive amounts of PCA affects the kinetics of alloying. It is therefore important that the amount of PCA is optimized to ensure a high yield and short downtimes during milling (Machio et al, 2011).

Temperature of milling

The temperature of milling has a determining influence in an alloy system through which diffusional processes take place in the formation of alloy phases. Two kinds of temperature are involved in the process: local temperature between balls during collision and overall temperature of the vial. The powders which are partly attached to the balls and the walls of the vial and free ones have different temperatures (Suryanarayana, 2001; Balaz, 2008; Balaz et al, 2013). The temperature of the powders influences the diffusivity and the defect concentration and hence influences the phase transformations in the powders. Temperature rises to only a moderate level during milling according to the measurement of the milling temperature (Murty and Ranganathan, 1998).

In the literature, there has been limited number of research investigations involving intentionally changed temperatures (Suryanarayana, 2001; Murty and Ranganathan, 1998; Balaz, 2008; El-Eskandarany, 2001). In these investigations, the temperature of milling was increased by electrical heating or liquid nitrogen was dripped into the milling container in order to lower the temperature (Suryanarayana, 2001).

In the mechanical milling, formation of an amorphous phase is considered to take place by the increase of free energy of the crystalline phase as the number of defects (e.g., anti-site chemical disorder or increased grain boundary area) introduced to the structure increase (Suryanarayana, 2001). Thus, an increase in amorphization is expected at lower temperatures. However, both increased and decreased kinetics have been reported (Kimura and Kimura, 1990; Koch et al, 1993).

2.3.2.3 Mechanism of mechanical alloying

MA is generally thought to proceed through the mechanical deformation of powder particles between the colliding milling tools and the accumulation of structural defects in crystalline lattices (Suryanarayana, 2001). However, there is no agreement on the mechanism that may underline the MA process on the atomic scale (Delogu and Mulas, 2010). The emphasis has been shifted on coupled thermally and mechanically induced phenomena in recent approaches from thermal processes in the former ones. The relative sliding events and local generation of frictional heat take place together, and this can easily usher in far-from equilibrium conditions promoting a transient improvement of chemical reactivity (Bellon and Averback, 1995; Hammerberg et al, 1998; Odunuga et al, 2005).

By a series of collisions of balls with each other and with the reactor walls, a fraction of powder is trapped between colliding surfaces of the milling tools and submitted to a mechanical load at relatively high strain-stress leading to work hardening and fracture (Figure 2.13). The powders are cold worked, welded and fragmented repeatedly, resulting in powders with a uniform atom distribution. The clean surfaces come into contact and weld together and particle size increases (Gilman and Benjamin, 1983; Suryanarayana, 2001; Fecht, 2002; Delogu and Mulas, 2010). At this stage, powder particles have a characteristically layered structure. During continued deformation, the fatigue failure mechanism and fragmentation of fragile flakes causes work hardening and fracture. And at this stage, fracturing becomes dominant over cold welding. In a high-energy ball mill, the efficiency of particle size reduction is very low, less than 1 %. The remaining energy is spent as heat and small amount is used for the elastic and plastic deformation. A steady-state equilibrium is reached when a balance is achieved between the rate of welding and the rate of fracturing (Suryanarayana, 2001).

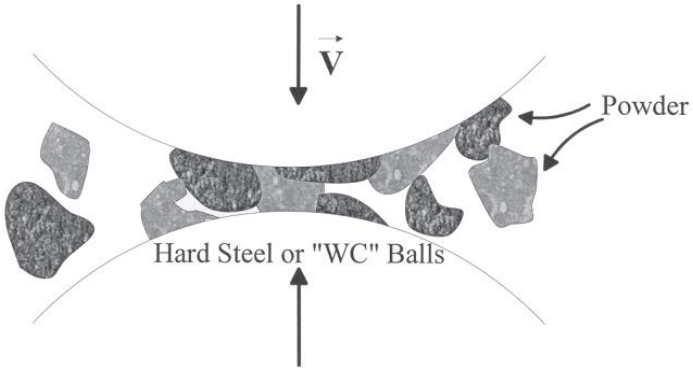

Figure 2.13 : Schematic sketch of the ball-powder-ball collision during mechanical alloying, adapted from Fecht (2002).

The frictional sliding of solid surface induces large plastic strains as well as high strain rates. These give rise to severe structural changes adjacent to the sliding interface. Plastic deformation at high strain rates (10^3-10^4 s^{-1}) within the particles takes place and the average particle size can be reduced to a few nanometers. Most of the mechanical energy is spent as heat but the remaining is stored in material (Miani and Fecht, 1999). As a result, the system departs from equilibrium conditions and chemical reactivity increases (Rigney and Hammerberg, 1999; Kim et al, 2007; Karthikeyan et al, 2009).

The optimum time in MA process can be determined as a function of the initial particle size and characteristics of the ingredients as well as the type of mill and operating parameters. However, in many instances, the rate of size reduction changes logarithmically with time (Figure 2.14) and therefore the initial particle size can be thought as unimportant (Suryanarayana, 2001; Fecht, 2002).

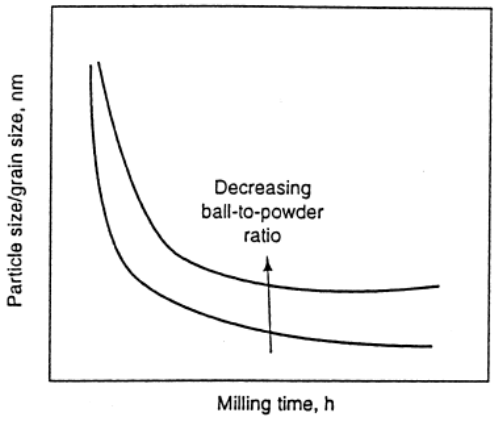

Figure 2.14 : Refinement of particle and grain sizes with milling time, adapted from Suryanarayana (2001).

Powder contamination

A major drawback in the mechanical alloying is the contamination resulting from the wear of the milling media, such as iron from steel balls and vials. If no special precautions are taken, this contamination can reach high levels. The large surface area of small particles and the emergence of new surfaces facilitate contamination of powder particles. Along with milling conditions such as grinding medium, time and intensity of milling, etc., the milling atmosphere also contributes to the contamination level. In the mechanochemically synthesized systems, oxygen contamination can be minimized by control of the factors like initial reactant powders and milling atmosphere (El-Eskandarany, 2001; Suryanarayana, 2001). In atomistic scale, contaminations can be either substitutional or interstitial, for example contaminations from milling atmosphere are mainly interstitial nature while ones originate from milling equipment are mostly substitutional, however carbon from steel milling medium can be interstitial impurity. The material of vial and the grinding balls should be harder than the powder to minimize impurities coming from milling medium. The major source of contamination in many cases is milling atmosphere. The air (oxygen and nitrogen) leaks into vial if it is not sealed properly and contaminates powder. Especially for reactive metals like titanium (Ti) and zirconium (Zr) and for non-oxide refractory compounds, oxygen as interstitial impurity can be detrimental for microstructural and mechanical properties of product (Suryanarayana, 2001; Suryanarayana et al, 2001; Balaz et al, 2013).

2.3.3 Mechanism of mechanochemical process

The term of mechanochemistry has been widely used for materials synthesis initiated by mechanical forces since it was first proposed by W. Ostwald (1887). Various methods have been applied for improving mechanochemical effects (Balaz, 2000; 2008). Among these methods applied to initiate or accelerate the chemical reactions, ball milling process is one of the most effective ways (Murty and Ranganathan, 1998; El-Eskandarany, 2001; Takacs, 2002). However, the terms ‘mechanical alloying’ (MA) and/or ‘reaction milling’ (RM) can be used instead of mechanochemical process in material synthesis field, although these terms do not precisely fulfil the process (Chen et al, 2010).

Mechanochemistry is defined as “a form of chemistry activated by non-hydrostatic mechanical stress” by Heinicke (1984) and Levitas (2004). Mechanochemical synthesis includes mechanical alloying and reactive milling which start after mechanical activation of reagents. Mechanical activation enhances the reactivity of solids by enlarging the surface area or accelerating the reaction by correct reagent ratios. Mechanical deformation of crystalline structural arrangements causes the local structural excitations to pull the system away from thermodynamic equilibrium which increase chemical reactivity significantly (Heinicke, 1984; Gutman, 1998; Levitas, 2004). The impact energy obtained in the processes of plastic deformation, fracture and friction is converted into other forms of energy such as structural defects, broken bonds and other types of excess energy. These energies accumulate in the system and a new, active state of the substances is obtained and chemical reactivity of solids rises (Chen et al, 1997). Moreover, by the increase in the surface areas of powder particles, the necessity for diffusion through the product layer is eliminated. The fresh contact surfaces allow reactions to occur at lower temperatures without any external applied heat. Alternatively, reduction in diffusion distances as a result of the particle refinement can reduce the reaction temperature considerably (Suryanarayana, 2001).

It was shown in the literature that CuO could be reduced to pure Cu by ball milling with a more reactive metal like Ca. The direct formation of β'-brass was achieved by milling together of CuO and ZnO with Ca (McCormick et al, 1989). This type of reactions has been referred as mechanochemical synthesis and was noted as early as 1984 (Heinicke, 1984; Suryanarayana, 2001). Matteazzi and Le Caer (1992), McCormick (1995) and Takacs (1996) have made important contributions to this subject.

Mechanochemical synthesis generally depends on displacement reactions of metal oxides, chlorides or sulphides by a more reactive metal (reductant or reducing agent) to pure metal (El-Eskandarany, 2001; Suryanarayana, 2001).

Reactive milling implicates part of the process including chemical reactions which can occur by two different kinetic mechanisms:

- a slowly developing reaction with each collision and resulting with gradual transformation of the substrate

- a self-propagating reaction initiated when the reaction enthalpy is sufficiently high (Schaffer and McCormick, 1990; Takacs, 1992; Wieczorek-Ciurowa, 2010).

In the first type of mechanical synthesis, reactions proceed more slowly up to the point where the processes turn to time controlled mechanism. The formation reactions of products develop gradually (Wieczorek-Ciurowa et al, 2007). The second type needs a critical milling time for the propagating reaction to be initiated. The temperature increases slowly at the beginning and after a period of milling, temperature climbs suddenly, which confirmed the fact that ignition has occurred. The reduction reaction occurs only beyond this time, reaction takes place within seconds (Wieczorek-Ciurowa, 2010). The time interval which is needed to reach sudden temperature increase is referred to as the ignition time and these values for various reactions can be found in data tables (Schaffer and McCormick, 1992; Suryanarayana, 2001). The ignition temperature is determined as a function enthalpy change and microstructural parameters such as interfacial area between the reactants. The ignition temperature can be decreased by means of diminution of particle size and increasing surface between interfacial contacts (Schaffer and McCormick, 1992).

The stress inside the powder concentrates at a few points such as the inner wall of the container. These 'hot spots' can start the reaction even if the average temperature of powder mixture is not sufficient to initiate a reaction front which propagates into other parts of the powder layers. Close contact between reactant phases is necessary for self-propagating synthesis and it is attainable in a ductile-brittle system (Wieczorek-Ciurowa, 2010).

An example of self-propagating reactions is given by Botta et al (2000), by milling aluminium and magnetite powders according to the reaction (2.30).

$$3\ Fe_3O_4 + 8\ Al \rightarrow 9\ Fe + 4\ Al_2O_3 \qquad \textbf{(2.30)}$$

It was stated that crystallinity of starting reactants decreased after a 30 min milling time and the aluminothermic reaction was completed after 37 min milling. Traditionally, this reaction would be thermally initiated during high temperature treatment (Botta et al, 2000). If milling time is less than 30 min, some active precursor products form by the energy gathered in the solid phase and this energy is released during thermal treatment. This effect can be seen in TiO_2-Al system where

aluminothermic reaction does not take place during milling. This phenomenon is named as solid activation, can be observed in metallic-ceramic composite powders (Wieczorek-Ciurowa, 2010).

The synthesis process can proceed by an explosive reaction or in a controlled steady way. The conditions of activation process can have determining effect on the reaction taking place at all. Additionally, heat conductivity of the milling medium can have determining effect on the formation of hot spots. Some examples of induction times for SHS reactions handled under given conditions are given in Table 2.4 (Wieczorek-Ciurowa, 2010). It is possible to use a process control agent (PCA) like toluene to control the explosiveness of reactions (Murty and Ranganathan, 1998; Takacs, 2002).

Table 2.4 : Under different milling conditions, examples of induction time intervals for selected SHS mechanochemical reactions, adapted from Wieczorek-Ciurowa (2010).

Reaction	Type of mill	BPR	Induction time (min)	References
$ZnO + Mg \rightarrow Zn + MgO$	Vibratory	7:1	45	Yang and McCormick, 1993a
$2FeO + Ti \rightarrow 2Fe + TiO_2$	Vibratory	8:1	20	Takacs, 2002
$8CuO + 3Fe \rightarrow 4Cu_2O + Fe_3O_4$	Planetary	30:1	153	Shen et al, 1992
$CuO + Zn \rightarrow Cu_2O + ZnO$	Vibratory	-	44	Takacs, 2002
$Cu_2S + Fe \rightarrow 2Cu + FeS$	Vibratory	8:1	-	McCormick et al, 1989

Amongst the products of displacement reactions, oxides or chlorides of reductants exist and these can be eliminated by leaching in a dilute acid or hot water or by vacuum distillation. It was reported that the salt (by-product $MgCl_2$) formed during the reduction of $TiCl_4$ with Mg was removed either by vacuum distillation at 900ºC for 24 h or by washing the powder in 10 % HNO_3 (McCormick et al, 1991).

The kinetics of mechanochemical reactions can be changed by synthesis conditions such as milling temperature, ball-to-powder weight ratio (BPR), the type of ball material, grinding ball diameter, process control agent and relative proportion of the reactants.

In most of the research investigations, generally about 10-15 % stoichiometric excess of the reductant has been used (Suryanarayana, 2001). The reactive reductant

powders can be exposed to partial surface oxidation so that excess amount is used to compensate this missing amount (Pardavi-Horvath and Takacs, 1992).

The diffusivity is expected to enhance at higher temperature which causes to increase the reaction kinetics and shorten the reduction time (McCormick et al, 1991). Also, an increase in the BPR will cause a reduction in the time required for the reaction to complete. The studies for reduction of $TiCl_4$ with Mg at 20ºC showed that with a BPR of 2:1 the time required to form Ti was 48 h, while it was only 18 h at a BPR of 12:1. This result has shown that at higher BPR ratios, the higher collisions enable the reaction to proceed faster (Suryanarayana, 2001).

Yang and McCormick (1993b) observed the effect of grinding ball diameter during milling of $TaCl_5$ and Mg powder mixtures. They reported that with an increase in ball diameter, the ignition time, t_{ig}, decreased for the combustion reaction. The ignition temperature, T_{ig}, has been found to decrease as expected with a refinement in the microstructure (Suryanarayana, 2001).

While a process control agent (PCA) is not needed in many investigations on reduction reactions where the components are brittle, nevertheless it is used in some specific studies. It was found that the use of a PCA can create a dilution effect which either delays or completely suppresses the reaction (Schaffer and McCormick, 1990). Also, inter-particle welding during collisions is hindered by the PCA, is slowing down the reaction rate as well as decreasing the particle size. It should be taken into consideration that the self-propagating combustion reaction may cause to coarsen grains because of partial melting and subsequent solidification. Moreover, there must be sufficient volume fraction of the by-product phase to prevent agglomeration for obtaining nanometer-sized particles (Suryanarayana, 2001).

Mechanochemical synthesis includes mechanical alloying and reactive milling which is derived from mechanical activation (Murty and Ranganathan, 1998; Suryanarayana et al, 2001; Boldyrev, 2006; Smolyakov et al, 2008). The term mechanical activation is explained as a process which causes an increase in reaction ability of a substance by mechanical treatment (Balaz, 2008). Butyagin (1984) explained the effect of mechanical energy on the solids by three main aspects: structural disordering, structural relaxation and structural mobility. It is stated that structural relaxation plays an important role in mechanical activation and after

interrupting the action of mechanical forces, solids reveal different times of relaxation (Ljachov, 1993). By this theory, the states whose relaxation time is less than reaction time does not influence the reactivity of activated solids and some long-lived states (e.g., surface area) may regard as having major influence. Therefore, mechanical activation is a multi-step process with changes in energetic parameters (Balaz, 2008). The term mechanical activation unites the four processes, namely, the accumulation of defects, amorphization, the formation of metastable polymorphous forms and chemical reaction (Boldyrev and Tkacova, 2000). Juhasz (1998) subdivided the processes under the influence of mechanical activation into primary and secondary processes: primary ones generally increase the reactivity of substance (increase of internal and surface energy, increase of surface area, decrease of the coherence energy of solids) and secondary processes (aggregation, adsorption, recrystallization) occur spontaneously and may complete after milling (Juhasz and Kollath, 1993; Juhasz, 1998).

Mechanical activation of milled material is achieved by increase of both the specific surface energy and the elastic strain energy. The surface free energy can be dissipated by agglomeration of new fracture surface or adsorption of environmental gaseous species and moisture. The relaxation processes for bulk activation are heating, fracturing of the brittle material, crystallographic lattice rearrangements, chemical reactions between adjoin points and imperfections (Boldyrev, 1986; Juhasz and Kollath 1993; Lin 1998; Pourghahramani, 2007). The elastic strain energy transforms into lattice defects such as point defects (vacancies), linear defects (dislocations), planar defects (stacking faults or sub-crystallite interfaces) and volumetric defects (structural disordering) (Lin, 1998; Pourghahramani, 2007).

Elastic energy relaxation can be completed in prolonged times and the remaining energy in the form of defects is the source of the excess Gibbs energy and enthalpy (Heegn, 1989). Hüttig (1943) elaborated this stage as a thermodynamically unstable state and defined the activated state of solid subtances by residual Gibbs energy.

In the equation (2.31), G_T^* and G_T are the Gibbs free energies of substance in activated and non-activated states, respectively. The Gibbs free energy between activated and non-activated solid states can be expressed by the difference in the enthalpy and entropy changes in regard of equation (2.32) (Hüttig, 1943).

$$\Delta G = G_T^* - G_T \quad \textbf{(2.31)}$$

$$\Delta G = \Delta H - T\Delta S \quad \textbf{(2.32)}$$

The ΔS can be very small and neglected if crystal disordering is low. However, highly deformed and disordered crystals have higher ΔS values which influence the Gibbs free energy. In activated solid substances the excess Gibbs free energy originates from specific surface energy and lattice defect formation. In a comminuted substance, only small amount of the excess energy comes from the surface area but mostly from the defect structure (Tkacova et al, 1993; Balaz, 2000).

In a mechanically activated state, the Gibbs free energy of substance rises therefore the activated material have enough potential to overcome activation energy barrier to start a reaction (Zelikman et al, 1983).

3. EXPERIMENTAL PROCEDURE

The experimental procedure of this dissertation comprises the identification of raw materials, the step-by-step synthesis of LaB_6, CeB_6 and SmB_6 powders, the purification treatments conducted on the synthesized powders, the consolidation of the purified powders and the characterization investigations carried out at each stage of the overall process.

3.1 Preparation of Raw Materials

The synthesis of rare-earth hexaborides (LaB_6, CeB_6 and SmB_6) were originated from their oxide powders such as La_2O_3 (ABCR^{TM}, in purity of 99.99 %), CeO_2 (ABCR^{TM}, in purity of 99.99 %) and Sm_2O_3 (ABCR^{TM}, in purity of 99.99 %). B_2O_3 (ETI Mine, in purity of 98 %) powders were used as a native boron source for the formations of boride phases. Mg (MME, in purity of 99.7 %) powders were used in the experiments as a strong metallic reducing agent. Ca (Alfa Aesar^{TM}, in purity of 99.5 %) granules were alternatively utilized as a reductant in order to examine their influence on the formation of LaB_6. The images of all raw materials were captured by using a Zeiss^{TM} Discovery.V12 Stereomicroscope (SM) coupled with a Zeiss^{TM} Axiocam ERc5s high resolution digital camera. SM images of the raw materials are represented in Figure 3.1(a) through Figure 3.1(f). Figures 3.1(a)-(f) more or less give an idea about their average particle sizes since their SM images, except those of B_2O_3 and Ca which have larger particle sizes, have the same magnification scale of 200 μm. Figure 3.1(f) obviously shows the average particle size of the Ca granules as 3 mm. Moreover, the crystalline phases of all raw materials were identified using a Bruker^{TM} D8 Advanced Series X-ray diffractometer (XRD) with CuKα (1.54060 Å) radiation in the 2θ range of 10-90° with 0.02° steps at a rate of 2°/min. International Centre for Diffraction Data® (ICDD) powder diffraction files were utilized for the crystalline phase identification of the raw materials. The XRD patterns of La_2O_3, CeO_2, Sm_2O_3, B_2O_3 and Mg powders and Ca granules are illustrated in Figure 3.2(a)

through Figure 3.2(f), respectively. Each figure shows diffraction peaks belonging only to the pure material with no trace of impurities. Although Figures 3.2(a), (b), (c) and (e) exhibit intense crystalline peaks belonging to their contents, Figure 3.2(d) shows the characteristic peak structure of amorphous B_2O_3. The XRD peaks of Ca given in Figure 3.2(f) have low intensities arising from its granule form which was very difficult to grind in an agate mortar applied for the proper analysis in the powder diffractometer.

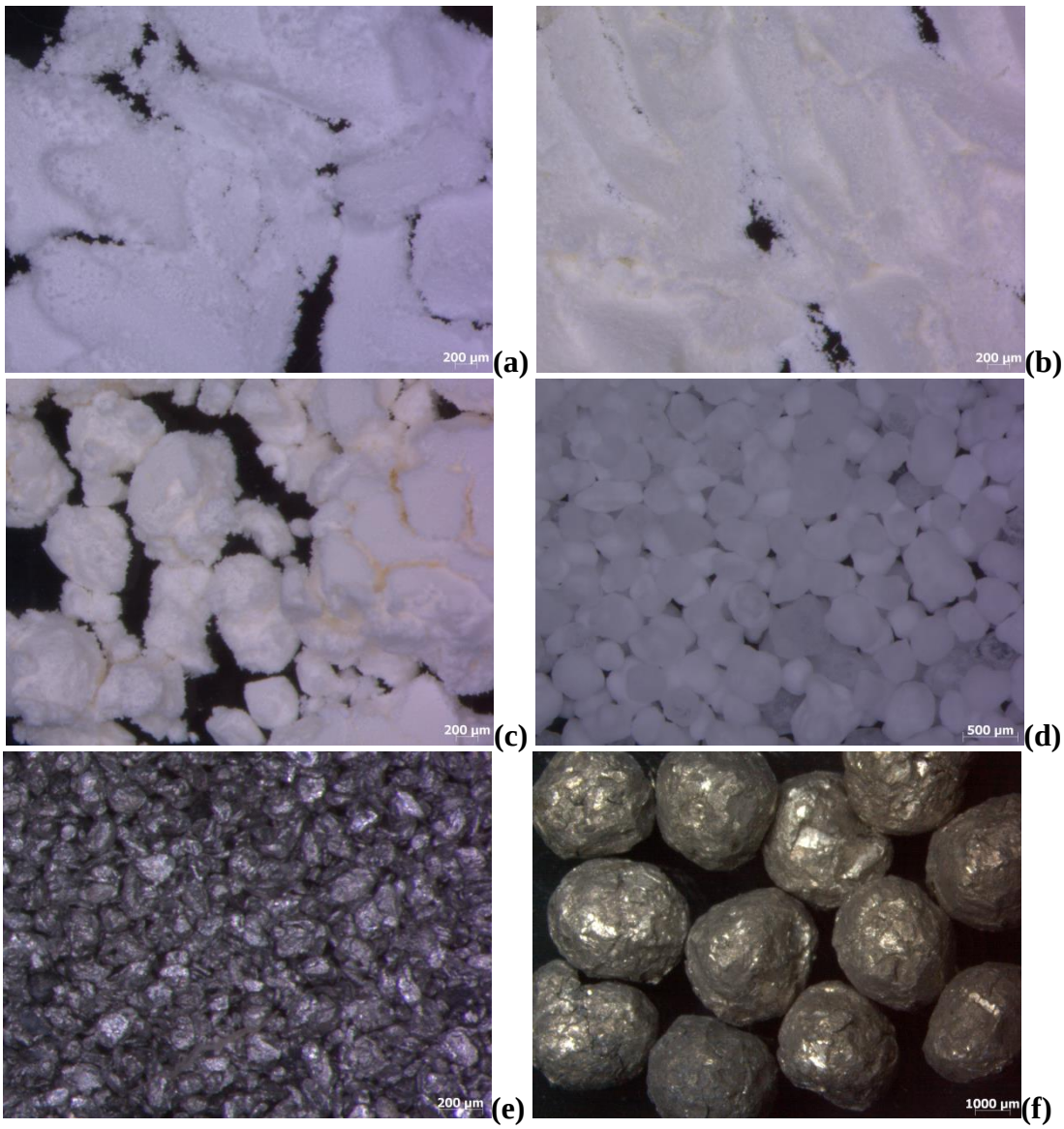

Figure 3.1 : SM images of the raw materials: (a) La_2O_3, (b) CeO_2, (c) Sm_2O_3, (d) B_2O_3, (e) Mg and (f) Ca.

Particle size measurements were conducted in a Malvern^{TM} Mastersizer 2000 particle analyzer using distilled water as the aqueous media in order to determine the accurate

particle sizes of the raw materials owning powder forms. Figures 3.3(a), (b), (c), (d) and (e) represent the respective particle size distributions of the La_2O_3 [d(0.1)=7.5 μm, d(0.5)=28.8 μm, d(0.9)=67.9 μm], CeO_2 [d(0.1)=2.7 μm, d(0.5)=7.4 μm, d(0.9)=18.3 μm], Sm_2O_3 [d(0.1)=0.73 μm, d(0.5)=3.3 μm, d(0.9)=6.6 μm], B_2O_3 [d(0.1)=268.5 μm, d(0.5)=438.8 μm, d(0.9)=708.2 μm] and Mg [d(0.1)=49.6 μm, d(0.5)=111.8 μm, d(0.9)=261.1 μm] powders. As seen in Figures 3.3(a)-(e), the average particle sizes of the La_2O_3, CeO_2, Sm_2O_3, B_2O_3 and Mg starting powders were measured as 33.6 μm, 9.5 μm, 3.6 μm, 466.9 μm and 142.7 μm, respectively.

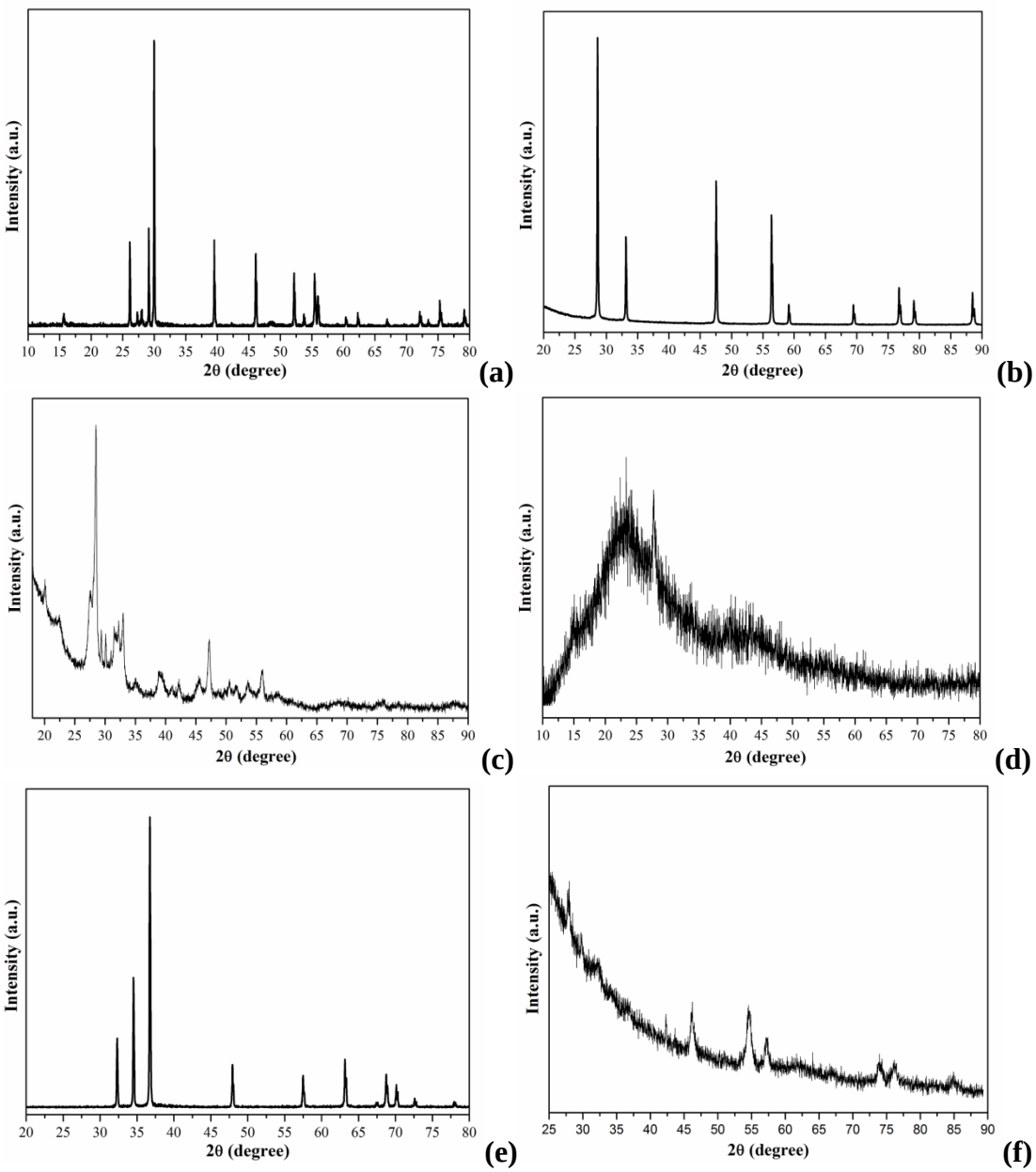

Figure 3.2 : XRD patterns of the raw materials: (a) La_2O_3, (b) CeO_2, (c) Sm_2O_3, (d) B_2O_3, (e) Mg and (f) Ca.

La_2O_3, CeO_2, Sm_2O_3 and Mg starting powders which had smaller average particle sizes than those of B_2O_3, Mg and Ca and whose particles could not be clearly identified by the respective SM images in Figures 3.1(a), (b), (c) and (e) were subjected to microstructural analysis by using a Hitachi^{TM} TM-1000 scanning electron microscope (SEM) operated at 15 kV. According to the SEM migrograph in Figure 3.4(a), La_2O_3 powders consist of particles having an average size below 5 μm. The controversy in the results of particle size analyzer and scanning electron microscope is probably due to the irregularly shaped La_2O_3 particles enabling a rapid agglomeration during the particle size measurement in the aqueous media. However, the particle sizes of CeO_2, Sm_2O_3 and Mg shown in respective SEM micrographs in Figures 3.4(b)-(d) were in good agreement with those of measured ones given in the graphs of Figures 3.3(b), (c) and (e). Moreover, CeO_2 and Sm_2O_3 powders have similar morphologies consisting of rectangular-shaped particles whereas Mg powder particles mostly have ellipsoidal shapes.

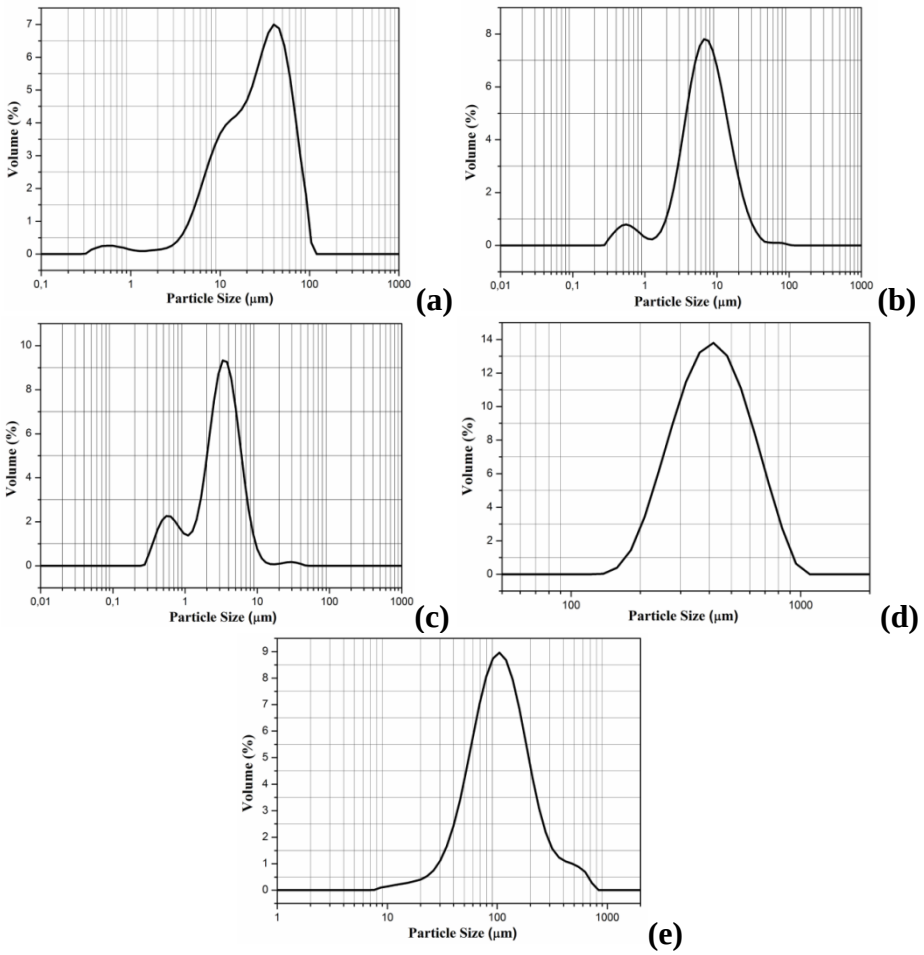

Figure 3.3 : Particle size distributions of the raw materials in powder forms: (a) La_2O_3, (b) CeO_2, (c) Sm_2O_3, (d) B_2O_3 and (e) Mg.

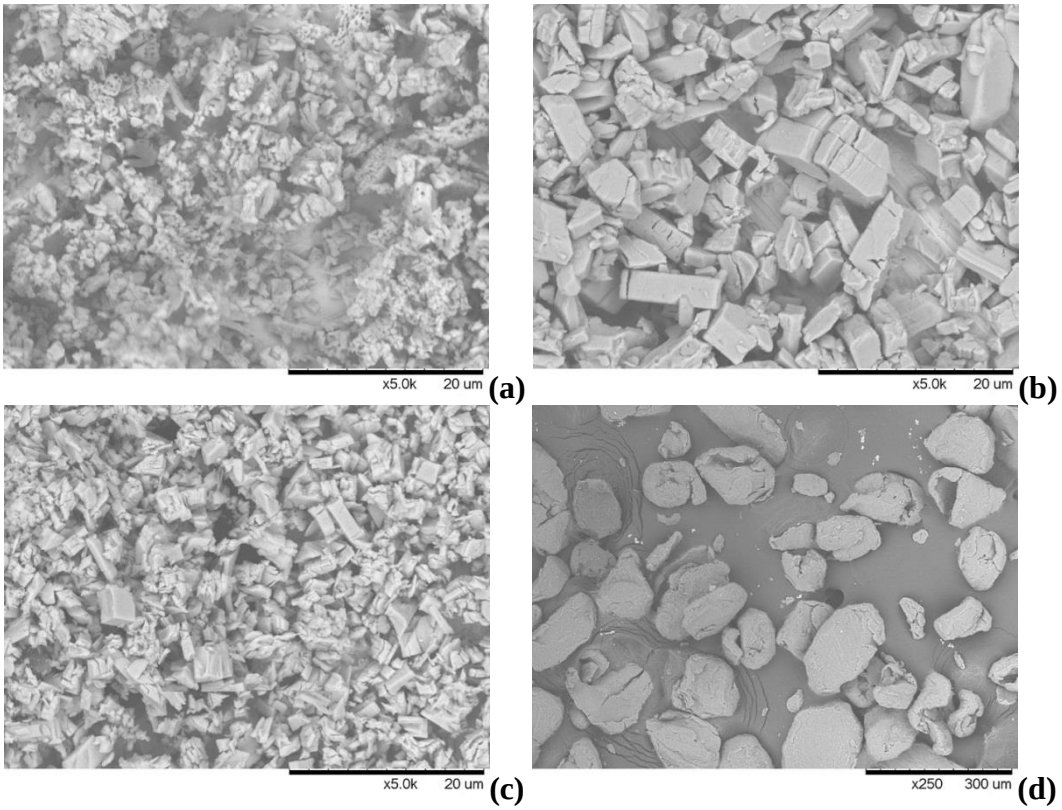

Figure 3.4 : SEM micrographs of the raw materials in small average particle sizes: (a) La_2O_3, (b) CeO_2, (c) Sm_2O_3 and (d) Mg.

Powder blends containing stoichiometric amounts of reactants for synthesizing LaB_6, CeB_6 and SmB_6 powders were prepared according to the overall reactions given in (3.1)-(3.4).

$$La_2O_3 + 6B_2O_3 + 21Mg \rightarrow 2LaB_6 + 21MgO \quad \textbf{(3.1)}$$

$$La_2O_3 + 6B_2O_3 + 21Ca \rightarrow 2LaB_6 + 21CaO \quad \textbf{(3.2)}$$

$$CeO_2 + 3B_2O_3 + 11Mg \rightarrow CeB_6 + 11MgO \quad \textbf{(3.3)}$$

$$Sm_2O_3 + 6B_2O_3 + 21Mg \rightarrow 2SmB_6 + 21MgO \quad \textbf{(3.4)}$$

For each run of LaB_6, CeB_6 and SmB_6 syntheses, powder batches of 6 g were weighed in a Precisa^{TM} XB320M sensitive balance (precision: 0.001 g). Powder batches contained 1.56 g La_2O_3, 2.0 g B_2O_3 and 2.44 g Mg or 1.233 g La_2O_3, 1.581 g B_2O_3 and 3.186 g Ca according to the LaB_6 formation reactions in (3.1) and (3.2). In regard of reaction (3.3), 1.593 g CeO_2, 1.933 g B_2O_3 and 2.474 g Mg powders were weighed to constitute the batches for the synthesis of CeB_6. Powder batches containing 1.639 g Sm_2O_3, 1.968 g B_2O_3 and 2.398 g Mg were prepared for the synthesis of SmB_6 on the basis of the reaction in (3.4). For the LaB_6 synthesizing

experiments carried out in larger volumes by using a different type of high-energy ball mill, the amount of powder batches was increased to 60 g. The prepared powder batches are hereafter referred to as La_2O_3-B_2O_3-Mg, La_2O_3-B_2O_3-Ca, CeO_2-B_2O_3-Mg and Sm_2O_3-B_2O_3-Mg powder blends.

In some experiments, 0.5 wt. % stearic acid ($C_{18}H_{36}O_2$, ZAG, in purity of 99.5 %) was added into the powder blends prepared according to the reaction (3.1) in order to investigate the effect of process control agent (PCA) on the formation mechanism of LaB_6 powders. Due to the identification of the utilized $C_{18}H_{36}O_2$ powders whose SM image is given in Figure 3.5(a), Fourier Transform Infrared Spectroscopy (FTIR) technique was applied to this organic material at the wavenumber values ranging between 400 and 3500 cm^{-1} and in the resolution of 4 cm^{-1} with sample and background scan time of 24 scans/min in a Bruker™ Alpha-T FTIR equipped with a platinum diamond Attenuated Total Reflection (ATR) module. As seen in the SM image in Figure 3.5(a), $C_{18}H_{36}O_2$ powders consist of particles with an average size of about 1 μm. Figure 3.5(b) illustrates the characteristic FTIR peaks of the stearic acid without trace of any impurities.

Additionally, commercial LaB_6 (Alfa Aesar™, in purity of 99.5 %), CeB_6 (ABCR™, in purity of 99.5 %) and SmB_6 (Alfa Aesar™, in purity of 99.9 %) powders whose SM images are given in Figures 3.6(a)-(c) were utilized for the comparison with the powders synthesized in this dissertation. The XRD patterns of the commercial LaB_6, CeB_6 and SmB_6 powders are demonstrated in Figures 3.7(a)-(c), respectively. Figures 3.7(a) and (b) display diffraction peaks belonging only to the pure hexaborides without trace of any contaminations. However, the peaks in Figure 3.7(c) which have low intensities indicates $SmBO_3$ impurity with the major SmB_6 phase.

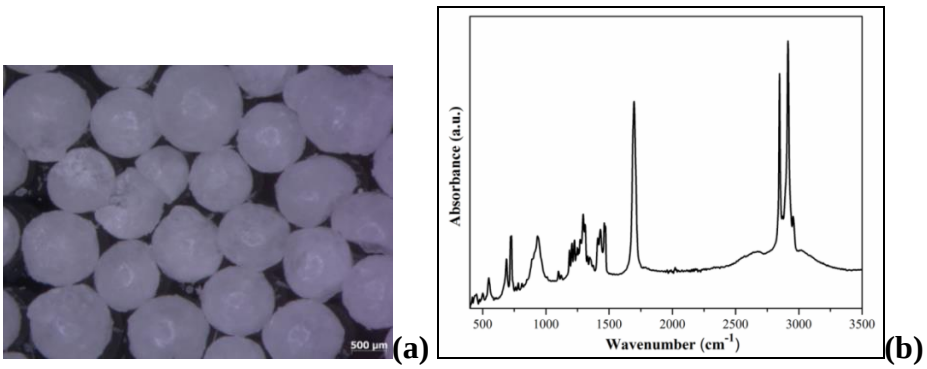

(a) **(b)**

Figure 3.5 : (a) SM image and (b) FTIR spectrum of the stearic acid used as PCA in the experiments.

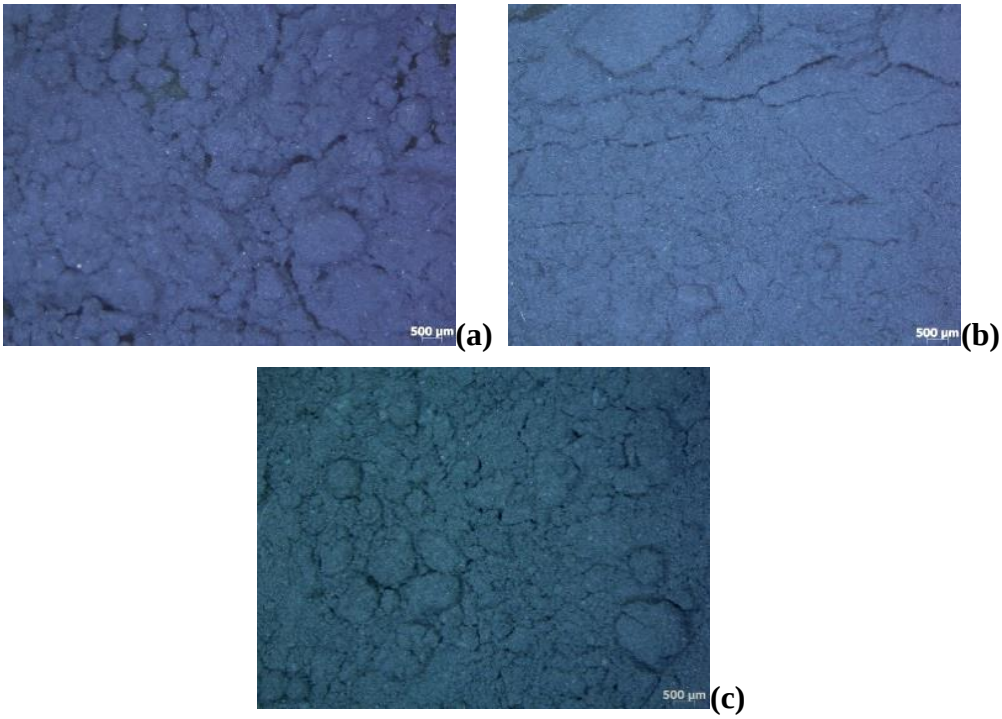

Figure 3.6 : SM images of the commercial powders: (a) LaB_6, (b) CeB_6 and (c) SmB_6.

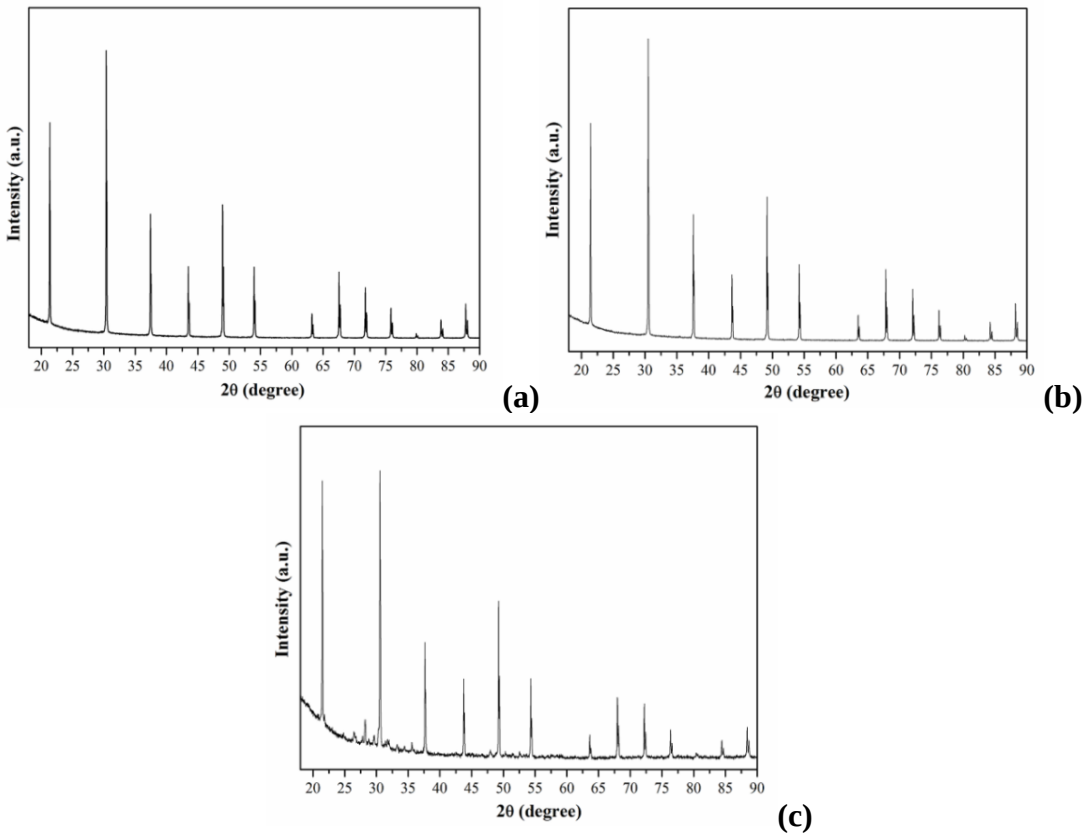

Figure 3.7 : XRD patterns of the commercial powders: (a) LaB_6, (b) CeB_6 and (c) SmB_6.

Figures 3.8(a) through 3.8(c) illustrate the particle size distributions of the commercial LaB_6 [d(0.1)=1.9 μm, d(0.5)=4.2 μm, d(0.9)=5.2 μm], CeB_6 [d(0.1)=4.1 μm, d(0.5)=10.1 μm, d(0.9)=15.7 μm] and SmB_6 [d(0.1)=0.6 μm, d(0.5)=3.3 μm, d(0.9)=24.2 μm] powders, respectively. As seen in Figures 3.8(a)-(c), the average particle sizes of the LaB_6, CeB_6 and SmB_6 powders were respectively measured as 4 μm, 10 μm and 8 μm.

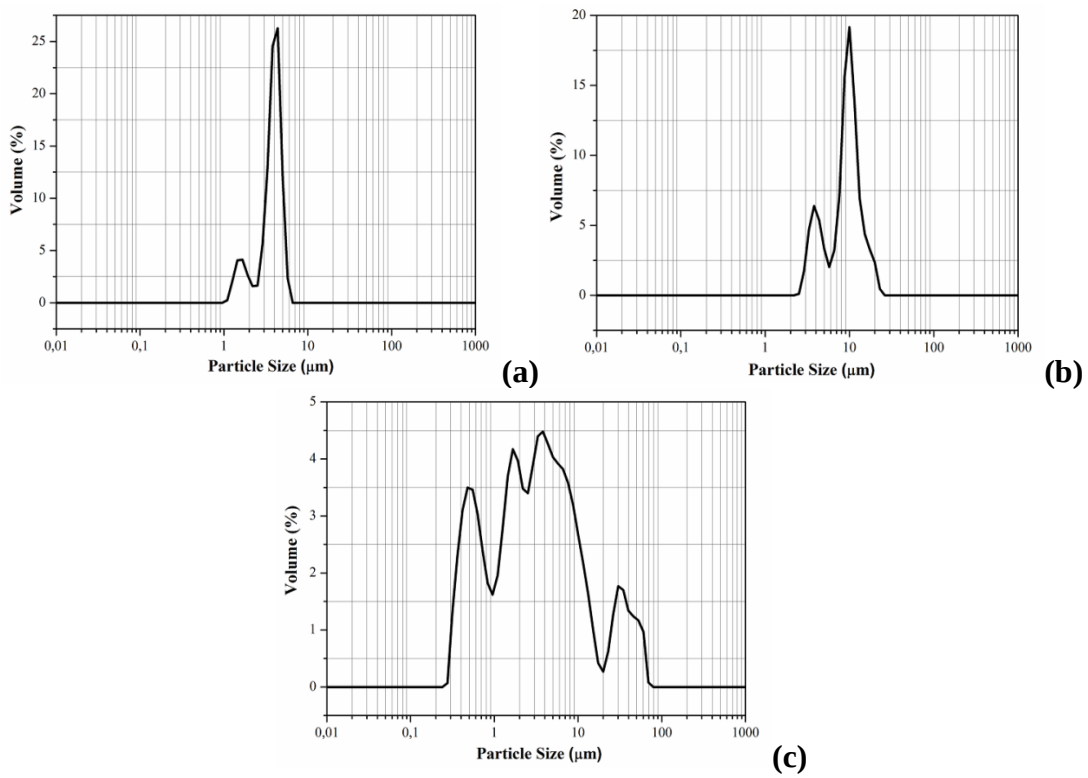

Figure 3.8 : Particle size distributions of the commercial powders: (a) LaB_6, (b) CeB_6 and (c) SmB_6.

Commercial LaB_6, CeB_6 and SmB_6 powders were used as the references for the property and hence quality determination of the laboratory-synthesized ones. The microstructural analyses of them were given in details in order to make accurate interpretations.

3.2 Mechanochemical Synthesis of the Powder Blends

All the prepared powder blends (La_2O_3-B_2O_3-Mg, La_2O_3-B_2O_3-Ca, CeO_2-B_2O_3-Mg and Sm_2O_3-B_2O_3-Mg) were homogenized in a WAB^{TM} T2C Turbula blender for 1 h prior to mechanochemical synthesis experiments. The homogenized powder blends were mechanochemically synthesized by using a multi-axial and vibratory high-

energy ball mill, Spex^{TM} 8000D Mixer/Mill, with a rotation speed of 1200 rpm. Alternatively, Fritsch^{TM} Pulverisette 5 Classic Line planetary ball mill with a rotation speed of 400 rpm was used for the mechanochemical synthesis of LaB_6 powders due to the comparison of the final products. Thus, the driving force of mechanochemical synthesis was mechanical milling carried out in different types of high-energy ball mills. Non-milled powders, which were homojenized but were not subjected to mechanochemical synthesis, were hereafter referred to as-blended (ab) powders and were used as references for the comparison with the milled ones.

In the mechanochemical synthesis experiments, ball-to-powder weight ratio (BPR) was chosen as 10:1. It is already known that the required time for the complete reaction decreased with an increase in the BPR. So, it seems obvious to employ larger BPRs to prevail the effect of mechanochemical synthesis at shorter times. Taking this into consideration, the BPR was also chosen as 18:1 for the mechanochemical synthesis of LaB_6 powders. In case of carrying out the experiments in Spex^{TM} 8000D Mixer/Mill, the milling container was a hardened steel vial with a capacity of 50 ml and the milling media was hardened steel balls with a diameter of 6 mm. During ball milling experiments in Fritsch^{TM} Pulverisette 5 Classic Line planetary ball mill, the milling container was zirconia vial with a capacity of 500 ml and the milling media was zirconia balls with a diameter of 10 mm. Ar gas (Linde^{TM}, in purity of 99.999 %) was preferred as the milling atmosphere. The milling vials were evacuated to about 10^{-2} Pa and back filled with Ar gas in a Plaslabs™ glove box to prevent surface oxidation and to prevent contamination of powder particles with oxide and nitride phases arising from the presence of air. After sealing the vials, milling was continually conducted at different durations up to 25 h in Spex^{TM} 8000D Mixer/Mill and up to 30 h in Fritsch^{TM} Pulverisette 5 Classic Line planetary ball mill.

Preliminary experiments carried out intermittently and continuously up to a certain milling duration resulted in different products because the complete reaction took place by means of the internal heat generated from the repeated collisions of the reactant particles. In order to determine the differences in the final product, milling was extended to longer durations than those of complete reactions. The milled powders were unloaded again under Ar atmosphere in the glove-box. They are hereafter referred to as mechanochemically synthesized or milled La_2O_3-B_2O_3-Mg,

La_2O_3-B_2O_3-Ca, CeO_2-B_2O_3-Mg and Sm_2O_3-B_2O_3-Mg powders. At least 5.4 g or 56 g of products according to the used high-energy ball mill were extracted from the vials for the subsequent treatments and characterizations.

3.3 Selective Acid Leaching of the Mechanochemically Synthesized Powders

After mechanochemical synthesis of the prepared La_2O_3-B_2O_3-Mg, La_2O_3-B_2O_3-Ca, CeO_2-B_2O_3-Mg and Sm_2O_3-B_2O_3-Mg powder blends up to a certain duration at which the reduction reaction completed, MgO or CaO containing LaB_6, CeB_6 and SmB_6 powders were obtained as the intermediate products. Selective HCl (Merck™, in concentration of 37 %) leaching was applied on these products under the effect of ultrasonic stirring and heating using a Bandelin Sonorex™ RK-100 H ultrasonic bath due to the fact that LaB_6, CeB_6 and SmB_6 are insoluble in HCl. Leaching treatment enabled the removal of the unwanted oxide phases (MgO or CaO) and the impurities (especially Fe, Cr and Ni) which were worn off from the milling vial and milling balls. 2 M, 3.6 M and 4 M HCl were used as the leaching solutions. In other words, the intermediate products were leached using excess HCl molarities with the intention of obtaining pure LaB_6, CeB_6 and SmB_6 powders. The molarity of commercial HCl solution in concentration of 37 % was calculated in equation (3.5).

$$\text{Molarity of HCl solution} = \frac{1\,\text{mol}}{36.46\,\text{g}} \times \frac{37}{100} \times \frac{1.19\,\text{g}}{1\,\text{ml}} \times \frac{1000\,\text{ml}}{1\,\text{L}} = 12.076\ \text{mol/L} \quad \textbf{(3.5)}$$

In regard of equation (3.5), 1 M HCl leaching solution can be obtained by mixing 83 ml HCl solution (1/12.076 = 0.083 L) with 917 ml distilled water. Thus, the leaching solutions used in the experiments (2 M, 3.6 M and 4 M HCl) were prepared by the help of these calculations. After a series of pre-experiments, leaching parameters such as solid-to-liquid ratio of the leaching solution, leaching duration and leaching temperature were fixed respectively to 1 g/10 cm^3, 15 min and 80°C. During the first few seconds of the leaching treatments, the intermediate products violently reacted with the leaching solutions, arising from the high solubility of MgO or CaO in HCl solution as given in reactions (3.6) and (3.8).

$$\text{MgO or CaO} + H_2O \rightarrow Mg(OH)_2 \text{ or } Ca(OH)_2 \quad \textbf{(3.6)}$$

$$\text{MgO or CaO} + 2HCl \rightarrow MgCl_2 \text{ or } CaCl_2 + H_2O \quad \textbf{(3.7)}$$

$$MgCl_2 \text{ or } CaCl_2 + 2H_2O \rightarrow Mg(OH)_2 \text{ or } Ca(OH)_2 + 2HCl \quad \textbf{(3.8)}$$

At the end of leaching treatment, the solutions containing insoluble solids were subjected to repeated centrifuging in a Hettich^{TM} Rotofix 32A centrifuge with a rotation speed of 3500 rpm for 30 min, repeated decanting, repeated washing with distilled water for several times and lastly remained solids were dried under air in a FN 500 stove at 120ºC for 24 h. Supernatant liquids decanted from the solids after each centrifuging-decanting-washing treatment were collected into a volumetric flask for the subsequent instrumental analyses. Besides, all the collected supernatant liquids which belonged to different products were equated to 150 ml with distilled water for the correct comparison. After each centrifuging-decanting-washing treatment, a few drop of leaching solution was added into a 1 M $AgNO_3$ solution (Fluka^{TM}, in purity of 99.5 %) due to the detection of chlorine by precipitating AgCl and these treatments were repeated until any AgCl precipitation was not detected. Since the leaching process was carried out by using excess HCl molarities, the HCl adsorption on the boride powders can be also prevented by this detection method. Moreover, pH measurements were carried out on the supernatant liquids decanted from the solids after the last washing procedure, by using Thermo Scientific^{TM} Orion Star A211 pH meter. The measured pH values varied between 5.5 and 6.5, indicating that there was not residual HCl in the media at the end of the repeated treatments. These findings conformed well with the results of AgCl precipitation method.

Consequently, the final powder products originated from the mechanochemically synthesized and leached La_2O_3-B_2O_3-Mg, La_2O_3-B_2O_3-Ca, CeO_2-B_2O_3-Mg and Sm_2O_3-B_2O_3-Mg powders. Figures 3.9(a)-(c) show respectively the LaB_6, CeB_6 and SmB_6 powders obtained as final products after 4 M HCl leaching of the mechanochemically synthesized La_2O_3-B_2O_3-Mg, CeO_2-B_2O_3-Mg and Sm_2O_3-B_2O_3-Mg powders. As clearly seen from Figures 3.9(a)-(c), these powders, on which subsequent treatments conducted, have distinctive color differences from each other. Additionally, annealing was conducted on some mechanochemically synthesized and leached powders in order to reveal any residual elements after leaching process which could not be detected by X-ray diffraction techniques. Leached powders placed in a quartz boat were annealed in a Thermoscientific^{TM} F21130 tube furnace at 800ºC for 5 h with a heating and cooling rate of 10ºC/min, under Ar gas flow of 500 ml/min.

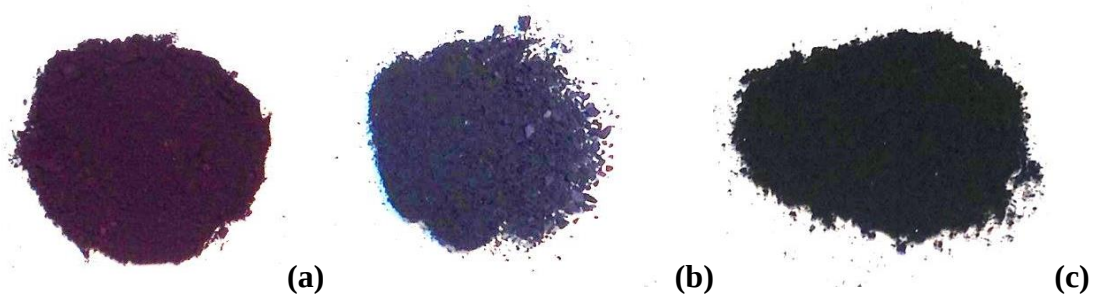

(a) **(b)** **(c)**

Figure 3.9 : The final powder products after 4 M HCl leaching of the mechanochemically synthesized La_2O_3-B_2O_3-Mg, CeO_2-B_2O_3-Mg and Sm_2O_3-B_2O_3-Mg powders: (a) LaB_6, (b) CeB_6 and (c) SmB_6.

3.4 Consolidation of the Leached Powders

After mechanochemical synthesis and leaching treatments, optimized conditions of obtaining pure LaB_6, CeB_6 and SmB_6 powders were determined. Thus, powders synthesized in high qualities were prepared in bulk forms. 2.5 g of the mechanochemically synthesized and leached La_2O_3-B_2O_3-Mg, CeO_2-B_2O_3-Mg and Sm_2O_3-B_2O_3-Mg powders were compacted in a 10 ton capacity MSE^{TM} MP-0710 uni-action hydraulic press under a uniaxial pressure of 800 MPa. Thus, green bodies in the shape of cylindrical preforms with a diameter of 12.7 mm and with a height of about 6 mm were obtained after cold pressing (CP).

The green bodies were sintered at 1700ºC for 5 h in a Linn^{TM} HT-1800 high temperature controlled atmosphere furnace with a heating and cooling rate of 10°C/min under Ar gas with a flow rate of 1000 ml/min. Furthermore, cold pressing and sintering processes were conducted on the commercial LaB_6, CeB_6 and SmB_6 powders for comparison some of their bulk properties with those of laboratory-synthesized bulks. Figures 3.10(a) through 3.10(g) illustrate all the bulk structures of LaB_6, CeB_6 and SmB_6 prepared from both laboratory-synthesized and commercial powders. Sintered compacts originated from commercial powders had some shape deformation especially at their lateral surfaces after sintering whereas laboratory-synthesized bulk compacts conserved their structures.

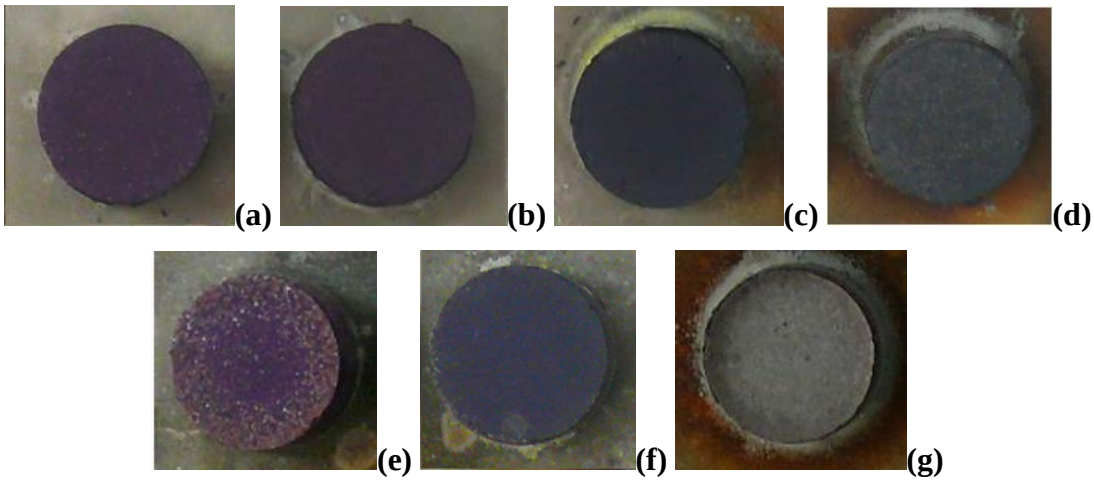

Figure 3.10 : Cold pressed and sintered bulk products: (a) LaB_6 originated from powders synthesized in Spex^{TM} 8000D Mixer/Mill, (b) LaB_6 originated from powders synthesized in planetary ball mill, (c) CeB_6 synthesized in Spex^{TM} 8000D Mixer/Mill, (d) SmB_6 synthesized in Spex^{TM} 8000D Mixer/Mill, (e) LaB_6 originated from commercial powders, (f) CeB_6 originated from commercial powders and (g) SmB_6 originated from commercial powders.

3.5 Characterization Investigations

X-ray diffraction (XRD) investigations of the as-blended, mechanochemically synthesized or milled, leached and annealed powders and of the sintered samples were performed in a Bruker^{TM} D8 Advanced Series powder diffractometer and in a PANalytical^{TM} X'Pert³ powder diffractometer, with CuKα (λ=0.154 nm, 40 kV and 40 mA) radiation in the 2θ range of 10-90° incremented at a step size of 0.02° at a rate of 2°/min. The International Center for Diffraction Data® (ICDD) powder diffraction files were utilized for the identification of crystalline phases. Average crystallite sizes and lattice strains of the mechanochemically synthesized LaB_6 powders were determined utilizing Bruker-AXS^{TM} TOPAS V3.0 software based on the modified Scherrer's formula (Suryanarayana and Norton, 1998). The phase amounts in the mechanochemically synthesized LaB_6 powders were identified by the semi-quantitative Rietveld method. The images of as-blended, mechanochemically synthesized and leached powders were captured by using a Zeiss^{TM} Discovery.V12 Stereomicroscope (SM) coupled with a Zeiss^{TM} Axiocam ERc5s high resolution digital camera. Particle size measurements were conducted on the leached powders using a Microtrac^{TM} Nano-flex particle size analyzer (PSA) equipped with a Bandelin Sonopuls^{TM} ultrasonic homogenizer. Thermal properties of the as-blended

and mechanochemically synthesized powders were examined in a TA™ Instruments SDT Q600 differential scanning calorimeter (DSC): For each run, 15 mg of powders was placed in an alumina crucible and heated up to 1150ºC at a heating rate of 10ºC/min under Ar atmosphere. Additional DSC analyses by using the same conditions were also performed on the dual powder blends such as B_2O_3-Mg, La_2O_3-Mg and La_2O_3-B_2O_3 for the evaluation of the reaction mechanism. After DSC analyses, mechanochemically synthesized and heated powders were subjected to additional XRD analyses to detect the obtained phases. Microstructural characterizations and energy dispersive spectroscopy (EDS) analyses of the mechanochemically synthesized and leached powders were carried out using a Hitachi™ TM-1000 and a FEI™ Quanta FEG 250 scanning electron microscope (SEM) operated at 15 kV and also using a Jeol™-JEM-2000EX transmission electron microscope (TEM) operated at 160 kV. For SEM analysis, the specimens of the mechanochemically synthesized and leached powders were prepared by following the procedure of dissolving the powders in the C_2H_5OH (Merck™, in purity of 99.9 %), syringing them onto a base plate, drying them in air and coating their surfaces with a thin layer of gold using a Polaron™ SC7620 Sputter Coater to enhance their conductivities. For TEM analysis of the leached powders, the particles were dispersed in the C_2H_5OH and a drop of it was taken on a porous carbon film supported on a copper grid and dried in a Jingke™ Scientific Instrument vacuum oven. EDS results were reported as the arithmetic means of three different measurements taken from the same regions in the samples.

The densities of the final powder products after leaching were measured by a Micromeritics™ AccuPyc II 1340 gas pycnometer in a 1 cm^3 sample chamber at room temperature using He gas (Linde™, in purity of 99.996 %) as the displacement medium. Density result of each powder product includes the arithmetic mean of ten successive measurements and standard deviations. Surface areas of the leached powders were determined using a Quantachrome™ Autosorb-IO/MP-XR surface area analyzer based on the Brunauer-Emmett-Teller (BET) theory, at 150°C by degassing under N_2 gas (Linde™, in purity of 99.999 %) for 5 h and by absorbing with N_2 (for analysis) and He (for reference) gases. Magnetic properties of the leached powders were identified by a vibrating sample magnetometer (VSM) at room temperature under DC-biased magnetization between 0 and 8000 Oe. Furthermore,

the amounts of elements (B, Mg and Fe) in the supernatant liquids after the purification by leaching processes were analyzed in a Perkin Elmer™ 1100B atomic absorption spectrometer (AAS).

The densities of the sintered samples were measured in ethanol using the Archimedes method and the results were reported as the arithmetic means of three different measurements taken from the same samples. Bulk densities were also determined by using the same He gas pycnometer. In order to obtain scratch-free mirror finish for electrical resistivity measurements, SEM analyses, Vickers microhardness measurements and sliding wear tests, all sintered samples were subjected to a series of metallographic treatments. Sintered samples were hot-mounted using 20 ml Akasel clear acrylic resin in a Struers™ LaboPress-1 under 20 kN with a heating and cooling duration of 7 min. Hot-mounted samples were ground and polished in a Struers™ Tegrapol-15 grinding/polishing instrument under 20 N with a rotation speed of 200 rpm, respectively using MD-Piano (with water) and MD-Largo (with Akasel 9 μm lubricant blue) grinding discs and MD-Dac (with Akasel 3 μm lubricant blue) and MD-Chem (with 50 nm colloidal silica) polishing discs, up to 5 min at each stage. These samples were cleaned ultrasonically in ethanol for 10 min at every step of the grinding and polishing treatment. Electrical resistivities of the polished specimens were measured at room temperature by using four-point probe method in a Signatone™ four-point probe system equipped with a high impedance current source and a voltmeter. Four-point probe consists of four equally spaced tungsten metal tips with finite radius, as shown in Figure 3.11.

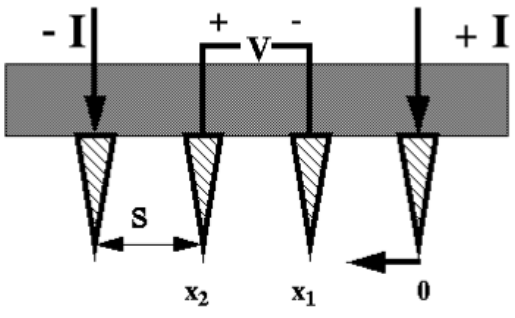

Figure 3.11 : Schematic representation of four-point probe configuration.

The expression for the calculation of electrical resistivity of bulk structures (ρ) is given in equation (3.9) in which s is the typical probe spacing (~1.58 mm), V is the voltage across the inner two probes, I is the current through the outer two probes.

Electrical resistivity result of each sample is the arithmetic mean of five different measurement series carried out at 100-300 mA and the standard deviations.

$$\rho = 2\pi s \frac{V}{I} \quad \textbf{(3.9)}$$

Vickers microhardness measurements of the sintered samples were conducted using a Shimadzu™ HMV Microhardness Tester under a load of 100 g (9.807 N) for 15 s. Microhardness test result for each sample includes the arithmetic mean of fifteen successive indentations and standard deviations. Surface roughness values of all the sintered samples were measured by using a Veeco™ Dektak 6 M Stylus Profiler under an applied force of 5 mg for 30 sec and with a length of 2 mm. All sintered samples were subjected to sliding wear tests at room temperature in a laboratory atmosphere in a Tribotech™ Oscillating Tribotester using an 6 mm alumina ball under an applied force of 4 N, with a sliding speed of 2 mm/s and a stroke length of 2 mm for a total sliding distance of 30000 mm. Wear tracks of all the sintered samples were imaged by using the SM and Hitachi™ TM-1000 SEM and examined by the profiler. Worn surfaces of the samples were coated with a thin layer of gold for 20 sec prior to the SEM analyses. Wear test results in terms of wear volume loss (WVL=(π/4)*width*depth*length) values are the arithmetic mean of five different measurements for each sample. Additionally, EDS measurements were performed on the wear tracks using the same SEM due to the detection of Al worn off from the alumina ball whose worn surfaces were screened with a Leica™ ICC50 HD optical microscope (OM).

3.6 Thermodynamic Investigations

HSC Chemistry™ Ver. 4.1 and FactSage™ 6.3 programs were utilized for the reaction interpretations of the La_2O_3-B_2O_3-Mg, La_2O_3-B_2O_3-Ca, CeO_2-B_2O_3-Mg and Sm_2O_3-B_2O_3-Mg systems. Since the database of the FactSage™ 6.3 program only includes CeB_6 phase as a rare-earth metal hexaboride and do not comprise the LaB_6 and SmB_6 phases, the interpretations of the reactions were detailed on the CeO_2-B_2O_3-Mg system. Therefore, the standard Gibbs free energy change and the standard enthalpy change versus temperature curves of the La_2O_3-B_2O_3-Mg, La_2O_3-B_2O_3-Ca and Sm_2O_3-B_2O_3-Mg systems up to 2000°C were graphed by using

HSC Chemistry™ Ver. 4.1 program and these graphs were illustrated respectively in Figures 3.12(a)-(c). As seen from these figures, all reactions have large negative standard free energy changes in the temperature range of 0-2000°C, between -3300 and -1700 kJ for La_2O_3-B_2O_3-Mg system, between -4100 and -2700 kJ for La_2O_3-B_2O_3-Ca system and between -3500 and -2000 kJ for Sm_2O_3-B_2O_3-Mg system. This means that reactions (3.1), (3.2) and (3.4) take place spontaneously and therefore they are thermodynamically feasible at room temperature and above. Moreover, large negative standard enthalpy changes of these reactions imply that large amount of heat is released during the occurrence of them. It can be predicted that the vial temperature will significantly increase during milling due to these exothermic reactions. As seen in Figures 3.12(a)-(c), the slopes of the standard enthalpy change-temperature curves vary at some intervals. This is due to the melting of B_2O_3 at 450°C, melting of Mg at 650°C, the formation of magnesium borate phases in different compositions (MgB_4O_7, $Mg_2B_2O_5$ and $Mg_3B_2O_6$) at 700-1100°C and boiling of Mg at 1095°C for Figures 3.12(a) and (c) and due to the formation of calcium borate phases in different compositions (CaB_2O_4, CaB_4O_7, $Ca_2B_2O_5$ and $Ca_2B_6O_{11}$) at 600-1000°C, melting of Ca at 840°C and boiling of Ca at 1485°C for Figure 3.12(b). Although calcium borate phases emerged at lower temperatures according to the calculation of standard enthalpy change in Figure 3.12(b) in the case of using Ca as a reducing agent, magnesium borate phases formed at relatively higher temperatures in the case of utilizing Mg. Furthermore, it is clearly understood from the Figures 3.12(a) and (b) that the calciothermic reductions of the rare-earth metal oxides are more favorable than their magnesiothermic reductions since their standard free energy difference at the same temperature is about 800-1000 kJ. Thus, the use of Ca instead of Mg as a reductant seems to be more suitable in the synthesis of LaB_6 powders according to the thermodynamic calculations. However, the calcium borates regarded as unwanted phases in the boride synthesis form in several compositions at relatively lower temperatures than those of magnesium borates and hence they can negatively influence the steps of the production process.

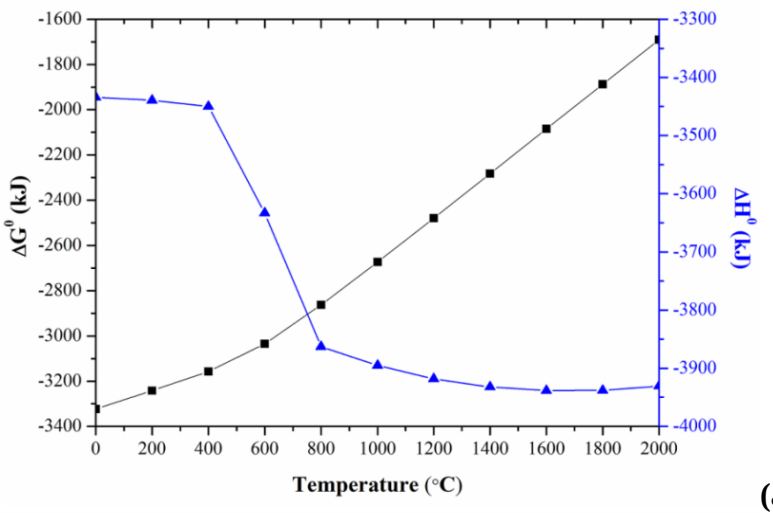

(a)

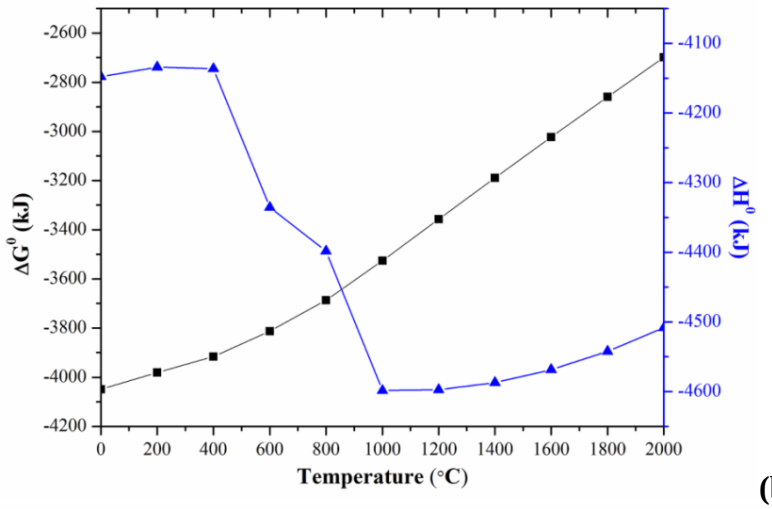

(b)

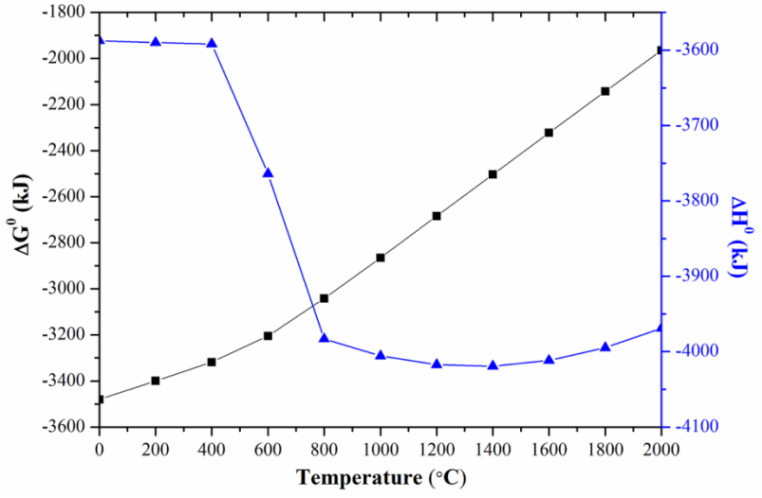

(c)

Figure 3.12 : Standard Gibbs free energy change and standard enthalpy change versus temperature curves of the (a) reaction (3.1), (b) reaction (3.2) and (c) reaction (3.4).

The standard Gibbs free energy change and the standard enthalpy change versus temperature curves of the CeO_2-B_2O_3-Mg system at temperatures between 0 and

2000°C were graphed by using FactSage™ 6.3 program, as shown in Figures 3.13(a) and (b). Reaction (3.3) have large negative standard free energy (between -2100 and -300 kJ) and standard enthalpy (between -2000 and -3800 kJ) changes, indicating that this reaction is possible at this temperature range and occurs spontaneously. Besides, the formations of LaB_6 and SmB_6 are comparably easier than that of CeB_6 because of their more negative standard free energy and enthalpy values. As seen in Figure 3.12(b), the slopes of the standard enthalpy change-temperature curve are arising from the melting of B_2O_3 at 450°C, melting of Mg at 650°C, boiling of Mg at 1095°C and the formation of magnesium borate phases until 1100°C. So, the results of the thermodynamic calculations in Figures 3.12(a)-(c) and 3.13(a)-(b) show that reduction reactions are possible to be carried out at room temperature processes.

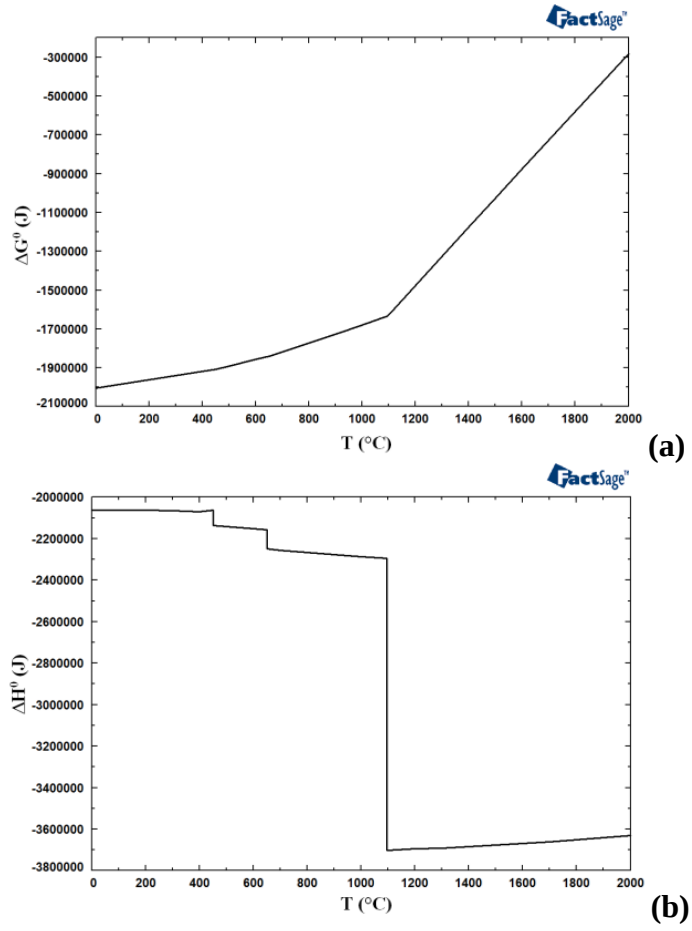

Figure 3.13 : Standard Gibbs free energy change (a) and enthalpy change (b) versus temperature curves of the reaction (3.3).

In order to comprehend the mole amounts of probable products of the reactants in the CeO_2-B_2O_3-Mg system, FactSage™ data were utilized to graph Figure 3.14(a) showing the mole amounts of the reactants and reaction products versus temperature

curves of the reaction (3.3) at stoichiometric conditions. According to Figure 3.14(a), a mole of CeB_6 forms in the presence of 11 moles of MgO up to 1800°C. After elevating the temperature above 1800°C, $Mg_3B_2O_6$ emerges together with the Mg gas and the amount of CeB_6 phase decreases to 0.5 mole with the decrease of MgO amount which completely vanishes at 1900°C. In addition, Figure 3.14(b) represents the mole amounts of the reactants and reaction products versus Mg mole amount curves of the reaction (3.3) at a constant temperature of 1200°C, which was the maximum applicable value in the DSC analyses. Based on Figure 3.14(b), it can be said that some amounts of CeO_2 and B_2O_3 phases remain without participating in the reaction and some amount of CeB_6 with the presence of $Mg_3B_2O_6$ emerges as the reaction product when Mg is used below 5 moles in the CeO_2-B_2O_3-Mg system.

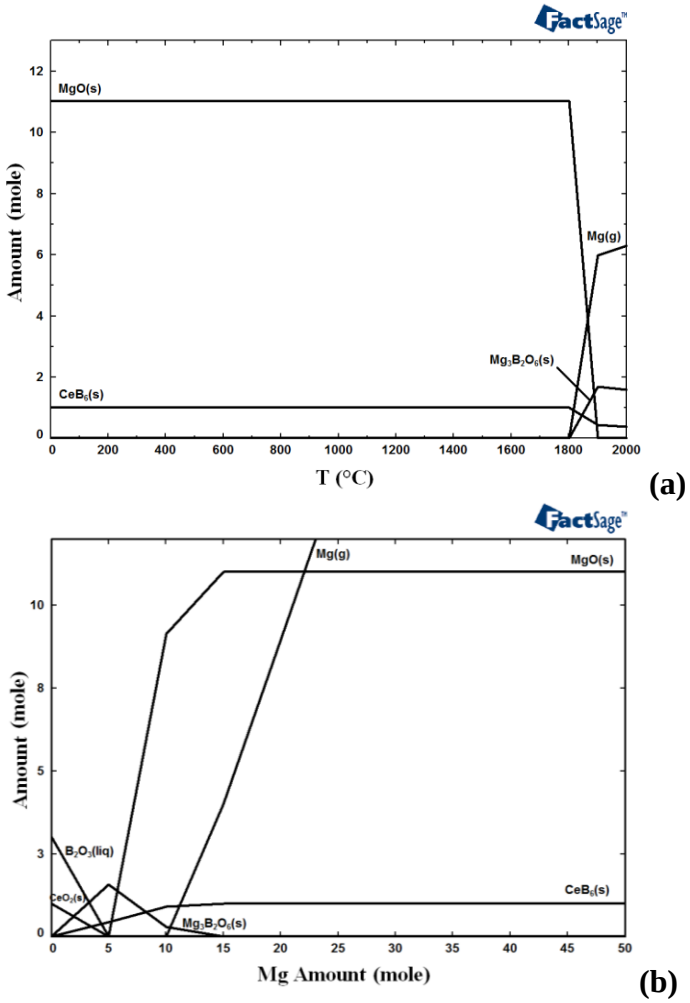

Figure 3.14 : Mole amount of reactants and reaction products versus (a) temperature and (b) Mg mole amount (at 1200°C) curves of the reaction (3.3).

Besides, CeB_6 and MgO reaction products form with an increasing tendency and the mole amount of unwanted $Mg_3B_2O_6$ phase decreases in the case of using Mg above 5 moles. If Mg in the amount of 15 moles or above is added to the initial CeO_2-B_2O_3-Mg powder blend, the mole amounts of MgO and CeB_6 become constant with absence of $Mg_3B_2O_6$ phase. However, the possibility of yielding unreacted Mg increases above 10 moles of Mg addition. As seen clearly seen from Figure 3.14(b), using stoichiometric amount of Mg (11 moles) results in almost the same amount of CeB_6 phase with the excess ones.

Due to understand the reaction mechanism of the CeO_2-B_2O_3-Mg system in stoichiometric amount, dual reactions in which Mg reduces the oxide raw materials are taken into account and they are given in equations (3.10) and (3.11). Standard Gibbs free energy change versus temperature curves of the reaction (3.10) and (3.11) are displayed in Figures 3.15(a) and (b).

$$B_2O_3 + 3Mg \rightarrow 2B + 3MgO \qquad \textbf{(3.10)}$$

$$CeO_2 + 2Mg \rightarrow Ce + 2MgO \qquad \textbf{(3.11)}$$

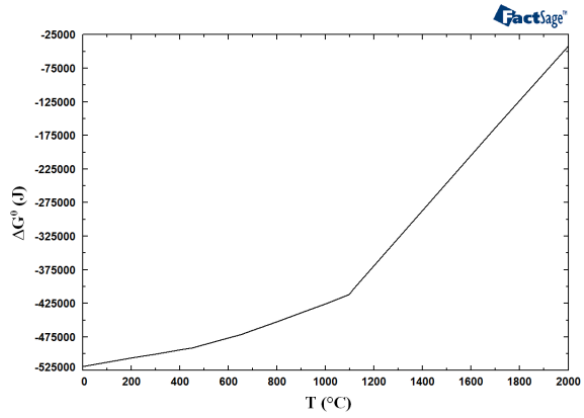

(a)

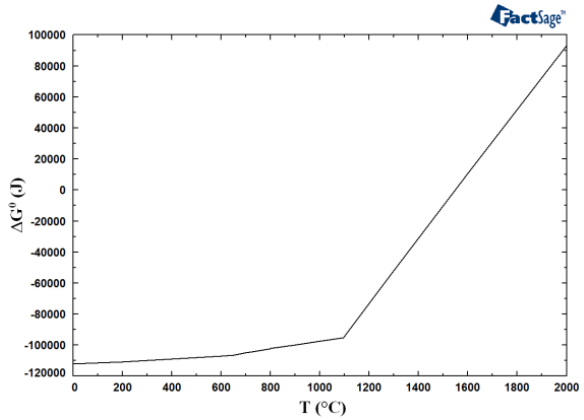

(b)

Figure 3.15 : Standard Gibbs free energy change versus temperature curves of the dual reactions: (a) reaction (3.10) and (b) reaction (3.11).

Standard free energy of the reaction (3.10) changes between -525 and -25 kJ at the temperature range of 0-2000°C according to Figure 3.15(a). However, Figure 3.15(b) shows that standard free energy of the reaction (3.11) vary between -120 and +100 kJ in the same temperature range. This means that the magnesiothermic reduction of B_2O_3 is more favourable than CeO_2. The first step of the overall reaction given in (3.3) can be regarded as the Mg reduction of B_2O_3 which initiates the total exothermic reaction. It is interpreted that the free boron come into contact with CeO_2 particles in the presence of Mg in regard of reaction (3.12). Standard free energy change-temperature curve of this reaction given in Figure 3.16 shows more negative values (-450 and -150 kJ for 0-2000°C) than that of reaction (3.11). On the basis of this, B_2O_3 and CeO_2 reductions with Mg can not take place seperately as mentioned in (3.10) and (3.11) during the overall reaction. The magnesiothermic reduction of B_2O_3 plays an important role on the reaction initiation and hence reduced free B particles significantly influence the reaction completion by acting like a bridge for the transfer of the oxygen atoms from CeO_2 to Mg in regard of (3.12).

$$CeO_2 + 6B + 2Mg \rightarrow CeB_6 + 2MgO \qquad \textbf{(3.12)}$$

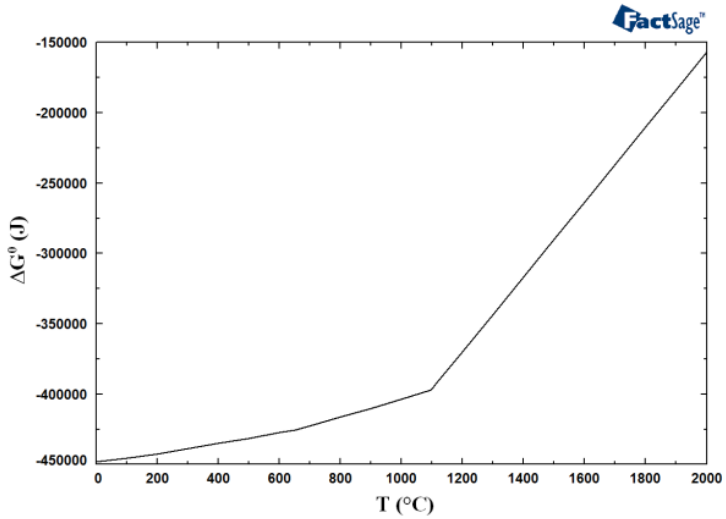

Figure 3.16 : Standard Gibbs free energy change versus temperature curve of the reaction (3.12).

The standard Gibbs free energy change versus temperature curves of the reactions (3.13) and (3.14) up to 2000°C were graphed (Figure 3.17) by using HSC Chemistry™ Ver. 4.1 program due to prove the conformity of the reaction mechanisms explained for the CeO_2-B_2O_3-Mg system with La_2O_3-B_2O_3-Mg and Sm_2O_3-B_2O_3-Mg systems. The (a) and (b) curves in Figure 3.17 indicates that the

reductions of La_2O_3 and Sm_2O_3 with Mg are not possible in the mentioned temperature range. The first steps of the overall reactions in (3.1) and (3.4) start with the magnesiothermic reduction of B_2O_3 but the subsequent steps can not be associated with the reductions of La_2O_3 and Sm_2O_3 by Mg which is not feasible according to Figure 3.17. Thus, the latter step should be proceeded with the reaction of La_2O_3 or Sm_2O_3, free boron and Mg particles. Consequently, the explained reaction mechanism is consistent with the thermodynamical data and seems to be valid for the La_2O_3-B_2O_3-Mg, CeO_2-B_2O_3-Mg and Sm_2O_3-B_2O_3-Mg systems.

$$La_2O_3 + 3Mg \rightarrow 2La + 3MgO \quad \textbf{(3.13)}$$

$$Sm_2O_3 + 3Mg \rightarrow 2Sm + 3MgO \quad \textbf{(3.14)}$$

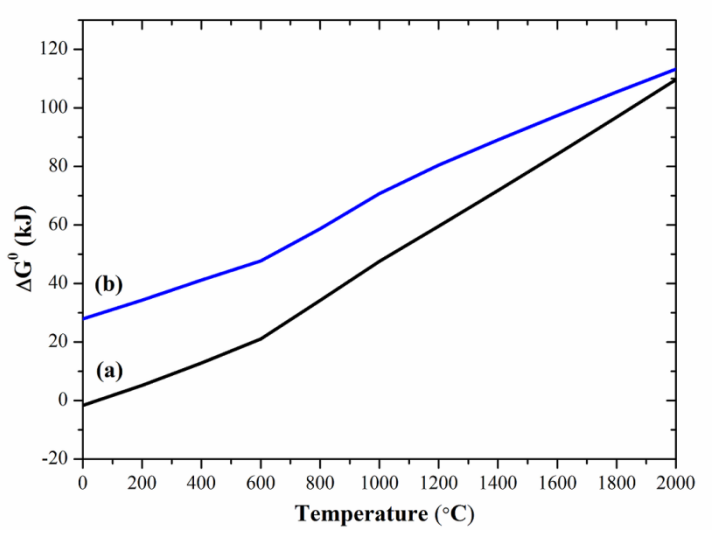

Figure 3.17 : Standard Gibbs free energy change versus temperature curves of the (a) reaction (3.13) and (b) reaction (3.14).

It should be also noted that the results of the thermodynamic calculations show only the equilibrium phase composition at room temperature without considering synthesis history and reaction kinetics. Actually, mechanochemical synthesis process is related to the fracturing and welding mechanism and the contact points between the particles provide favorable conditions for the formation of the products. Due to the fact that mechanochemical synthesis process is far from equilibrium, synthesized phases can not be expected to have complete consistence with the thermodynamically calculated phases.

4. RESULTS AND DISCUSSION

This chapter of the dissertation includes five sections which explain and discuss about the experimental results of LaB_6, CeB_6 and SmB_6 syntheses supported by the detailed characterization investigations. The first three sections explain respectively the mechanochemical synthesis and selective acid leaching of LaB_6, CeB_6 and SmB_6 powders from La_2O_3-B_2O_3-Mg, La_2O_3-B_2O_3-Ca, CeO_2-B_2O_3-Mg and Sm_2O_3-B_2O_3-Mg powder blends. In the fourth section, microstructural, physical (density and surface area) and magnetic properties of laboratory-synthesized LaB_6, CeB_6 and SmB_6 powders are compared with each other and with their commercial counterparts. Finally, the bulk properties in terms of microstructure, density, electrical resistivity, roughness, friction coefficient, hardness and relative wear volume loss of the sintered LaB_6, CeB_6 and SmB_6 originated from the laboratory-synthesized powders are elaborated and compared with each other and those of commercial ones in the last section. The mechanochemical process parameters such as milling duration, ball-to-powder weight ratio (BPR), type of mill type, process control agent (PCA) and reducing agent were varied during the synthesis of LaB_6 powders and LaB_6 was assumed as a reference for the latter processes. The syntheses of CeB_6 and SmB_6 powders were carried out in the light of optimized parameters determined by the obtained results of LaB_6.

4.1 Mechanochemical Synthesis and HCl Leaching of LaB_6 Powders

4.1.1 Mechanochemical Synthesis of LaB_6 Powders

In this section, the utilization of La_2O_3-B_2O_3-Mg powder blends for the mechanochemical synthesis of LaB_6 powders are explained in terms of milling duration, ball-to-powder weight ratio, type of mill and process control agent with the help of XRD, SEM/EDS, SM and DSC analyses. For the comparison of reducing agents, the results obtained from the usage of La_2O_3-B_2O_3-Ca powder blends are also evaluated on the basis of XRD, SEM/EDS, SM and DSC analyses.

Figure 4.1 illustrates the XRD patterns of the La_2O_3-B_2O_3-Mg powder blend and mechanochemically synthesized powders using a 10:1 BPR in a Spex^{TM} 8000D Mixer/Mill for different durations. The XRD pattern of the as-blended (non-milled) La_2O_3-B_2O_3-Mg powders are also plotted (Figure 4.1(a)) for comparison with the milled ones. It is evident from the XRD patterns shown in Figure 4.1(b), (c) and (d) that there is no reaction after milling for 1, 2 and 2.5 h since La_2O_3 (ICDD Card No: 071-5408, Bravais lattice: primitive hexagonal, a=b=0.393 nm, c=0.614 nm) and Mg (ICDD Card No: 035-0821, Bravais lattice: primitive hexagonal, a=b=0.329 nm, c=0.521 nm) phases are still present in the microstructures. However, the XRD patterns of the as-blended, 1 and 2 h milled powders (Figure 4.1(a)-(c)) distinctly demonstrate the gradual decrease in the crystallite sizes of the La_2O_3 and Mg phases, which means that the reaction gets closer step by step. No peaks belonging to the B_2O_3 phase can be observed in the XRD patterns of the as-blended, 1, 2 and 2.5 h milled powders (Figure 4.1(a)-(d)), whose absence is attributed to its amorphous nature and further amorphization during milling. After milling for 2 h 45 min (Figure 4.1(e)), the LaB_6 (ICDD Card No: 034-0427, Bravais lattice: primitive cubic, a=b=c=0.416 nm) and MgO (ICDD Card No: 045-0946, Bravais lattice: face-centered cubic, a=b=c=0.421 nm) phases emerge in the microstructure as the products of the reaction (3.1). Further milling for 15 min (from 2 h 30 min to 2 h 45 min) enables a rapid solid-state chemical reaction between the raw materials resulting in the reaction products. X-ray reflections for the LaB_6 phase contain ten peaks at values of 21.354°, 30.387°, 37.445°, 43.517°, 48.969°, 53.995°, 63.218°, 67.564°, 71.757°, 75.849° which are respectively indexed as (100), (110), (111), (200), (210), (211), (220), (300), (310) and (311) crystal planes (Figure 4.1(e)-(j)). Additionally, the La-B binary phase diagram in Figure 2.1(a) shows the presence of the stable LaB_4 and LaB_6 phases and the unstable LaB_9 phase (Massalski et al, 1990). The absence of the LaB_4 and LaB_9 phases in the XRD patterns and the X-ray reflections of the LaB_6 phase were also reported in the literature in which micro/nano structures of LaB_6 were synthesized by several different methods (Zhang et al, 2008b; Xu et al, 2006; Selvan et al, 2008; Yuan et al, 2011; Wenyuan et al, 2007; Ji et al, 2011; Xu et al, 2008b; Szépvölgyi et al, 2008; Kanakala et al, 2010; Late et al, 2009). Although the LaB_6 formation was achieved after milling for 2 h 45 min, milling was prolonged in order to observe any probable degradation of the reaction

products. Extended milling durations up to 25 h only result in the broadening of the LaB_6 and MgO peaks which represents decrease in their crystallite sizes (Figure 4.1(e)-(j)). Therefore, the mechanochemical reaction proceeding from 2 h 45 min to 25 h is in complete agreement with the reaction (3.1). There are no additional compounds between Mg-B, Mg-B-O, La-B-O, La-Mg, etc. which can be detected by the XRD analyses. Moreover, Rietveld analyses of the LaB_6 phases in the La_2O_3-B_2O_3-Mg powders mechanochemically synthesized for 2 h 45 min up to 25 h are given in Table 4.1 since it is very important to determine the exact milling duration to obtain LaB_6 phase in accordance with the stoichiometric amount (32.5 wt.% LaB_6 and 67.5 wt.% MgO) in reaction (3.1). However, the probable change in the amount of LaB_6 phase dependent on the milling duration can be approximately observed with the semi-quantitative Rietveld analysis. According to Table 1, the weight amount of LaB_6 is only 15 % after milling for 2 h 45 min because the reaction has just taken place toward to the end of this duration. There is an increase in the amount of LaB_6 phase up to 25 h but this increase is not very remarkable after a milling duration of 5 h.

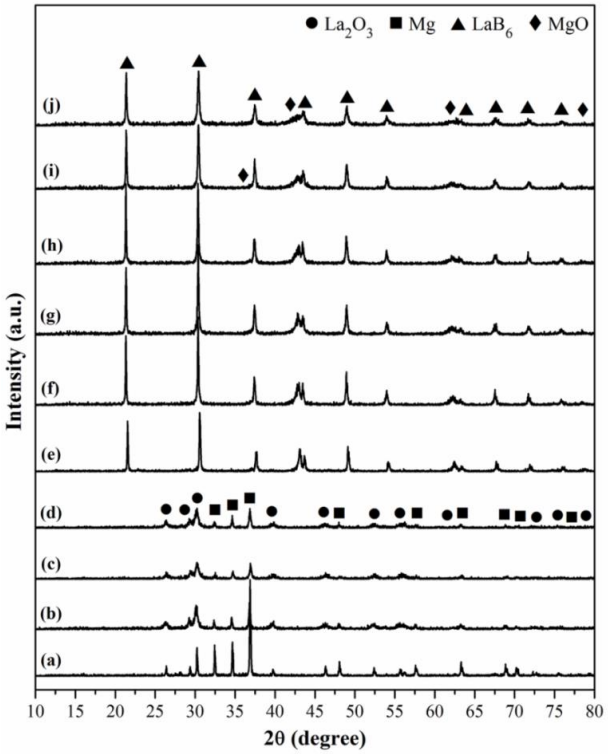

Figure 4.1 : XRD patterns of the La_2O_3-B_2O_3-Mg powder blend and powders mechanochemically synthesized using a 10:1 BPR in a Spex^{TM} 8000D Mixer/Mill for different durations: (a) ab, (b) 1 h, (c) 2 h, (d) 2.5 h, (e) 2 h 45 min, (f) 3 h, (g) 5 h, (h) 6 h, (i) 11 h and (j) 25 h.

Table 4.1 : Rietveld analyses of the LaB_6 phase in the La_2O_3-B_2O_3-Mg powders mechanochemically synthesized using a 10:1 BPR in a Spex^{TM} 8000D Mixer/Mill for different durations.

Duration	Amount (wt.%)
2 h 45 min	15
3 h	18
5 h	31
6 h	31
11 h	33
25 h	34

Figure 4.2 exhibits the average crystallite size and lattice strain curves of the LaB_6 in the La_2O_3-B_2O_3-Mg powders mechanochemically synthesized using a 10:1 BPR in a Spex^{TM} 8000D Mixer/Mill for different durations. In other words, the decrease in average crystallite sizes and hence the increase in lattice deformations are graphed as a function of milling duration in the La_2O_3-B_2O_3-Mg powders milled for 2 h 45 min, 3, 5, 6, 11 and 25 h. As reported previously, the lattice strain in the material can increase drastically from 0.1-0.3 % up to 30-100 % (Pourghahramani, 2007).

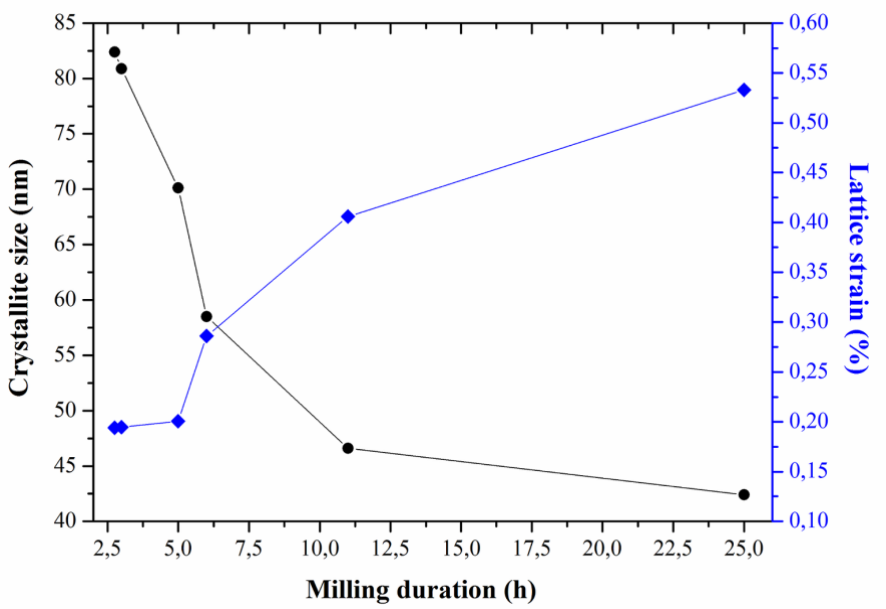

Figure 4.2 : Average crystallite sizes and lattice strains of LaB_6 versus milling duration curves, originated from the La_2O_3-B_2O_3-Mg powders mechanochemically synthesized using a 10:1 BPR in a Spex^{TM} 8000D Mixer/Mill.

The average crystallite size of LaB_6 decreases from 82.4 nm (for 2 h 45 min) to 42.4 nm (for 25 h). The decrease is sharp until 11 h of milling (46.6 nm) due to

relatively effective fracturing of powder particles, however after a sufficient milling time, it slows down. In contrast to the average crystallite size, the lattice strain of LaB_6 increases from 0.194 % (for 2 h 45 min) to 0.533 % (for 25 h) with progressive milling. As expected, the lattice deformation has higher values between 6 and 25 h milling durations than those between 2 h 45 min and 6 h. The broadening and the gradual decrease in the intensities of LaB_6 peaks in Figure 4.1(e)-(j) correlate with the pertinent average crystallite sizes and lattice strains in Figure 4.2.

Figures 4.3(a)-(j) show the stereomicroscope (SM) images of the La_2O_3-B_2O_3-Mg powder blend and powders mechanochemically synthesized using a 10:1 BPR in a Spex^{TM} 8000D Mixer/Mill for different durations. The difference between non-milled (as-blended) and milled powders is clearly seen from Figures 4.3(a)-(j). As-blended powders contain white B_2O_3 and La_2O_3 clusters in the microstructure (Figure 4.3(a)) whereas Mg particles cover these clusters in the milled powders for 1 and 2 h (Figures 4.3(b) and (c)). The microstructure slowly starts to change in the 2 h 30 min milled powders (Figure 4.3(d)) although it includes the same phases (La_2O_3 and Mg) with the 1 and 2 h milled powders according to its XRD pattern in Figure 4.1(d). As the reaction takes place at the 2 h 45 min milling duration, the morphologies of the powders change from granular to an agglomerated form. The SM images in Figures 4.3(e)-(j) are almost the same with each other since they only have LaB_6 and MgO phases after the reaction. It should be noted that the kinetics or the overall rate of the mechanochemical synthesis process depends on the kinetics of the milling in which newly fractured surfaces become active for the reaction initiated by the reducing agent. Meanwhile, fresh surfaces of the particles have tendencies to agglomerate with each other. This phenomenon results in a morphological difference between the 2 h and 2 h 45 min milled powders.

As already mentioned that mechanochemical synthesis is related to the repeated welding, fracturing and rewelding mechanism of the reactants and the contact points between the powder particles provide favourable conditions for the formation of the products. Two different reaction kinetics could be possible for the synthesis of the LaB_6 powders from the La_2O_3-B_2O_3-Mg blends.

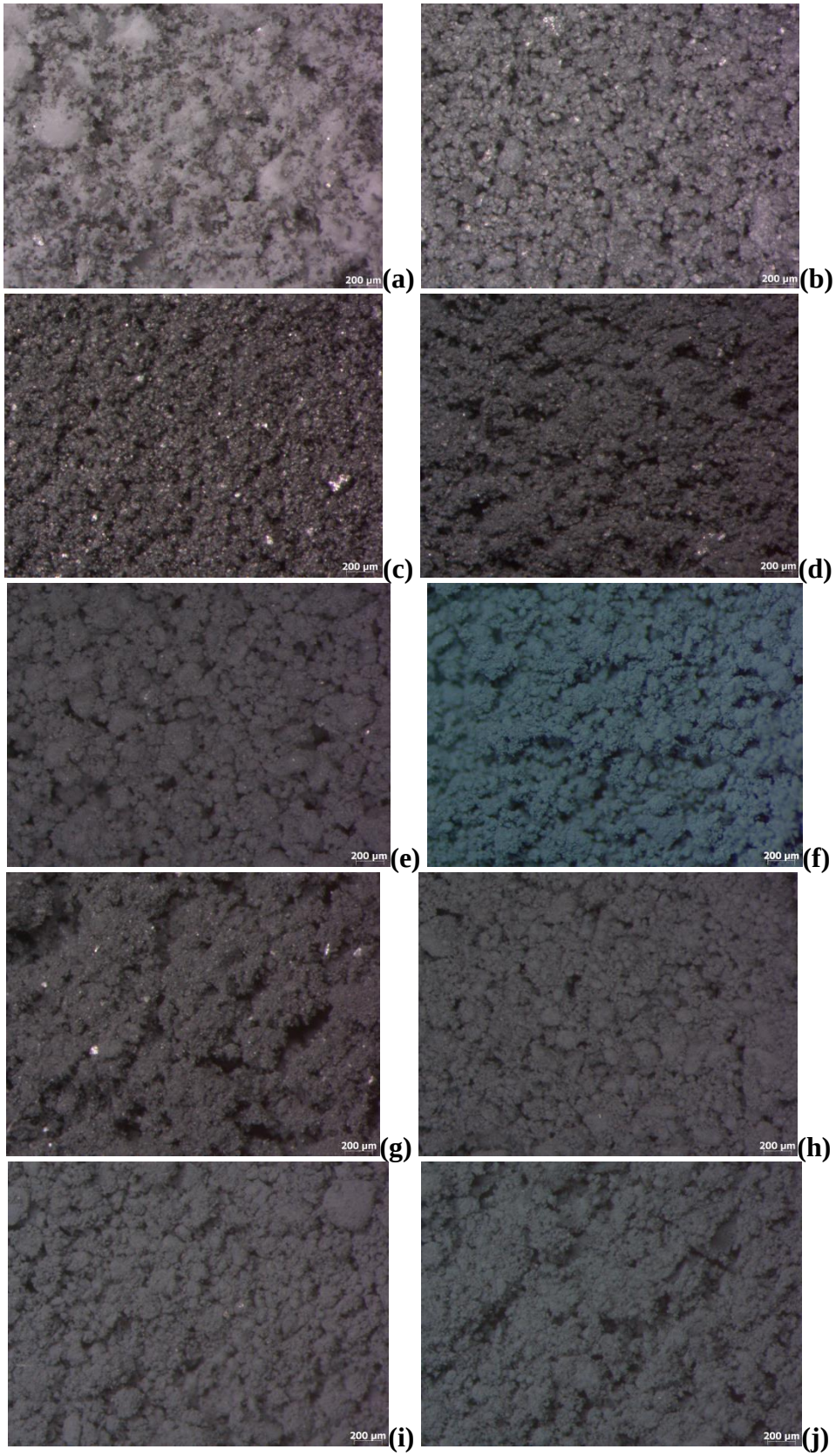

Figure 4.3 : SM images of the La_2O_3-B_2O_3-Mg powder blend and powders mechanochemically synthesized using a 10:1 BPR in a Spex^{TM} 8000D Mixer/Mill for different durations: (a) ab, (b) 1 h, (c) 2 h, (d) 2.5 h, (e) 2 h 45 min, (f) 3 h, (g) 5 h, (h) 6 h, (i) 11 h and (j) 25 h.

The first one may be explained by the extension of the reaction to a very small volume with each collision which results in a gradual transformation (Suryanarayana, 2001). The second one could arise from the occurrence of the ignition initiated by the exothermic reactions (negative enthalpy change in Figure 3.12(a)) and attained by the critical milling duration (Murthy and Ranganathan, 1998). It is considered that there is only particle refinement during milling until the ignition temperature is reached. Continuous deformation of product particles, subsequent to the mechanochemical reaction accomplished by means of ignition, again results in crystallite refinement and increase in lattice strain.

Figures 4.4(a)-(c) are the respective SEM images of the La_2O_3-B_2O_3-Mg powder blend and powders after mechanochemically synthesized for 5 and 25 h. As seen in Figure 4.4(a), as-blended powders have white irregular agglomerates and dark gray leaf-like particles. EDS measurements revealed that white irregular agglomerates contain about 25.50±1.60 wt.% Mg, 23.40±3.20 wt.% B and 50.87±2.45 O and dark gray leaf-like particles involve about 84.77±2.63 wt.% La and 13.93±1.42 wt.% O, explaining respectively the mixture of B_2O_3 and Mg particles and the La_2O_3 particle. SEM image of the 5 h milled powders in Figure 4.4(b) shows white rounded-shaped particles embedded in the dark gray irregular agglomerates, with sizes not larger than 800 nm. Although observable average particle size is generally around 350 nm, agglomeration of the powder particles prevents the observation of smaller ones. On the basis of several EDS measurements, white particles have the composition of 65.27±2.58 wt.% La and 30.38±1.90 wt.% B and dark gray irregular agglomerates include 58.30±3.25 wt.% Mg and 37.55±3.15 wt.% O. EDS results are compatible with the calculated weight percentages of the elements in the LaB_6 and MgO phases. With the extension of the milling duration to 25 h, dark gray MgO agglomerates in Figure 4.4(b) disappeared and are replaced with the particles ranging in size between 100 and 500 nm, as obviously seen in Figure 4.4(c). In addition, white LaB_6 particles with a maximum size of 250 nm achieve a more homogeneous distribution throughout the surface as milling duration increases. SEM images in Figures 4.4(a)-(c) and their EDS measurements are in good agreement with the XRD patterns shown in Figure 4.1(a), (g) and (j) and the calculated crystallite sizes shown in Figure 4.2.

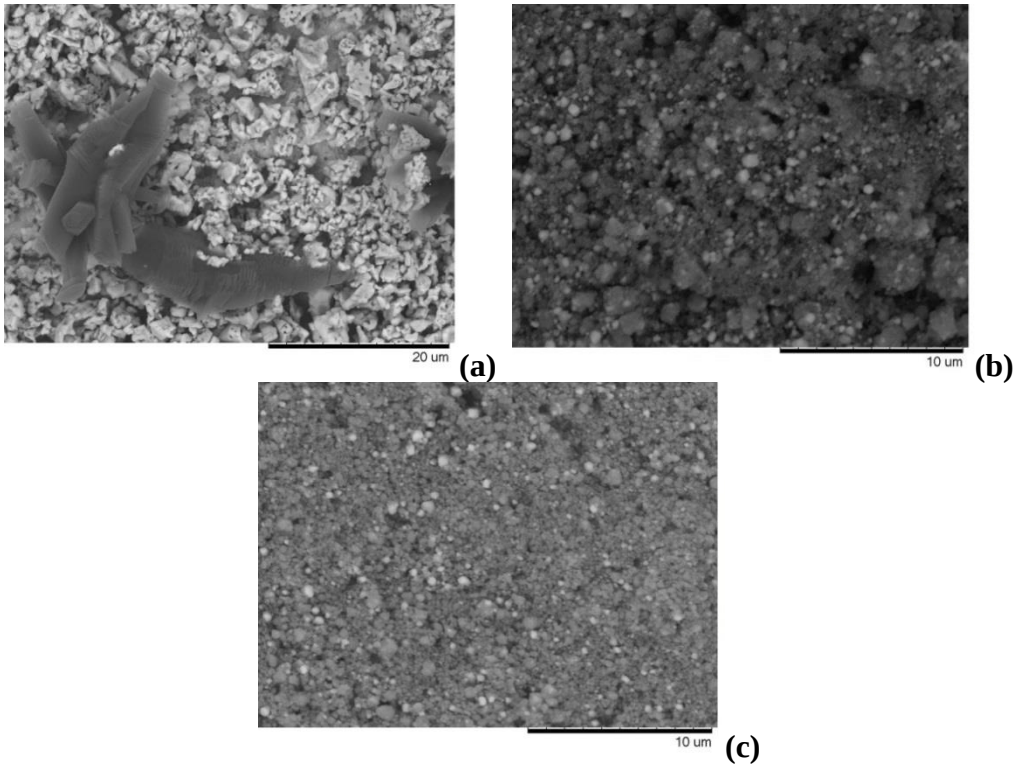

Figure 4.4 : SEM images of the La_2O_3-B_2O_3-Mg powder blend and powders mechanochemically synthesized using a 10:1 BPR in a Spex^{TM} 8000D Mixer/Mill for different durations: (a) ab, (b) 5 h and (c) 25 h.

In order to determine the thermal behaviour, resultant reactions and the reaction completion of the La_2O_3-B_2O_3-Mg powders, DSC analyses were conducted on the as-blended and milled products. Figure 4.5(a)-(j) represents the DSC thermograms of the La_2O_3-B_2O_3-Mg powder blend and powders mechanochemically synthesized using a 10:1 BPR in a Spex^{TM} 8000D Mixer/Mill for different durations from 1 to 25 h. The DSC curve of the as-blended powders (Figure 4.5(a)) have three small endotherm peaks at about 140, 170 and 350°C, which correspond respectively to the release of humidity arised from the handling of powders in laboratory atmosphere and the dehydration of small amount of H_3BO_3 in the structure of B_2O_3. As-blended powders (Figure 4.5(a)) have also a narrow endotherm peaking at about 650°C, a narrow exotherm peaking at about 700°C and a large endotherm with two peaking points at about 760 and 790°C. These peaks respectively belong to the melting of Mg, formation of Mg borate phases, formation of La and formation of B. DSC curve indicates that Mg was completely consumed in the reaction until its boiling temperature was reached. Milling for 1 h utterly changes the thermal behavior of the La_2O_3-B_2O_3-Mg powders, as seen from the DSC curve in Figure 4.5(b). 1 h milled

powders have only the similar endothermic peaks at 140 and 170°C. There are no other endotherms indicating the melting of Mg or separate formations of La and B. However, an exotherm peaking at about 660°C, which implies the oxidation of Mg, is detected. The DSC curves of the powders milled for 2 h and 2 h 30 min given in Figure 4.5(c) and (d) show respectively that there are only sharp exotherms at about 630ºC and 650°C with onset temperatures of 610 and 675ºC. On the basis of Figure 4.1(b), (c) and (d), 1 h, 2 h and 2 h 30 min milled powders contain La_2O_3, B_2O_3 and Mg phases. Although B_2O_3 and Mg melt respectively at 450 and 650ºC, there are no endothermic peaks corresponding to their melting. However, the sharp exothermic peak emerges as a consequence of the oxidation of Mg. This also means that Mg was completely consumed in the dominant exothermic reaction before its melting point was reached. The DSC curve of the 2 h milled powders conforms well with ignition derived reaction kinetics since it is based on the negative enthalpy change (Figure 3.12(a)) and hence on the exothermic reactions. Similarly, a study in the current literature reports the achievement of TiO_2, Mg and MgO main phases when TiO_2-B_2O_3-Mg powder blend (undetermined molar ratio) was treated at 630ºC (Weimin et al, 2002). As seen in Figure 4.5(e), the shape and place of the main exotherm changed after 2 h 45 min milling. It became a very small and narrow exotherm between 645 and 660ºC with a maximum point of 651ºC. The temperature of the exotherm peaking point shifts about 21ºC, as a result of the comparison of Figure 4.5(e) with Figure 4.5(c). According to the XRD pattern in Figure 4.1(e), there are only LaB_6 and MgO phases in the 2 h 45 min milled powders. However, the presence of a small exothermic peak corresponds to the oxidation of the residual Mg in the milled powders. The contradiction between the outcomes of the XRD and DSC analyses arises from the amount of Mg which is below the XRD detection limit. Also, it can be said that mechanochemical synthesis and very small amount of remaining Mg postpone the exothermic reaction and cause the temperature shift. The DSC curves of the powders milled between 3 and 25 h shown in Figure 4.5(f)-(j) have the same shapes: there exist no endothermic or exothermic peaks in all DSC thermograms. This implies the completion of the reaction with no evidence of unreacted Mg, as compatible with the presence of LaB_6 and MgO phases in the XRD pattern in Figure 4(f-j). On the basis of Figures 4.1(a)-(j) and 4.5(a)-(j), it can be stated that the La_2O_3, B_2O_3 and Mg powders completely reacts after 3 h milling to

form LaB_6 and MgO. In other words, the level of the energy barrier that initiates the reduction reaction or the activation energy for the chemical reaction was exceeded after 2 h 45 min milling. During mechanochemical synthesis, there is an increase in the standard Gibbs free energy of the system enabling the materials to reach a high enough potential to overcome the activation barrier to initiate the reaction. As sufficient Gibbs free energy was reached to overcome the activation energy and this Gibbs free energy increased to progress the reaction during milling, the reaction completely took place without any unreacted Mg at the end of 3 h milling.

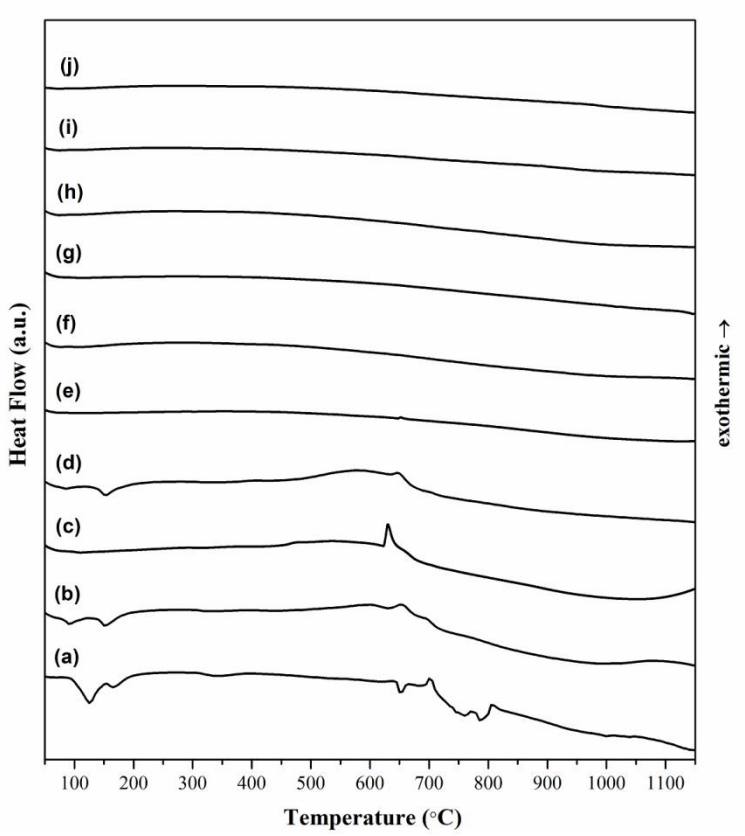

Figure 4.5 : DSC thermograms of the La_2O_3-B_2O_3-Mg powder blend and powders mechanochemically synthesized using a 10:1 BPR in a Spex^{TM} 8000D Mixer/Mill for different durations: (a) ab, (b) 1 h, (c) 2 h, (d) 2.5 h, (e) 2 h 45 min, (f) 3 h, (g) 5 h, (h) 6 h, (i) 11 h and (j) 25 h.

In order to systematically follow and analyze the reaction mechanism occurred in the mechanochemically synthesized La_2O_3-B_2O_3-Mg powders, powders of binary systems such as B_2O_3-Mg, La_2O_3-Mg and La_2O_3-B_2O_3 were heated up to 1150°C in the differential scanning calorimeter. Figure 4.6(a)-(c) shows the DSC thermograms of the as-blended B_2O_3-Mg, La_2O_3-Mg and La_2O_3-B_2O_3 powders, respectively. Comparing with Figure 4.5(b)-(j), it is evident that Figure 4.6(a)-(c) has no similar

DSC peaks except the oxidation exotherm of Mg: the dissimilarity of DSC thermograms proves the effect of milling on the powder blends. As seen from the Figure 4.6(a), there are three endotherms peaking at about 650, 810 and 1100°C in the B_2O_3-Mg powder blend, indicating the melting of Mg, formation of B and boiling of Mg. The La_2O_3-Mg powder blend exhibits two endothermic peaks at 320 and 780°C corresponding respectively to the release of the humidity adsorbed onto the particle surfaces of La_2O_3 and formation of La. Also, heated La_2O_3-Mg powder blend has a very small exotherm peaking at about 550°C which denotes the oxidation of some amount of Mg. As seen from Figure 4.6(b), there is not an additional endotherm for the boiling of Mg at about 1100°C: the broad endoterm having a maximum point at 780°C also contains the evaporation of remaining Mg. The DSC curve of the La_2O_3-B_2O_3 powder blend shown in Figure 4.6(c) comprises two endotherms at about 320 and 470°C, indicating the dehydration of a small amount of H_3BO_3 in the structure of B_2O_3 and melting of B_2O_3. Besides, the heated La_2O_3-B_2O_3 powder blend has three exothermic peaks at about 800, 900 and 970°C corresponding to the formations of different lanthanum borate phases which are low-temperature orthorhombic and high-temperature monoclinic $LaBO_3$ and $La(BO_2)_3$ phases (Shmyt'ko et al, 2013). Subsequent XRD analyses can not be conducted on the B_2O_3 containing binary powder blends (B_2O_3-Mg and La_2O_3-B_2O_3) due to the adherence of heated powders to the alumina crucible. It has already been known from a related study carried out on HfO_2-B_2O_3-Mg powders that B_2O_3 melts and reacts with the quartz boat if the same experiments are intended to be performed in a tube furnace (Balcı et al, 2010). Thus, only the La_2O_3-Mg powder blend was subjected to the XRD analysis after heating, whose XRD pattern is given in Figure 4.7. According to the XRD pattern of the heated La_2O_3-Mg powder blend, there is a major La_2O_3 phase and also are small amounts of MgO and La (ICDD Card No: 51-1165, Bravais lattice: primitive hexagonal, a=b=0.377 nm, c=1.203 nm) phases in the microstructure. The presence of a small amount of MgO is in good aggrement with the small exotherm at 550°C. Moreover, the absence of Mg peak in the XRD pattern completely explains the boiling of Mg which is in accordance with the broad endotherm peaking at 780°C (Figure 4.6(b)). The DSC curve in Figure 4.6(b) and the XRD pattern in Figure 4.7 also reveal that the complete magnesiothermic reduction of La_2O_3 is not possible up to 1150°C. This analysis result fits well with the standard

Gibbs free energy change versus temperature graph in Figure 3.17(a) obtained from the thermodynamical data. On the basis of the DSC and XRD analyses conducted on the binary powder blends, interpreted mechanism, in which the reaction initiates with the Mg reduction of B_2O_3 and proceeds with the reaction between La_2O_3, free boron particles and Mg, should be evaluated as the correct mechanism for the La_2O_3-B_2O_3-Mg powder blends.

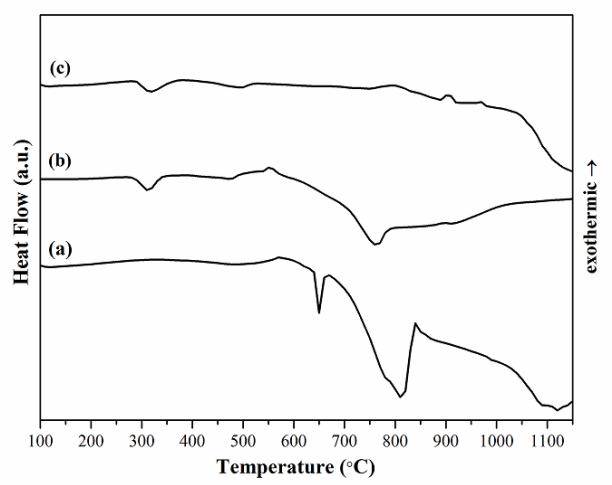

Figure 4.6 : DSC thermograms of the (a) B_2O_3-Mg, (b) La_2O_3-Mg and (c) La_2O_3-B_2O_3 dual powder blends.

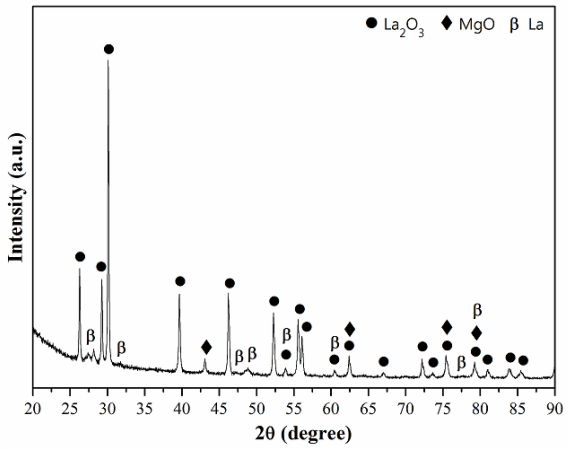

Figure 4.7 : XRD pattern of the La_2O_3-Mg dual powder blend after DSC analyses up to 1150°C.

Figure 4.8(a)-(i) illustrates the XRD investigations carried out on the mechanochemically synthesized (1-25 h) La_2O_3-B_2O_3-Mg powders using a 10:1 BPR in a Spex^{TM} 8000D Mixer/Mill after DSC scans up to 1150ºC in order to detect the existing phases. All XRD patterns in Figure 4.8(a)-(i) have the LaB_6, MgO $LaBO_3$ (ICDD Card No: 012-0762, Bravais lattice: primitive orthorhombic, a=0.587 nm,

b=0.826 nm, c=0.511 nm) and $Mg_3B_2O_6$ (ICDD Card No: 038-1475, Bravais lattice: primitive orthorhombic, a=0.540 nm, b=0.842 nm, c=0.451 nm) phases. The XRD patterns of the La_2O_3-B_2O_3-Mg powders milled for 1 h, 2 h and 2 h 30 min shown respectively in Figure 4.8(a), (b) and (c) have higher peak intensities than those milled for 2 h 45 min and at longer durations. Since La_2O_3-B_2O_3-Mg powders milled for 1 h, 2 h and 2 h 30 min contain La_2O_3 and Mg phases (Figure 4.1(b)-(d)) after mechanochemical synthesis, they react intensely to form LaB_6, MgO, $LaBO_3$ and $Mg_3B_2O_6$ phases in the presence of applied external heat. It can be considered that the LaB_6, $LaBO_3$ and $Mg_3B_2O_6$ phases emerge at the same time with the oxidation of Mg to form MgO since any other related exotherms are not detected in the DSC curves in Figure 4.5(b)-(d)). As seen from Figure 4.8(d)-(i), the intensities of the XRD patterns decrease because the powders mechanochemically synthesized for 2 h 45 min and at longer times have already LaB_6 and MgO phases before heating up to 1150°C. However, small amounts of $LaBO_3$ and $Mg_3B_2O_6$ phases occur in the mechanochemically synthesized powders after heating. Surprisingly, borate formations are not detected in the DSC thermograms of the mechanochemically synthesized powders in Figure 4.5(f)-(j). In other words, the LaB_6 and MgO phases which form during milling (≥ 2 h 45 min) are not thermally very stable because they have tendency to transform to small amounts of lanthanum or magnesium borate phases when exposed to high temperature. It is clear from Figure 4.8(a)-(j) that the amount of borates decreases as milling duration increases. On the other hand, only milling without subsequent heat treatment results in the formation of both LaB_6 and MgO phases in the absence of borates. Milling increases the reactivity of the components towards desired reduction reaction (3.1) since it provides particle refinement of the starting materials and thereby a more homogeneous particle size distribution throughout the powder blend can be achieved. Besides, it is certain that only lanthanum and magnesium borate phases can be obtained when milling process prior to the heating is not conducted on the powder blends (Ağaoğulları et al, 2012a; 2012b; Shmyt'ko et al, 2013). The results indicate that if milling are not carried out on the La_2O_3-B_2O_3-Mg powder blends, the heating process has no chance of resulting complete conversion of the reactants without additional compounds. Therefore, the significance of the mechanochemical synthesis and its effect on the reduction

mechanism of La_2O_3, B_2O_3 and Mg can be emphasized once more by means of the DSC thermograms and XRD patterns given in Figures 4.5, 4.6, 4.7 and 4.8.

The mechanochemical synthesis experiments carried out on the La_2O_3-B_2O_3-Mg powder blends using a 10:1 BPR in a Spex^{TM} 8000D Mixer/Mill for different durations and their XRD, DSC, Rietveld, TOPAS, SM and SEM/EDS characterizations given in Figure 4.1 through Figure 4.8 also prove that extending the milling duration up to 25 h does not provide higher contributions than those of the shorter durations in which the reaction took place. So, the ideal milling duration can be selected as 5 h and this duration is used as the maximum milling time for the latter experiments conducted in Spex^{TM} 8000D Mixer/Mill.

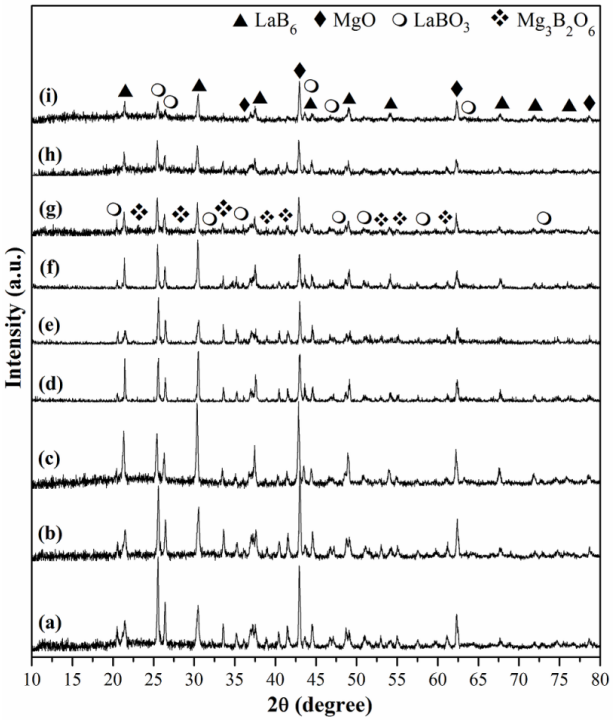

Figure 4.8 : XRD patterns of the mechanochemically synthesized La_2O_3-B_2O_3-Mg powders, using a 10:1 BPR in a Spex^{TM} 8000D Mixer/Mill for different durations, after DSC analyses up to 1150°C: (a) 1 h, (b) 2 h, (c) 2.5 h, (d) 2 h 45 min, (e) 3 h, (f) 5 h, (g) 6 h, (h) 11 h and (i) 25 h.

Mechanochemical synthesis of La_2O_3-B_2O_3-Mg powder blends was carried out using a higher ball-to-powder weight ratio considering that the increase in the BPR provides a decrease in the reaction time. Figure 4.9(a)-(g) displays the XRD patterns of the La_2O_3-B_2O_3-Mg powder blend and powders mechanochemically synthesized using a 18:1 BPR in a Spex^{TM} 8000D Mixer/Mill for different durations (1-5 h).

La_2O_3-B_2O_3-Mg powders milled for 1 and 1.5 h contain La_2O_3 and Mg phases, as seen from Figure 4.9(b) and (c). The intensities of these phases decrease from 0 (ab) to 1.5 h milling (Figure 4.9(a)-(c)) due to the decreases in their average crystallite sizes which enable the gradual participation of the particles in the chemical reaction. After milling for 2 h, as seen in the XRD pattern in Figure 4.9(d), the reduction reaction takes place by yielding LaB_6 and MgO phases in the presence of a very small amount of $LaBO_3$. Further 1 h milling results in the disappearance of $LaBO_3$ peaks, as shown in Figure 4.9(e). Prolonging the reaction duration to 4 and 5 h does not cause any changes in the type of formed products; i.e. the powders mechanochemically synthesized for 4 and 5 h have the same LaB_6 and MgO phases without $LaBO_3$. Besides, it is clearly observed from Figure 4.9(d)-(g) that the XRD peak intensities of the LaB_6 and MgO milled for 2 h increase to those milled for 5 h, indicating the increase in the amounts of products without creating a remarkable difference in their average crystallite sizes.

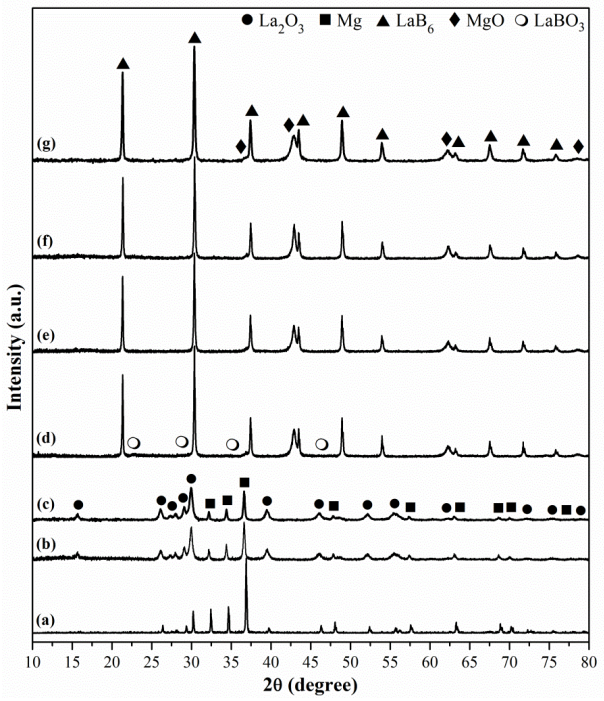

Figure 4.9 : XRD patterns of the La_2O_3-B_2O_3-Mg powder blend and powders mechanochemically synthesized using a 18:1 BPR in a Spex^{TM} 8000D Mixer/Mill for different durations: (a) ab, (b) 1 h, (c) 1.5 h, (d) 2 h, (e) 3 h, (f) 4 h and (g) 5 h.

Figures 4.10(a) through (f) represent the SM images of the La_2O_3-B_2O_3-Mg powders mechanochemically synthesized using a 18:1 BPR in a Spex^{TM} 8000D Mixer/Mill for

1-5 h. After 1 and 1.5 h milling and hence before the reduction reaction, La_2O_3 and B_2O_3 containing Mg particles are observed in the microstructure (Figures 4.10(a) and (b)). Figures 4(c)-(e) show a different microstructure from the milled powders for 1 and 1.5 h since the reaction took place after milling for 2 h and fine Mg particles transformed to MgO agglomerates in which LaB_6 particles embedded. To increase the BPR from 10:1 to 18:1 triggers an earlier chemical reaction, approximately by 45 min. The decrease in the reaction duration arises from the increase in the number of collisions both between La_2O_3, B_2O_3 and Mg powder particles and between these particles and milling balls. Thus, the increase in the number of collisions creates more fresh and active surfaces to come into contact for the reduction reaction ignited with Mg. Additionally, the temperature in the milling vial increases with the increase in the number of collisions.

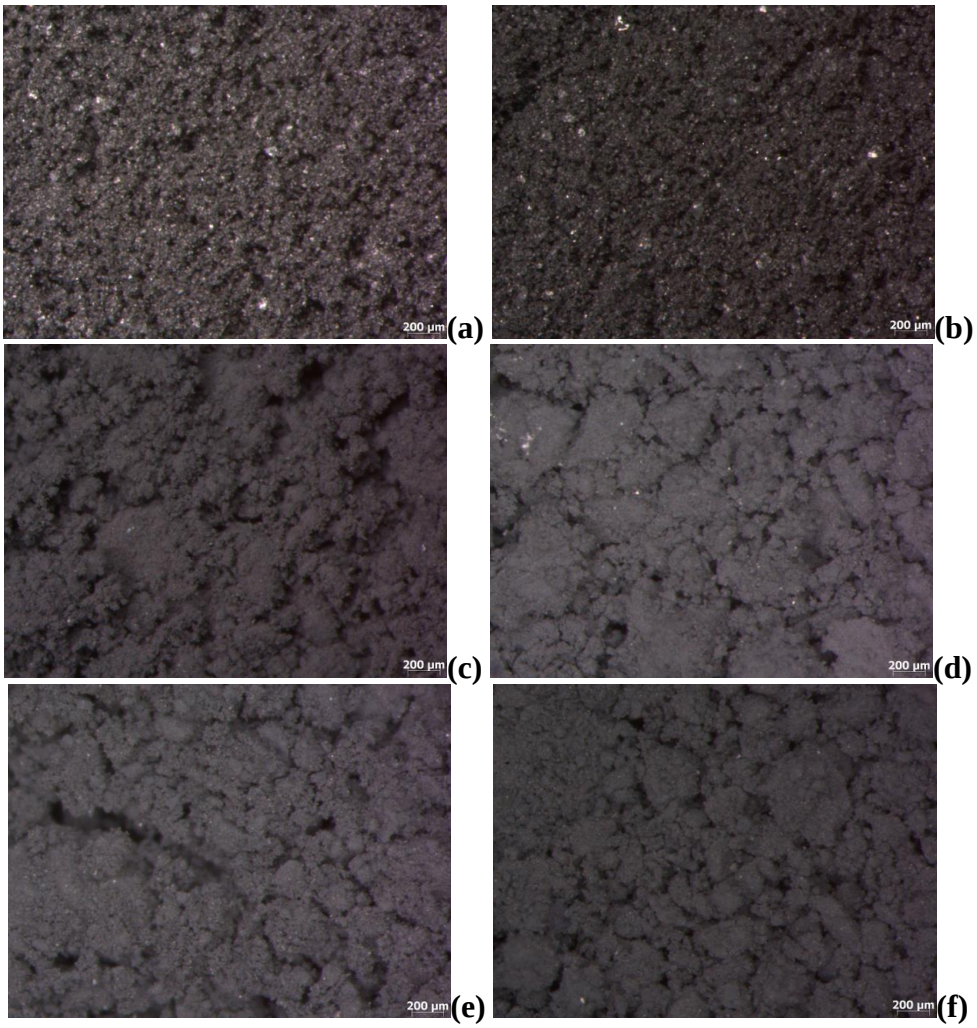

Figure 4.10 : SM images of the La_2O_3-B_2O_3-Mg powders mechanochemically synthesized using a 18:1 BPR in a Spex^{TM} 8000D Mixer/Mill for different durations: (a) 1 h, (b) 1.5 h, (c) 2 h, (d) 3 h, (e) 4 h and (f) 5 h.

Although mechanochemical synthesis is accepted as a room temperature process, the temperature in the milling vial increases with the repeated fracturing and welding of the particles whose Gibbs free energies want to overcome the activation energy of the system (Suryanarayana, 2001). As BPR and hence the vial temperature increase, the kinetic energy transfer to the reactant particles becomes high for them to overcome the activation energy of the chemical reaction at a shorter duration. DSC thermograms of the La_2O_3-B_2O_3-Mg powders mechanochemically synthesized using a 18:1 BPR in a Spex^{TM} 8000D Mixer/Mill for durations between 1 and 5 h are given in Figure 4.11(a)-(f). As seen from Figure 4.11(a) and (b), La_2O_3-B_2O_3-Mg powders milled for 1 and 1.5 h have broad exothermic peaks between 500 and 700°C with maximum points respectively at about 600 and 570°C, indicating that the formation of MgO and simultaneous formation of lanthanum borate and magnesium borate phases. Figure 4.11(c) shows the DSC curve of the 2 h milled powders having a very small exotherm peak at about 650°C, corresponding to the oxidation of Mg and the formation of borate phases. Although the XRD pattern of the 2 h milled powders contains LaB_6, MgO and an amount of $LaBO_3$ (Figure 4.9(d)), there is still unreacted free Mg in the structure which is under the detection limit (≤ 2 wt.%) of XRD.

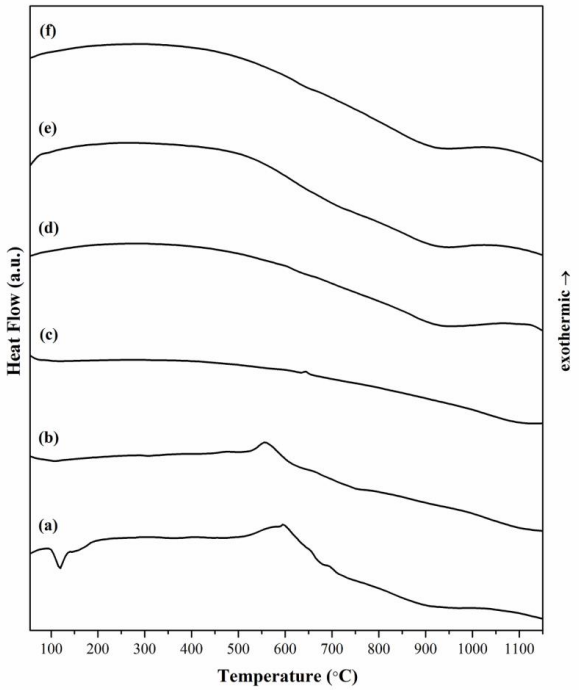

Figure 4.11 : DSC thermograms of the La_2O_3-B_2O_3-Mg powders mechanochemically synthesized using a 18:1 BPR in a Spex^{TM} 8000D Mixer/Mill for different durations: (a) 1 h, (b) 1.5 h, (c) 2 h, (d) 3 h, (e) 4 h and (f) 5 h.

No endothermic or exothermic peaks are observed in the 3, 4 and 5 h milled La_2O_3-B_2O_3-Mg powders (Figure 4.11(d), (e) and (f)). According to the DSC analyses in Figure 4.11(a)-(f), the reduction reaction was completed after 3 h milling when a BPR of 18:1 was used. Besides, Figure 4.12(a) and (b) display the XRD patterns of the mechanochemically synthesized La_2O_3-B_2O_3-Mg powders, using a 18:1 BPR in a Spex^{TM} 8000D Mixer/Mill for 1.5 and 5 h, following the DSC scans up to 1150°C. After heating the 1.5 h milled powders, LaB_6, MgO, $LaBO_3$ and $Mg_3B_2O_6$ phases emerged in high intensities since these powders only have La_2O_3, Mg and B_2O_3 phases at the end of milling. 5 h milled and heated powders contain the same phases as the 1.5 h milled one. However, the intensity of LaB_6 phase is higher in the 5 h milled and heated powders than that of milled for 1.5 h. If the milled powders still include the reactants (La_2O_3, B_2O_3 and Mg) or the reaction is not complete (as in the 2 h milled powders), $LaBO_3$ and $Mg_3B_2O_6$ simultaneously emerge with the oxidation of Mg, as seen in the DCS curves (Figure 4.11(a)-(c)). If the milled powders contain LaB_6 and MgO phases and there is no Mg to be oxidized in the structure, $LaBO_3$ and $Mg_3B_2O_6$ phases would form from the heating of LaB_6 and MgO up to 1150°C but this phenomenon can not be observed with sharp peaks from the DSC curves given in Figure 4.11(d)-(f).

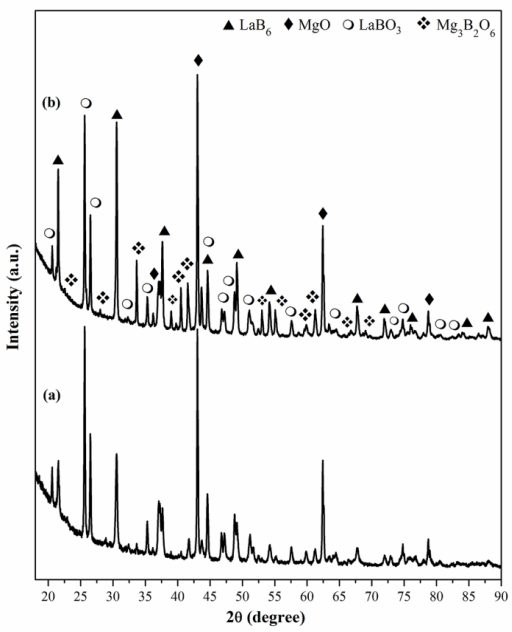

Figure 4.12 : XRD patterns of the mechanochemically synthesized La_2O_3-B_2O_3-Mg powders, using a 18:1 BPR in a Spex^{TM} 8000D Mixer/Mill for different durations, after DSC analyses up to 1150°C: (a) 1.5 h and (b) 5 h.

The type of high-energy ball mill is changed to monitor its effects on the reaction time and product properties, considering that the kinetics of the mechanochemical synthesis process depend on the stress conditions in the milling devices. Figure 4.13(a)-(g) demonstrates the XRD patterns of the La_2O_3-B_2O_3-Mg powder blend (ab) and powders mechanochemically synthesized using a 10:1 BPR in a planetary ball mill up to 30 h. There are only the peaks of La_2O_3 and Mg phases in the XRD patterns of the powders milled for 10, 15 and 18 h (Figure 4.13(b), (c) and (d)). In other words, no reaction takes place between La_2O_3, B_2O_3 and Mg powders after milling for 18 h. However, the XRD patterns of the 10, 15 and 18 h milled powders distinctly demonstrate the gradual decrease in the intensities and hence in the average crystallite sizes of the La_2O_3 and Mg phases towards reduction reaction.

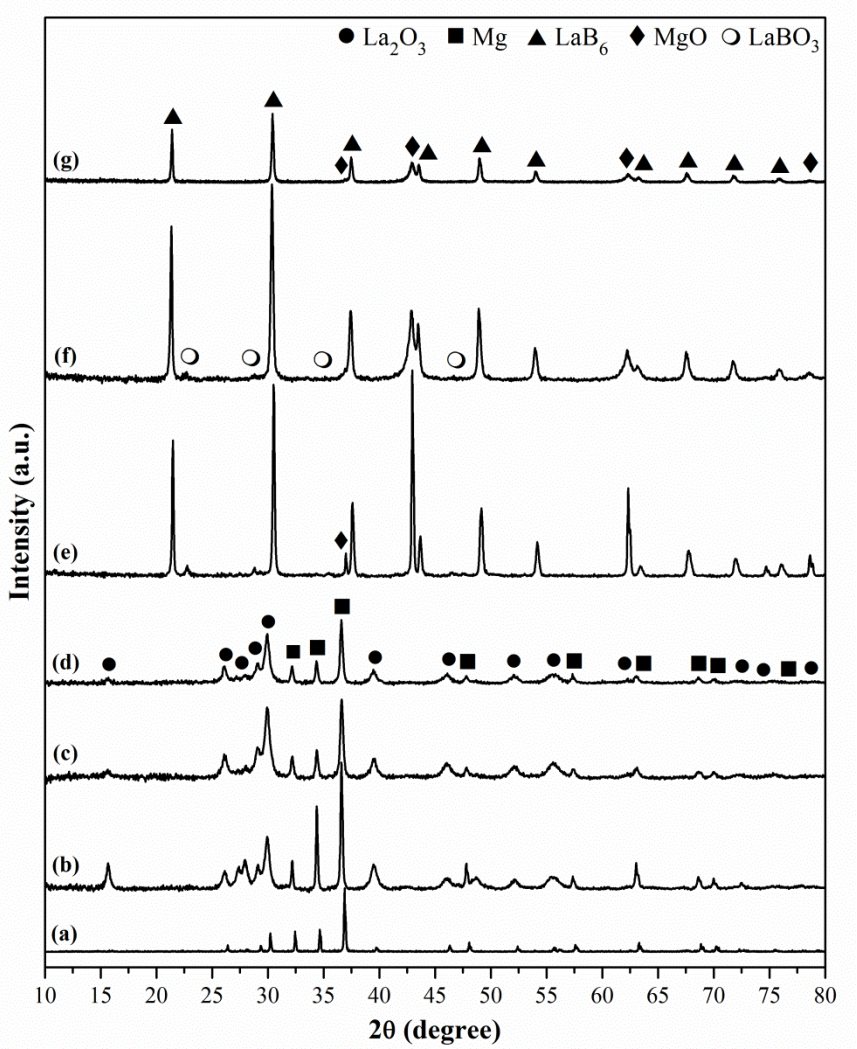

Figure 4.13 : XRD patterns of the La_2O_3-B_2O_3-Mg powder blend and powders mechanochemically synthesized using a 10:1 BPR in a planetary ball mill for different durations: (a) ab, (b) 10 h, (c) 15 h, (d) 18 h, (e) 20 h, (f) 25 h and (g) 30 h.

The boride formation reaction takes place after milling for 20 h since the LaB_6 and MgO phases occur as the reaction products (Figure 4.13(e)). Further milling for 2 h enables a rapid solid-state chemical reaction of the starting powders towards reaction (3.1). In addition to LaB_6 and MgO, 20 h milled powders contain a small amount of the $LaBO_3$ phase. Mechanochemical synthesis for 25 h again results in the emergence of the LaB_6, MgO and $LaBO_3$ phases (Figure 4.13(f)). Moreover, the intensity of the $LaBO_3$ phase decreases from 20 to 25 h mechanochemically synthesized powders, most probably pertaining to the decrease in its amount. As seen in Figure 4.13(f), extended milling duration up to 30 h only results in the occurrence of the LaB_6 and MgO peaks without formation of any additional compounds. It can be interpreted that if sufficient milling duration to consume the stoichiometric reactants is not reached, $LaBO_3$ emerges as an unstable phase at the end of the milling process. Both the intensity decrease and the peak broadening in the LaB_6 and MgO phases formed after 20 h milling imply decline in their average crystallite sizes and increase in their lattice strains (Figure 4.13(e)-(g)). Comparing XRD analysis results of the powders (Figure 4.13(a)-(g)) with those of mechanochemically synthesized in Spex^{TM} 8000D Mixer/Mill (Figure 4.1(a)-(j)), it can be stated that almost 10 times greater reaction duration is required for the reduction reaction in a planetary ball mill. Since there has been no need of producing large amounts of LaB_6 powders for this dissertation work, the synthesis have been carried out in Spex^{TM} 8000D Mixer/Mill because it is advantageous in the reaction duration. However, the LaB_6 amounts produced in Spex^{TM} 8000D Mixer/Mill is very limited for commercial scales.

Figures 4.14(a)-(f) illustrate the SM images of the La_2O_3-B_2O_3-Mg powders mechanochemically synthesized using a 10:1 BPR in a planetary ball mill for different durations from 10 to 30 h. 10, 15 and 18 h milled powders have almost the same microstructure revealing the major Mg phase containing white La_2O_3 and B_2O_3 particles. The reductions in the particle sizes can be observed from Figure 4.14(a) through 4.14(c). Figure 4.14(d) shows the microstructure of the 20 h milled powders shortly after the reduction reaction. After mechanochemical synthesis for 25 and 30 h, the powders own very similar images given in Figure 4.14(e) and (f) since they have major LaB_6 and MgO phases. Although 25 h milled powders also include a very small amount of $LaBO_3$, it can not be distinguished from the images in Figure 4.14

(d)-(f). Also, the general SM images of the synthesized powders in different high-energy ball mills (Spex^{TM} 8000D Mixer Mill and planetary ball mill) using the same BPR (10:1) become very similar with each other following the reduction reaction.

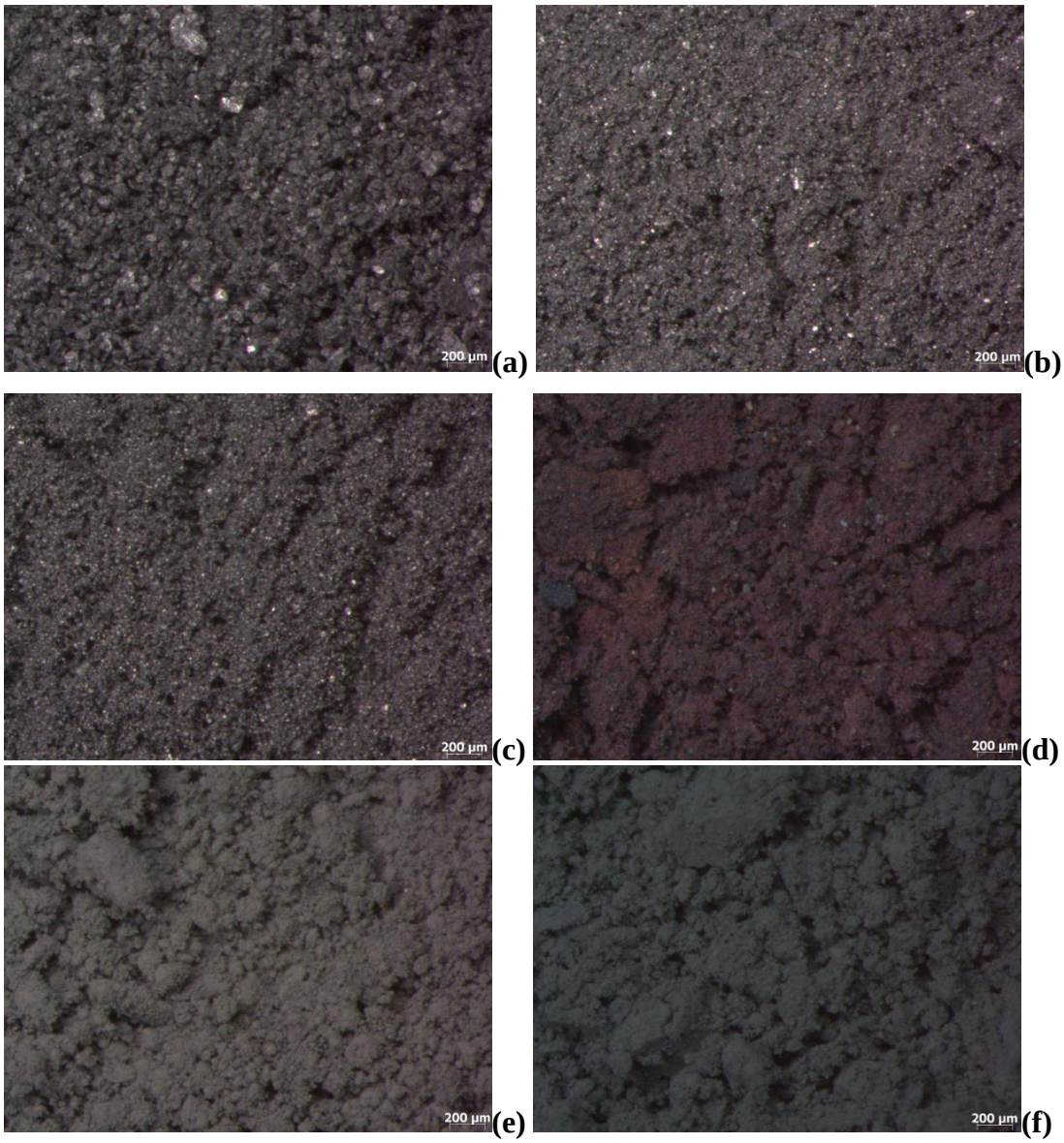

Figure 4.14 : SM images of the La_2O_3-B_2O_3-Mg powders mechanochemically synthesized using a 10:1 BPR in a planetary ball mill for different durations: (a) 10 h, (b) 15 h, (c) 18 h, (d) 20 h, (e) 25 h and (f) 30 h.

Figure 4.15(a) and (b) are the respective SEM/EDS images of the La_2O_3-B_2O_3-Mg powders mechanochemically synthesized using a 10:1 BPR in a planetary ball mill for 10 and 30 h. La_2O_3-B_2O_3-Mg powders milled for 10 h have irregular shaped particles in sizes below 25 µm. EDS measurement carried out on 10 h milled powders represents the presence of La, Mg and Au elements. The EDS system used was not appropriate for analyzing boron and oxygen. The Au element seen in the

EDS graph arised from the coating material sputtered for the enhancement of conductivity during the SEM analysis. The La and Mg elements in the EDS spectra belong to the La_2O_3 and Mg phases and no additional element was detected in the EDS due to contamination. As seen in Figure 4.15(b), 30 h milled powders have polygonal/spheroidal-shaped particles with average particle size less than 1 μm. The La and Mg elements detected in the EDS measurement of the 30 h milled powders are attributed to the LaB_6 and MgO phases which are previously revealed by the XRD pattern in Figure 4.13(g).

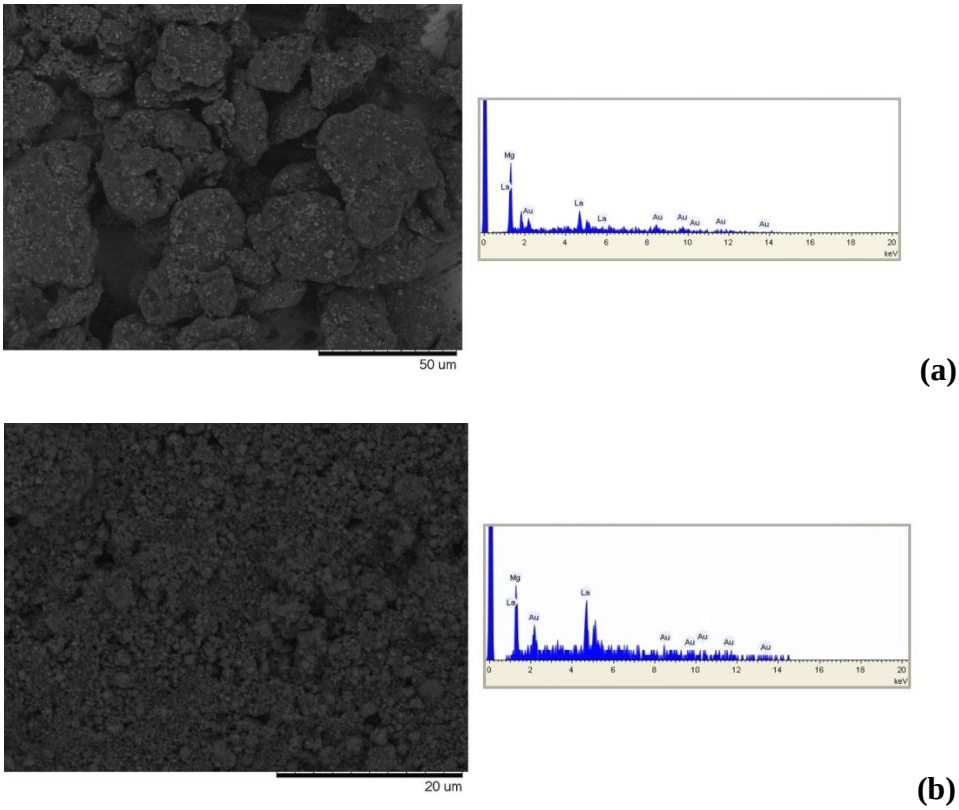

Figure 4.15 : SEM/EDS images of the La_2O_3-B_2O_3-Mg powders mechanochemically synthesized using a 10:1 BPR in a planetary ball mill for different durations: (a) 10 h and (b) 30 h.

Figure 4.16(a)-(f) displays the DSC thermograms of the La_2O_3-B_2O_3-Mg powders mechanochemically synthesized using a 10:1 BPR in a planetary ball mill up to 30 h. DSC curve of the 10 h milled powders shows that there is a broad exotherm between 500 and 700°C owning two peaking points at about 570°C and at about 630°C (Figure 4.16(a)). On the basis of Figure 4.13(b), 10 h milled powders contain La_2O_3, B_2O_3 and Mg phases. Although B_2O_3 and Mg melt respectively at 450 and 650°C, there exist no endothermic peaks corresponding to their melting. The broad

exothermic peak with two peaking points respectively indicates the $LaBO_3$ formation and Mg oxidation. As seen from Figure 4.16(b) and (c), the shape and location of this exotherm varied after 15 and 18 h milling. It became a very broad single exotherm between 525 and 600°C with a maximum peak at 575°C for the 15 h milled powders and between 500 and 625°C with a maximum peak at 550°C for the 18 h milled powders. This points out a more dominant formation of $LaBO_3$ phase. DSC curve of the 20 h milled powders does not show any indication of Mg oxidation. This is in good aggrement with its XRD pattern (Figure 4.13(e)) showing the presence of LaB_6, MgO and $LaBO_3$ phases. However, a very small exotherm at 750°C which is considered to be related with the magnesium borate formation is seen in Figure 4.16(d). 25 h milled powders have a straight DSC curve without any endothermic or exothermic peaks (Figure 4.16(e)). It conforms well with the detected LaB_6, MgO and $LaBO_3$ phases in its XRD pattern (Figure 4.13(f)). The DSC curves of the 30 h milled powders display no exothermic peak (Figure 4.16(f)), implying the completion of the reaction with no evidence of unreacted Mg. This is in agreement with the presence of LaB_6 and MgO phases in the XRD pattern in Figure 4.13(g).

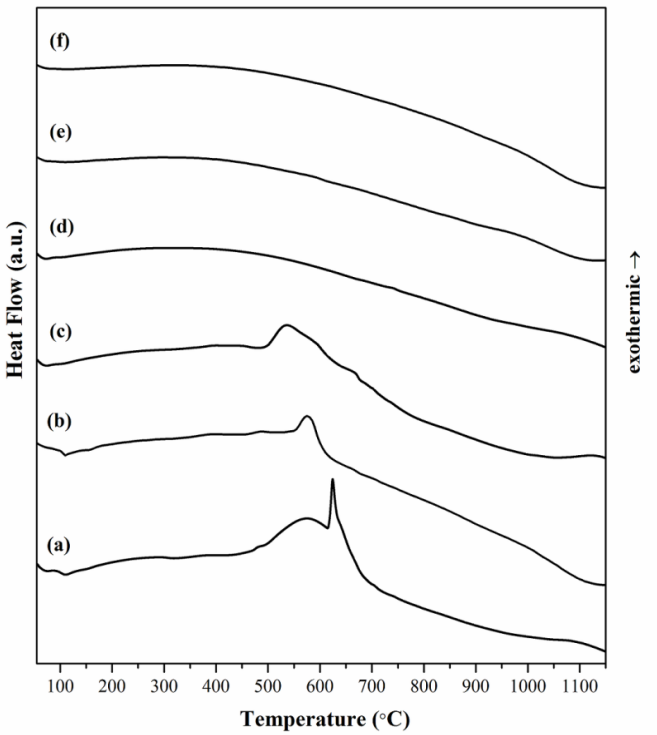

Figure 4.16 : DSC thermograms of the La_2O_3-B_2O_3-Mg powders mechanochemically synthesized using a 10:1 BPR in a planetary ball mill for different durations: (a) 10 h, (b) 15 h, (c) 18 h, (d) 20 h, (e) 25 h and (f) 30 h.

Figure 4.17(a)-(f) shows the XRD patterns of the mechanochemically synthesized La_2O_3-B_2O_3-Mg powders, using a 10:1 BPR in a planetary ball mill up to 30 h, after DSC analyses up to 1150°C. 10, 15 and 18 h milled La_2O_3-B_2O_3-Mg powders in which reduction reaction does not take place (Figure 4.17(a)-(c)) and 20, 25 and 30 h milled powders in which readuction reaction takes place (Figure 4.17(d)-(f)) have the same resultant phases (LaB_6, MgO, $LaBO_3$ and $Mg_3B_2O_6$) after heating up to 1150°C. However, the intensity of LaB_6 is higher in the 25 and 30 h milled powders after heating because they already contain this phase at the end of mechanochemical synthesis. Besides, the phase content after heating did not change according to the type of high-energy ball mill.

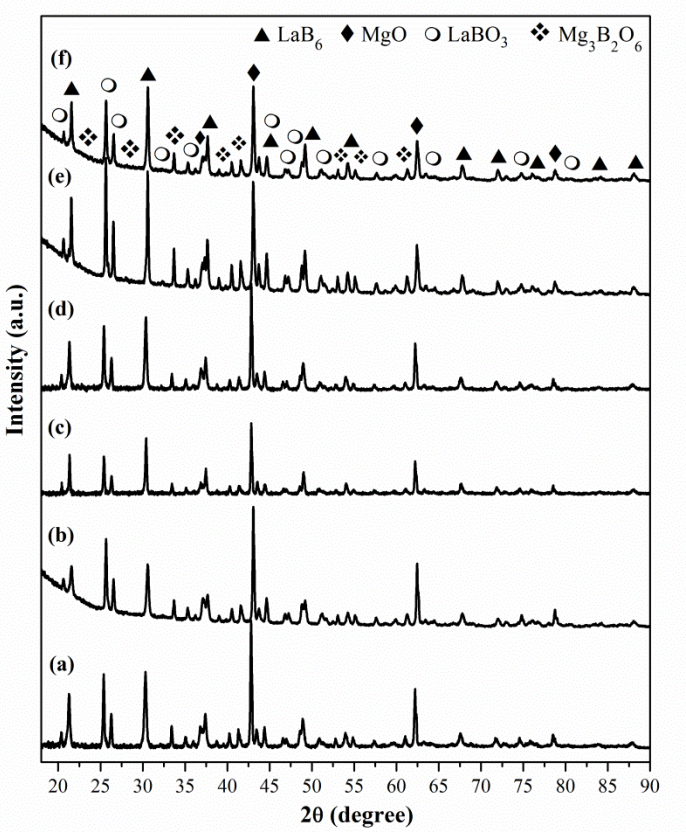

Figure 4.17 : XRD patterns of the mechanochemically synthesized La_2O_3-B_2O_3-Mg powders, using a 10:1 BPR in a planetary ball mill for different durations, after DSC analyses up to 1150°C: (a) 10 h, (b) 15 h, (c) 18 h, (d) 20 h, (e) 25 h and (f) 30 h.

Figure 4.18(a)-(e) exhibits the XRD patterns of the 0.5 wt.% stearic acid added La_2O_3-B_2O_3-Mg powder blend and powders mechanochemically synthesized using a 10:1 BPR in a Spex^{TM} 8000D Mixer/Mill for 3, 5, 8 and 12 h, respectively. It is a known fact that process control agents act as surface-active aids and reduce the effect

of cold welding by lowering the surface tension, preventing agglomeration by adsorbing on the surfaces of the powder particles and providing more homogeneous particle size distribution (El-Eskandarany, 2001; Suryanarayana, 2001; Murthy and Ranganathan, 1998). As previously seen from Figure 4.1(e), a milling duration of 2 h 45 min is sufficient to start the reaction for synthesizing the LaB_6 and MgO phases, using the same milling conditions (Spex^{TM} 8000D Mixer/Mill, 10:1 BPR). However, no reaction takes place even after 8 h of milling (Figure 4.18(a)-(d)) with the addition of 0.5 wt.% stearic acid into the powder blend. There are still La_2O_3 and Mg phases in the microstructure of 3, 5 and 8 h milled powders. XRD patterns of the 3, 5 and 8 h milled powders in Figure 4.18(b)-(d) show a gradual reduction in crystallite sizes of La_2O_3 and Mg. Moreover, there is only a very small incubation of MgO at about 42.5° after milling for 8 h. As shown in Figure 4.18(e), LaB_6 and MgO phases emerged in the microstructure after 12 h milling in the presence of the PCA whereas the reaction was completed after 5 h milling in the absence of it (Figure 4.1(g)).

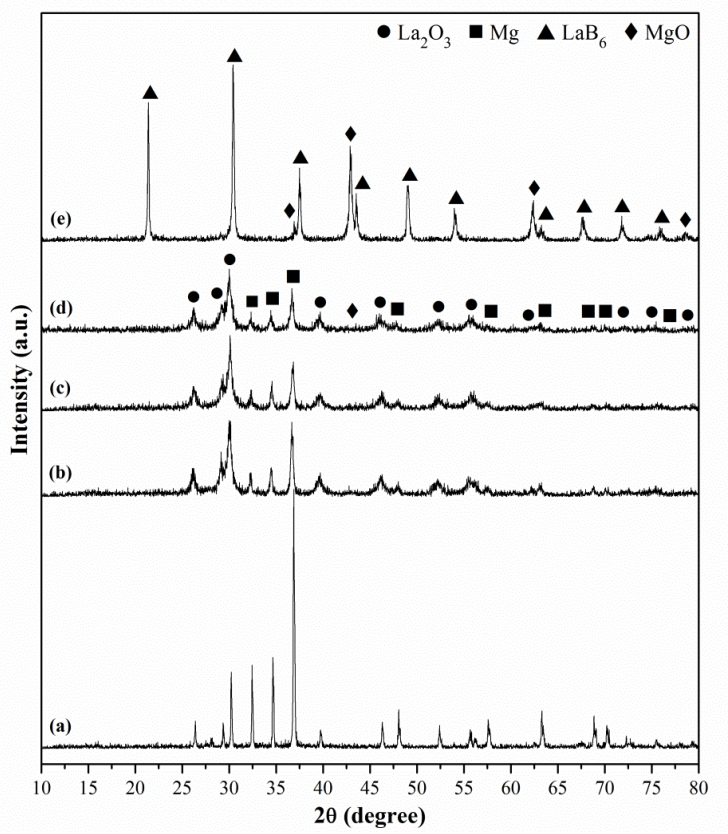

Figure 4.18 : XRD patterns of the 0.5 wt.% stearic acid added La_2O_3-B_2O_3-Mg powder blend and powders mechanochemically synthesized using a 10:1 BPR in a Spex^{TM} 8000D Mixer/Mill for different durations: (a) ab, (b) 3 h, (c) 5 h, (d) 8 h and (e) 12 h.

On the basis of this observation, it can be stated that the stearic acid slows down the reaction rate as well as decreases the particle size by inhibiting interparticle welding during collisions (Suryanarayana, 2001). If only the reaction is taken as basis without considering milling duration, the effect of PCA on the crystallite size of LaB_6 is incontrovertible. LaB_6 has a crystallite size of 44.7 nm and a lattice strain of 0.332 % in the PCA added powder blend milled for 12 h while the crystallite size of LaB_6 in the 2 h 45 min milled powders without PCA is about 82.4 nm with a lattice strain of 0.194 % (Figure 4.2). Furthermore, the approximate value of the LaB_6 crystallite size in the PCA added powder blend can be reached after 11 h milling with higher lattice strain value (0.406 %) in the absence of PCA. Although PCA partially eradicates the agglomeration and also adhesion problems because of its waxy structure, it prevents ignition and postpones the complete reaction. Therefore, the use of PCA can not be considered as an economical way to synthesize LaB_6 powders but it nevertheless provides smaller crystallite sizes which are impossible to attain without it. On the other hand, the amount of stearic acid may be reduced to less than 0.5 wt.% or the type of PCA may be changed to shorten the reaction times. Moreover, carbon, hydrogen and oxygen containing stearic acid is likely to contaminate the powder blend by introducing carbides and/or oxides into the powder particles. The probable contamination is under the detection limit of XRD since the added stearic acid is about 0.03 g for each run. Consequently, the nature and amount of the PCA and the type of the milled powder may determine the reaction time, final size, final shape and the purity of the powder particles.

SM images of the 0.5 wt.% stearic acid added La_2O_3-B_2O_3-Mg powder blend and powders mechanochemically synthesized using a 10:1 BPR in a Spex^{TM} 8000D Mixer/Mill for 3, 5, 8 and 12 h are given in Figure 4.19(a)-(e). As seen from Figure 4.19(a), as-blended powders have white regions containing a mixture of La_2O_3 and B_2O_3 particles and gray regions consist of Mg particles. The stearic acid particles are not observed in this region of the non-milled powders due to its very small amount in the overall blend. If Figure 4.19(a) is compared with Figure 4.19(b), it can be said that milling for 3 h totally changes the microstructure of the La_2O_3-B_2O_3-Mg powder blend. The microstructure of the 3, 5 and 8 h milled powders are seen very similar until the reduction reaction takes place (Figure 4.19(b), (c) and (d)). Extending the milling duration to 12 h enables the reduction reaction and hence the transformation

of the microstructure from a granulated to an agglomerated morphology (Figure 4.19(e)). Besides, there are some white small particles in the 12 h milled powders arising from the remained process control agent which can not be volatilized during mechanochemical synthesis process. SEM image of the 12 h milled powders are given in Figure 4.20. It is obviously observed from the micrograph that very small gray particles far below 1 μm are embedded in the agglomerated surfaces of MgO.

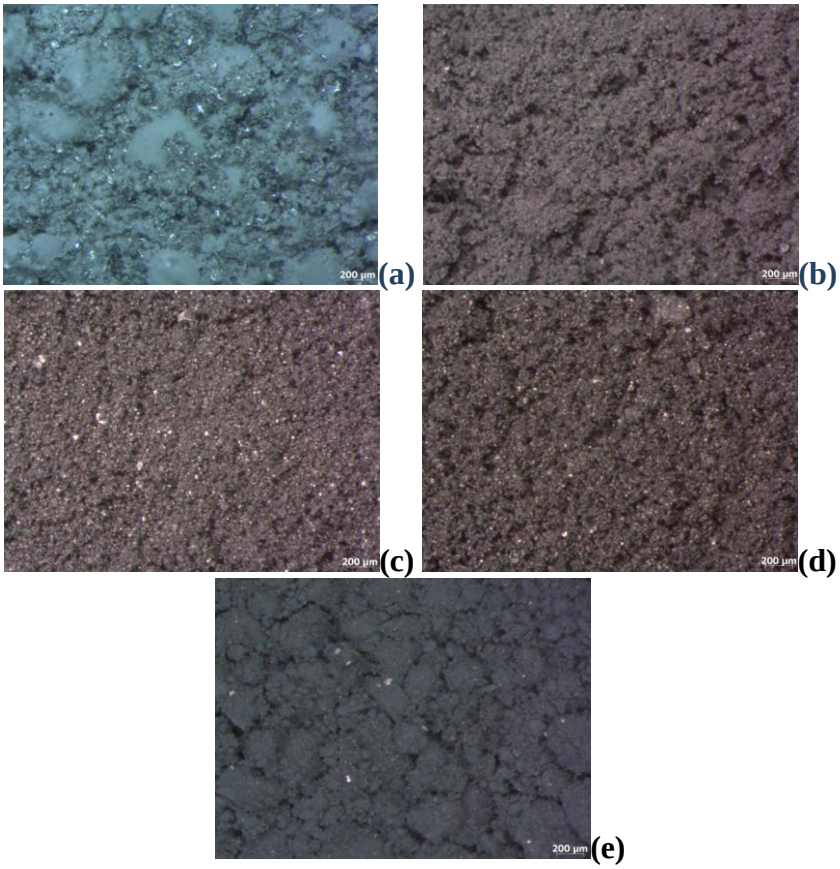

Figure 4.19 : SM images of the 0.5 wt.% stearic acid added La_2O_3-B_2O_3-Mg powder blend and powders mechanochemically synthesized using a 10:1 BPR in a Spex^{TM} 8000D Mixer/Mill for different durations: (a) ab, (b) 3 h, (c) 5 h, (d) 8 h and (e) 12 h.

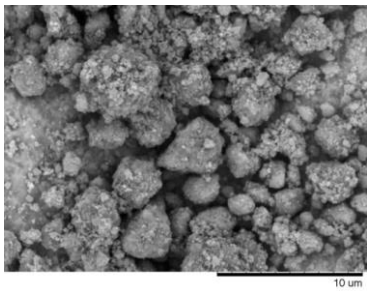

Figure 4.20 : SEM images of the 0.5 wt.% stearic acid added La_2O_3-B_2O_3-Mg powder powders mechanochemically synthesized using a 10:1 BPR in a Spex^{TM} 8000D Mixer/Mill for 12 h.

The DSC thermograms of the 0.5 wt.% stearic acid added La_2O_3-B_2O_3-Mg powder blend (non-milled) and powders mechanochemically synthesized using a 10:1 BPR in a Spex^{TM} 8000D Mixer/Mill for 3, 5, 8 and 12 h duration are shown in Figure 4.21(a)-(e). As-blended powders (Figure 4.21(a)) have a small endothermic peak having a maximum point at about 325°C. This peak can be attributed both to the dehydration of H_3BO_3 adsorbed to the surfaces of B_2O_3 and earlier melting of stearic acid which normally melts at 382°C. DSC curve of the as-blended powders contain also a small exotherm at about 580°C, a small endotherm at about 650°C and a broad endotherm with two peaking points at about 750 and 800°C, respectively indicating the emergence of lanthanum borate phases, the melting of Mg and earlier boiling of Mg in the presence of La_2O_3 and B_2O_3. According to Figure 4.21(b), the DSC curve of the 3 h milled powders has a broad exotherm between 500 and 650°C, which owns two peaking points nearly at 550 and 620°C. These two peaks correspond respectively to the formation/incubation of borate phases and the oxidation of Mg.

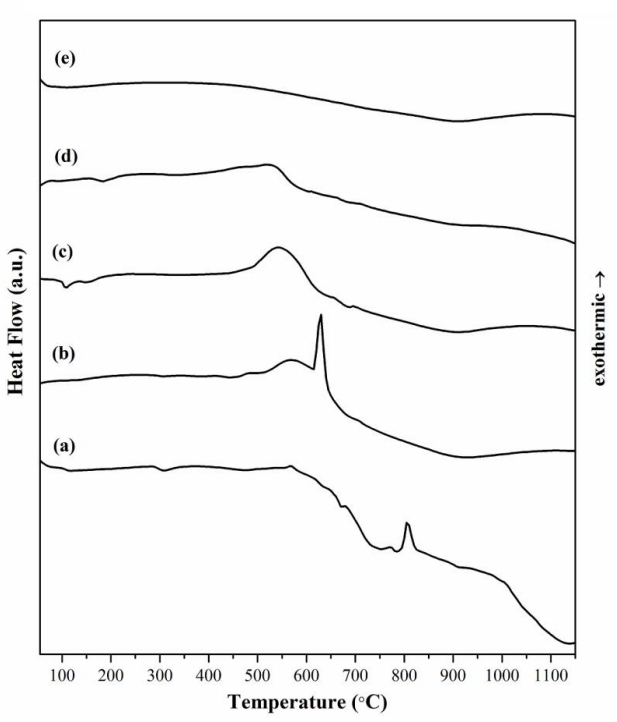

Figure 4.21 : DSC thermograms of the 0.5 wt.% stearic acid added La_2O_3-B_2O_3-Mg powder blend and powders mechanochemically synthesized using a 10:1 BPR in a Spex^{TM} 8000D Mixer/Mill for different durations: (a) ab, (b) 3 h, (c) 5 h, (d) 8 h and (e) 12 h.

The two peaking points of the broad exotherm in Figure 4.21(b) merge in the DSC curves of the 5 and 8 h milled powders (Figure 4.21(c) and (d)) and its maximum

peaking point shifts respectively to about 550 and 530°C. At the end of 12 h milling duration, DSC curve does not exhibit any endothermic or exothermic peaks since there is no remnant Mg in the structure. In the case of using stearic acid, the complete reaction can be attained after 12 h milling. As clearly seen from Figure 4.21(b) through (e) that continuous deformation derived during mechanochemical synthesis yields more active surfaces for the powder particles which react to form compounds at earlier temperatures than that of usual one. So, the temperature shifts of the peaks should be expected as milling duration increases. Figure 4.22(a)-(d) shows the XRD patterns of the 0.5 wt.% stearic acid added and mechanochemically synthesized (for 3, 5, 8 and 12 h) La_2O_3-B_2O_3-Mg powders after DSC analyses up to 1150°C. Unsurprisingly, LaB_6, MgO, $LaBO_3$ and $Mg_3B_2O_6$ phases are detected in all the milled and heated powders. The decomposition of PCA during milling, the interaction of it with the powders to form compounds and the incorporation of these compounds in the form of inclusions and/or dispersoids into the powder particles were previously reported by Öveçoğlu and Nix (1986), Öveçoğlu (1987), Suryanarayana (2001) and El-Eskandarany (2001).

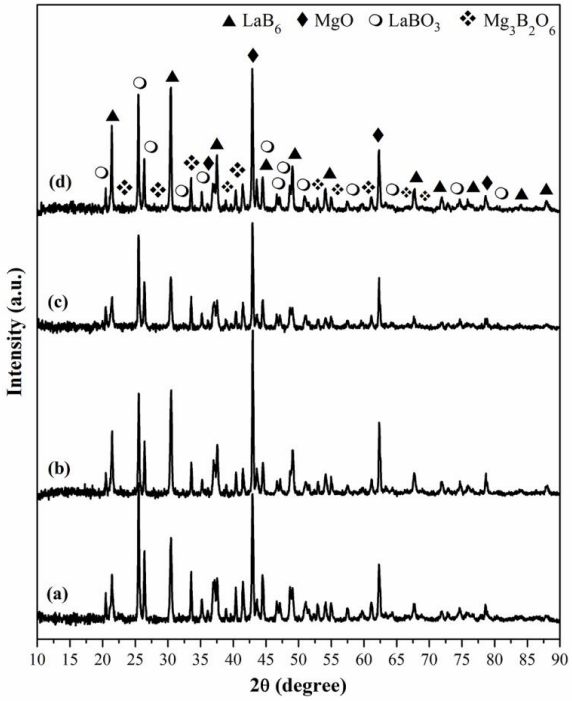

Figure 4.22 : XRD patterns of the 0.5 wt.% stearic acid added and mechanochemically synthesized La_2O_3-B_2O_3-Mg powders, using a 10:1 BPR in a Spex^{TM} 8000D Mixer/Mill for different durations, after DSC analyses up to 1150°C: (a) 3 h, (b) 5 h, (c) 8 h and (d) 12 h.

However, an emergence of a new phase can not be observed after the DSC and subsequent XRD analyses in Figure 4.21(a)-(e) and Figure 4.22(a)-(d). The DSC thermograms (Figure 4.21) and XRD patterns (Figure 4.22) of the 0.5 wt.% PCA added La_2O_3-B_2O_3-Mg powders are similar to those without PCA addition (Figures 4.5 and 4.8). Since the amount of stearic acid is only 0.5 wt.%, most of it volatilizes as a result of the temperature increment during mechanochemical synthesis and adheres to the walls of the milling vials which become waxy at the end of process.

On the basis of thermodynamical interpretations in Figures 3.12(a) and (b), the calciothermic reduction of La_2O_3 is more favorable than its magnesiothermic reduction since reaction (3.2) has more negative standard Gibbs free energy values than that of (3.1). For this, mechanochemical experiments were carried out using Ca reducing agent instead of Mg in order to compare the reaction products. Figure 4.23(a)-(g) represents the XRD patterns of the La_2O_3-B_2O_3-Ca powder blend and powders mechanochemically synthesized using a 10:1 BPR in a Spex^{TM} 8000D Mixer/Mill up to a milling duration of 3 h.

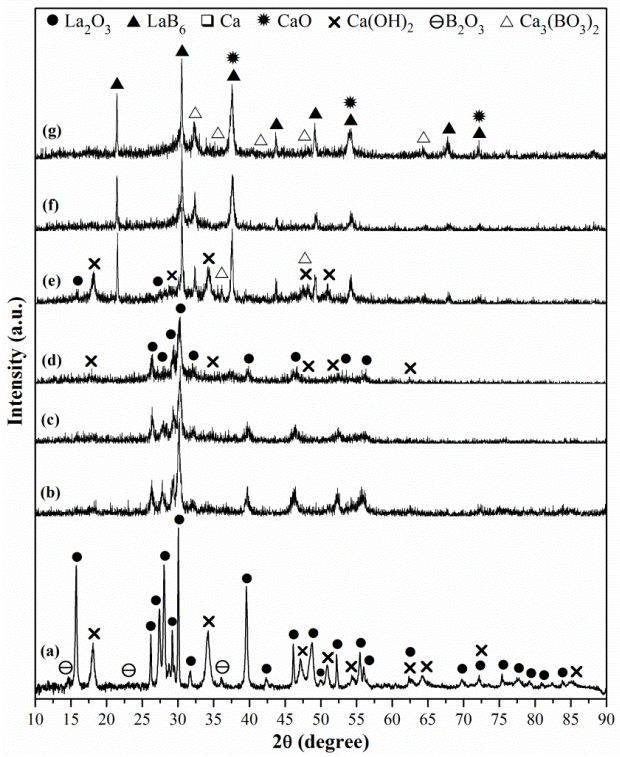

Figure 4.23 : XRD patterns of the La_2O_3-B_2O_3-Ca powder blend and powders mechanochemically synthesized using a 10:1 BPR in a Spex^{TM} 8000D Mixer/Mill for different durations: (a) ab, (b) 30 min, (c) 45 min, (d) 1 h, (e) 1.5 h, (f) 2 h and (g) 3 h.

According to Figure 4.23(a), as-blended powders contain La_2O_3, B_2O_3 (ICDD Card No: 76-1655, Bravais lattice: primitive hexagonal, a=b=0.433 nm, c=0.839 nm) and $Ca(OH)_2$ (ICDD Card No: 72-0156, Bravais lattice: primitive hexagonal, a=b=0.358 nm, c=0.489 nm) phases. Since Ca powders easily absorb humidity during handling in the laboratory atmosphere, $Ca(OH)_2$ phase is present instead of Ca in the as-blended powders. As seen in Figures 4.23(b), (c) and (d), the 30 min, 45 min and 1 h milled powders have La_2O_3 and $Ca(OH)_2$ phases. Besides, the intensities of these phases decrease as milling duration increases from 30 min to 1 h. The release of absorbed moisture by leaving Ca phase behind is expected during milling due to temperature increases inside the milling vial. However, no Ca peak can be observed in the milled powders. The absence of a Ca phase can be attributed to its amorphization during milling. Besides, there is a very small incubation of LaB_6 and CaO (ICDD Card No: 70-5490, Bravais lattice: face-centered cubic, a=b=c=0.482 nm) phases at about 37.5° at the end of 1 h milling (Figure 4.23(d)). Further 30 min milling (Figure 4.23(e)) results in LaB_6 and CaO phases in the presence of La_2O_3, $Ca(OH)_2$ and $Ca_3(BO_3)_2$ (ICDD Card No: 70-0868, Bravais lattice: primitive rhombohedral, a=b=0.864 nm, c=1.185 nm). After 2 h milling, La_2O_3 and $Ca(OH)_2$ phases disappear and the composition of the 2 h milled powder contains only LaB_6, CaO and $Ca_3(BO_3)_2$ phases (Figure 4.23(f)). Dissimilar to the magnesiothermic reduction of La_2O_3 and B_2O_3 powder blends, milled products include the borate compound of the reducing agent since Ca is more favorable to form borate phase than Mg. As seen in Figure 4.23(g), the intensities of LaB_6, CaO and $Ca_3(BO_3)_2$ phases increase after 3 h milling. It should be also mentioned that the obtained LaB_6 phase can be sub-borides such as $La_{0.983}B_6$ (ICDD Card No: 70-8265, Bravais lattice: primitive cubic, a=b=c=0.41561 nm), $LaB_{5.83}$ (ICDD Card No: 78-2381, Bravais lattice: primitive cubic, a=b=c=0.41566 nm), $LaB_{5.832}$ (ICDD Card No: 75-1414, Bravais lattice: primitive cubic, a=b=c=0.41566 nm), $LaB_{5.784}$ (ICDD Card No: 75-1402, Bravais lattice: primitive cubic, a=b=c=0.41569 nm) and $LaB_{5.892}$ (ICDD Card No: 75-1415, Bravais lattice: primitive cubic, a=b=c=0.41571 nm). The possibility of being a sub-boride phase such as LaB_{6-x} instead of a stoichiometric boride (LaB_6) is higher than that of $La_{1-x}B_6$. Because an amount of $Ca_3(BO_3)_2$ formation can decrease the number of boron atoms for the boride occurrence. Consequently, the use of Ca reductant rather than Mg can change the composition and hence the quality of the

boride products. Figures 4.24(a)-(g) show the SM images of the La_2O_3-B_2O_3-Ca powder blend (ab) and powders mechanochemically synthesized using a 10:1 BPR in a Spex^{TM} 8000D Mixer/Mill up to 3 h. In accordance with the XRD patterns in Figure 4.23(a)-(g), the microstructure of the powders changes after 1 h 30 min milling (Figure 4.24(e)) in which the reaction took place.

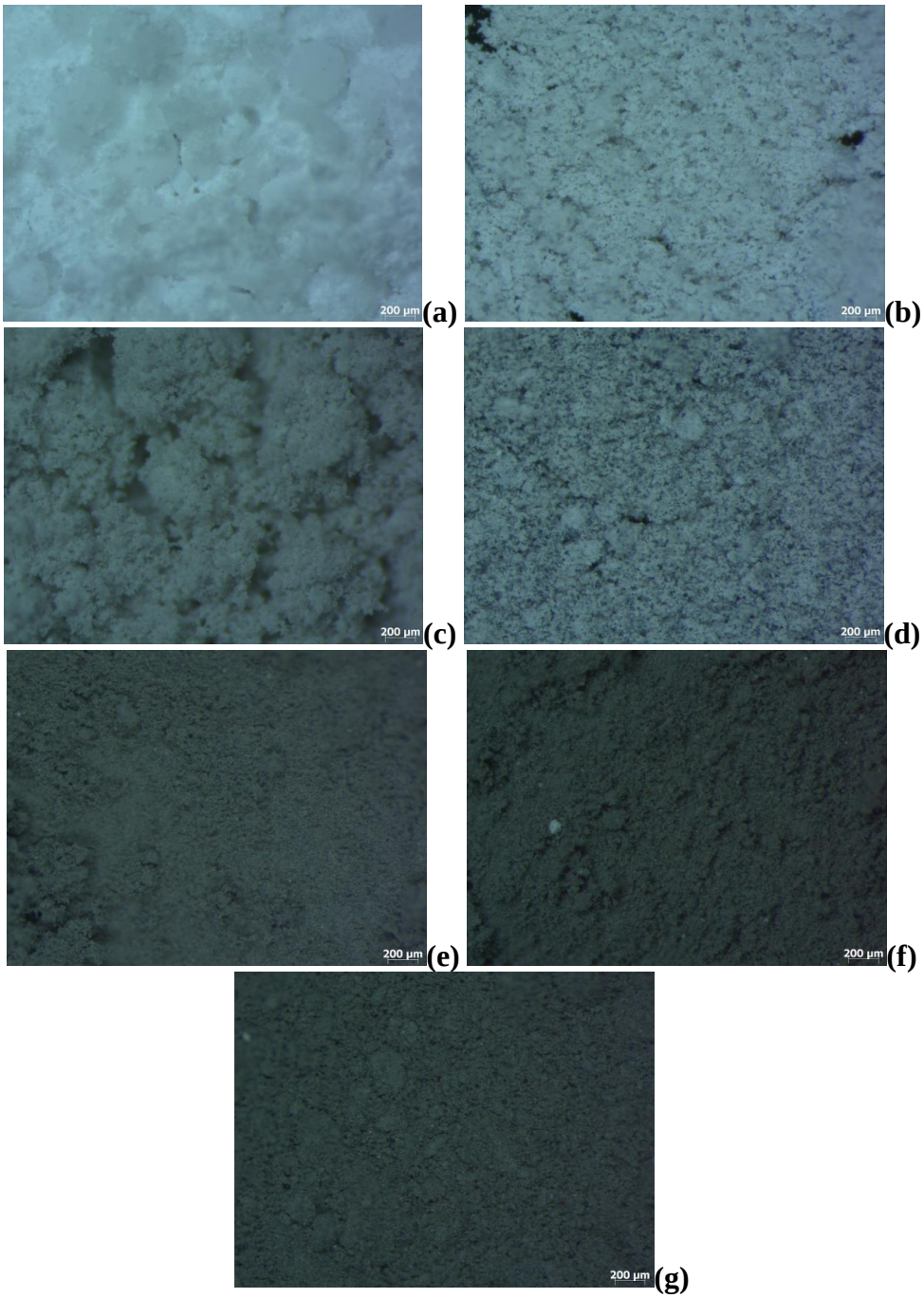

Figure 4.24 : SM images of the La_2O_3-B_2O_3-Ca powder blend and powders mechanochemically synthesized using a 10:1 BPR in a Spex^{TM} 8000D Mixer/Mill for different durations: (a) ab, (b) 30 min, (c) 45 min, (d) 1 h, (e) 1.5 h, (f) 2 h and (g) 3 h.

SEM image of the La_2O_3-B_2O_3-Ca powders, mechanochemically synthesized using a 10:1 BPR in a Spex^{TM} 8000D Mixer/Mill for 3 h, is given in Figure 4.25. Although the XRD pattern of the 3 h milled powders reveals the presence of LaB_6, CaO and $Ca_3(BO_3)_2$ phases, there are also dendritic $Ca(OH)_2$ phases adsorbed on the small rounded-shaped particles. The dendritic $Ca(OH)_2$ phase was also observed in our previous study related with the synthesis of CaB_6 powders via mechanochemical reaction of Ca-B_2O_3 blends (Balcı et al, 2012). The discrepancy between XRD and SEM analyses about the presence of $Ca(OH)_2$ can arise from the detection limit of XRD or from its amorphization during milling.

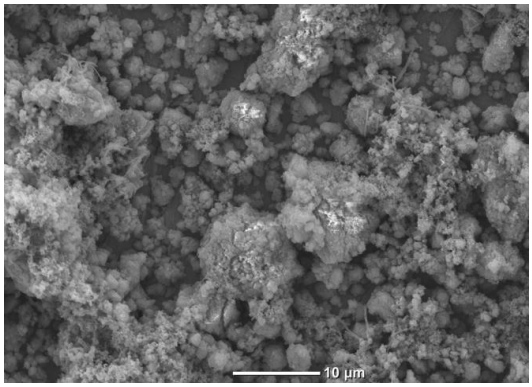

Figure 4.25 : SEM image of the La_2O_3-B_2O_3-Ca powders mechanochemically synthesized using a 10:1 BPR in a Spex^{TM} 8000D Mixer/Mill for 3 h.

The DSC thermograms of the La_2O_3-B_2O_3-Ca powder blend and powders mechanochemically synthesized using a 10:1 BPR in a Spex^{TM} 8000D Mixer/Mill for different durations up to 3 h are illustrated in Figure 4.26(a)-(g). As-blended powders have an endotherm at about 520°C and three respective small exotherms at about 700, 820 and 1000°C (Figure 4.26(a)), indicating the dehydration of $Ca(OH)_2$ to form CaO, the formations of calcium borate phases in different compositions and oxidation of Ca (Erfani et al, 2012). As seen in Figure 4.26(b), (c) and (d), 30 min, 45 min and 1 h milling cause shifts in the temperatures of these endothermic and exothermic peaks. They all have the same exothermic peaks corresponding to the formation of calcium borate phases and the oxidation of Ca, with a small difference in their temperatures. Figure 4.26(e)-(g) only shows the same endothermic peaks at about 450°C pertinent to the dehydration of $Ca(OH)_2$. Since 1 h 30 min milled powders contain LaB_6, CaO, $Ca_3(BO_3)_2$ and $Ca(OH)_2$ phases, the DSC curve only exhibits the dehydration endotherm. Although 2 and 3 h milled powders have LaB_6, CaO and $Ca_3(BO_3)_2$ phases according to the XRD patterns in Figure 4.23(f) and (g),

the presence of adsorbed $Ca(OH)_2$ phase is proved by its dehydration endotherm in Figure 4.26(f) and (g) which agrees very well with the SEM analysis in Figure 4.25. After the reaction takes place at the end of 1 h 30 min, the DSC curves do not include any exotherms belonging to the formation of calcium borates and oxidation of calcium.

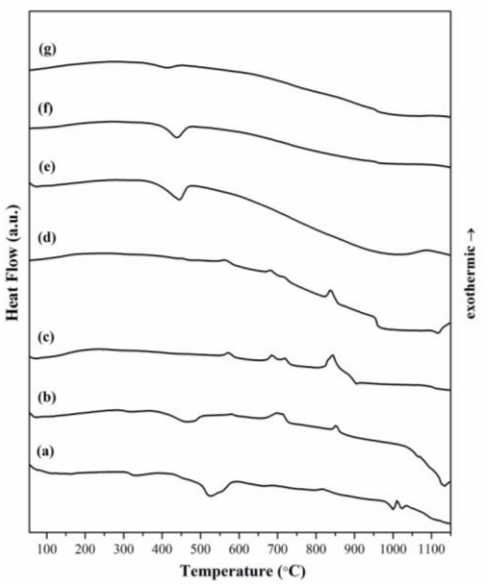

Figure 4.26 : DSC thermograms of the La_2O_3-B_2O_3-Ca powder blend and powders mechanochemically synthesized using a 10:1 BPR in a Spex^{TM} 8000D Mixer/Mill for different durations: (a) ab, (b) 30 min, (c) 45 min, (d) 1 h, (e) 1.5 h, (f) 2 h and (g) 3 h.

The XRD patterns of the mechanochemically synthesized La_2O_3-B_2O_3-Ca powders, using a 10:1 BPR in a Spex^{TM} 8000D Mixer/Mill for 45 min to 3 h, after DSC analyses up to 1150°C are given in Figure 4.27(a)-(e). After 45 min or 1 h milling and heating (Figure 4.27(a) and (b)), the powders contain CaO, $Ca_3(BO_3)_2$ and CaB_2O_4 (ICDD Card No: 72-1859, Bravais lattice: primitive orthorhombic, a=0.838 nm, b=1.382 nm, c=0.501 nm) phases with very small amount of LaB_6 phase. After 1 h 30 min milling and heating, the intensities of the phase, especially that of LaB_6, get higher (Figure 4.27(c)) and this increasing tendency continues as milling duration increases up to 3 h (Figure 4.27(d) and (e)). Heating up to 1150°C results in the formation of a new borate phase, CaB_2O_4, in addition to the $Ca_3(BO_3)_2$ which is already obtained after mechanochemical synthesis. Erfani et al (2012) also obtained CaB_2O_4 phase after heating the reactants between 750 and 900°C, which corresponds to the same temperature interval of borate formations in the DSC curves in Figure 4.26(a)-(d).

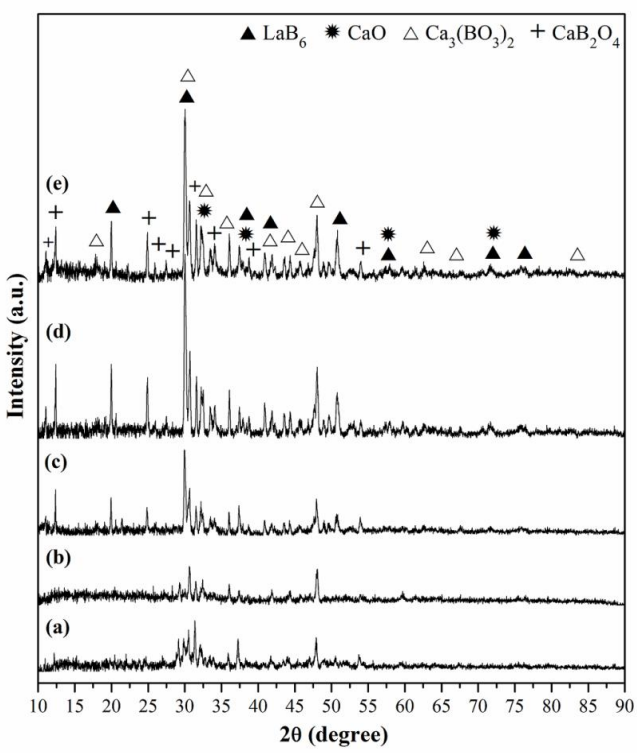

Figure 4.27 : XRD patterns of the mechanochemically synthesized La_2O_3-B_2O_3-Ca powders, using a 10:1 BPR in a Spex^{TM} 8000D Mixer/Mill for different durations, after DSC analyses up to 1150°C: (a) 45 min, (b) 1 h, (c) 1.5 h, (d) 2 h and (e) 3 h.

Following the mechanochemical synthesis, all powders produced by using different process parameters should be purified to achieve high quality products without any contaminations.

4.1.2 HCl Leaching of LaB_6 Powders

At the end of mechanochemical synthesis, five different kinds of LaB_6 products are obtained from the utilization of different process parameters. These are LaB_6 powders: (a) synthesized from La_2O_3-B_2O_3-Mg powder blends in a Spex^{TM} 8000D Mixer/Mill using 10:1 BPR with and (b) without PCA addition, (c) in a Spex^{TM} 8000D Mixer/Mill using 18:1 BPR, (d) in a planetary ball mill using 10:1 BPR and finally (e) synthesized from La_2O_3-B_2O_3-Ca powder blends in a Spex^{TM} 8000D Mixer/Mill using 10:1 BPR. After the detailed characterizations of the mechanochemically synthesized powders, different milling durations were selected according to the process parameters for the achievement of complete reaction and hence intermediate products which are compatible with the reaction (3.1) and (3.2).

According to the characterization investigations in Figures 4.1-4.5, Table 4.1 and Figure 4.8, 5 h was chosen as the optimum milling duration for the mechanochemical synthesis of LaB_6 powders from La_2O_3-B_2O_3-Mg powder blends in a Spex^{TM} 8000D Mixer/Mill using a 10:1 BPR. Thus, the following processes such as leaching and annealing were conducted on these 5 h milled powders.

Figure 4.28(a)-(c) shows the XRD patterns of the laboratory-synthesized LaB_6 powders obtained after mechanochemical synthesis of the La_2O_3-B_2O_3-Mg powder blends using a 10:1 BPR in a Spex^{TM} 8000D Mixer/Mill for 5 h and leaching with 2, 3.6 and 4 M HCl. 5 h milled powders were selectively leached with 2, 3.6 and 4 M HCl under the effect of ultrasonic stirring which accelerates the interaction of powder particles in the leach solution. HCl acid was very vigorous initially for few seconds with gas evolution. As seen in Figure 4.28(a), 2 M HCl is not sufficient to purify the LaB_6 powders since a small amount of MgO and adsorbed $Mg(OH)_2$ (ICDD Card No: 83-0114, Bravais lattice: primitive hexagonal, a=b=0.315 nm, c=0.477 nm) are present in the their composition. To observe a residual $Mg(OH)_2$ phase is not surprising because the propable leaching products are already given in reactions (3.6)-(3.8). According to Figure 4.28(b), 3.6 M HCl is almost enough to remove unwanted MgO but there are some small noises in its XRD pattern which can be related to the adsorbed $Mg(OH)_2$, $MgCl_2$, $MgCl_2.xH_2O$ or MgOHCl phases under the detection limit of XRD. Leaching with 4 M HCl enables the removal of the MgO phase completely without leaving behind any residual $Mg(OH)_2$, $MgCl_2$, $MgCl_2.xH_2O$ and MgOHCl phases since there are no small fluctuations or noises in the XRD pattern of the 4 M leached powders (Figure 4.28(c)).

In order to prove the effectiveness of leaching with 4 M HCl, subsequent annealing was carried out on these leached powders. Figure 4.28(d) is the XRD pattern of the powders leached with 4 M HCl followed by annealing at 800°C for 5 h. There is any emergence of residual elements or compounds after annealing. This is an important proof of obtaining pure LaB_6 powders after leaching with 4 M HCl. Besides, Figure 4.28(e) is the XRD pattern of the commercial LaB_6 powders. When laboratory-synthesized and commercial powders are compared with each other (Figure 4.28(c) and (e)), no phase differences are observed but the LaB_6 intensities in the commercial powders are higher than those of laboratory-synthesized ones.

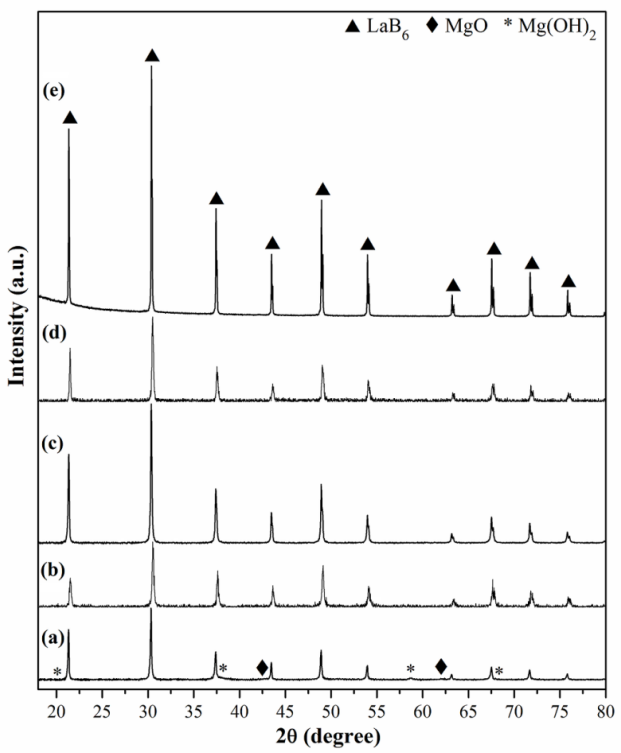

Figure 4.28 : XRD patterns of the laboratory-synthesized LaB_6 powders obtained after mechanochemical synthesis of the La_2O_3-B_2O_3-Mg powder blends using a 10:1 BPR in a Spex^{TM} 8000D Mixer/Mill for 5 h and leaching with (a) 2 M HCl, (b) 3.6 M HCl, (c) 4 M HCl, (d) 4 M HCl and annealing at 800°C for 5 h and (e) XRD pattern of the commercial LaB_6 powders.

Figure 4.29(a) and (b) are the respective SM images of the laboratory-synthesized LaB_6 powders obtained after mechanochemical synthesis of the La_2O_3-B_2O_3-Mg powder blends using 10:1 BPR in a Spex^{TM} 8000D Mixer/Mill for 5 h and leaching with 2 and 4 M HCl.

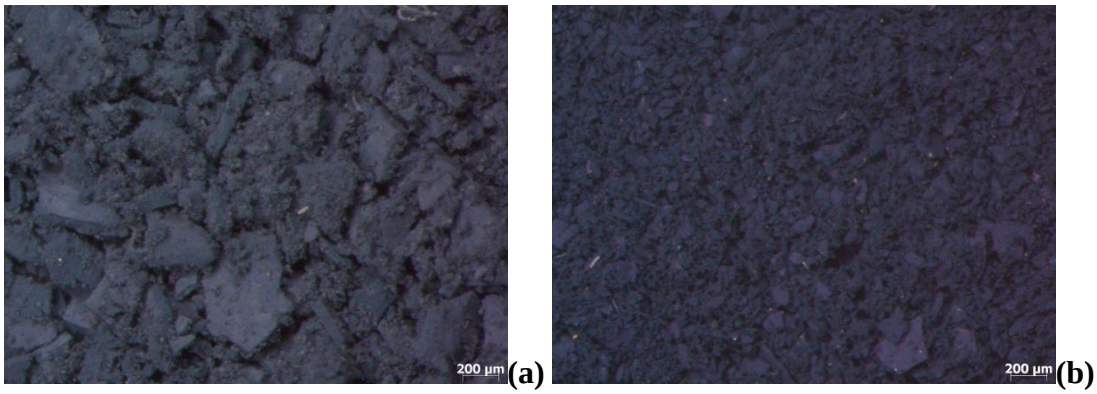

Figure 4.29 : SM images of the laboratory-synthesized LaB_6 powders obtained after mechanochemical synthesis of the La_2O_3-B_2O_3-Mg powder blends using a 10:1 BPR in a Spex^{TM} 8000D Mixer/Mill for 5 h and leaching with (a) 2 M HCl and (b) 4 M HCl.

On the basis of the SM images in Figure 4.29(a) and (b), it can be stated that leaching with 4 M HCl provides more dissolution of the LaB_6 particles since those leached with 2 M HCl have larger surfaces containing MgO which is not dissolved in the HCl acid with insufficient concentration. Additionally, the color differences between the leached powders can be clearly observed from the SM images: 2 M HCl leached powders have gray-like particles arising from the remaining MgO and adsorbed $Mg(OH)_2$ whereas 4 M HCl leached powders are intense purple.

Table 1 contains the AAS analyses results of the supernatant liquids decanted from the mechanochemically synthesized La_2O_3-B_2O_3-Mg powders using 10:1 BPR in a Spex^{TM} 8000D Mixer/Mill for 5 h and leached at 2, 3.6 and 4 M HCl concentrations. As stated earlier, the XRD pattern of the 5 h milled powders (Figure 4.1(g)) does not comprise any peaks belonging to the Fe impurity contaminations by the milling vial and milling balls due to their very small contents. Even if they somehow had, the contaminatiom would be removed by HCl leaching as well as MgO. According to the Table 2, the amount of removed Fe impurity from the powders increases as the concentration of HCl increases from 2 M (trace amount or under the detection limit of AAS) to 4 M (21.25 ppm). Moreover, the amount of dissolved Mg increases from 2700 ppm (for 2 M HCl) to 9375 ppm (for 4 M HCl). It is believed that the presence of B element in the supernatant liquid can only arise from the slight dissolution of LaB_6 phase in the concentrated HCl solution since there is no unreacted B_2O_3 phase in the 5 h mechanochemically synthesized powders as verified by the DSC analysis in Figure 4.5(g). Thus, 4 M HCl is regarded as a sufficient concentration in order not to cause any LaB_6 dissolution. Consequently, the XRD pattern of the 4 M leached (Figure 4.28(c)) and 4 M leached and annealed powders (Figure 4.28(d)) and also AAS analyses of the decanted supernatant liquids demonstrate that final LaB_6 powders are sufficiently pure and they do not contain any remnants of residual elements during HCl leaching.

As given in Figure 4.2, the crystallite size and lattice deformation of LaB_6 in the 5 h mechanochemically synthesized powders are 70.1 nm and 0.201 %, respectively. After leaching, the crystallite size and lattice strain reduces respectively to 53.3 nm and to 0.029 % indicating that larger MgO particles and nearly the whole effect of milling on the lattice were removed and hence relaxation of the particles is provided. Furthermore, the crystallite size and lattice strain of LaB_6 increases to 139 nm and

0.052 % after annealing. The lattice strain is expected to be reduced or removed by annealing. However it could result from the appreciable increase in the crystallite size and thereby it can be considered as tolerable.

Table 4.2 : AAS analyses of the supernatant liquids decanted from the powders mechanochemically synthesized from the La_2O_3-B_2O_3-Mg powder blends using a 10:1 BPR in a Spex^{TM} 8000D Mixer/Mill for 5 h and leached at different HCl concentrations.

HCl Concentration (M)	Elements in the Supernatant Liquids (ppm)		
	B	**Fe**	**Mg**
2 M	52.92	trace amount	2700
3.6 M	305.3	14.32	6825
4 M	307.7	21.25	9375

Figures 4.30(a)-(c) are the SEM images of the laboratory-synthesized LaB_6 powders obtained after mechanochemical synthesis of the La_2O_3-B_2O_3-Mg powder blend using 10:1 BPR in a Spex^{TM} 8000D Mixer/Mill for 5 h and leaching with 4 M HCl. Figure 4.30(d) is the graph of the particle size measurement conducted on the same powders. According to Figure 4.30(a), the 5 h milled and leached powders have a homogeneous particle size distribution and consist of equiaxed particles smaller than 500 nm. The removal of dark gray irregular agglomerates in which white LaB_6 particles are embedded and the distinct particle size reduction of LaB_6 in the leached powders can be obviously seen by comparing Figure 4.30(a) with Figure 4.4(b). EDS spectra taken from large region of this sample indicates that the synthesized powders do not involve any residual element or contamination since only 67.40±1.83 wt.% La and 32.90±0.80 wt.% B were present in the microstructure. Although Figure 4.30(a) shows the presence of homogeneous LaB_6 particles having average sizes below 500 nm, a high magnification is needed to determine the accurate particle size of the LaB_6 phase. The SEM images in Figures 4.30(b) and (c) display the LaB_6 particles ranging in size between 20 and 100 nm. As compatible with the SEM images in Figure 4.30(b) and (c), the graph of the particle analyzer (Figure 4.30(d)) displays the average particle size of LaB_6 as 62 nm. Any contamination of the LaB_6 particles was not detected during SEM operated at high magnification. All particle size measurements and purity determinations are consistent with each other. Thus, LaB_6 powders having an intense purple color were obtained as the final products after milling for 5 h (La_2O_3-B_2O_3-Mg powder blend using 10:1 BPR in a Spex^{TM} 8000D

Mixer/Mill) and leaching with 4 M HCl, with a minimum purity of 99.99 % and an average particle size of 62 nm. Consequently, mechanochemical synthesis and subsequent HCl leaching processes yield LaB_6 powders with a high purity in a nanometer-scale, and such a product can not be obtained by the common or conventional synthesis methods.

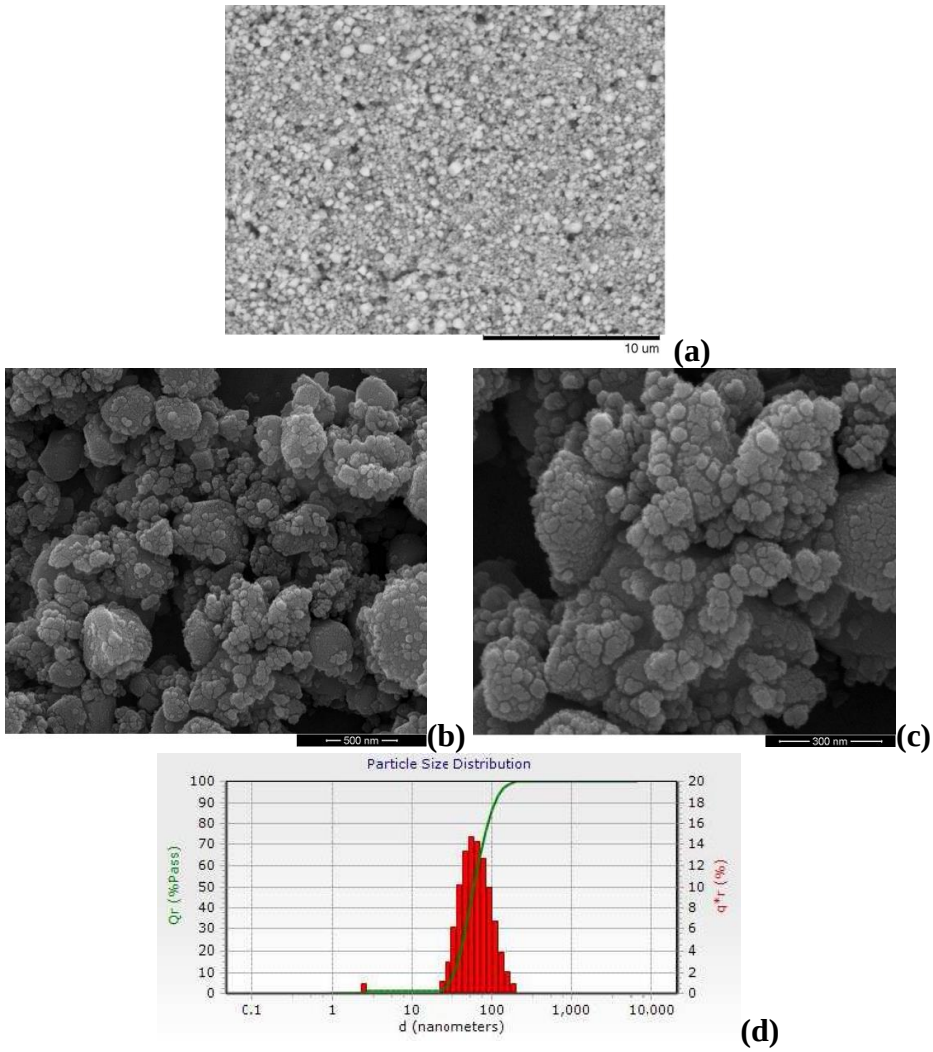

Figure 4.30 : SEM/EDS and PSA images of the laboratory-synthesized LaB_6 powders obtained after mechanochemical synthesis of the La_2O_3-B_2O_3-Mg powder blends using a 10:1 BPR in a Spex^{TM} 8000D Mixer/Mill for 5 h and leaching with 4 M HCl: (a) 10000X, (b) 120000X and (c) 240000X and (d) particle size measurement.

Figure 4.31(a) illustrates the XRD pattern of the laboratory-synthesized LaB_6 powders obtained after mechanochemical synthesis of the La_2O_3-B_2O_3-Mg powder blends using 18:1 BPR in a Spex^{TM} 8000D Mixer/Mill for 5 h and leaching with 4 M HCl. After leaching with 4 M HCl, the powders contain LaB_6 and a very small amount of FeB_{49} (ICDD Card No: 39-0418, Bravais lattice: primitive rhombohedral,

a=b=1.095 nm, c=2.386 nm) phases. When Figure 4.31(a) is compared with the XRD pattern of the commercial LaB_6 powders in Figure 4.31(b), it is clearly seen that XRD pattern of the laboratory-synthesized powders have some noises arising from the FeB_{49} phase. The emergence of an iron compound after leaching is not very surprising since the number of collisions between milling balls and reactant particles increase in the milling vial as BPR increases from 10:1 to 18:1. When 10:1 BPR is used, some amount of Fe impurity is worn off from the milling vial and balls in the powders after milling. However, this Fe impurity can be completely removed by the leaching treatments because Fe is found in elemental form in the microstructure. When 18:1 BPR is utilized, Fe worn off from the vials and balls has a tendency to react with free boron particles to form FeB_{49} which can not be removed by HCl leaching. FeB_{49} phase is not detected in the XRD patterns of the mechanochemically synthesized powders (Figure 4.9(g)) due to its very small amount. The fact that any other boride compounds such as FeB, Fe_2B and Fe_3B do not emerge resulting from Fe contamination is the wear of small amounts of Fe from the hardened steel vials and balls and the presence of too many free boron particles in the reaction medium. If the milling duration is extended over 5 h in the case of 18:1 BPR, the amount of Fe impurity will increase and various iron boride compounds will form.

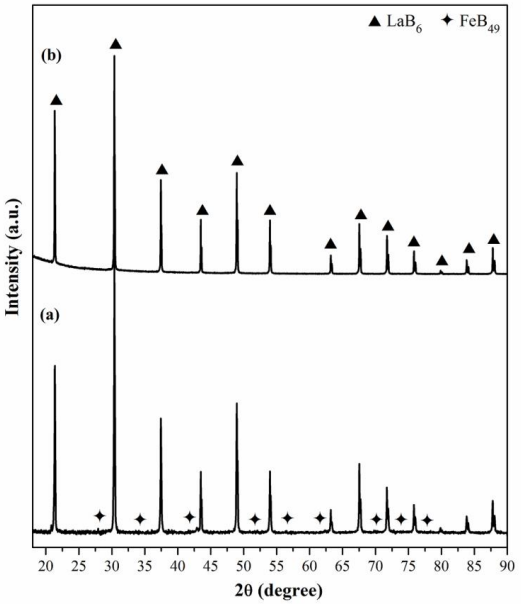

Figure 4.31 : XRD pattern of the (a) laboratory-synthesized LaB_6 powders obtained after mechanochemical synthesis of the La_2O_3-B_2O_3-Mg powder blends using a 18:1 BPR in a Spex^{TM} 8000D Mixer/Mill for 5 h and leaching with 4 M HCl and (b) commercial LaB_6 powders.

Figure 4.32 illustrates the SM image and Figure 4.33(a)-(c) display the SEM/EDS image of the laboratory-synthesized LaB_6 powders obtained after mechanochemical synthesis of the La_2O_3-B_2O_3-Mg powder blends using 18:1 BPR in a Spex^{TM} 8000D Mixer/Mill for 5 h followed by leaching with 4 M HCl. Figure 4.32 shows distinctly purple LaB_6 powders with small contaminations on it. The LaB_6 particles are seen separated not in the form of large combined surfaces because 4 M HCl concentration is sufficient to dissolve the unwanted MgO phase by completely penetrating into the particles.

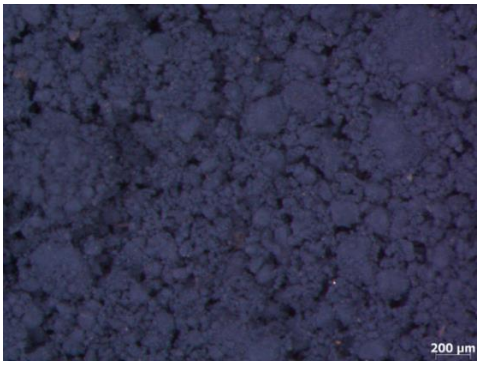

Figure 4.32 : SM image of the laboratory-synthesized LaB_6 powders obtained after mechanochemical synthesis of the La_2O_3-B_2O_3-Mg powder blends using a 18:1 BPR in a Spex^{TM} 8000D Mixer/Mill for 5 h and leaching with 4 M HCl.

The SEM micrographs in Figures 4.33(a)-(c) reveal irregular-shaped LaB_6 particles ranging in size between 40 nm and 400 nm. It can be said that using 18:1 BPR changes the morphologies of the LaB_6 particles, if Figures 4.33(a)-(c) is compared with the equiaxed particles in Figure 4.30(a)-(c). Repeated fracturing and welding of reactants using a higher BPR result in the irregular-shaped LaB_6 particles. EDS chemistry of the leached powders involves 74.10±0.20 wt.% La, 23.39±0.35 wt.% B, 0.71±0.03 wt.% Fe and 1.80±0.04 wt.% Au arised from the sputtered coating material for analysis. The results of EDS measurement are in good agreement with the calculated amounts of the products in regard of reaction (3.1). Moreover, particle size distribution graph of the leached powders (Figure 4.33(d)) indicates that the average particle size of LaB_6 is about 100 nm, which is consistent with the SEM micrographs in Figures 4.33(a)-(c). The AAS analysis of the supernatant liquid decanted from the leached powders gives the elemental results of 6421 ppm Mg, 225 ppm B and 28.13 ppm Fe originating from the free particles which do not participate in the reaction to form the FeB_{49} phase.

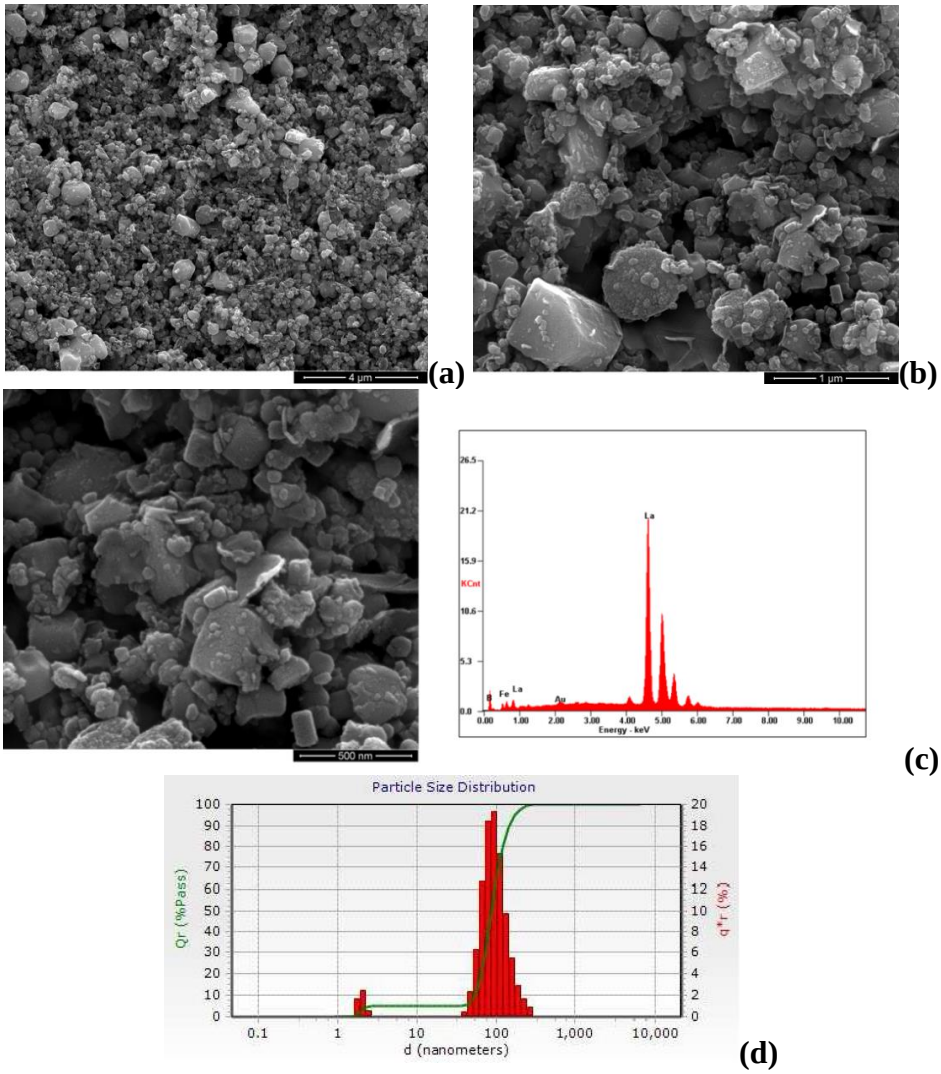

Figure 4.33 : SEM/EDS and PSA images of the laboratory-synthesized LaB_6 powders obtained after mechanochemical synthesis of the La_2O_3-B_2O_3-Mg powder blends using a 18:1 BPR in a Spex^{TM} 8000D Mixer/Mill for 5 h and leaching with 4 M HCl: (a) 20000X, (b) 80000X, (c) 200000X and (d) particle size measurement.

XRD patterns of the laboratory-synthesized LaB_6 powders obtained after mechanochemical synthesis of the La_2O_3-B_2O_3-Mg powder blends using a 10:1 BPR in a planetary ball mill for 30 h and leaching with 2 and 4 M HCl are respectively presented in Figure 4.34(a) and (b). In addition to the LaB_6 phase, a very small amount of MgO is observed in Figure 4.34(a) indicating the fact that the unwanted MgO phase can not be removed after leaching with 2 M HCl. On the other hand, Figure 4.34(b) shows the complete purification of the LaB_6 powders without any contamination of MgO or other residual compounds such as $Mg(OH)_2$, $MgCl_2$, $MgCl_2.xH_2O$ and MgOHCl. This means that leaching with 4 M HCl enables the fabrication and synthesis of pure intense purple LaB_6 powders as the final product.

This is also proven by the comparison of its XRD pattern (Figure 4.34(b)) with the XRD pattern of the commercial LaB_6 powders in Figure 4.34(c). Since the ZrO_2 milling vial and balls used in the planetary ball mil are very hard and wear resistant, any impurity/contamination worn off from them is almost impossible. The respective SM images of the 2 and 4 M leached powders are given in Figures 4.35(a) and (b). There are small white MgO particles distributed throughout the microstructure of the 2 M HCl leached powders, as seen in Figure 4.35(a), which is compatible with its XRD pattern (Figure 4.34(a)).

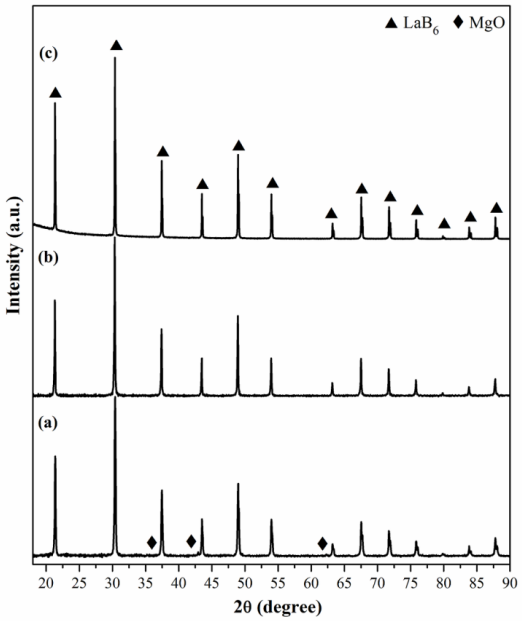

Figure 4.34 : XRD patterns of the laboratory-synthesized LaB_6 powders obtained after mechanochemical synthesis of the La_2O_3-B_2O_3-Mg powder blends using a 10:1 BPR in a planetary ball mill for 30 h and leaching with (a) 2 M HCl and (b) 4 M HCl and (c) XRD pattern of the commercial LaB_6 powders.

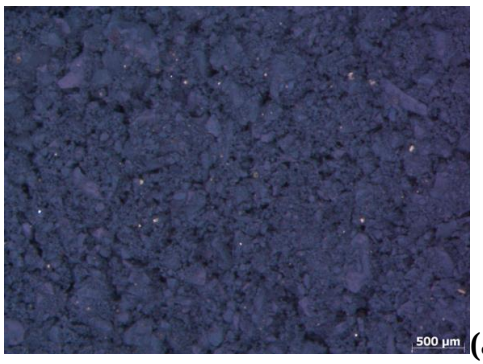

(a)

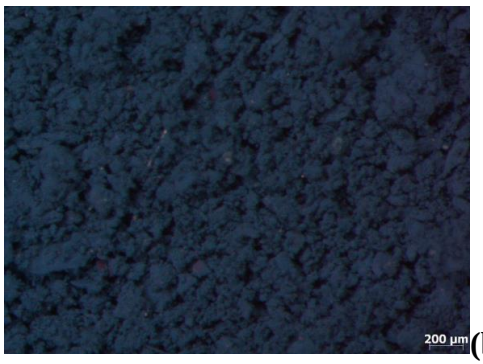

(b)

Figure 4.35 : SM images of the laboratory-synthesized LaB_6 powders obtained after mechanochemical synthesis of the La_2O_3-B_2O_3-Mg powder blends using a 10:1 BPR in a planetary ball mill for 30 h and leaching with (a) 2 M HCl and (b) 4 M HCl.

Figure 4.35(b) do not contain these white particles due to their disappearance after 4 M HCl leaching. Thus, Figure 4.34(b) and Figure 4.35(b) conform very well with each other.

The AAS analyses of the supernatant liquids decanted from the powders mechanochemically synthesized from the La_2O_3-B_2O_3-Mg powder blends using a 10:1 BPR in a planetary ball mill for 30 h and leached with 2 and 4 M HCl are given in Table 4.3. Supernatant liquid decanted from the 2 M HCl leached powders includes 234.5 ppm B and 5350 ppm Mg whereas that of 4 M HCl leached contains 772.4 ppm B and 17062.5 ppm Mg. The amounts of dissolved elements (Table 4.3) obtained after the experiments in planetary ball mill are approximately twice of those carried out in the Spex^{TM} 8000D Mixer/Mill (Table 4.1) at the same conditions. Since 6 g starting materials were used in the Spex^{TM} 8000D Mixer/Mill and 60 g reactants were used in the planetary ball mil, which their amounts were arranged according to the vial volume of the mill, the amounts of dissolved elements changed.

Table 4.3 : AAS analyses of the supernatant liquids decanted from the powders mechanochemically synthesized from the La_2O_3-B_2O_3-Mg powder blends using a 10:1 BPR in a planetary ball mill for 30 h and leached at different HCl concentrations.

HCl Concentration (M)	Elements in the Supernatant Liquids (ppm)	
	B	Mg
2 M	234.5	5350
4 M	772.4	17062.5

As the HCl concentration increases from 2 to 4 M HCl, the amounts of dissolved Mg and B increase. In order to remove all MgO impurity from the powders, concentrated HCl should be used with tolerable amounts of LaB_6 dissolution. So, XRD (Figure 3.34), SM (Figure 3.35) and AAS (Table 4.3) analyses proved that using 4 M HCl concentration as a leaching parameter provides higher dissolution of MgO and results in pure LaB_6 powders.

SEM micrographs of the laboratory-synthesized LaB_6 powders, obtained via mechanochemical synthesis of the La_2O_3-B_2O_3-Mg powder blends using 10:1 BPR in a planetary ball mill for 30 h and leaching with 4 M HCl, are illustrated in Figures 4.36(a), (b) and (c). Although a homogeneous particle distribution throughout the microstructure is seen from Figure 4.36(a), a higher magnification is required for the

exact determination of particle sizes. Furthermore, the corresponding EDS measurement only reveals the presence of La and Au elements since the utilized EDS is not capable of detecting boron and oxygen. It is proved by the EDS analysis that the obtained LaB_6 powders have no contamination in their structures. Figure 4.36(b) and (c) represent LaB_6 particles ranging in sizes between 50 and 250 nm. Based on the graph in Figure 4.36(d), the average particle size of the LaB_6 powders is measured as 74 nm, which is in good agreement with the SEM micrographs in Figure 4.36(b) and (c). Additionally, the morphologies of the LaB_6 particles synthesized in the planetary ball mill are similar to those synthesized in Spex^{TM} 8000D Mixer/Mill (Figure 4.30(b) and (c)) when the same milling conditions are used for both.

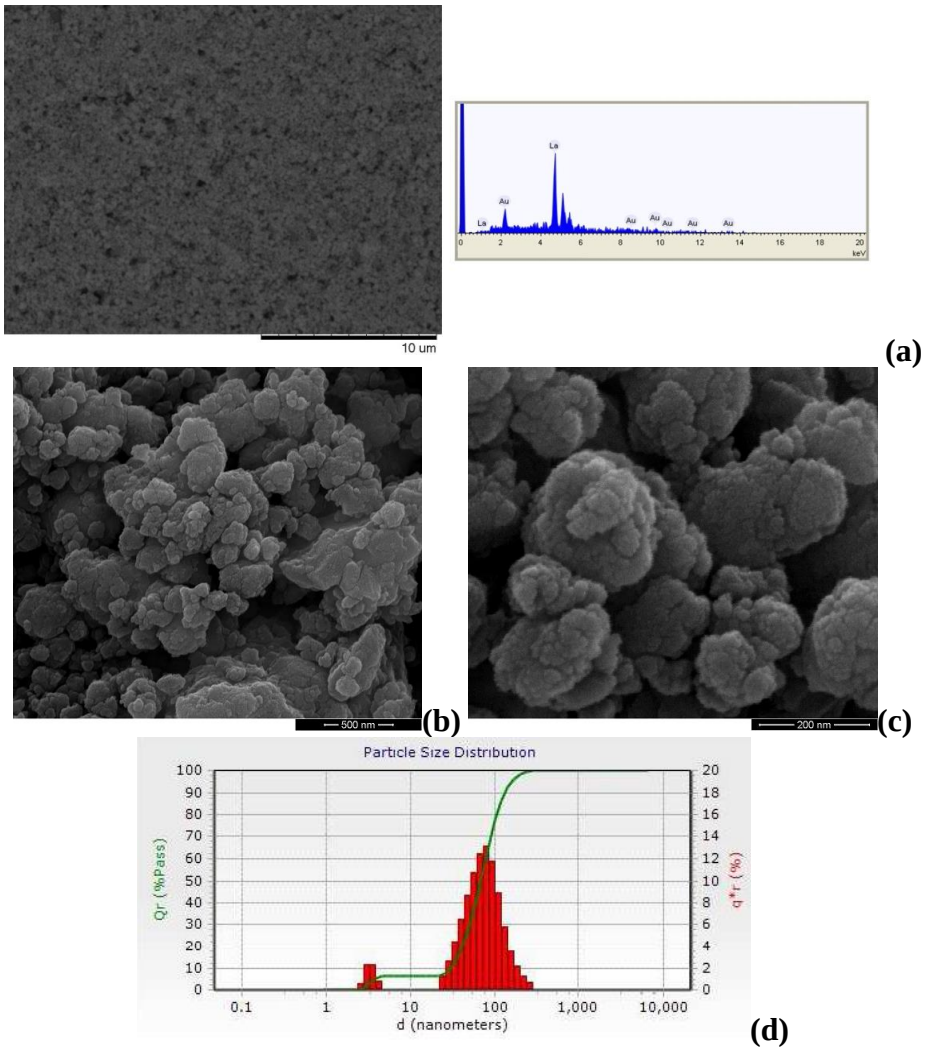

Figure 4.36 : SEM/EDS and PSA images of the laboratory-synthesized LaB_6 powders via mechanochemical synthesis of the La_2O_3-B_2O_3-Mg powder blends using a 10:1 BPR in a planetary ball mill for 30 h and leaching with 4 M HCl: (a) 10000X, (b) 120000X, (c) 400000X and (d) particle size measurement.

Figure 4.37(a) is the XRD pattern of the laboratory-synthesized LaB_6 powders obtained after mechanochemical synthesis of the 0.5 wt.% stearic acid added La_2O_3-B_2O_3-Mg powder blends using 10:1 BPR in a Spex^{TM} 8000D Mixer/Mill for 12 h and leaching with 4 M HCl. As seen from the XRD pattern, the leached powders have no additional compounds or no contaminations in their microstructure. Besides, XRD pattern hardly shows any noise in the background, which points out additional phases or adsorbed Mg-based compounds under the detection limit of XRD. Therefore, XRD pattern of the commercial LaB_6 powders in Figure 4.37(b) is almost the same with the laboratory-synthesized powders (Figure 4.37(a)), except the difference in their intensities.

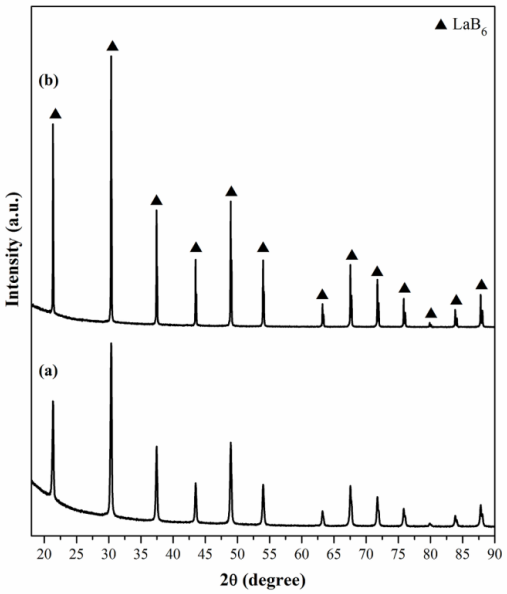

Figure 4.37 : XRD pattern of the (a) laboratory-synthesized LaB_6 powders obtained after mechanochemical synthesis of the 0.5 wt.% stearic acid added La_2O_3-B_2O_3-Mg powder blends using a 10:1 BPR in a Spex^{TM} 8000D Mixer/Mill for 12 h and leaching with 4 M HCl and (b) commercial LaB_6 powders.

Figure 4.38(a) is a SM image of the laboratory-synthesized LaB_6 powders obtained via mechanochemical synthesis of the 0.5 wt.% stearic acid added La_2O_3-B_2O_3-Mg powder blends using a 10:1 BPR in a Spex^{TM} 8000D Mixer/Mill for 12 h and leaching with 4 M HCl. Morphologically, distinct agglomerates are seen in which 4 M HCl completely penetrated to remove the unwanted MgO phase. In the SEM micrograph of this powder illustrated in Figure 4.38(b), there are very small particles in the form of connected clusters which are seen in a blurred image. The PSA graph displayed in Figure 4.38(c) indicates that the average particle size of LaB_6 powders is

about 53 nm. Mechanochemical synthesis of the PCA added La_2O_3-B_2O_3-Mg powder blend for 12 h and subsequent leaching treatment with 4 M HCl results in very low LaB_6 particle size without leaving behind any contamination. The average particle size value of LaB_6 synthesized at the same conditions without PCA is about 62 nm. Thus, the particle size reduction contribution of PCA is clearly understood by the comparison of the PSA analyses in Figure 4.30(d) and Figure 4.38(c). Moreover, the AAS analysis of the supernatant liquid decanted from the leached powders gives the elemental results of 8920 ppm Mg, 114.4 ppm B and 2.7 ppm Fe. If the AAS results are compared with the results of 4 M leached powders in Table 4.2 (without PCA addition), the differences in the amount of Fe impurity can be easily remarked. It can be said that PCA lubricates the walls of the milling vial and the milling balls and hence decreases the Fe impurity amount which is worn off from the hardened steel vial and balls. Therefore, PCA addition both reduces the final particle size of the LaB_6 phase and decreases the Fe impurity emerged during milling. However, most of the Fe impurity can be completely eliminated from the LaB_6 powders by leaching with concentrated HCl. It can be mentioned that although PCA addition has some advantageous in particle size and impurity reduction, it is not seen as very economical considering its longer (approximately four times) mechanochemical synthesis duration than that of without PCA addition.

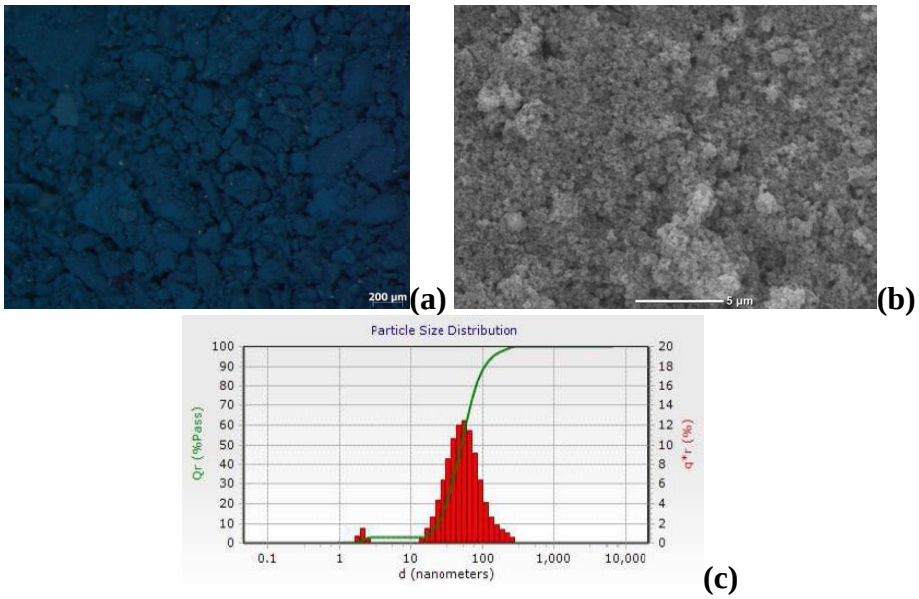

Figure 4.38 : SM (a), SEM (b) and PSA (c) images of the laboratory-synthesized LaB_6 powders via mechanochemical synthesis of the 0.5 wt.% stearic acid added La_2O_3-B_2O_3-Mg powder blends using a 10:1 BPR in a Spex^{TM} 8000D Mixer/Mill for 12 h and leaching with 4 M HCl.

Figure 4.39(a) is the XRD pattern of the laboratory-synthesized LaB_6 powders obtained after mechanochemical synthesis of the La_2O_3-B_2O_3-Ca powder blends using 10:1 BPR in a Spex^{TM} 8000D Mixer/Mill for 3 h and leaching with 4 M HCl. As seen from the pattern, leached powders contain LaB_6 with a very small amount of $Ca_3(BO_3)_2$. 4 M HCl leaching provides the complete removal of CaO and the partial removal of $Ca_3(BO_3)_2$. Compared Figure 4.39(a) with the XRD pattern of the commercial LaB_6 powders in Figure 4.39(b), it can be stated that the commercial production method of LaB_6 powders can not be the calciothermic reduction since Ca has an excessive tendency to form borate phase which cannot be removed only by HCl leaching.

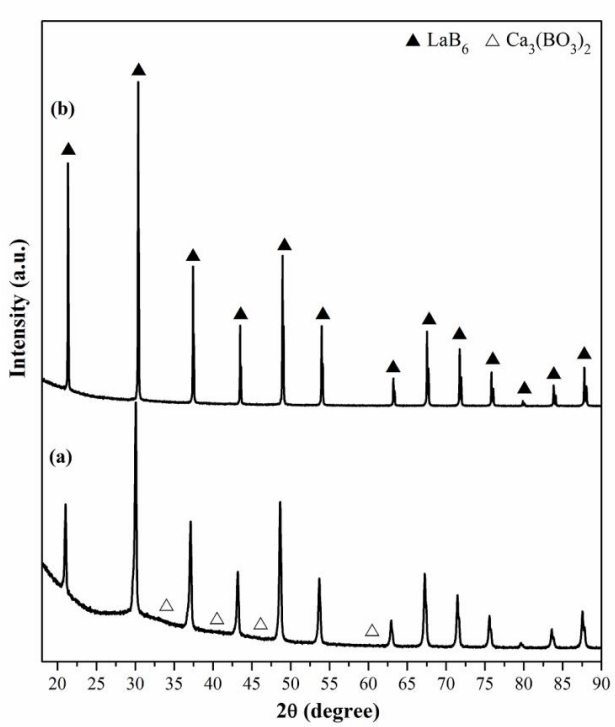

Figure 4.39 : XRD pattern of the (a) laboratory-synthesized LaB_6 powders obtained after mechanochemical synthesis of the La_2O_3-B_2O_3-Ca powder blends using a 10:1 BPR in a Spex^{TM} 8000D Mixer/Mill for 3 h and leaching with 4 M HCl and (b) commercial LaB_6 powders.

Figures 4.40(a) through (d) show the SM, SEM and PSA images of the laboratory-synthesized LaB_6 powders obtained after mechanochemical synthesis of the La_2O_3-B_2O_3-Ca powder blends using 10:1 BPR in a Spex^{TM} 8000D Mixer/Mill for 3 h and leaching with 4 M HCl. As seen in Figure 4.40(a), there are some contaminations possibly arising from the adsorbed $Ca(OH)_2$ phase throughout the microstructure. SEM images of the same powders in Figure 4.40(b) and (c) show round-shaped LaB_6

particles together with the embedded $Ca_3(BO_3)_2$, ranging in sizes between 250 nm and 1 µm. However, agglomeration of the particles prevents the observation of smaller ones. According to the PSA graph in Figure 4.40(d), the average particle size of the LaB_6 particles is about 80 nm. Furthermore, the AAS analysis of the supernatant liquid decanted from the leached powders gives the elemental results of 5710 ppm Ca, 309.3 ppm B and 3.76 ppm Fe. The Ca element in the supernatant liquid arises from the complete dissolution of CaO and the partial dissolution of $Ca_3(BO_3)_2$. So, the amount of Ca is lower than the expected amount since there is still remaining $Ca_3(BO_3)_2$ phase in the leached powders.

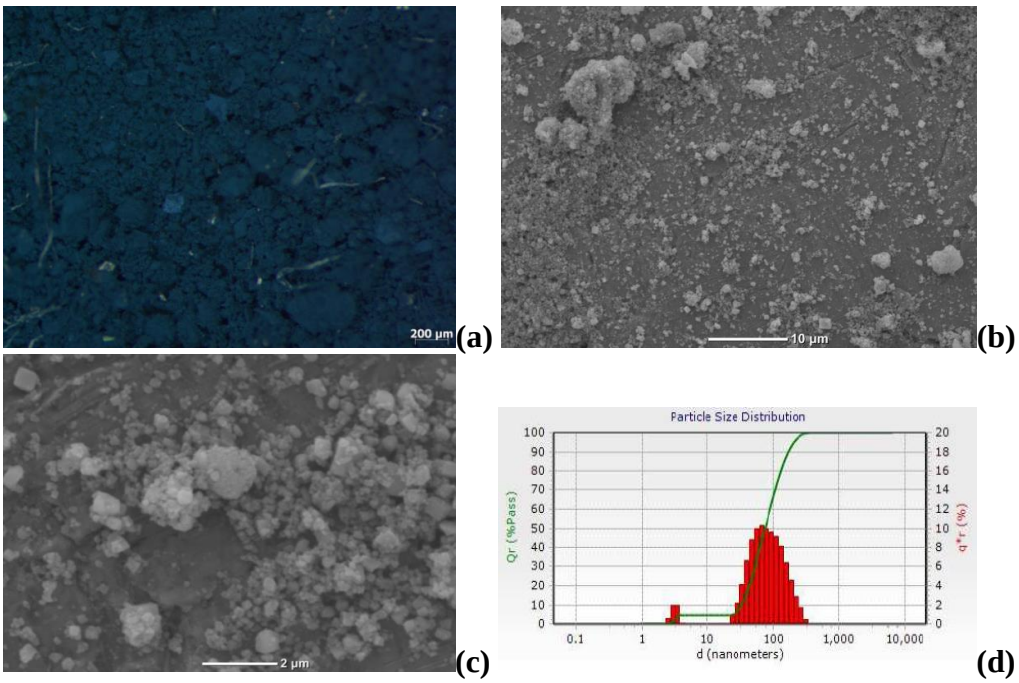

Figure 4.40 : SM (a), SEM ((b): 2000X and (c): 10000X) and PSA (c) images of the laboratory-synthesized LaB_6 powders via mechanochemical synthesis of the La_2O_3-B_2O_3-Ca powder blends using a 10:1 BPR in a Spex^{TM} 8000D Mixer/Mill for 3 h and leaching with 4 M HCl.

After mechanochemical synthesis and leaching processes carried out by using several parameters, ideal parameters for the production of LaB_6 powders are selected and subsequent consolidation treatments are conducted on the selected powder products such as: LaB_6 powders produced by mechanochemical synthesis of La_2O_3-B_2O_3-Mg powder blends in Spex^{TM} 8000D Mixer/Mill for 5 h using a 10:1 BPR and by leaching with 4 M HCl and LaB_6 powders produced by mechanochemical synthesis of La_2O_3-B_2O_3-Mg powder blends in planetary ball mill for 30 h using a 10:1 BPR and by leaching with 4 M HCl.

4.2 Mechanochemical Synthesis and HCl Leaching of CeB_6 Powders

Figure 4.41(a)-(h) illustrates the XRD patterns of the CeO_2-B_2O_3-Mg powder blend and powders mechanochemically synthesized using 10:1 BPR in a Spex^{TM} 8000D Mixer/Mill for different durations up to 5 h. Figure 4.41(a) is the XRD pattern of the as-blended (non-milled) powders containing CeO_2 (ICDD Card No: 81-0792, Bravais lattice: face-centered cubic, a=b=c= 0.541 nm), B_2O_3 and Mg phases. The characteristic peaks of B_2O_3 are not detected in the XRD pattern of the as-blended powders due to its amorphous nature and/or its further amorphization during milling. After 1 h, 1.5 h and 1 h 45 min milling, there is still no reduction reaction since CeO_2 and Mg phases are present in the structures of the milled powders, as seen in Figure 4.41(b) through (d). Besides, the intensities of the CeO_2 and Mg phases decrease from as-blended powders to 1 h 45 min milled powders (Figure 4.41(a)-(d)). This indicates a reduction in the average crystallite sizes of the CeO_2 and Mg phases during milling and hence an increase in their reactivities for the forthcoming reduction reaction. As seen from Figure 4.41(e), 2 h milled powders contain CeO_2, Mg, $CeBO_3$ (ICDD Card No: 21-0177, Bravais lattice: primitive orthorhombic, a=0.508 nm, b=0.820 nm, c=0.581 nm), CeB_6 (ICDD Card No: 38-1455, Bravais lattice: primitive cubic, a=b=c=0.414 nm) and MgO phases. 2 h milling duration shows the initial conversion point of the CeO_2-B_2O_3-Mg powders to the borate and boride phases because the reactant and the product phases are present in the powders at the same time. At the end of 3 h milling, the composition includes only CeB_6, $CeBO_3$ and MgO phases (Figure 4.41(f)). Further milling for 1 h (Figure 4.41(g)) provides the disappearance of $CeBO_3$ which is an intermediate phase for the CeB_6 formation. In other words, reaction (3.3) takes place after mechanochemical synthesis for 4 h (Figure 4.41(g)). Extending the milling duration to 5 h does not change the nature of products: CeB_6 and MgO phases are present in the 5 h milled powders (Figure 4.41(h)). X-ray reflections for the CeB_6 phase contain twelve peaks at values of 21.439°, 30.491°, 37.575°, 43.665°, 49.138°, 54.193°, 63.471°, 67.825°, 72.044°, 76.174°, 84.229° and 88.202° which are respectively indexed as (100), (110), (111), (200), (210), (211), (220), (300), (310), (311), (320) and (321) crystal planes (Figure 4.41(e)-(h)). As expected, X-ray reflections and crystal planes of CeB_6 are very similar to those of LaB_6. The intensities of the CeB_6 and MgO peaks

decreases from 3 to 5 h milling, as obviously seen from Figure 4.41(f)-(h). The average crystallite sizes of CeB_6 in the 3, 4 and 5 h milled powders were respectively calculated as 178, 149 and 90 nm, which are consistent with the decrease in their intensities (Figure 4.41(f)-(h)).

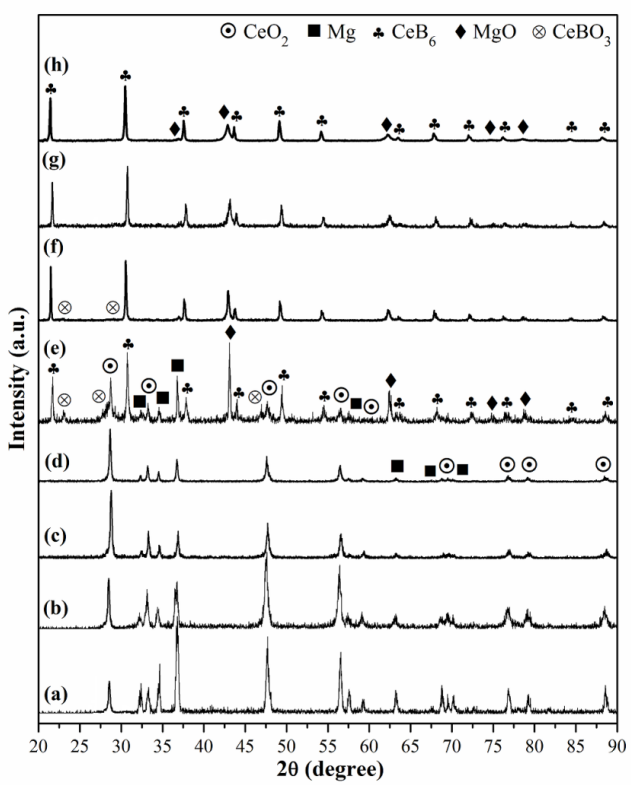

Figure 4.41 : XRD patterns of the CeO_2-B_2O_3-Mg powder blend and powders mechanochemically synthesized using a 10:1 BPR in a Spex^{TM} 8000D Mixer/Mill for different durations: (a) ab, (b) 1 h, (c) 1.5 h, (d) 1 h 45 min, (e) 2 h, (f) 3 h, (g) 4 h and (h) 5 h.

LaB_6 phase in regard of reaction (3.1) was obtained after milling for 2 h 45 min in a Spex^{TM} 8000D Mixer/Mill using a 10:1 BPR whereas CeB_6 was achieved after 3 h milling in the same conditions. As already known, a large activation energy slows down the chemical reaction. It can be said that CeB_6 formation reaction has larger activation energy to overcome than that for the LaB_6. The standard Gibbs free energy change versus temperature curves of the reaction (3.1) and (3.3) shown in Figure 3.12(a) and 3.13(a) are also in good agreement with the experimental results. Reaction (3.1) has more negative free energy values than that of (3.3), which means that LaB_6 formation is easier than CeB_6. These interpretations are confirmed by the longer reaction duration of CeB_6 (3 h) than that of LaB_6 (2 h 45 min) in the mechanochemical synthesis.

SM images of the CeO_2-B_2O_3-Mg powder blend and powders mechanochemically synthesized using 10:1 BPR in a Spex^{TM} 8000D Mixer/Mill for different durations up to 5 h are given in Figure 4.42(a)-(h).

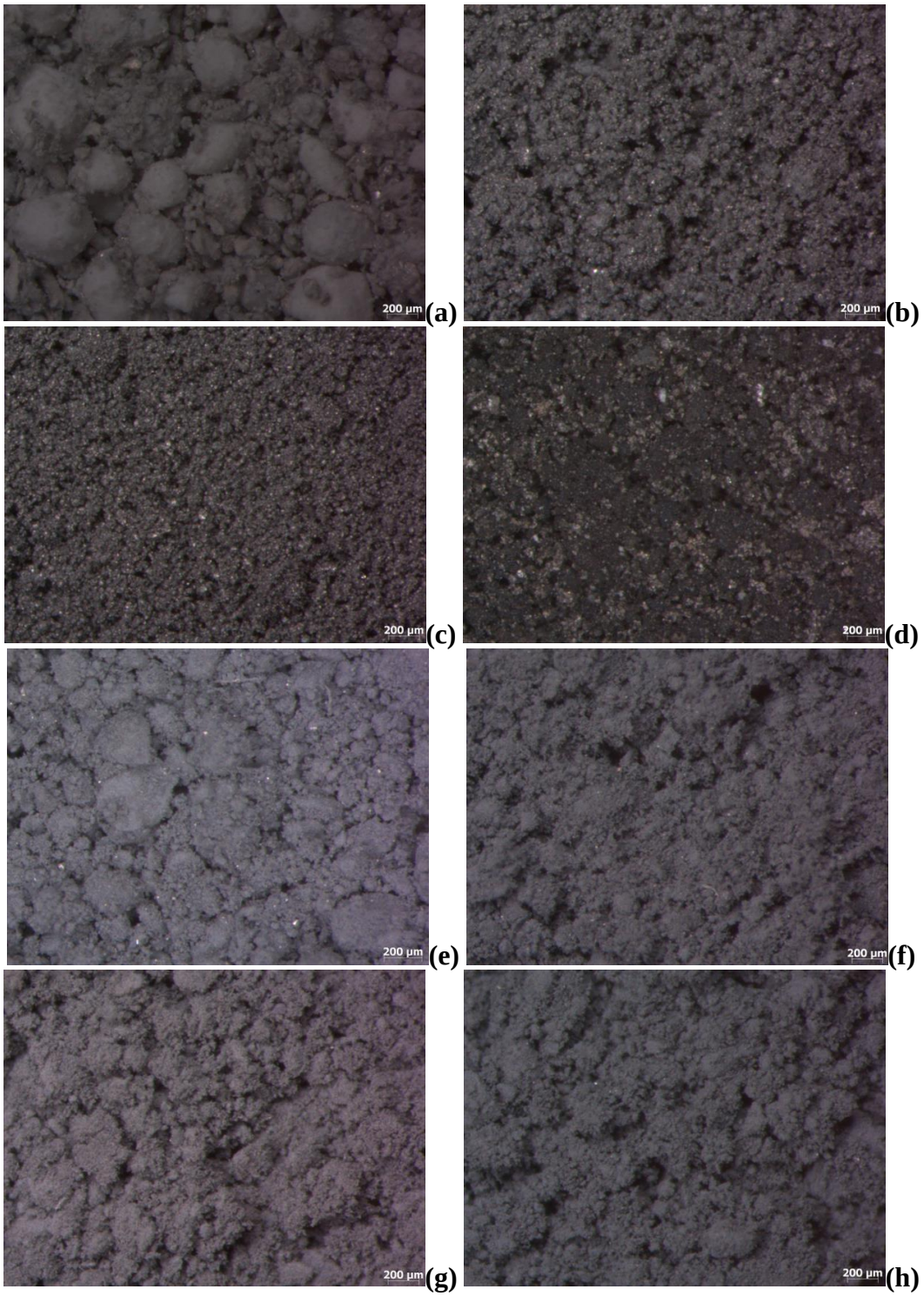

Figure 4.42 : SM images of the CeO_2-B_2O_3-Mg powder blend and powders mechanochemically synthesized using a 10:1 BPR in a Spex^{TM} 8000D Mixer/Mill for different durations: (a) ab, (b) 1 h, (c) 1.5 h, (d) 1 h 45 min, (e) 2 h, (f) 3 h, (g) 4 h and (h) 5 h.

After milling for 1 h, large particles present in the as-blended powders (Figure 4.42(a)) get fragmented and a homogenous distribution of the particles throughout the microstructure is achieved (Figure 4.42(b)). The microstructure consisting of CeO_2, B_2O_3 and Mg particles have a granular morphology at the end of 1.5 h and 1 h 45 min milling (Figure 4.42(c) and (d)). When the reaction partially takes place after 2 h milling, the morphology is converted into an agglomerated form (Figure 4.42(e)) and remains almost unchanged after 3, 4 and 5 h of milling with a reduction in particle size (Figure 4.42(f)-(h)).

Figure 4.43(a)-(h) displays the DSC thermograms of the CeO_2-B_2O_3-Mg powder blend and powders mechanochemically synthesized using 10:1 BPR in a Spex^{TM} 8000D Mixer/Mill for different durations up to 5 h. DSC curve of the as-blended powders (Figure 4.43(a)) has a very broad endotherm displaying a peak around 920°C, indicating the melting of Mg and formations of Ce and B. Surprisingly, as-blended powders have no endotherm belonging to the melting of B_2O_3.

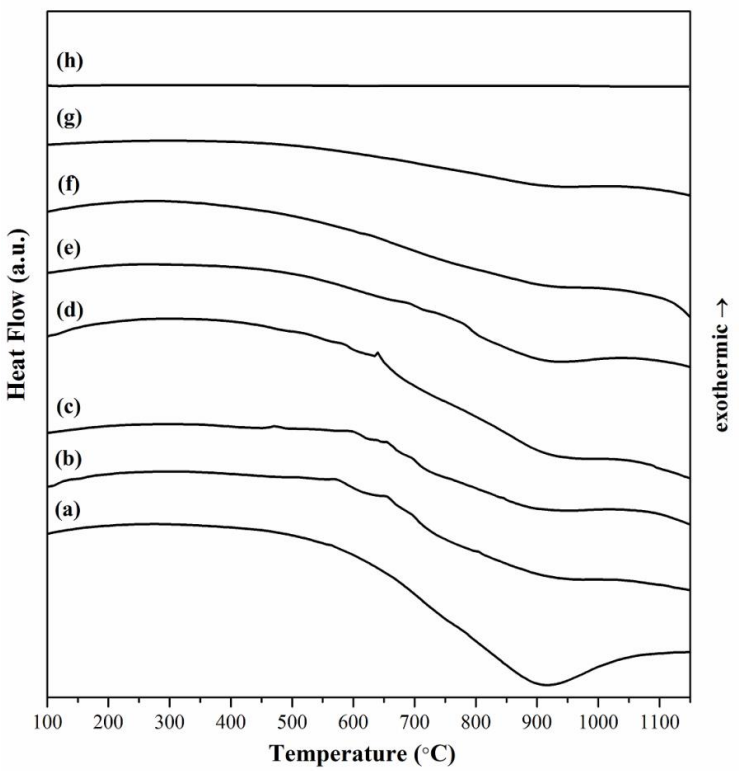

Figure 4.43 : DSC thermograms of the CeO_2-B_2O_3-Mg powder blend and powders mechanochemically synthesized using a 10:1 BPR in a Spex^{TM} 8000D Mixer/Mill for different durations: (a) ab, (b) 1 h, (c) 1.5 h, (d) 1 h 45 min, (e) 2 h, (f) 3 h, (g) 4 h and (h) 5 h.

DSC curves of the 1 h, 1.5 h and 1 h 45 min milled powders have the same characteristics since they have CeO_2, B_2O_3 and Mg phases in their compositions. They have three small and broad exothermic peaks at about 600, 650°C and 700°C, corresponding to the formation of $CeBO_3$ phase, the oxidation of Mg and the formation of $Mg_3B_2O_6$ phase, respectively (Figure 4.43(b), (c) and (d)). The latter two exotherms shift and get smaller in the DSC curve of the 2 h milled powders (Figure 4.43(e)) because they contain CeO_2, Mg, $CeBO_3$ and CeB_6 phases after milling. In the DSC curves of the 3, 4 and 5 h milled powders, no endothermic and exothermic peaks are observed due to the fact that they already have the CeB_6 and MgO reaction products (Figure 4.43(f)-(h)).

Figure 4.44(a) through (d) represents the XRD patterns of the mechanochemically synthesized CeO_2-B_2O_3-Mg powders, using a 10:1 BPR in a Spex^{TM} 8000D Mixer/Mill for 1-5 h, after DSC analyses up to 1150°C: All the milled and heated powders have the same phases: CeB_6, MgO, $Mg_3B_2O_6$ and $CeBO_3$ (Figure 4.44(a)-(d)). However, 1 h and 1 h 45 min milled and heated powders (Figure 4.44(a) and (b)) tend to form $CeBO_3$ rather than CeB_6.

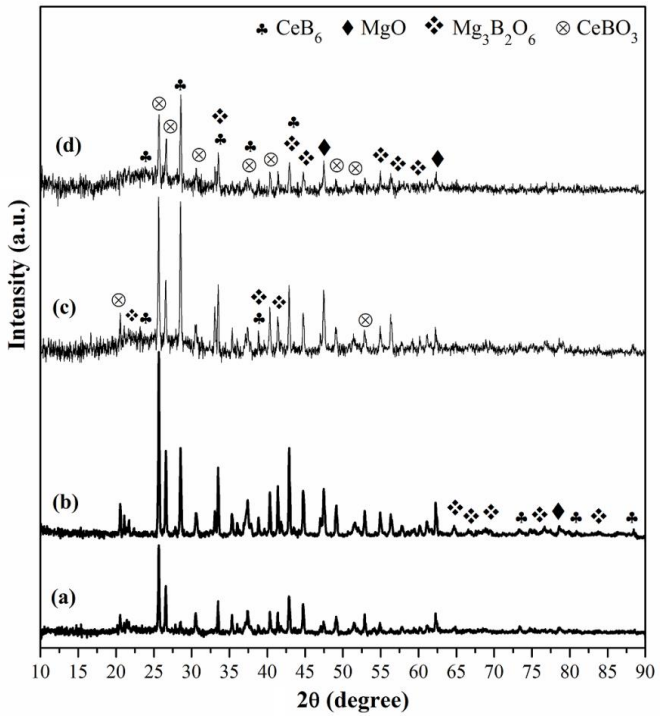

Figure 4.44 : XRD patterns of the mechanochemically synthesized CeO_2-B_2O_3-Mg powders, using a 10:1 BPR in a Spex^{TM} 8000D Mixer/Mill for different durations, after DSC analyses up to 1150°C: (a) 1 h, (b) 1 h 45 min, (c) 2 h and (d) 5 h.

It can be stated that mechanochemical synthesis is a direct process for the production of CeB_6 powders. If subsequent heat treatment is conducted on the milled powders, additional $CeBO_3$ and $Mg_3B_2O_6$ phases occur instead of yielding only CeB_6 and MgO phases.

Figure 4.45(a) and (b) are the XRD patterns of the laboratory-synthesized CeB_6 powders obtained after mechanochemical synthesis of the CeO_2-B_2O_3-Mg powder blends using a 10:1 BPR in a Spex^{TM} 8000D Mixer/Mill for 3 h and leached with 2 M HCl and those milled for 5 h and leached with 4 M HCl, respectively. As seen in Figure 4.45(a), 2 M HCl is not sufficient to remove all the MgO content in the 3 h milled powders which already have $CeBO_3$ phase after mechanochemical synthesis. Furthermore, 2 M HCl is not sufficient for the partial dissolution of $CeBO_3$. On the other hand, 4 M HCl leaching of the 5 h milled powders completely removes the unwanted MgO phase (Figure 4.45(b)). The XRD pattern of the commercial CeB_6 powders shown in Figure 4.45(c) is identical to that of the laboratory-synthesized CeB_6 powders milled for 5 h and leached with 4 M HCl in Figure 4.45(b). Therefore, 4 M HCl can be accepted as the ideal leaching concentration (Figure 4.45(b)) because there is no difference between them.

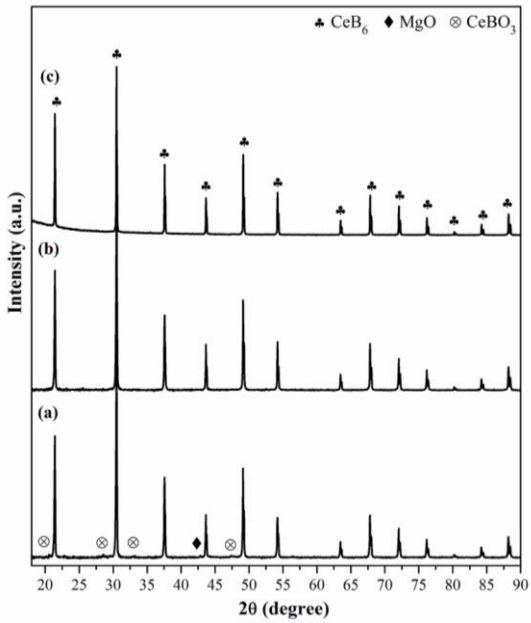

Figure 4.45 : XRD patterns of the laboratory-synthesized CeB_6 powders obtained after mechanochemical synthesis of the CeO_2-B_2O_3-Mg powder blends using a 10:1 BPR in a Spex^{TM} 8000D Mixer/Mill (a) for 3 h and leaching with 2 M HCl, (b) for 5 h and leaching with 4 M HCl and (c) XRD pattern of the commercial CeB_6 powders.

Table 4.4 shows the AAS analyses of the supernatant liquids decanted from the leached powders. Supernatant liquid decanted from the 3 h milled and 2 M HCl leached powders contain 144.1 ppm B, 3.34 ppm Fe and 4842.5 ppm Mg whereas that decanted from the 5 h milled and 4 M HCl leached powders includes 198 ppm B, 5.99 ppm Fe and 6562.5 ppm Mg. As HCl concentration increases from 2 to 4 M, the amounts of dissolved Mg, B and Fe increase.

Table 4.4 : AAS analyses of the supernatant liquids decanted from the powders mechanochemically synthesized from the CeO_2-B_2O_3-Mg powder blends using a 10:1 BPR in a Spex^{TM} 8000D Mixer/Mill for different durations and leached at different HCl concentrations.

Milling Duration (h), HCl Concentration (M)	**Elements in the Supernatant Liquids (ppm)**		
	B	**Fe**	**Mg**
3 h, 2 M	144.1	3.34	4862.5
5 h, 4 M	198.0	5.99	6562.5

It was reported in a related study that leaching the CeB_6, MgO and Fe containing MCP products in a 1 M HCl solution for 30 min was sufficient to remove the MgO phase (Akgun et al, 2013). Although leaching the CeB_6, MgO and $Mg_3B_2O_6$ containing combustion synthesis (CS) products in a 1 M HCl solution for 15 h enables to eliminate the MgO phase, it is not adequate for the dissolution of $Mg_3B_2O_6$ (Akgun et al, 2013). However, MgO and $Mg_3B_2O_6$ phases were completely removed from CeB_6 powders after leaching CS products for more than 4 h by a 6 M HCl solution with mechanical agitation of 200 rpm at 50°C (Dou et al, 2011a; Dou et al, 2011b). Besides, HCl concentration of 3 M was found as a sufficient leaching parameter to obtain pure (> 99 %) CeB_6 powders without MgO and $Mg_3B_2O_6$ contaminations (Dou et al, 2012). In an another related study, primary products of the synthesis which contained LaB_6, SmB_6 and CeB_6 nanopowders were purified by applying post treatments such as stirring in 1-6 M HCl at 95°C, filtering, washing and drying (Qian et al, 2011). Similarly, intermediate products comprising CeB_6 diffused in MgO were subjected to diluted H_2SO_4 leaching (15-25 % excess of theoretical amount) at 50-80°C for 24-40 h and subsequent filtering, washing and drying processes were carried out on the leach solution and filter residue (Liu et al, 2010).

Figures 4.46(a) and (b) display the SM images of the laboratory-synthesized CeB_6 powders obtained after mechanochemical synthesis of the CeO_2-B_2O_3-Mg powder

blends using a 10:1 BPR in a Spex^{TM} 8000D Mixer/Mill for 3 and 5 h and leaching with 2 and 4 M HCl. There are some contaminations on the 3 h milled and 2 M HCl leached powders (Figure 4.46(a)), belonging to the MgO and $CeBO_3$ phases. However, no impurities are observed on the surfaces of the 5 h milled and 4 M HCl leached powders. SM images are consistent with the XRD patterns in Figure 4.45(a) and (b) and with the AAS results in Table 4.4.

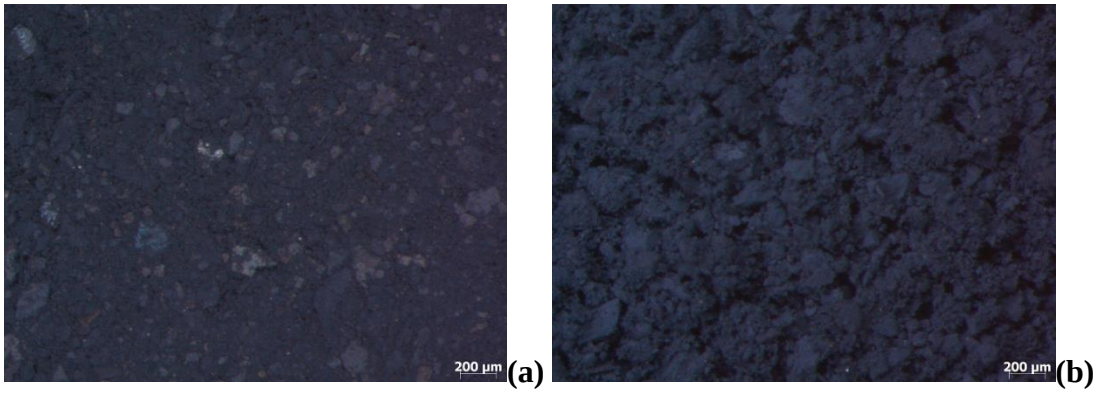

Figure 4.46 : SM images of the laboratory-synthesized CeB_6 powders obtained after mechanochemical synthesis of the CeO_2-B_2O_3-Mg powder blends using a 10:1 BPR in a Spex^{TM} 8000D Mixer/Mill (a) for 3 h and leaching with 2 M HCl and (b) for 5 h and leaching with 4 M HCl.

Figures 4.47(a)-(c) are the SEM/EDS images of the laboratory-synthesized CeB_6 powders obtained after mechanochemical synthesis for 5 h and leaching with 4 M HCl. As seen from the SEM micrograph in Figure 4.47(a), round-shaped CeB_6 particles in sizes below 1 µm are homogeneously distributed throughout the structure. The general EDS measurement taken from this micrograph reveals the presence of Ce and Au elements, indicating that only CeB_6 particles are present in the microstructure (Figure 4.47(a)). The SEM micrographs in higher magnifications enable the observation of smaller CeB_6 particles ranging in size between 50 and 150 nm (Figure 4.47(b) and (c)). The PSA graph in Figure 4.47(d) indicates that the average particle size of the CeB_6 is about 86 nm, which is in the range determined by the SEM micrographs.

In a related study carried out on the growth of CeB_6 particles, it was reported that spherical MgO particles acted as crystal seeds for CeB_6 particles to grow (Dou et al, 2012). It means that CeB_6 crystal grows directly on the MgO crystals to form a CeB_6 dispersed spherical MgO matrix. Besides, the distribution of both cube-shaped and flocculent CeB_6 particles is more uniform after leaching (Dou et al, 2012).

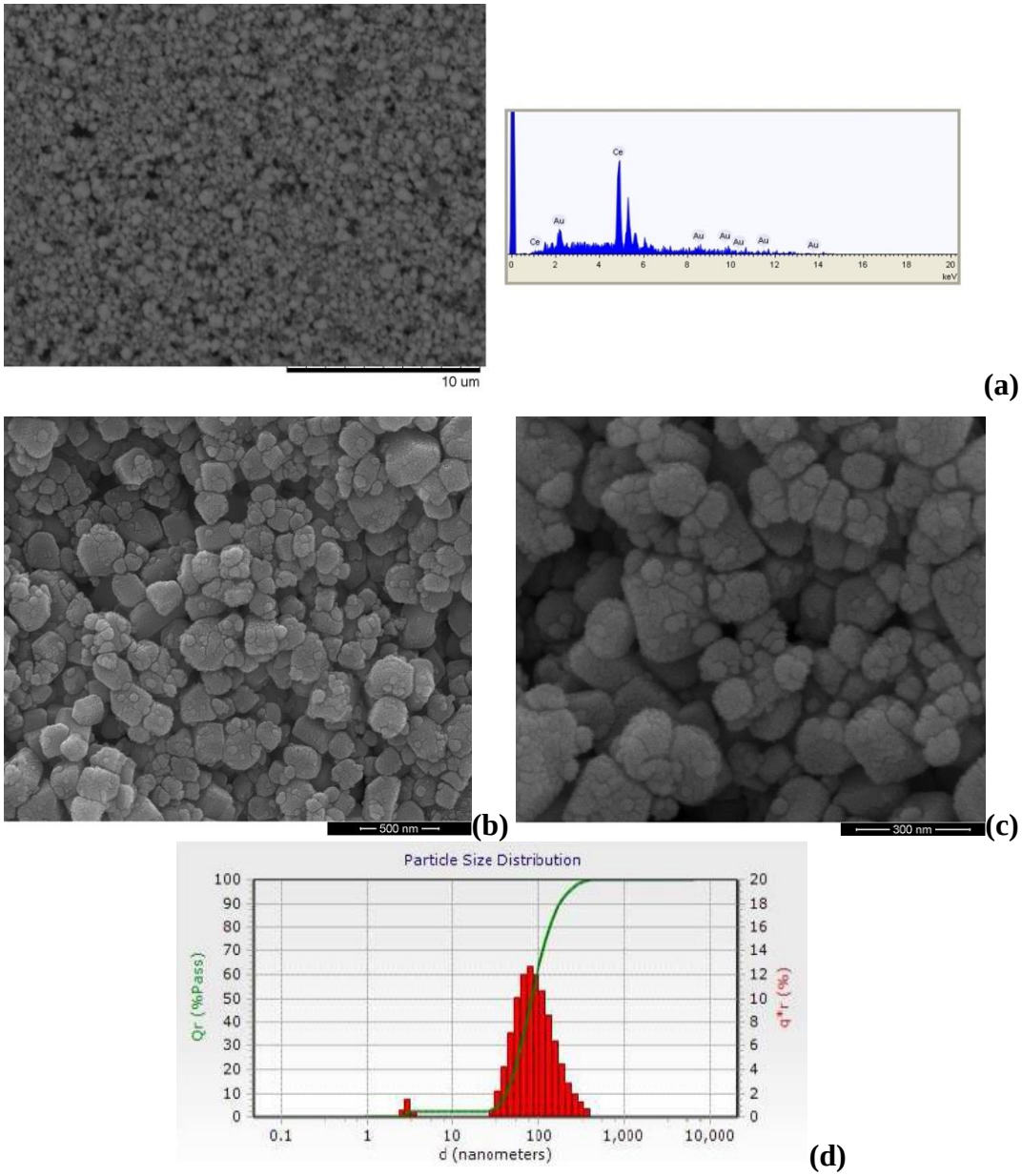

Figure 4.47 : SEM/EDS and PSA images of the laboratory-synthesized CeB_6 powders obtained via mechanochemical synthesis of the CeO_2-B_2O_3-Mg powder blends using a 10:1 BPR in a Spex^{TM} 8000D Mixer/Mill for 5 h and leaching with 4 M HCl: (a) 10000X, (b) 120000X, (c) 240000X and (d) particle size measurement.

On the basis of the XRD (Figure 4.45), AAS (Table 4.4), SEM/EDS and PSA analyses (Figure 4.47), laboratory-synthesized CeB_6 powders, obtained after mechanochemical synthesis of the CeO_2-B_2O_3-Mg powder blends using a 10:1 BPR in a Spex^{TM} 8000D Mixer/Mill for 5 h and leaching with 4 M HCl, have a minimum purity of 99.99 % and have an average particle size of 86 nm.

4.3 Mechanochemical Synthesis and HCl Leaching of SmB_6 Powders

Figure 4.48(a)-(h) represents the XRD patterns of the Sm_2O_3-B_2O_3-Mg powder blend (non-milled) and these as-blended powders mechanochemically synthesized using 10:1 BPR in a Spex^{TM} 8000D Mixer/Mill at different durations up to 5 h. Figure 4.48(a) is the XRD patern of the as-blended powders containing Sm_2O_3 (ICDD Card No: 15-0813, Bravais lattice: body-centered cubic, a=b=c=1.093 nm), B_2O_3 and Mg phases. XRD peaks of the B_2O_3 are not detected in the as-blended powders due to its amorphous nature (Figure 4.48(a)). As seen from Figure 4.48(b), there are Sm_2O_3, Mg and a very small incubation of $SmBO_3$ (ICDD Card No: 13-0479, Bravais lattice: primitive hexagonal, a=b=0.386 nm, c=0.896 nm) phases in the structure of 1 h milled powders. Further milling for 30 min results in very small incubations of the SmB_6 (ICDD Card No: 65-3293, Bravais lattice: primitive cubic, a=b=c=0.413 nm) and MgO phases in addition to the present Sm_2O_3, Mg and $SmBO_3$ (Figure 4.48(c)). The phases in the 1 h 45 min milled powders are the same with those of the 1 h 40 min milled powders.

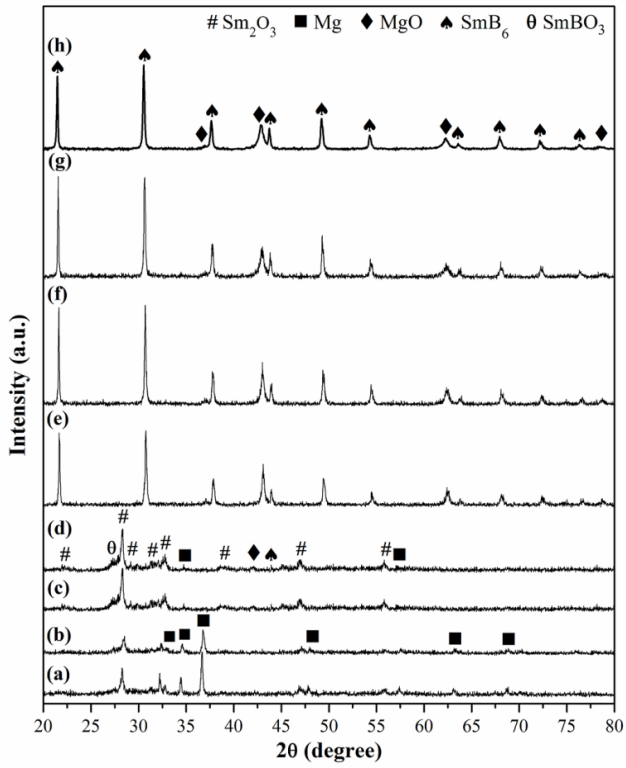

Figure 4.48 : XRD patterns of the Sm_2O_3-B_2O_3-Mg powder blend and powders mechanochemically synthesized using a 10:1 BPR in a Spex^{TM} 8000D Mixer/Mill for different durations: (a) ab, (b) 1 h, (c) 1.5 h, (d) 1 h 45 min, (e) 1 h 50 min, (f) 2 h, (g) 3 h and (h) 5 h.

In other words, further 15 min milling does not bring about any changes in the quality of the phases (Figure 4.48(d)). However, the reduction reaction takes place after 1 h 50 min milling, as seen in Figure 4.48(e). Further 5 min milling enables to overcome the activation energy of the reaction and hence enables to ignite the reducing agent for the formation of the reaction products in (3.4). The intensities of the SmB_6 and MgO phases increase from 1 h 50 min to 2 h milling duration (Figure 4.48(e) and (f)). X-ray reflections for the SmB_6 phase contain twelve peaks at values of 21.509°, 30.603°, 37.714°, 43.827°, 49.323°, 54.398°, 63.713°, 68.085°, 72.327°, 76.471°, 84.568° and 88.567° which are respectively indexed as (100), (110), (111), (200), (210), (211), (220), (300), (310), (311), (320) and (321) crystal planes (Figure 4.48(e)-(h)). As expected, X-ray reflections and crystal planes of SmB_6 are very similar to those of LaB_6 and CeB_6. Extending the milling duration up to 5 h does not change the type of the formed phases: SmB_6 and MgO are still present in the microstructure. After the reaction is completed, the intensities of the obtained SmB_6 and MgO phases start to decrease because of the decrease in their average crystallite sizes (from Figure 4.48(f) to (g)). The average crystallite sizes of SmB_6 in the 2, 3 and 5 h milled powders were respectively calculated as 157, 126 and 95 nm, which are consistent with the decrease in their intensities (Figure 4.48(f)-(h)).

The standard Gibbs free energy change versus temperature curves of the reaction (3.1) and (3.4) shown in Figure 3.12(a) and 3.12(c) are in good agreement with the experimental results. Reaction (3.4) has negative free energy values (approximately -200 kJ for the same temperatures) than that of (3.1), which means that SmB_6 formation is easier than that of LaB_6. These interpretations can be verified considering the longer reaction duration of LaB_6 (2 h 45 min) than that of SmB_6 (1 h 50 min) in the mechanochemical synthesis. Besides, CeB_6 formation has more positive standard Gibbs free energy values (Figure 3.13(a)) than those of LaB_6 (Figure 3.12(a)) and SmB_6 (Figure 3.12(c)), corresponding to the longer reaction duration (3 h).

SM images of the Sm_2O_3-B_2O_3-Mg powder blend and powders mechanochemically synthesized using a 10:1 BPR in a Spex^{TM} 8000D Mixer/Mill up to 5 h are given in Figures 4.49(a)-(h). As previously experienced in the SM images of the La_2O_3-B_2O_3-Mg and CeO_2-B_2O_3-Mg powders, the microstructure of the powders changes from

granular form to an agglomerated structure after the reduction reaction takes place (Figures 4.49(e)-(h)). Before the reaction, at the milling durations of 1 h, 1.5 h and 1 h 45 min, dark gray Mg particles containing white Sm_2O_3 and B_2O_3 particles dominate the image of the microstructure (Figures 4.49(b)-(d)). If all the SM images of the milled powders (Figures 4.49(b)-(h)) are compared with that of the as-blended one (Figure 4.49(a)), the significant difference in their microstructures provided with the effect of milling can be obviously remarked.

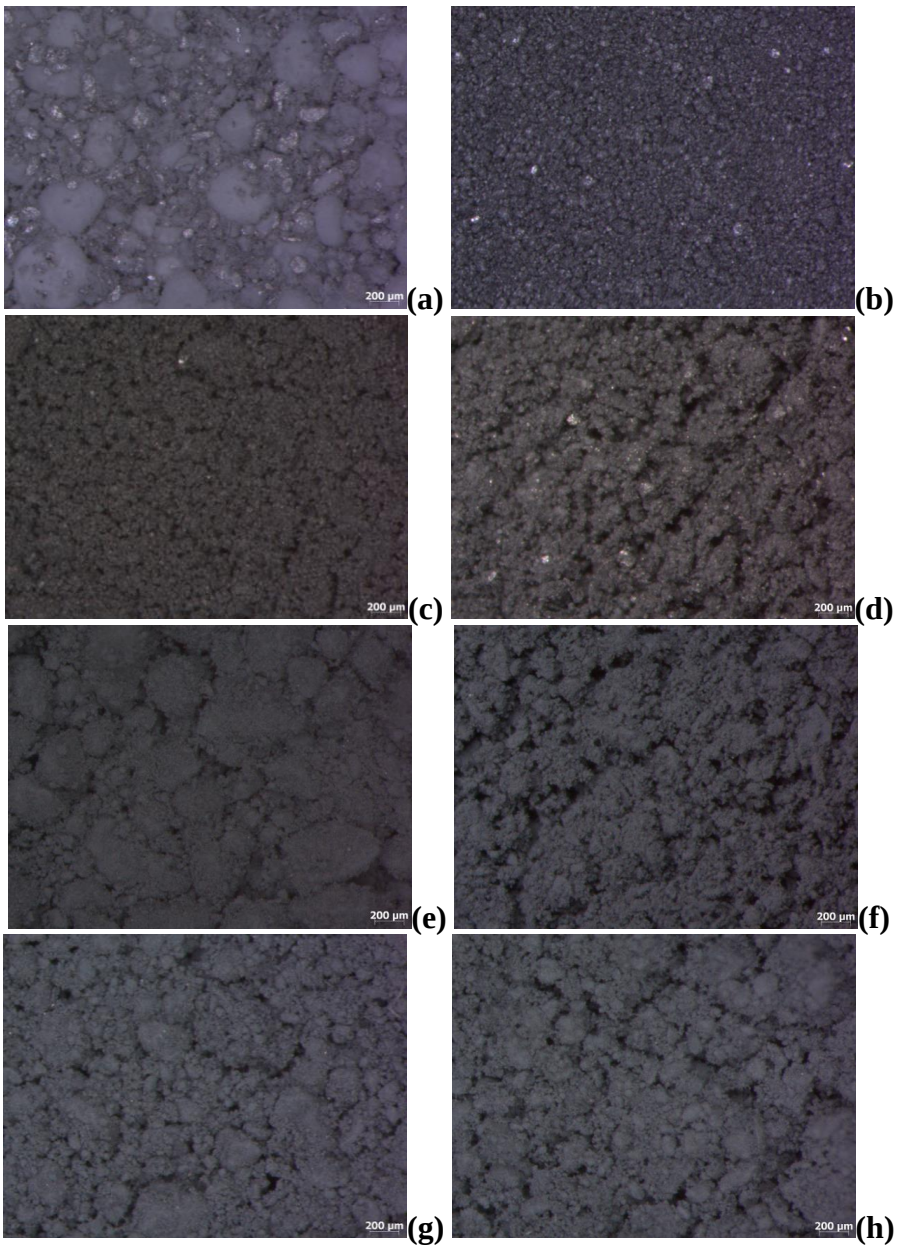

Figure 4.49 : SM images of the Sm_2O_3-B_2O_3-Mg powder blend and powders mechanochemically synthesized using a 10:1 BPR in a Spex^{TM} 8000D Mixer/Mill for different durations: (a) ab, (b) 1 h, (c) 1.5 h, (d) 1 h 45 min, (e) 1 h 50 min, (f) 2 h, (g) 3 h and (h) 5 h.

Figure 4.50(a) through (e) shows the DSC thermograms of the Sm_2O_3-B_2O_3-Mg powder blend and powders mechanochemically synthesized using a 10:1 BPR in a Spex^{TM} 8000D Mixer/Mill for different durations up to 5 h. According to Figure 4.50(a), as-blended powders have two endotherms peaking at about 650 and 775°C, corresponding to the melting of Mg and formations of Sm and Ce, respectively. The emergence of endothermic peaks is expected since there are Sm_2O_3, B_2O_3 and Mg phases in the composition (Figure 4.48(a)). The DSC curves of the powders milled for 1 h 50 min, 2, 3 and 5 h (Figure 4.50(b)-(e)) have not any endothermic and exothermic phases corresponding to a phase transformation and phase formation. XRD patterns of these milled powders indicate already SmB_6 and MgO phases. However, additional DSC analyses also show that there is no unreacted Mg in the reaction medium whose amount is under the detection limit of the XRD. Consequently, the reduction reaction is completed after 1 h 50 min milling.

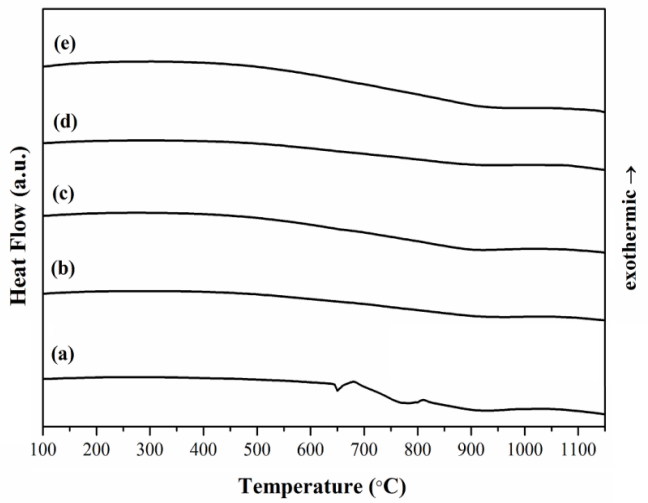

Figure 4.50 : DSC thermograms of the Sm_2O_3-B_2O_3-Mg powder blend and powders mechanochemically synthesized using a 10:1 BPR in a Spex^{TM} 8000D Mixer/Mill for different durations: (a) ab, (b) 1 h 50 min, (c) 2 h, (d) 3 h and (e) 5 h.

Figure 4.51(a)-(e) displays the XRD patterns of the mechanochemically synthesized Sm_2O_3-B_2O_3-Mg powders, using a 10:1 BPR in a Spex^{TM} 8000D Mixer/Mill for different durations, after DSC analyses up to 1150°C. All the milled (1 h, 1 h 45 min, 1 h 50 min, 2 and 5 h) and heated powders include SmB_6, $SmBO_3$, MgO and $Mg_3B_2O_6$ phases. However, the intensities of the SmB_6 phase are very low due to the favorable formation of $SmBO_3$ instead of SmB_6 under the effect of heating. It can be stated that the obtained SmB_6 and MgO phases after mechanochemical synthesis

process partially converts to $SmBO_3$, $Mg_3B_2O_6$ phases by heating. 1 h and 1 h 45 min milled powders, in which the reaction does not take place, have lower amounts of $SmBO_3$ phase than those of 1 h 50 min, 2 and 5 h milled powders in which the reaction takes place. Heating conducted on the milled powders after the reaction completed causes the partial decomposition of SmB_6 and MgO phase into SmB_6, $SmBO_3$, MgO and $Mg_3B_2O_6$ phases (Figure 4.51(c)-(e)) whereas that of before the reaction takes place enables the newly formation of SmB_6, $SmBO_3$, MgO and $Mg_3B_2O_6$ phases together in the structure (Figure 4.51(a) and (b)).

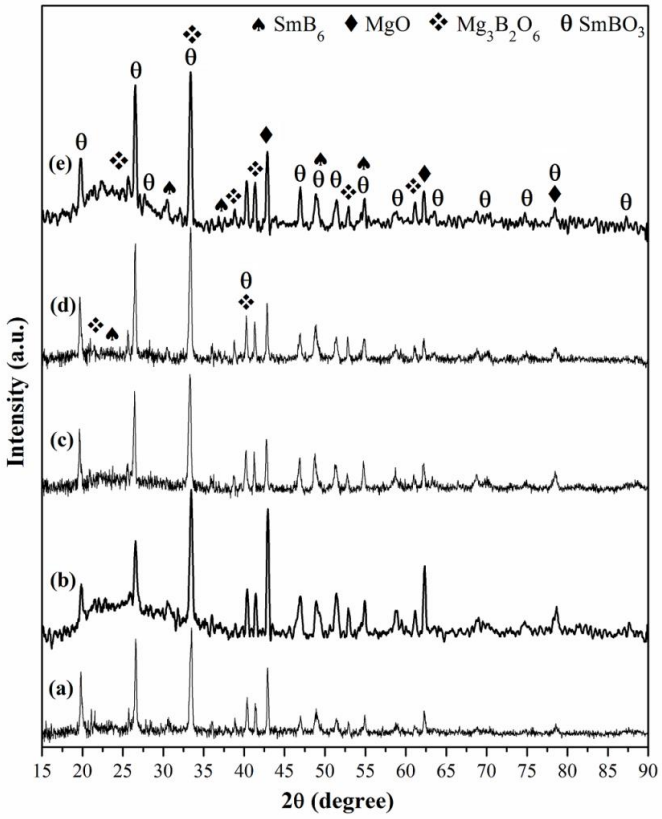

Figure 4.51 : XRD patterns of the mechanochemically synthesized Sm_2O_3-B_2O_3-Mg powders, using a 10:1 BPR in a Spex^{TM} 8000D Mixer/Mill for different durations, after DSC analyses up to 1150°C: (a) 1 h, (b) 1 h 45 min, (c) 1 h 50 min, (d) 2 h and (e) 5 h.

Figure 4.52(a)-(c) displays the XRD patterns of the laboratory-synthesized SmB_6 powders obtained after mechanochemical synthesis of the Sm_2O_3-B_2O_3-Mg powder blends using a 10:1 BPR in a Spex^{TM} 8000D Mixer/Mill for 3 and 5 h and leaching with 2 and 4 M HCl. As seen from Figure 4.52(a), 2 M HCl is not sufficient in removing the whole MgO content of the 3 h milled powders and leaving behind the SmB_6 phase without any contamination. The increase in the HCl concentration (from

2 to 4 M) provides the complete removal of the MgO phase and yields pure SmB_6 powders (Figure 4.52(b)). If Figure 4.52(b) is compared with Figure 4.52(c), it is clearly understood that there are no differences in the obtained SmB_6 powders. In other words, leaching conducted on the powders mechanochemically synthesized for 5 h does not create any differences in the resultant phases. Figure 4.52(d) is the XRD pattern of the commercial SmB_6 powders wich also contains $SmBO_3$ contamination. It can be said that the production method of commercial SmB_6 powders is not appropriate for obtaining pure products without unwanted $SmBO_3$ phase. The XRD pattern in Figure 4.52(d) shows that this commercial method can be an high-temperature production process, which is evaluated as that by means of XRD patterns in Figure 4.51(a)-(e). As Figure 4.52(b) and (c) are compared with Figure 4.52(d), it is understood that the purity of the laboratory-synthesized powders is higher than that of the commercial one. Consequently, mechanochemical synthesis process is more advantageous than all high-temperature methods.

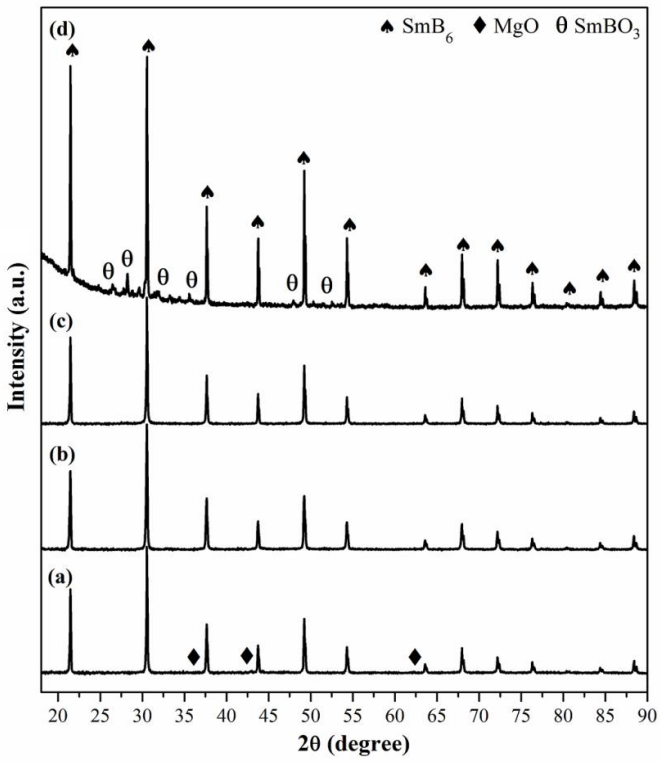

Figure 4.52 : XRD patterns of the laboratory-synthesized SmB_6 powders obtained after mechanochemical synthesis of the Sm_2O_3-B_2O_3-Mg powder blends using a 10:1 BPR in a Spex^{TM} 8000D Mixer/Mill (a) for 3 h and leaching with 2 M HCl, (b) for 3 h and leaching with 4 M HCl, (c) for 5 h and leaching with 4 M HCl and (d) XRD pattern of the commercial SmB_6 powders.

SM images of the laboratory-synthesized SmB_6 powders obtained after mechanochemical synthesis of the Sm_2O_3-B_2O_3-Mg powder blends using a 10:1 BPR in a Spex^{TM} 8000D Mixer/Mill for 3 and 5 h and leaching with 2 and 4 M HCl are given in Figure 4.53(a)-(c). As compatible with the XRD pattern in Figure 4.52(a), 3 h milled and 2 M HCl leached powders contain white MgO contaminations over the SmB_6 phase (Figure 4.53(a)). As HCl concentration increases to 4 M, white MgO particles completely disappear leaving behind only pure SmB_6 powders (Figure 4.53(b)). The only difference in the SM images of the 3 and 5 h milled and 4 M HCl leached powders is their particle size: particle size decreases in the 5 h milled powders (Figure 4.53(b) and (c)). Moreover, any contamination can not be observed in the SM images of these powders.

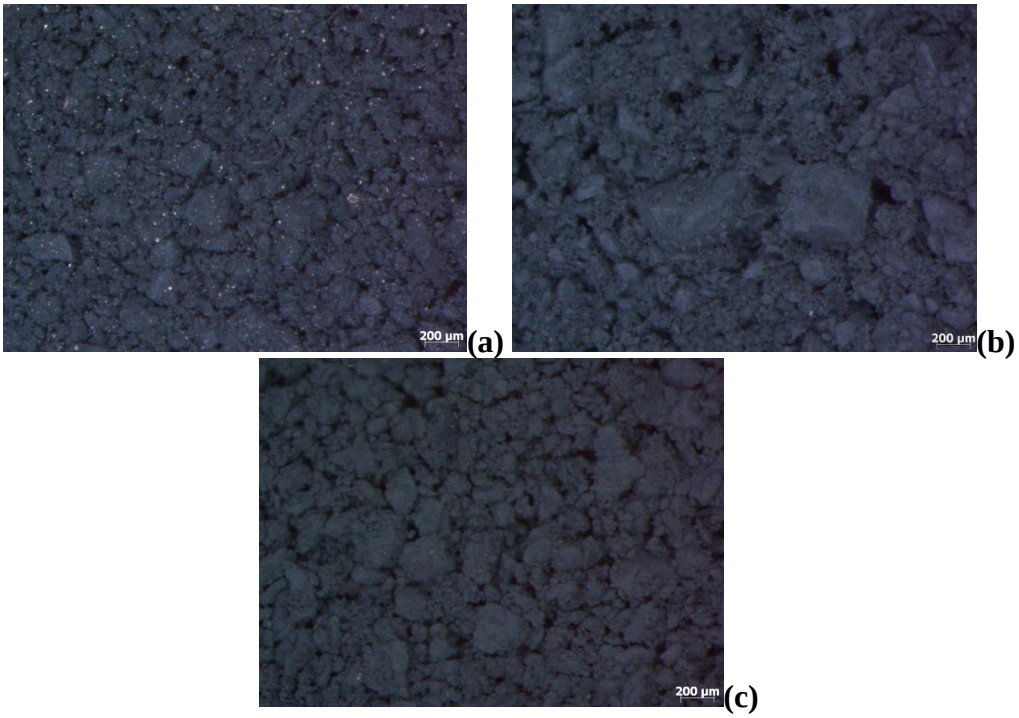

Figure 4.53 : SM images of the laboratory-synthesized SmB_6 powders obtained after mechanochemical synthesis of the Sm_2O_3-B_2O_3-Mg powder blends using a 10:1 BPR in a Spex^{TM} 8000D Mixer/Mill (a) for 3 h and leaching with 2 M HCl, (b) for 3 h and leaching with 4 M HCl and (c) for 5 h and leaching with 4 M HCl.

AAS analysis results of the supernatant liquids decanted from the mechanochemically synthesized powders are given in Table 4.5. When milling duration is kept constant at 3 h, increasing the HCl concentration increases the amounts of B (from 129.8 to 172.1 ppm), Fe (from 0.226 to 7.15 ppm) and Mg (from 4812.5 to 5337.5 ppm) dissolved in the solution. 4 M HCl leaching of the 5 h milled

powders results in higher B and Mg dissolution since the reactivities of the SmB_6 and MgO phases increase from 3 to 5 h milling due to the reduction in their average crystallite sizes. There is also a small increase in the amount of dissolved Fe from 3 h (7.15 ppm) to 5 h (7.81 ppm) milling.

Table 4.5 : AAS analyses of the supernatant liquids decanted from the powders mechanochemically synthesized from the Sm_2O_3-B_2O_3-Mg powder blends using a 10:1 BPR in a Spex^{TM} 8000D Mixer/Mill for different durations and leached at different HCl concentrations.

Milling Duration (h), HCl Concentration (M)	**Elements in the Supernatant Liquids (ppm)**		
	B	**Fe**	**Mg**
3 h, 2 M	129.8	0.226	4812.5
3 h, 4 M	172.1	7.15	5337.5
5 h, 4 M	246.4	7.81	9500

In a related study carried out on the low-temperature combustion synthesis of $Sm_{0.8}B_6$ nanocubes using samarium nitrate ($Sm(NO_3)_3.6H_2O$), carbohydrazide ($CO(NHNH_2)_2$) and B powders at 320°C, as-synthesized powders containing $Sm_{0.8}B_6$, high-temperature $SmBO_3$ and unreacted B phases were leached with diluted HCl and H_2SO_4 (Kanakala et al, 2010). After cleaning/washing process, $Sm_{0.8}B_6$ powders obtained in the presence of a small $SmBO_3$ residue with a process yield of 10 % (Kanakala et al, 2010). Similar to the leaching treatments, SmB_6 crystals, prepared by the high-temperature solution growth method at 1500°C under Ar atmosphere using Al as a solvent and Sm_2O_3 and B as initial materials, were seperated by dissolving the Al ingot in a diluted HCl solution (Trunov et al, 1991).

Figure 4.54(a), (b) and (c) are the SEM/EDS images of the laboratory-synthesized SmB_6 powders obtained via mechanochemical synthesis of the Sm_2O_3-B_2O_3-Mg powder blends using a 10:1 BPR in a Spex^{TM} 8000D Mixer/Mill for 5 h and leaching with 4 M HCl. Figure 4.54(a) represents round-shaped SmB_6 particles below 1 μm. The general EDS measurement taken from this region reveals that there is only Sm and Au in the microstructure since the utilized EDS is not appropriate for the determination of boron element. Au element is arised from the sputtered coating material present on the sample surface. Thus, only the SmB_6 phase is obtained without any contamination after leaching (Figure 4.54(a)). The SEM micrographs with higher magnifications in Figure 4.54(b) and (c) indicate that SmB_6 particles have sizes ranging between 20 and 500 nm. As seen clearly in Figure 4.54(b), SmB_6

particles with a size of about 20 nm cluster on the larger particles and this prevents their detection in lower magnifications, as experienced in Figure 4.54(a). The PSA graph in Figure 4.54(d) shows that the average particle size of SmB_6 powders is about 81 nm, which is in good agreement with the range determined by the SEM micrographs in Figure 4.54(b) and (c).

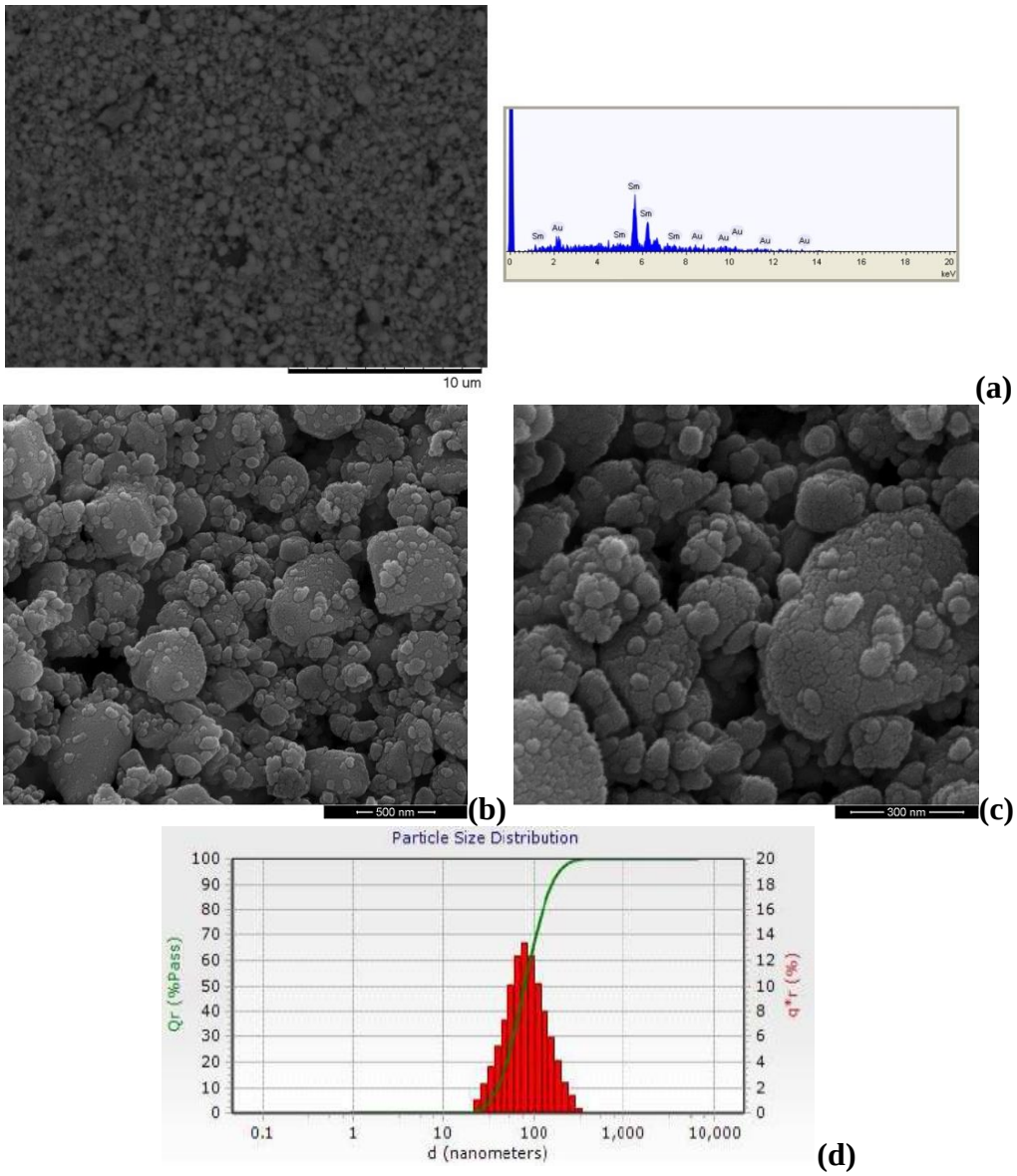

Figure 4.54 : SEM/EDS and PSA images of the laboratory-synthesized SmB_6 powders obtained via mechanochemical synthesis of the Sm_2O_3-B_2O_3-Mg powder blends using a 10:1 BPR in a Spex^{TM} 8000D Mixer/Mill for 5 h and leaching with 4 M HCl: (a) 10000X, (b) 120000X, (c) 240000X and (d) particle size measurement.

In overall, SmB_6 powders were obtained after mechanochemical synthesis of the Sm_2O_3-B_2O_3-Mg powder blends using a 10:1 BPR in a Spex^{TM} 8000D Mixer/Mill

for 5 h and after leaching with 4 M HCl, with an average particle size of 81 nm and a minimum purity of 99.99 %.

4.4 Properties of Pure LaB_6, CeB_6 and SmB_6 Powders

After mechanochemical synthesis and leaching processes by using several parameters, nano-sized LaB_6, CeB_6 and SmB_6 powders were obtained in high purity. Amongst all the synthesized powders, some of them were selected as the ideal/optimized products according to their consistent analysis results and to their convenient production procedure. These optimized products are: LaB_6 powders obtained after mechanochemical synthesis of the La_2O_3-B_2O_3-Mg powder blends using a 10:1 BPR in a Spex^{TM} 8000D Mixer/Mill for 5 h and leaching with 4 M HCl, LaB_6 powders obtained after mechanochemical synthesis of the La_2O_3-B_2O_3-Mg powder blends using a 10:1 BPR in a planetary ball mill for 30 h and leaching with 4 M HCl, CeB_6 powders obtained after mechanochemical synthesis of the CeO_2-B_2O_3-Mg powder blends using a 10:1 BPR in a Spex^{TM} 8000D Mixer/Mill for 5 h and leaching with 4 M HCl and SmB_6 powders obtained after mechanochemical synthesis of the Sm_2O_3-B_2O_3-Mg powder blends using a 10:1 BPR in a Spex^{TM} 8000D Mixer/Mill for 5 h and leaching with 4 M HCl. Consequently, there are four different laboratory-synthesized powders selected for the determination of their physical, microstructural and magnetic properties.

Figures 4.55(a), (b) and (c) are the the bright-field (BF), dark-field (DF) and selected area diffraction pattern (SADP, from the white-circled region of the BF image) micrographs taken from the laboratory-synthesized LaB_6 powders obtained after mechanochemical synthesis of the La_2O_3-B_2O_3-Mg powder blends using a 10:1 BPR in a Spex^{TM} 8000D Mixer/Mill for 5 h and leaching with 4 M HCl. For the TEM images in Figures 4.55(a)-(c), the objective aperture is on (011), camera length is 100 cm and zone axis is $[01\bar{1}]$. Figure 4.55(a) is a BF image taken from a general region showing agglomerates comprising polygonal/spheroidal-shaped particles in sizes varying between 75 and 300 nm. Spheroidal-shaped LaB_6 crystallites ranging in sizes between 25 and 65 nm can be unambiguously identified from the micrographs in Figures 4.55(b) and (c). These findings conform well with the XRD pattern (Figure 4.28(c)), AAS results (Table 4.2), SEM/EDS and PSA analyses (Figure 4.30(a)-(d)).

The average crystallite size reduction from 5 h milled powders to leached powders was also supported by the SEM (Figure 4.30(a)-(c)) and TEM micrographs (Figure 4.55(a)-(c)). As already known, the selected area diffraction spot pattern without any additional diffraction from the nearest atom indicates that the material have a single-crystalline behavior. Although the SADP in Figure 4.55(c) is a spot pattern, there are some additional diffractions originated from other planes between the two distinct spots. On the basis of Figure 4.55(a)-(c), it can be said that the synthesized LaB_6 is a polycrystalline material. However, the specific region, where the aperture is on, is a single crystal.

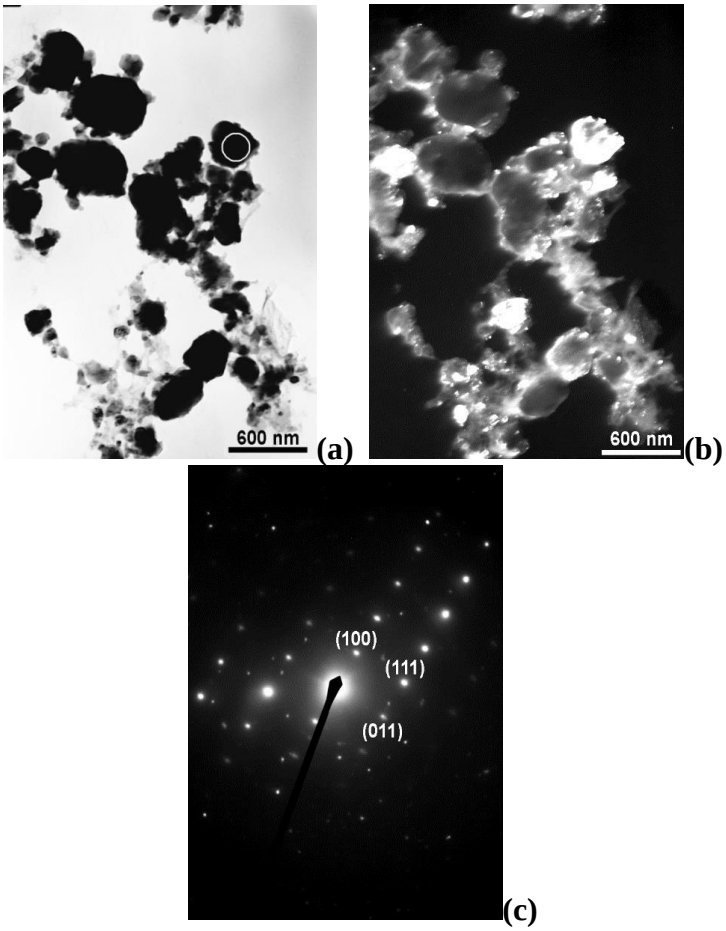

Figure 4.55 : TEM micrographs of the laboratory-synthesized LaB_6 powders obtained after mechanochemical synthesis of the La_2O_3-B_2O_3-Mg powder blends using a 10:1 BPR in a Spex^{TM} 8000D Mixer/Mill for 5 h and leaching with 4 M HCl: (a) Bright-field (BF) image, (b) Dark-field (DF) image and (c) Selected area diffraction pattern (SADP) of LaB_6 particles.

Figures 4.56(a), (b) and (c) are the BF, DF and SADP (from the white-circled region of the BF image) micrographs taken from the same LaB_6 powders. For the TEM

micropraphs, objective aperture is on $(0\,\bar{2}\,\bar{1})$, camera length is 100 cm and zone axis is $[01\bar{2}]$. Figure 4.56(a) is a BF image taken from a general region showing agglomerates containing polygonal/spheroidal-shaped particles in sizes varying between 75 and 350 nm. Spheroidal-shaped LaB_6 crystallites ranging in sizes between 10 and 75 nm can be clearly identified from the micrographs in Figures 4.56(b) and (c).

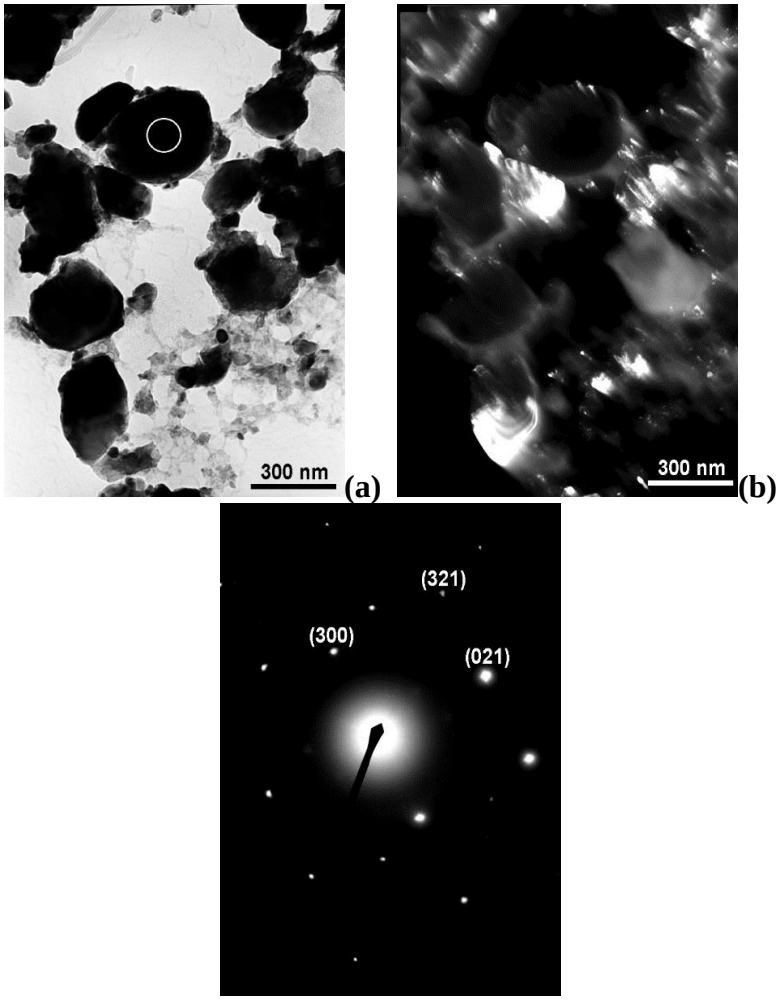

Figure 4.56 : TEM micrographs of the laboratory-synthesized LaB_6 powders obtained after mechanochemical synthesis of the La_2O_3-B_2O_3-Mg powder blends using a 10:1 BPR in a Spex^{TM} 8000D Mixer/Mill for 5 h and leaching with 4 M HCl: (a) BF image, (b) DF image and (c) SADP of the LaB_6 particles.

The BF images, corresponding SADP micrographs and EDS measurement of the laboratory-synthesized LaB_6 powders obtained via mechanochemical synthesis of the La_2O_3-B_2O_3-Mg powder blends using a 10:1 BPR in a planetary ball mill for 30 h and leaching with 4 M HCl are given in Figures 4.57(a)-(e).

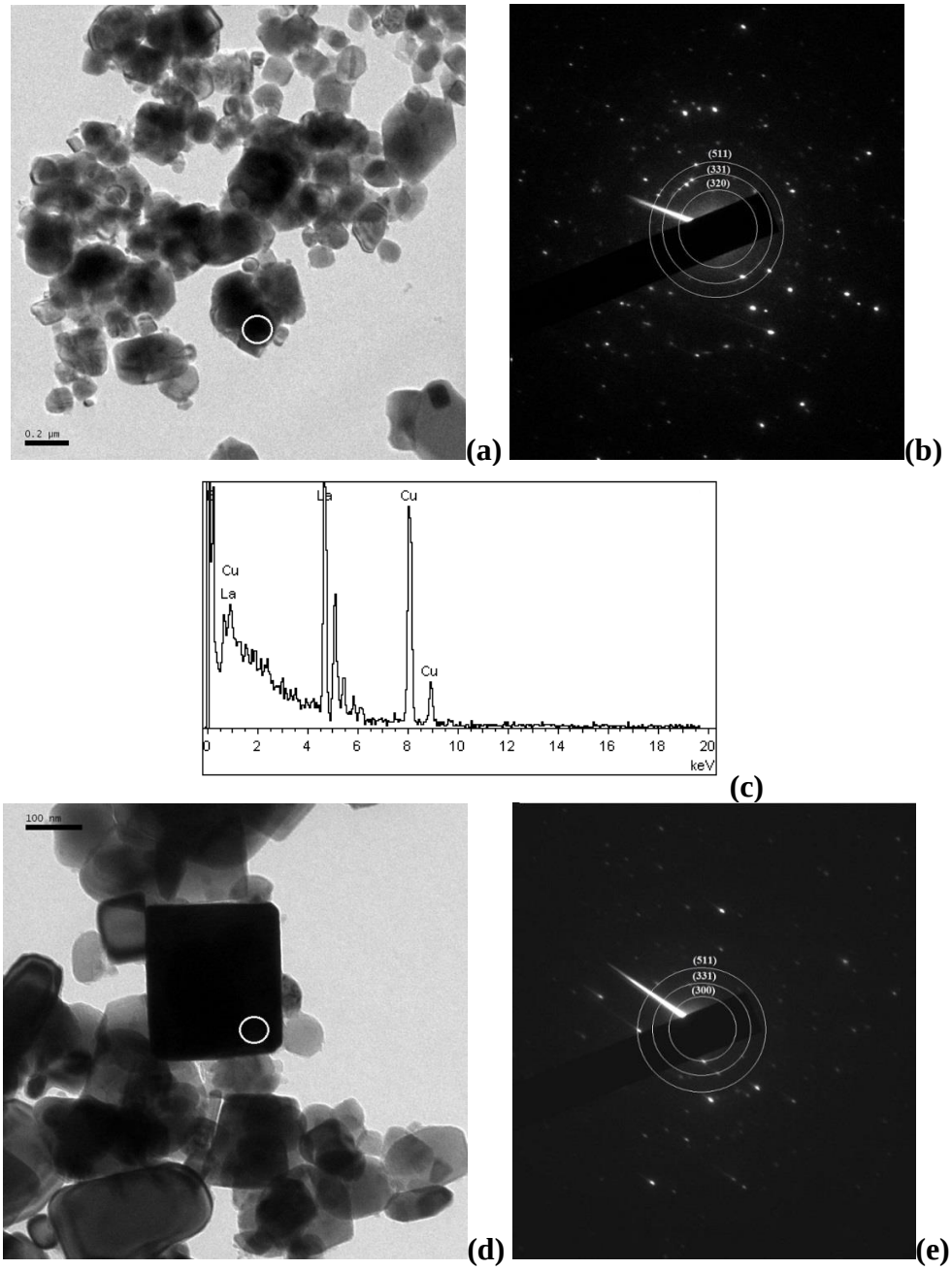

Figure 4.57 : TEM micrographs of the laboratory-synthesized LaB_6 powders via mechanochemical synthesis of the La_2O_3-B_2O_3-Mg powder blends using a 10:1 BPR in a planetary ball mill for 30 h and leaching with 4 M HCl: (a) BF image, (b) its SADP revealing the LaB_6 particles, (c) general EDS analysis, (d) BF image and (e) its SADP revealing the LaB_6 particles (Objective aperture is on (001) and camera length is 100 cm).

For the TEM micrographs in Figure 4.57(a), (b), (d) and (e), objective aperture is on (001) and camera length is 100 cm. Figure 4.57(a) is a BF image showing polygonal/spheroidal-shaped crystallites varying in sizes between 50 and 200 nm. Figure 4.57(b) is the corresponding SADP micrograph of the BF image in Figure

4.57(a), indicating the presence of polycrystalline LaB_6 particles. EDS measurement in Figure 4.57(c) reveals that there is 70.20±1.30 wt.% La and 29.80±0.75 wt.% B in the composition of LaB_6 phase, which is consistent with the amounts of elements in the stoichiometric phase. The detected Cu element arises from the copper grid on which the powders were supported. Figure 4.57(d) is a BF image showing rectangular and equiaxed-shaped particles varying in sizes between 50 and 225 nm. Corresponding SADP micrograph (Figure 4.57(e)) of the BF image in Figure 4.57(d) represents the presence of polycrystalline LaB_6 particles.

Figures 4.58(a)-(c) are the TEM/EDS micrographs of the laboratory-synthesized CeB_6 powders obtained after mechanochemical synthesis of the CeO_2-B_2O_3-Mg powder blends using a 10:1 BPR in a Spex^{TM} 8000D Mixer/Mill for 5 h and leaching with 4 M HCl.

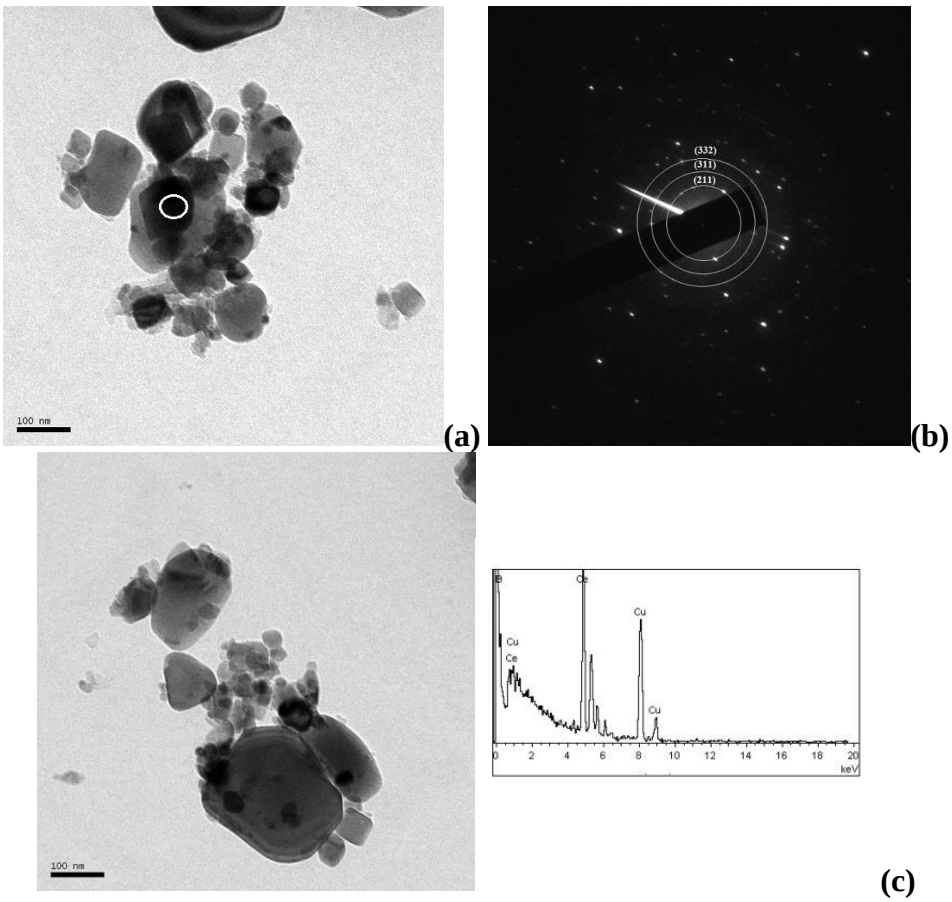

Figure 4.58 : TEM micrographs of the laboratory-synthesized CeB_6 powders via mechanochemical synthesis of the CeO_2-B_2O_3-Mg powder blends using a 10:1 BPR in a Spex^{TM} 8000D Mixer/Mill for 5 h and leaching with 4 M HCl: (a) BF image, (b) its SADP revealing the CeB_6 particles and (c) BF image with general EDS analysis (Objective aperture is on (001) and camera length is 100 cm).

For the TEM micrographs in Figure 4.58(a)-(c), objective aperture is on (001) and camera length is 100 cm. Figure 4.58(a) is a BF image showing equiaxed-shaped particles varying in sizes between 75 and 100 nm and Figure 4.58(b) is the corresponding SADP micrograph of this BF image, indicating the polycrystalline CeB_6 particles. Figure 4.58(c) is a BF image representing irregular-shaped particles varying in sizes between 50 and 150 nm. The general EDS measurement taken on this BF image reveals out that the powders have the composition of 71.79±0.93 wt.% Ce and 28.21±0.36 wt.% B.

Figures 4.59(a)-(c) demonstrate the TEM/EDS micrographs of the laboratory-synthesized SmB_6 powders obtained after mechanochemical synthesis of the Sm_2O_3-B_2O_3-Mg powder blends using a 10:1 BPR in a Spex^{TM} 8000D Mixer/Mill for 5 h and leaching with 4 M HCl.

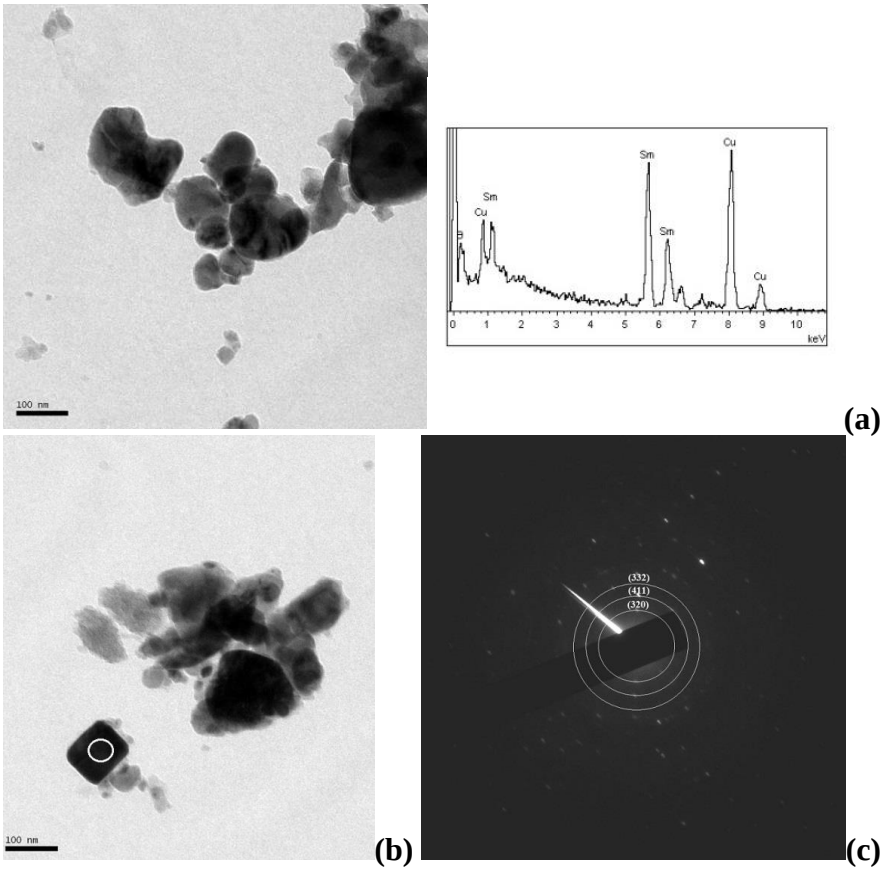

Figure 4.59 : TEM micrographs of the laboratory-synthesized SmB_6 powders via mechanochemical synthesis of the Sm_2O_3-B_2O_3-Mg powder blends using a 10:1 BPR in a Spex^{TM} 8000D Mixer/Mill for 5 h and leaching with 4 M HCl: (a) BF image with general EDS analysis, (b) BF image and (c) its SADP revealing the SmB_6 particles (Objective aperture is on (001) and camera length is 100 cm).

Figure 4.59(a) is a BF image representing equiaxed and round-shaped particles ranging in sizes between 50 and 200 nm. The general EDS measurement taken on this BF image reveals that the powders have the composition of 75.63±1.72 wt.% Sm and 24.37±1.36 wt.% B. The BF image in Figure 4.59(b) contains irregular-shaped particles owning sizes between 20-100 nm. Figure 4.59(c) is the corresponding SADP micrograph of this BF image. It indicates that the region where the TEM analysis was made is polycrystalline.

On the basis of the TEM analyses given in Figure 4.55 through Figure 4.59, the calculated lattice parameters of the laboratory-synthesized LaB_6, CeB_6 and SmB_6 are respectively 0.415, 0.413 and 0.413 nm which are in good agreement with the theoretical lattice parameters (0.416, 0.414 and 0.413 nm for LaB_6, CeB_6 and SmB_6) present in the ICDD cards.

The density values of the laboratory-synthesized LaB_6, CeB_6 and SmB_6 powders are given in Table 4.6. For the comparison, the density values of the commercial powders are also presented in Table 4.6. The theoretical densities of LaB_6, CeB_6 and SmB_6 are 4.7, 4.79 and 5.07 g/cm^3, respectively. The obtained LaB_6 powders originated from the mechanochemical synthesis in Spex^{TM} 8000D Mixer/Mill have the density value of 4.58±0.007 g/cm^3 whereas that of originated from the synthesis in planetary ball mill has the density value of 4.47±0.006 g/cm^3. A maximum density difference of 0.24 g/cm^3 was found between the laboratory-synthesized and commercial LaB_6 powders, which can be accepted as a tolerable value. The density value of the laboratory-synthesized CeB_6 powders is 4.77±0.009 g/cm^3. This value is close to the density value of commercial one (4.81±0.008 g/cm^3). The difference in their density values is only 0.04 g/cm^3.

Table 4.6 : Density values of the laboratory-synthesized and commercial LaB_6, CeB_6 and SmB_6 powders.

Sample	Density (g/cm^3)
LaB_6 - synthesized in Spex^{TM} 8000D Mixer/Mill	4.58 ± 0.007
LaB_6 - synthesized in planetary ball mill	4.47 ± 0.006
Laboratory-synthesized CeB_6	4.77 ± 0.009
Laboratory-synthesized SmB_6	5.14 ± 0.002
Commercial LaB_6	4.71 ± 0.009
Commercial CeB_6	4.81 ± 0.008
Commercial SmB_6	5.10 ± 0.006

The laboratory-synthesized SmB_6 powders have the density value of 5.14±0.002 g/cm^3 whereas the density value of commercial SmB_6 is 5.10±0.006 g/cm^3. Lundström (1985) mentioned in a related study on rare-earth hexaborides that the shifts in the lattice parameters can disturb the density measurements. In other words, a very small shift (0.001 nm) in the lattice parameters of the laboratory-synthesized LaB_6 and CeB_6 powders can cause a decrease in their densities (about 0.24 for LaB_6 g/cm^3 and 0.04 g/cm^3 for CeB_6) than those of commercial ones. However, the density values of the laboratory-synthesized and commercial LaB_6, CeB_6 and SmB_6 powders are more or less the same.

Table 4.7 shows the surface area values of the laboratory-synthesized and commercial LaB_6, CeB_6 and SmB_6 powders. The obtained LaB_6 powders originated from the mechanochemical synthesis in Spex^{TM} 8000D Mixer/Mill have the surface area value of 17.84 m^2/g whereas that of originated from the synthesis in planetary ball mill has the values of 11.11 m^2/g. These values are consistent with their average particle sizes measured respectively as 62 and 74 nm. The lower value of average particle size results in a higher value of surface area.

Laboratory-synthesized CeB_6 and SmB_6 powders have the surface area value of 13.45 and 8.70 m^2/g, respectively. The surface areas of the laboratory-sythesized LaB_6, CeB_6 and SmB_6 powders are very high since they have nano-scale particles. However, commercial LaB_6, CeB_6 and SmB_6 powders have the surface area values of 1.06, 0.48 and 0.68 m^2/g due to their micron-scale particles.

Table 4.7 : Surface area values of the laboratory-synthesized and commercial LaB_6, CeB_6 and SmB_6 powders.

Sample	Surface Area (m^2/g)
LaB_6 - synthesized in Spex^{TM} 8000D Mixer/Mill	17.84
LaB_6 - synthesized in planetary ball mill	11.11
Laboratory-synthesized CeB_6	13.45
Laboratory-synthesized SmB_6	8.70
Commercial LaB_6	1.06
Commercial CeB_6	0.48
Commercial SmB_6	0.68

Figures 4.60(a)-(g) represent the magnetic measurements of the laboratory-synthesized and commercial LaB_6, CeB_6 and SmB_6 powders at room temperature. The remaining Fe impurity in terms of ppm can be also determined from the magnetic measurements, if the magnetic behavior of the material is ferromagnetic.

According to the Figures 4.60(a)-(c), the obtained LaB_6 powders originated from the mechanochemical synthesis in Spex^{TM} 8000D Mixer/Mill are paramagnetic (Figure 4.60(a)), the obtained LaB_6 powders originated from the mechanochemical synthesis in planetary ball mill are diamagnetic (Figure 4.60(b)) and commercial LaB_6 powders are ferromagnetic (Figure 4.60(c)). As seen Figures 4.60(d) and (e), the laboratory-synthesized CeB_6 powders are paramagnetic whereas commercial powders are ferromagnetic. Figures 4.60(f) and (g) respectively show that the laboratory-synthesized and commercial SmB_6 powders are paramagnetic and ferromagnetic. As previously reported in the literature, rare-earth hexaborides displays an amazing diversification in magnetic properties (Lundström, 1985). There are diamagnetic, Pauli-paramagnetic, ferromagnetic, anti-ferromagnetic and more complex spin-ordered hexaborides. Most of the magnetic properties are considered as very sensitive to the number of valence electrons available in the valence band: In other words, properties of the rare-earth hexaborides strongly depend on stoichiometry (RE/B ratio), impurity and homogeneity ranges. Thus, there are inconsistencies amongst the numerous reported magnetic investigations of rare-earth hexaborides due to the differences in compositon arising from the preparation method (Lundström, 1985).

In overall, commercial LaB_6, CeB_6 and SmB_6 powders have an amount of Fe impurity in the order of ppm in their structures whereas laboratory-synthesized powders do not include any contamination (Figure 4.60). The higher density values of the commercial powders can be arised from the Fe impurity (in the order of ppm) whose density is 7.874 g/cm^3.

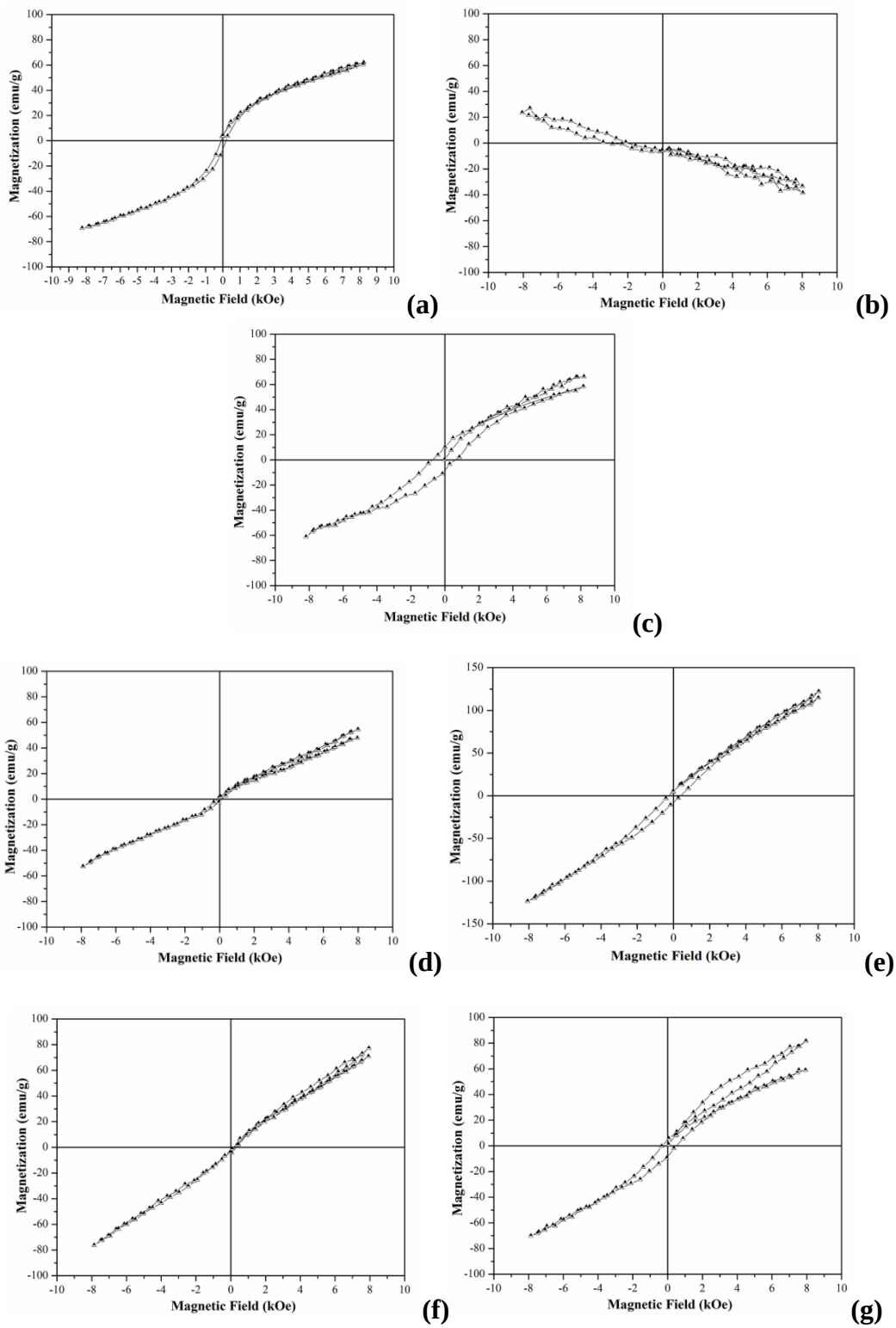

Figure 4.60 : Magnetic measurements of the laboratory-synthesized and commercial LaB_6, CeB_6 and SmB_6 powders: (a) laboratory-synthesized LaB_6 in Spex^{TM} 8000D Mixer/Mill, (b) laboratory-synthesized LaB_6 in planetary ball mill, (c) commercial LaB_6, (d) laboratory-synthesized CeB_6, (e) commercial CeB_6, (f) laboratory-synthesized SmB_6 and (g) commercial SmB_6.

4.5 Properties of LaB_6, CeB_6 and SmB_6 Sintered Compacts

After mechanochemical synthesis and leaching processes, LaB_6, CeB_6 and SmB_6 powders were obtained in high purity (≥ 99.99 %) with nano-scaled average particle sizes. These powders were sintered at 1700°C for 5 h subsequent to the cold pressing. In order to determine the probable contaminations occurred during sintering, sintered compacts were subjected to the XRD analyses. Figure 4.61(a)-(g) illustrates the XRD patterns of the bulk samples originated from the laboratory-synthesized and commercial LaB_6, CeB_6 and SmB_6 powders. Based on the XRD patterns in Figure 4.61(a)-(g), it can be said that there is no contamination in the microstructures of the bulk samples: pure LaB_6, CeB_6 and SmB_6 sintered compacts were obtained after sintering.

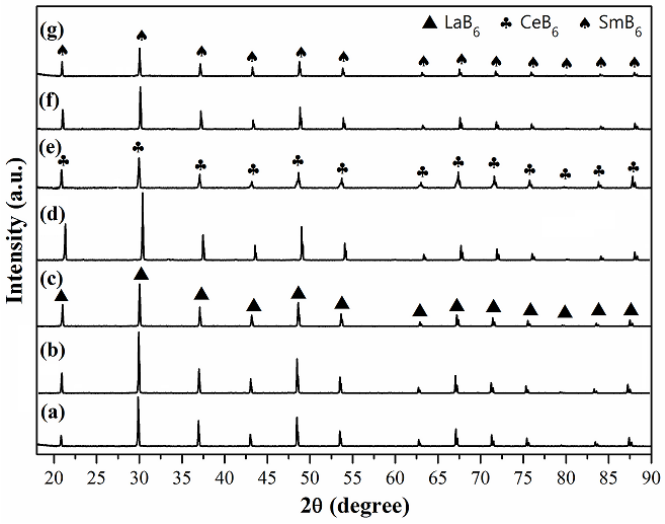

Figure 4.61 : XRD patterns of the bulk samples originated from the laboratory-synthesized and commercial LaB_6, CeB_6 and SmB_6 powders: (a) laboratory-synthesized LaB_6 in Spex^{TM} 8000D Mixer/Mill, (b) laboratory-synthesized LaB_6 in planetary ball mill, (c) commercial LaB_6, (d) laboratory-synthesized CeB_6, (e) commercial CeB_6, (f) laboratory-synthesized SmB_6 and (g) commercial SmB_6.

The electrical resistivity values of the bulk samples originated from the laboratory-synthesized and commercial LaB_6, CeB_6 and SmB_6 powders are given in Table 4.8. As already known, the higher electrical resistivity, the lower electrical conductivity. At first view, it can be easily seen from Table 4.8 that electrical resistivity values of the bulk samples originated from the laboratory-synthesized powders are higher than those of originated from commercial powders. LaB_6 sintered compact originated

from the powders mechanochemically synthesized in Spex^{TM} 8000D Mixer/Mill has the electrical resistivity value of 37.00±2.50 μΩ.cm whereas that of synthesized in planetary ball mill has the value of 35.20±1.40 μΩ.cm. Changing the type of mill does not result in a very significant difference in the electrical conductivity of the LaB_6 bulks. The electrical resistivities of the CeB_6 sintered compacts originated from laboratory-synthesized and commercial powders are respectively 57.50±3.80 and 41.50±3.20 μΩ.cm. Moreover, SmB_6 sintered compacts originated from laboratory-synthesized and commercial powders have the respective electrical resistivity values of 211.00±4.50 and 192.30±5.10 μΩ.cm. The lower electrical resistivities of the commercial LaB_6, CeB_6 and SmB_6 bulks are probably due to the Fe impurities present in their compositions in the order of ppm. Since Fe has the electrical resitivity value of about 10 μΩ.cm, the presence of it, even if in very small amounts, can decrease their resistivity values and hence positively contribute into the electrical conduction. Moreover, electrical resistivity values increase from LaB_6 to SmB_6 both in the laboratory-synthesized and commercial origins. This increase is also consistent with the reported values of electrical resistivity given in Table 2.1. Weimer (1977) reported the electrical resistivity values of some borides such as CrB (45.5 μΩ.cm), CrB_2 (30 μΩ.cm), HfB_2 (10.6 μΩ.cm), NbB_2 (25.7 μΩ.cm), TaB_2 (32.5 μΩ.cm), TiB_2 (9 μΩ.cm), VB (35 μΩ.cm), VB_2 (22.7 μΩ.cm), ZrB_2 (9.7 μΩ.cm). As compared with the values in Table 4.8, it can be stated that LaB_6 and CeB_6 have approximate electrical resistivity values with those excluding IVB group metal diborides (TiB_2, ZrB_2 and HfB_2).

Table 4.8 : Electrical resistivity values of the bulk samples originated from the laboratory-synthesized and commercial LaB_6, CeB_6 and SmB_6 powders.

Sample	ρ (μΩ.cm)
LaB_6 - synthesized in Spex^{TM} 8000D Mixer/Mill	37.00 ± 2.50
LaB_6 - synthesized in planetary ball mill	35.20 ± 1.40
Laboratory-synthesized CeB_6	57.50 ± 3.80
Laboratory-synthesized SmB_6	211.00 ± 4.50
Commercial LaB_6	32.60 ± 2.10
Commercial CeB_6	41.50 ± 3.20
Commercial SmB_6	192.30 ± 5.10

Lundström (1985) reported that the rare-earth hexaborides exhibits an incredible variation in electrical properties. There are normal electrical conductor,

superconductor and semiconductor hexaborides. Most of the electrical properties are very sensitive to the number of valence electrons available in the valence band and depend on the stoichiometry, impurity and homogeneity ranges of the materials. Moreover, the electrical resistivity values of rare-earth hexaborides may differ because of the differences in compositon arising from the synthesis method (Lundström, 1985). For example, the resistivity of the crystals obtained by the flux method is higher than that of floating zone method due to the deviation in the stoichiometric value of B/Ce and the presence of uncontrolled Al impurity and due to the higher oxygen content (Petrosyan et al, 2012). Electrical resistivity of CeB_6 bulk prepared from nanopowders (50-100 nm) by SPS method at 1550°C under 50 MPa increased from 36.34 to 60.54 μΩ.cm with increasing temperature from 25 to 500°C, indicating a metallic conducting behavior (Bao et al, 2011a). Besides, CeB_6 has approximately 20 μΩ.cm higher electrical resistivity values than those of LaB_6 in the temperature range between 25 and 500°C, pointing out a more suitable direct heating cathode (Bao et al, 2011a).

Table 4.9 shows the density values of the bulk samples originated from the laboratory-synthesized and commercial LaB_6, CeB_6 and SmB_6 powders. Both Archimedes method-based and gas pycnometer-based densities are given in Table 4.9. The densities measured by Archimedes method are lower than those measured by gas pycnometer. However, both of them exhibit the same tendency in the density values: the density increases from LaB_6 to SmB_6 bulks and laboratory-synthesized bulks have approximate density values with those of commercial ones. Since the densities measured by using gas pycnometer have some values over the theoretical density of LaB_6, CeB_6 and SmB_6, the relative density values were calculated according to the Archimedes densities. Amongst the bulk samples originated from the laboratory-synthesized LaB_6, CeB_6 and SmB_6 powders, a maximum relative density of 96.80 % is reached by the cold-pressing and conventional sintering methods. Moreover, LaB_6 bulks originated from the mechanochemical synthesis in Spex^{TM} 8000D Mixer/Mill have higher relative density value (96.80 %) than that of synthesized in planetary ball mill (94.25 %). It means that high specific surface areas of the nano-scale particles (17.84 m^2/g for Spex^{TM} 8000D Mixer/Mill and 11.11 m^2/g for planetary ball mill) resulted from the surface damage during ball milling process provides accelerating densification.

Bao et al (2011a) reported that spark plasma sintering of CeB_6 nanopowders and coarse powders placed into a graphite die at a temperature of 1550°C and at a pressure of 50 MPa without holding time respectively results in a relative density of 99.1 % and 76.7 %. In an earlier study related with the conventional hot pressing of rare-earth hexaborides, the sintering temperature and the relative density were respectively reported as 1900°C and 90 %, indicating that this method is not sufficient to obtain full densification (Bao et al, 2011a).

Table 4.9 : Density values of the bulk samples originated from the laboratory-synthesized and commercial LaB_6, CeB_6 and SmB_6 powders.

Sample	Density (g/cm^3)		Relative Density (%)
	Gas Pycnometer	Archimedes Method	
LaB_6 - synthesized in Spex^{TM} 8000D Mixer/Mill	4.71 ± 0.004	4.55	96.80
LaB_6 - synthesized in planetary ball mill	4.70 ± 0.003	4.43	94.25
Laboratory-synthesized CeB_6	4.83 ± 0.003	4.56	95.20
Laboratory-synthesized SmB_6	5.11 ± 0.004	4.91	96.84
Commercial LaB_6	4.69 ± 0.005	4.60	97.87
Commercial CeB_6	4.82 ± 0.003	4.58	95.61
Commercial SmB_6	5.22 ± 0.003	4.94	97.44

Table 4.10 shows the microhardness values of the bulk samples originated from the laboratory-synthesized and commercial LaB_6, CeB_6 and SmB_6 powders. LaB_6 sintered compact originated from the powders mechanochemically synthesized in Spex^{TM} 8000D Mixer/Mill has the microhardness value of 12.75±0.70 GPa whereas that of synthesized in planetary ball mill has the value of 13.35±0.40 GPa. The microhardness values of the CeB_6 and SmB_6 bulks originated from laboratory-synthesized powders are 11.65±0.50 and 10.08±0.80 GPa, respectively. All the bulk samples originated from laboratory-synthesized powders have approximately two times higher hardness values than those of originated from commercial powders. In a previous investigation carried out on the TiB_2 ceramics prepared via pressureless sintering, a microhardness value of 18.46±0.40 GPa was achieved with the addition of 10 wt.% Co sintering aid and after 9 h mechanical alloying (Ağaoğulları et al, 2011). Compared the hardness values of LaB_6, CeB_6 and SmB_6 with that of Co incorporated TiB_2, it can be stated that the achieved microhardness values are enough high for the utilized consolidation process.

In a related study carried out on rare-earth hexaborides, the hardness of the LaB_6, CeB_6 and SmB_6 crystals prepared by traveling solvent floating zone method from their oxides and boron powders was found as 1160, 1090 and 940 kg/mm^2 at 900°C (Otani et al, 2000). Polycrystalline bulk CeB_6 cathodes fabricated by SPS method using optimum process parameters (1500°C, 50 MPa and 5 min) have a relative density of 99.61 % and a hardness value of 2051 kg/mm^2 (Zhou et al, 2009). According to a different investigation, hardness values of the bulk LaB_6, CeB_6 and SmB_6 samples were respectively reported as 2600, 2550 and 2520 HV_{50} (Mitterer et al, 1996). Vickers hardness values of the CeB_6 bulks sintered from nanopowders and coarse powders by SPS (at 1550°C under 50 MPa) were respectively found as 2160 and 1435 kg/mm^2 which was attributed to the higher density, finer particle size and more homogeneous microstructure provided by the usage of nanopowders (Bao et al, 2011a). Consequently, the hardness values of the LaB_6, CeB_6 and SmB_6 are very different with each other since hardness strongly depends on the synthesis method and consolidation techniques.

Table 4.10 : Microhardness values of the bulk samples originated from the laboratory-synthesized and commercial LaB_6, CeB_6 and SmB_6 powders.

Sample	$HV_{0.1}$ (GPa)
LaB_6 - synthesized in Spex^{TM} 8000D Mixer/Mill	12.75 ± 0.70
LaB_6 - synthesized in planetary ball mill	13.35 ± 0.40
Laboratory-synthesized CeB_6	11.65 ± 0.50
Laboratory-synthesized SmB_6	10.08 ± 0.80
Commercial LaB_6	5.20 ± 0.20
Commercial CeB_6	6.59 ± 0.35
Commercial SmB_6	6.47 ± 0.55

Figure 4.62 and Figure 4.63 respectively illustrate the surface roughness and friction coefficient values of the bulk samples originated from the laboratory-synthesized and commercial LaB_6, CeB_6 and SmB_6 powders. Amongst the bulk samples originated from the laboratory-synthesized powders, LaB_6 synthesized in planetary ball mill has the lowest surface roughness value (0.115 μm) whereas CeB_6 synthesized in Spex^{TM} 8000D Mixer/Mill has the highest value (0.605 μm). Bulk samples originated from commercial LaB_6, CeB_6 and SmB_6 powders have surface roughness values over 2.3 μm. The order of surface roughness values are very different from each other (Figure 4.62). It was reported in a related study that surfaces of the CeB_6 crystals

grown by flux and floating zone methods are considerably different. The roughness amplitudes of the samples obtained by floating zone method are higher than those of obtained by flux method (Petrosyan et al, 2012). Friction coefficients of the bulk samples originated from the laboratory-synthesized powders have lower than those of originated from commercial powders (Figure 4.63), as compatible with the surface roughness values in Figure 4.62. The higher values in the surface roughness yield the higher values in the friction coefficient.

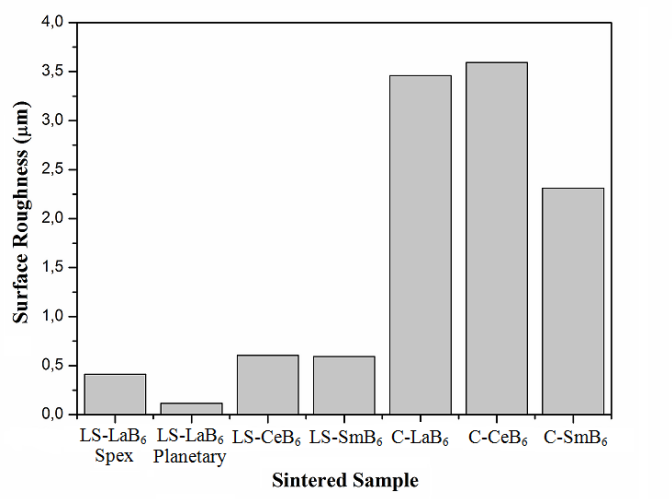

Figure 4.62 : Surface roughness values of the bulk samples originated from the laboratory-synthesized and commercial LaB_6, CeB_6 and SmB_6 powders.

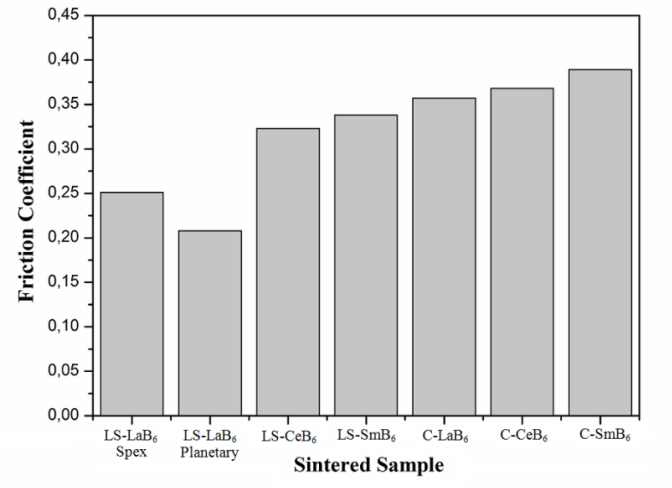

Figure 4.63 : Friction coefficients of the bulk samples originated from the laboratory-synthesized and commercial LaB_6, CeB_6 and SmB_6 powders.

Table 4.11 shows the wear volume loss values of the bulk samples originated from the laboratory-synthesized and commercial LaB_6, CeB_6 and SmB_6 powders, in terms

of wear width, wear depth, wear area, wear volume loss and relative wear volume loss. According to Table 4.10, SmB_6 bulk originated from the commercial powders has the highest wear volume loss as 0.2627 mm^3 amongst all the sintered samples and its relative wear volume loss value is regarded as 100 %. LaB_6 and CeB_6 bulks originated from the commercial powders have the wear volume loss value of 97.64 and 98.51 %, respectively. Amongst the bulks prepared from laboratory-synthesized LaB_6, CeB_6 and SmB_6 powders, SmB_6 has the highest wear volume loss (7.35).

Table 4.11 : Wear volume loss values of the bulk samples originated from the laboratory-synthesized and commercial LaB_6, CeB_6 and SmB_6 powders.

Sample	Width (μm)	Depth (μm)	Wear Area (μm^2)	Volume Loss (mm^3)	Relative Volume Loss (%)
LaB_6 - synthesized in Spex^{TM} 8000D Mixer/Mill	612.20	12.17	5851.03	0.0117	4.45
LaB_6 - synthesized in planetary ball mill	570.40	11.44	5123.32	0.0102	3.88
Laboratory-synthesized CeB_6	709.00	15.75	8765.89	0.0175	6.66
Laboratory-synthesized SmB_6	719.60	17.09	9651.64	0.0193	7.35
Commercial LaB_6	1700.00	96.11	128258.80	0.2565	97.64
Commercial CeB_6	1686.80	97.71	129381.52	0.2588	98.51
Commercial SmB_6	1696.33	98.65	131364.22	0.2627	100

Relative wear volume loss values of the bulk samples both originated from laboratory-synthesized and commercial LaB_6, CeB_6 and SmB_6 powders decrease from SmB_6 to LaB_6. The lowest value of the relative wear volume loss (3.88 %) belongs to the LaB_6 bulk originated from the mechanochemically synthesized powders in planetary ball mill. Relative wear volume loss values (Table 4.11) are compatible with the results of microhardness (Table 4.10), surface roughness (Figure 4.62) and friction coefficient (Figure 4.63) measurements. The higher values in the microhardness results in the lower values of the relative wear volume loss. Besides, the higher values of the surface roughness and friction coefficient cause higher values of the relative wear volume loss. The relative wear volume loss values of the commercial LaB_6, CeB_6 and SmB_6 bulks are far different than those of laboratory-synthesized ones, as consistent with the hardness values in Table 4.10.

Figures 4.64(a) through (g) represents the SM images of the wear tracks on the bulk samples originated from the laboratory-synthesized and commercial LaB_6, CeB_6 and SmB_6 powders. As clearly seen from Figures 4.64(e)-(g), commercial bulks have very wide elipsoidal wear tracks, indicating the higher relative wear volume loss values than those of laboratory-synthesized ones (Figures 4.64(a)-(d)). It can obviously be deduced from the comparison of the Figures 4.64(a)-(d) that SmB_6 bulk originated from the laboratory-synthesized powders has the widest wear track and hence has the highest relative wear volume loss value (Figure 4.64(d)). Moreover, it is clear in Figure 4.64(b) that wear track of the LaB_6 bulk originated from the mechanochemically synthesized powders in planetary ball mill is the narrowest track amongst all the sintered samples and hence has the lowest relative wear volume loss.

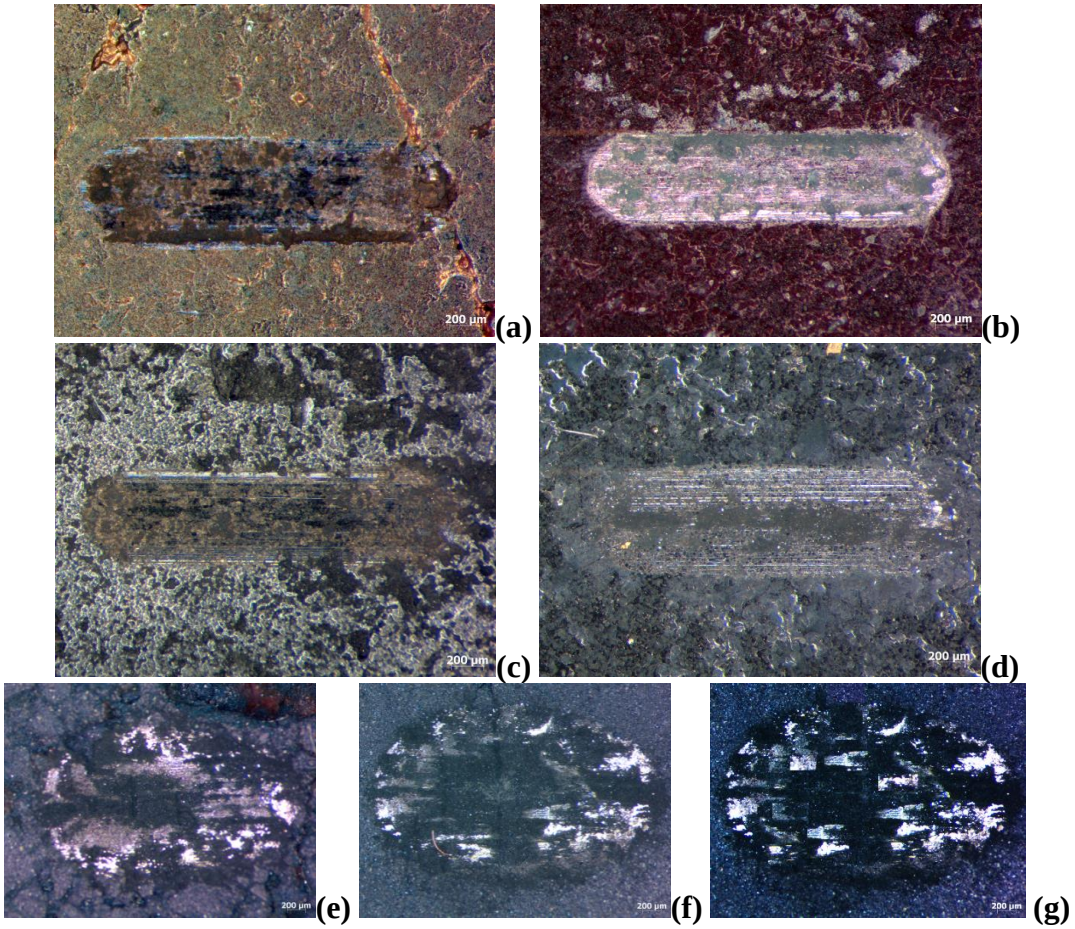

Figure 4.64 : Wear track SM images of the bulk samples originated from the laboratory-synthesized and commercial LaB_6, CeB_6 and SmB_6 powders: (a) laboratory-synthesized LaB_6 in Spex^{TM} 8000D Mixer/Mill, (b) laboratory-synthesized LaB_6 in planetary ball mill, (c) laboratory-synthesized CeB_6, (d) laboratory-synthesized SmB_6, (e) commercial LaB_6, (f) commercial CeB_6 and (g) commercial SmB_6.

Figures 4.65(a)-(g) display the OM images of the worn surfaces belonging to the alumina balls slided at the surfaces of the bulk samples originated from the laboratory-synthesized and commercial LaB_6, CeB_6 and SmB_6 powders. Surfaces of the alumina balls slided on the commercial bulk LaB_6, CeB_6 and SmB_6 samples (Figures 4.65(e)-(g)) wear out more than the laboratory-synthesized ones (Figures 4.65(a)-(d)). The worn surfaces of the alumina balls are seen as compatible with the SM images of the wear tracks in Figure 4.64 and relative wear volume loss values in Table 4.11. The EDS measurements of Al worn off from the alumina balls slided at the surfaces of the bulk samples are given in Table 4.12.

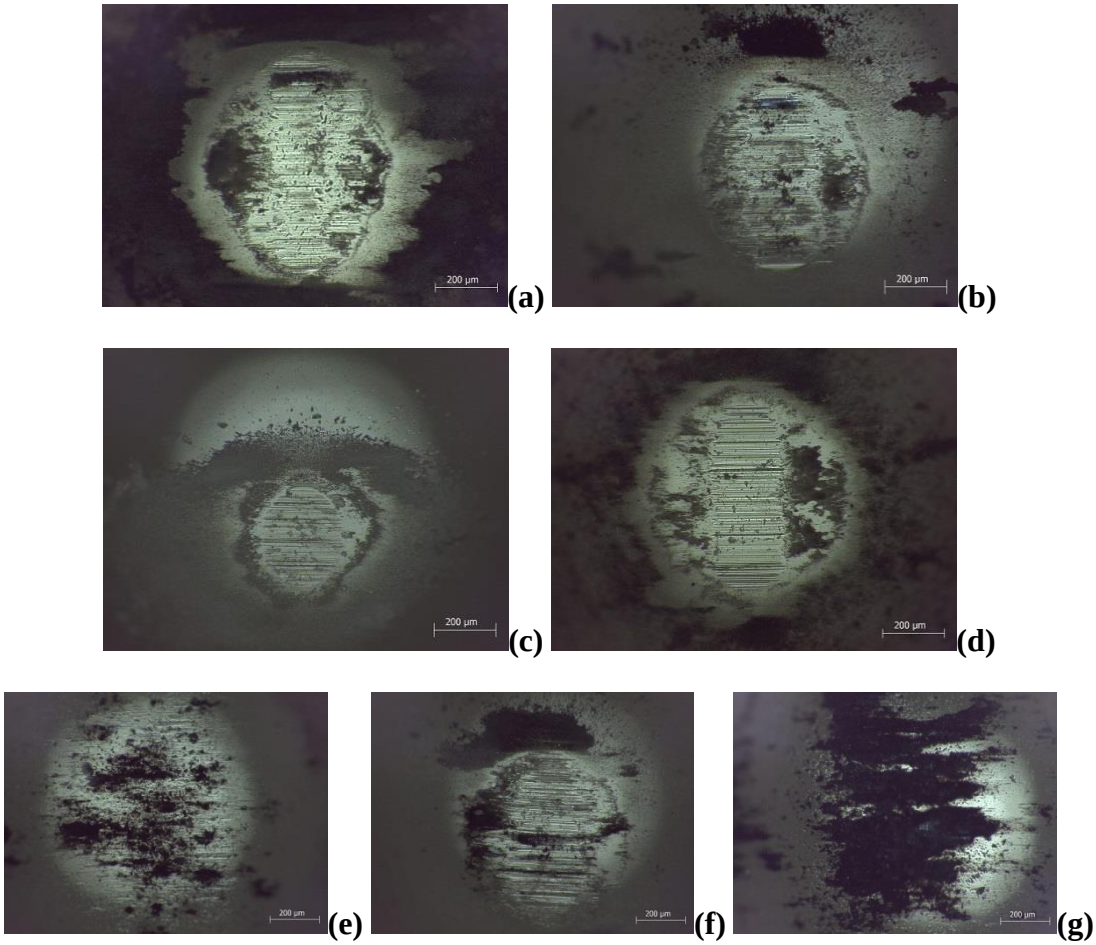

Figure 4.65 : Worn surface OM images of the alumina balls slided at the surfaces of the bulk samples originated from the laboratory-synthesized and commercial LaB_6, CeB_6 and SmB_6 powders: (a) laboratory-synthesized LaB_6 in Spex^{TM} 8000D Mixer/Mill, (b) laboratory-synthesized LaB_6 in planetary ball mill, (c) laboratory-synthesized CeB_6, (d) laboratory-synthesized SmB_6, (e) commercial LaB_6, (f) commercial CeB_6 and (g) commercial SmB_6.

Table 4.12 : EDS measurements of Al worn off from the alumina balls slided at the surfaces of the bulk samples originated from the laboratory-synthesized and commercial LaB_6, CeB_6 and SmB_6 powders.

Sample	Al (wt.%)
LaB_6 - synthesized in Spex^{TM} 8000D Mixer/Mill	0.8 ± 0.02
LaB_6 - synthesized in planetary ball mill	0.3 ± 0.01
Laboratory-synthesized CeB_6	1.9 ± 0.04
Laboratory-synthesized SmB_6	2.3 ± 0.02
Commercial LaB_6	4.9 ± 0.03
Commercial CeB_6	5.3 ± 0.05
Commercial SmB_6	5.8 ± 0.04

As expected, the amounts of detected Al on the surfaces of the commercial LaB_6, CeB_6 and SmB_6 bulk samples are 4.9±0.03, 5.3±0.05 and 5.8±0.04 wt.%, respectively. These amounts are higher than those detected on the surfaces of the bulk samples originated from the laboratory-synthesized LaB_6, CeB_6 and SmB_6 powders. EDS results are in consistent with the microhardness and relative wear volume loss values, for all the sintered samples.

Figure 4.66 is a representative SEM/EDS image of the worn surface belonging to the LaB_6 bulk sample originated from the laboratory-synthesized powders in planetary ball mill. EDS measurement reveals the presence of La and Al elements on the surfaces. The utilized EDS is not capable of detecting B particles and hence La arised from the LaB_6 surface. The lowest amount of Al worn off from the alumina ball is detected in this sample as 0.3±0.01 wt.%.

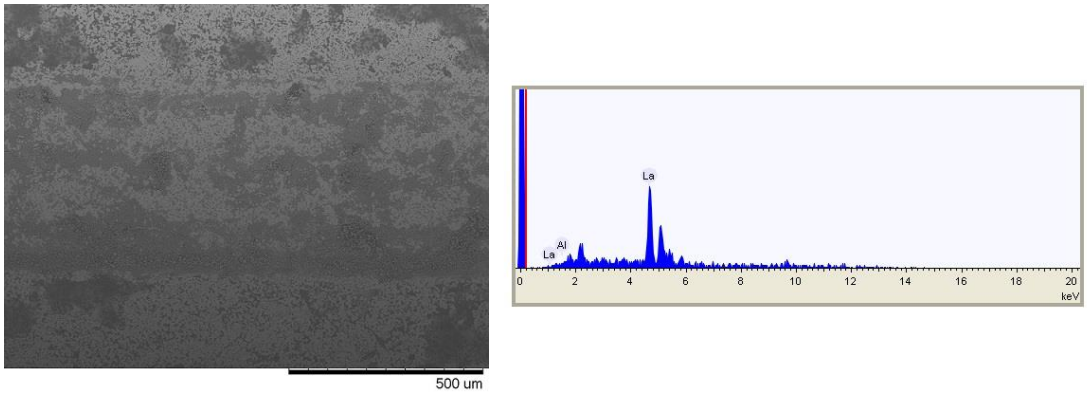

Figure 4.66 : A representative worn surface SEM/EDS image of the bulk sample originated from the laboratory-synthesized LaB_6 powders in planetary ball mill.

5. CONCLUSIONS

In this dissertation, a novel and simple process for synthesizing LaB_6, CeB_6 and SmB_6 powders was achieved by mechanochemical reaction of stoichiometric La_2O_3-B_2O_3-Mg, La_2O_3-B_2O_3-Ca, CeO_2-B_2O_3-Mg and Sm_2O_3-B_2O_3-Mg powder blends. After mechanochemical synthesis, a subsequent purification process, selective HCl leaching, was used for the obtainment of LaB_6, CeB_6 and SmB_6 powders in high purity. Thus, the synthesis of highly pure LaB_6, CeB_6 and SmB_6 powders contains a two step route containing mechanochemical synthesis and HCl leaching. The mechanochemical process parameters such as milling duration, ball-to-powder weight ratio, type of mill type, process control agent and reducing agent were tested on the synthesis of LaB_6 powders. The latter syntheses of CeB_6 and SmB_6 powders were carried out in the light of optimized parameters determined by the obtained results in the synthesis of LaB_6. Besides, experimental results of the mechanochemical synthesis procedure were evaluated according to the thermodynamic interpretations. After all powder production experiments were completed, some yielded products were selected as the ideal laboratory-synthesized powders. After that, laboratory-synthesized LaB_6, CeB_6 and SmB_6 powders are compared with each other and their commercial ones in terms of microstructural, physical (density and surface area) and magnetic properties. Conventional consolidation process including cold pressing and pressureless sintering were conducted on the selected laboratory-synthesized LaB_6, CeB_6 and SmB_6 powders. Finally, the bulk properties of the sintered LaB_6, CeB_6 and SmB_6 originated from the laboratory-synthesized powders are elaborated in terms of microstructure, density, electrical resistivity, roughness, friction coefficients, hardness and relative wear volume loss and compared with each other and those of commercial ones. Based on the results reported in the present study, the following conclusions can be drawn:

- The formation reaction of the LaB_6 and MgO phases took place after mechanochemical synthesis of La_2O_3-B_2O_3-Mg powder blends for 2 h 45 min

in Spex^{TM} 8000D Mixer/Mill using a 10:1 BPR, without any emergence of additional compounds between Mg-B, Mg-B-O, La-B-O, La-Mg or without any emergence of other unstable La-B compounds. This reaction was completed after 3 h milling. Extending the reaction up to 25 h did not cause any change in the resultant phases but it increases the weight amount of formed LaB_6 phase from 15 wt.% (for 2 h 45 min) to 34 wt.% (for 25 h), in accordance with its stoichiometric amount (32.5 wt.% LaB_6). Additionally, it decreased the average crystallite size of LaB_6 from 82.4 to 42.4 nm and increased the lattice deformation from 0.195 to 0.533 %. All mechanochemically synthesized powders had the same LaB_6, MgO, $LaBO_3$ and $Mg_3B_2O_6$ phases after heating up to 1150°C but there was a decreasing tendency in the occurance of $LaBO_3$ and $Mg_3B_2O_6$ phases as the milling duration increased. The reaction mechanism was determined by the DSC analyses conducted on the mechanochemically synthesized La_2O_3-B_2O_3-Mg powders and as-blended B_2O_3-Mg, La_2O_3-Mg and La_2O_3-B_2O_3 powders and by the subsequent XRD analyses conducted on these heated powders. According to this mechanism, the reaction started with the magnesiothermic reduction of B_2O_3 and the latter step was proceeded with the reaction of La_2O_3, free boron and Mg particles, which was also consistent with the thermodynamical data.

- The formation of the LaB_6 and MgO phases was achieved in the presence of very small amount of $LaBO_3$ via mechanochemical synthesis of La_2O_3-B_2O_3-Mg powder blends in Spex^{TM} 8000D Mixer/Mill using a 18:1 BPR for 2 h. Extending the milling duration to 3-5 h provided the disappearance of $LaBO_3$ peaks. To increase the BPR from 10:1 to 18:1 resulted in an earlier chemical reaction, approximately 45 min. The reduction reaction completed after 3 h milling as the same in the case of using 10:1 BPR. Milled powders contain LaB_6, MgO, $LaBO_3$ and $Mg_3B_2O_6$ phases after heating up to 1150°C and there was an increasing tendency in the emergence of LaB_6 phase as the milling duration increased.

- LaB_6 and MgO phases were obtained in the presence of a small amount of $LaBO_3$ phase after 20 h milling of the La_2O_3-B_2O_3-Mg powder blends in planetary ball using a 10:1 BPR. Extended milling duration up to 30 h

resulted in the occurrence of the LaB_6 and MgO peaks without formation of any additional compounds. All mechanochemically synthesized powders has the same LaB_6, MgO, $LaBO_3$ and $Mg_3B_2O_6$ phases after heating up to 1150°C and there was an increasing tendency in the occurance of LaB_6 as the milling duration increased.

- LaB_6 and MgO phases occurred after mechanochemical synthesis of the 0.5 wt.% stearic acid added La_2O_3-B_2O_3-Mg powder blends in Spex^{TM} 8000D Mixer/Mill using a 10:1 BPR for 12 h. PCA slowed down the reaction rate as well as decreases the particle size by inhibiting interparticle welding during collisions. At the end of 12 h milling, LaB_6 had a crystallite size of 44.7 nm and a lattice strain of 0.332 %. All mechanochemically synthesized powders had the same LaB_6, MgO, $LaBO_3$ and $Mg_3B_2O_6$ phases after heating up to 1150°C and there was an increasing tendency in the occurance of LaB_6 and $LaBO_3$ phases as the milling duration increases.
- After mechanochemical synthesis of the La_2O_3-B_2O_3-Ca powder blends in Spex^{TM} 8000D Mixer/Mill using a 10:1 BPR for 1 h 30 min, LaB_6 and CaO phases were obtained in the presence of La_2O_3, $Ca(OH)_2$ and $Ca_3(BO_3)_2$. Extending the milling duration to 2 and 3 h resulted in the disappearance of La_2O_3 and $Ca(OH)_2$ phases and the composition contained only LaB_6, CaO and $Ca_3(BO_3)_2$ phases. The obtained LaB_6 phase can be a sub-boride such as $LaB_{5.83}$, $LaB_{5.832}$, $LaB_{5.784}$ and $LaB_{5.892}$ since Ca is very favorable to form borate phase and reduces the number of boron atom present in the stoichiometric LaB_6 compound. A dendritic $Ca(OH)_2$ phase adsorbed on the LaB_6, CaO and $Ca_3(BO_3)_2$ particles was observed in the microstructure of the 2 and 3 h milled powders. All mechanochemically synthesized powders had the same LaB_6, CaO, $Ca_3(BO_3)_2$ and CaB_2O_4 phases after heating up to 1150°C and there was an increasing tendency in the occurence of LaB_6, $Ca_3(BO_3)_2$ and CaB_2O_4 phases as the milling duration increased.
- LaB_6 powders were obtained with an average particle size of 62 nm and minimum purity of 99.99 % after mechanochemical synthesis of the La_2O_3-B_2O_3-Mg powder blends using a 10:1 BPR in Spex^{TM} 8000D Mixer/Mill for 5 h and leaching with 4 M HCl. 2 M HCl leaching of these powders was not

sufficient to remove all unwanted MgO phase and Fe contamination present in the composition.

- LaB_6 powders were obtained with an average particle size of 100 nm in the presence of very small amounts of FeB_{49} phase after mechanochemical synthesis of the La_2O_3-B_2O_3-Mg powder blends using a 18:1 BPR in Spex^{TM} 8000D Mixer/Mill for 5 h and leaching with 4 M HCl.
- LaB_6 powders mechanochemically synthesized from La_2O_3-B_2O_3-Mg powder blends using a 10:1 BPR in planetary ball mill for 30 h and leached with 4 M HCl had a minimum purity value of 99.99 % and an average particle size value of 74 nm.
- LaB_6 powders were obtained with an average particle size of 53 nm and minimum purity of 99.99 % after mechanochemical synthesis of the 0.5 wt.% PCA added La_2O_3-B_2O_3-Mg powder blends using a 10:1 BPR in Spex^{TM} 8000D Mixer/Mill for 12 h and leaching with 4 M HCl. The PCA addition decreased the average particle size of LaB_6 since the synthesized one at the same conditions without PCA was 62 nm.
- LaB_6 powders were achieved with an average particle size of 80 nm and in the presence of very small amount of $Ca_3(BO_3)_2$ phase via mechanochemical synthesis of La_2O_3-B_2O_3-Ca powder blends using a 10:1 BPR in a Spex^{TM} 8000D Mixer/Mill for 3 h and leaching with 4 M HCl.
- The formation reaction of the CeB_6 and MgO phases took place after mechanochemical synthesis of CeO_2-B_2O_3-Mg powder blends for 2 h in Spex^{TM} 8000D Mixer/Mill using a 10:1 BPR. 2 h milled powders contained CeO_2, Mg, $CeBO_3$, CeB_6 and MgO phases. At the end of 3 h milling, only CeB_6, $CeBO_3$ and MgO phases occurred. Extending the milling duration to 4-5 h provided the disappearance of $CeBO_3$. The average crystallite sizes of CeB_6 in the 3, 4 and 5 h milled powders were respectively calculated as 178, 149 and 90 nm. All mechanochemically synthesized powders had the same CeB_6, MgO, $Mg_3B_2O_6$ and $CeBO_3$ phases after heating up to 1150°C and there was an increasing tendency in the occurance of CeB_6 phase as the milling duration increased. CeB_6 powders were obtained with a minimum purity of 99.99 % and with an average particle size of 86 nm after mechanochemical synthesis for 5 h and leaching with 4 M HCl.

- The formation reaction of the SmB_6 and MgO phases took place after mechanochemical synthesis of the Sm_2O_3-B_2O_3-Mg powder blends for 1 h 50 min in Spex^{TM} 8000D Mixer/Mill using a 10:1 BPR. Extending the milling duration up to 5 h does not change the kind of occurred phases. The average crystallite sizes of SmB_6 in the 2, 3 and 5 h milled powders were respectively calculated as 157, 126 and 95 nm. All mechanochemically synthesized powders had the same SmB_6, MgO, $Mg_3B_2O_6$ and $SmBO_3$ phases after heating up to 1150°C and there was an increasing tendency in the occurance of SmB_6 and $SmBO_3$ phases as the milling duration increased. SmB_6 powders with a minimum purity of 99.99 % and with an average particle size of 81 nm were obtained after mechanochemical synthesis for 5 h and leaching with 4 M HCl.
- Optimized powder products were selected as LaB_6 powders obtained after mechanochemical synthesis of the La_2O_3-B_2O_3-Mg powder blends using a 10:1 BPR in a Spex^{TM} 8000D Mixer/Mill for 5 h and leaching with 4 M HCl, LaB_6 powders obtained after mechanochemical synthesis of the La_2O_3-B_2O_3-Mg powder blends using a 10:1 BPR in a planetary ball mill for 30 h and leaching with 4 M HCl, CeB_6 powders obtained after mechanochemical synthesis of the CeO_2-B_2O_3-Mg powder blends using a 10:1 BPR in a Spex^{TM} 8000D Mixer/Mill for 5 h and leaching with 4 M HCl and SmB_6 powders obtained after mechanochemical synthesis of the Sm_2O_3-B_2O_3-Mg powder blends using a 10:1 BPR in a Spex^{TM} 8000D Mixer/Mill for 5 h and leaching with 4 M HCl.
- According to the TEM micrographs, all obtained LaB_6, CeB_6 and SmB_6 powders are polycrystalline. The calculated lattice parameters of the laboratory-synthesized LaB_6, CeB_6 and SmB_6 are respectively 0.415, 0.413 and 0.413 nm, which are in good agreement with the theoretical lattice parameters.
- LaB_6 powders originated from the mechanochemical synthesis in Spex^{TM} 8000D Mixer/Mill have the density and surface area values of 4.58±0.007 g/cm^3 and 17.84 m^2/g whereas that of originated from the synthesis in planetary ball mill have the density value and surface area values of 4.47±0.006 g/cm^3 and 11.11 m^2/g. The density and surface area values of the

laboratory-synthesized CeB_6 powders are 4.77±0.009 g/cm^3 and 13.45 m^2/g. The density and surface area values of the laboratory-synthesized SmB_6 powders are found as 5.14±0.002 g/cm^3 and 8.70 m^2/g. These density values are consistent with the theoretical values. The surface area values are in good agreement with their average particle sizes.

- LaB_6 powders originated from the mechanochemical synthesis in Spex^{TM} 8000D Mixer/Mill are paramagnetic whereas that of originated from the mechanochemical synthesis in planetary ball mill are diamagnetic. Laboratory-synthesized CeB_6 and SmB_6 powders are paramagnetic. Commercial LaB_6, CeB_6 and SmB_6 powders are found as ferromagnetic.

- Any contamination was not detected in the microstructures of the bulk samples: pure LaB_6, CeB_6 and SmB_6 sintered compacts were obtained after sintering.

- Electrical resistivity values of the bulk samples originated from the laboratory-synthesized powders are higher than those of originated from commercial powders. LaB_6 sintered compact originated from the powders mechanochemically synthesized in Spex^{TM} 8000D Mixer/Mill has the electrical resistivity value of 37.00±2.50 μΩ.cm whereas that of synthesized in planetary ball mill has the value of 35.20±1.40 μΩ.cm. The electrical resistivities of the CeB_6 and SmB_6 sintered compacts originated from laboratory-synthesized powders are 57.50±3.80 and 211.00±4.50 μΩ.cm, respectively.

- LaB_6 bulks originated from the mechanochemical synthesis in Spex^{TM} 8000D Mixer/Mill had higher relative density value (96.80 %) than that of synthesized in planetary ball mill (94.25 %). CeB_6 and SmB_6 bulks originated from the mechanochemical synthesis in Spex^{TM} 8000D Mixer/Mill had relative density values of 95.20 and 96.84 %.

- LaB_6 sintered compact originated from the powders mechanochemically synthesized in Spex^{TM} 8000D Mixer/Mill had the microhardness value of 12.75±0.70 GPa whereas that of synthesized in planetary ball mill had the value of 13.35±0.40 GPa. The microhardness values of the CeB_6 and SmB_6 bulks originated from laboratory-synthesized powders were 11.65±0.50 and

10.08±0.80 GPa respectively. All the bulks originated from laboratory-synthesized powders have approximately two times higher hardness values than those of originated from commercial powders.

- LaB_6, CeB_6 and SmB_6 bulks originated from the laboratory-synthesized powders had the relative wear volume loss values of 4.45 % (for LaB_6 synthesized in Spex^{TM} 8000D Mixer/Mill), 3.88 % (for LaB_6 synthesized in planetary ball mill), 6.66 % (for CeB_6) and 7.35 % (for SmB_6). Bulks prepared from commercial LaB_6, CeB_6 and SmB_6 powders had the relative wear volume loss values of 97.64, 98.51 % and 100 %. These values are consistent with the values of surface roughness and friction coefficient and with the EDS results of the worn bulk surfaces on which alumina ball slided.

Some suggestions for the future work that will be carried out on the rare-earth hexaborides can be made as: i) the distributions of the elements in the microstructures of the LaB_6, CeB_6 and SmB_6 bulk samples will be mapped by using electron probe micro-analyzer (EPMA), ii) magnetic measurements will be carried out on the pure and fine-grained LaB_6, CeB_6 and SmB_6 powders at very low temperatures (down to the absolute zero), iii) different kinds of consolidation processes (cold isostatic pressing, hot pressing, hot isostatic pressing, spark plasma sintering, etc.) will be performed with/without sintering aid to provide the full densification of the bulk samples and iv) thermionic emission properties of LaB_6, CeB_6 and SmB_6 will be determined with the collaboration of an international laboratory.

REFERENCES

Abazova, A. K. H., Kushkhov, K. H. B., Mukozheva, R. A., Tlenkopachev, M. R., Uzdenova, A. S. and Vindizheva, M. K. (2012). Electroliytic method of producing ultrafine cerium hexaboride powder using cerium source and boron source, *Russia Patent No. RU2466090-C1*. Retrieved from Scopus.

Ağaoğulları, D., Gökçe, H., Duman, İ. and Öveçoğlu M. L. (2011). Influences of metallic Co and mechanical alloying on the microstructural and mechanical properties of TiB_2 ceramic prepared via pressureless sintering, *Journal of European Ceramic Society, 32,* 1949-1956.

Ağaoğulları, D., Balcı, Ö., Gökçe, H., Duman, İ. and Öveçoğlu, M. L. (2012a). Synthesis of magnesium borates by mechanically activated annealing, *Metalurgical and Materials Transactions A, 43A,* 2520-2533.

Ağaoğulları, D., Duman, İ. and Öveçoğlu M. L. (2012b). Synthesis of LaB_6 powders from La_2O_3, B_2O_3 and Mg blends via a mechanical route, *Ceramics International, 38,* 6203-6214.

Ahmed, H., Kanitkar, P. L., Dharmadhikari, C. V. and Joag, D. S. (1975). A new method for melting and recrystallization of lanthanum hexaboride (LaB_6) for preparing field emitters, *Journal of Physics E: Scientific Instruments, 9,* 4-5.

Akgun, B., Sevinc, N., Camurlu, H. E. and Topkaya, Y. (2013). Mechanochemical and combustion synthesis of CeB_6, *International Journal of Materials Research, 104,* 403-407.

Allen, J. W., Batlogs, B. and Wachter, P. (1979). Large low-temperature hall-effect and resistivity in mixed-valent SmB_6, *Physical Review, 20,* 40807-4813.

Amalajyothi, K., Berchmans, L. J., Angappan, S. and Visuvasam, A. (2008). Electrosynthesis of cerium hexaboride by the molten salt technique, *Journal of Crystal Growth, 310,* 3376-3379.

Amalajyothi, K., Berchmans, L. J., Visuvasam, A. and Angappan, S. (2011). Electrosynthesis of cerium hexaboride using lithium tetra borate melt, *Materials and Manufacturing Processes, 26,* 792-795.

Aprea, A., Maspero, A., Masciocchi, N., Guagliardi, A., Albisetti, A. F. and Giunchi, G. (2013). Nanosized rare-earth hexaborides: low-temperature preparation and microstructural analysis, *Solid State Sciences, 21,* 32-36.

Arockiam, V., Chanassery, O. A., Lawrance, J. B. and Sankaramahalingam, A. (2009). Electrolytic preparation of rare earth hexaboride using oxy-fluoride melt, *Indian Patent No. IN200700695-I1*. Retrieved from Scopus.

Avvakumov, E., Senna, M. and Kosova, N. (2001). *Soft Mechanochemical Synthesis*. Dordrecht, Netherlands: Kluwer Academic Publisher.

Bakr, M., Kinjo, R., Choi, Y. W., Omer, M., Yoshida, K., Ueda, S., Takasaki, M., Ishida, K., Kimura, N., Zen, H., Sonobe, T., Kii, T., Masuda, K. and Ohgaki, H. (2011). Comparison of the heating properties of LaB_6 and CeB_6 due to the back bombardment effect in a thermionic RF gun, *Journal of the Korean Physical Society, 59,* 3273-3279.

Balakrishnan, G., Lees, M. R. and Paul, D. M^{c}K. (2004). Rare earth hexaborides: large single crystals, *Journal of Magnetism and Magnetic Materials, 272-276,* 601-602.

Balaz, P. (2000). *Extractive Metallurgy of Activated Minerals*. Kosice, Slovakia: Elsevier.

Balaz, P. (2008). *Mechanochemistry in Nanoscience and Minerals Engineering*. Kosice, Slovakia: Springer.

Balaz, P., Achimovicova, M., Balaz, M., Billik, P., Cherkezova-Zheleva, Z., Criado, J. M., Delogu, F., Dutkova, E., Gaffet, E., Gotor, F. J., Kumar, R., Mitov, I., Rojac, T., Senna, M., Streletskii, A. and Wieczorek-Ciurowa, K. (2013). Hallmarks of mechanochemistry: from nanoparticles to technology, *Chemical Society Reviews, 42,* 7571-7637.

Balcı, Ö., Ağaoğulları, D. and Duman, İ. (2010). The production of HfO_2-HfB_2 composite powder from B_2O_3 and Mg by solid state reaction and subsequent annealing, *Solid State Science and Technology, 18,* 91-98.

Balcı, Ö., Ağaoğulları, D., Duman, İ. and Öveçoğlu, M. L. (2012). Synthesis of CaB_6 powders via mechanochemical reaction of Ca/B_2O_3 blends, *Powder Technology, 225,* 136-142.

Bao, L., Zhang, J., Zhou, S. and Wei, Y. (2010). Preparation and characterization of grain size controlled LaB_6 polycrystalline cathode material, *Chinese Physics Letters, 27,* 107901.

Bao, L., Zhang, J. and Zhou, S. (2011a). Effect of particle size on the polycrystalline CeB_6 cathode prepared by spark plasma sintering, *Journal of Rare Earths, 29,* 580-584.

Bao, L., Zhang, J., Zhou, S., Zhang, N. and Xu, H. (2011b). Floating zone growth and thermionic emission property of single crystal CeB_6, *Chinese Physics Letters, 28,* 088101-1-088101-4.

Bao, L. H., Zhang, J. X., Zhang, N., Li, X. N. and Zhou, S. L. (2012). In situ $(La_xGd_{1-x})B_6$ cathode materials prepared by the spark plasma sintering technique, *Physica Scripta, 85,* 035710, 1-5.

Baranovskiy, A. E., Grechnev, G. E., Fil, V. D., Ignatova, T. V., Logosha, A. V., Panfilov, A. S., Svechkarev, I. V., Shitsevalova, N. Y., Filippov, V. B. and Eriksson, O. (2007). Electronic structure, bulk and magnetic properties of MB_6 and MB_{12} borides, *Journal of Alloys and Compounds, 442,* 228-230.

Barla, A., Derr, J., Sanchez, J. P., Salce, B., Lapertot, G., Doyle, B. P., Ruffer, R., Lengsdorf, R., Abd-Elmeguid, M. M. and Flouquet, J. (2005). High-pressure ground state of SmB_6: electronic conduction and long range magnetic order, *Physical Review Letters B, 94,* 166401-1-166401-4.

Bellon, P. and Averback, R. S. (1995). Nonequilibrium roughening of interfaces in crystals under shear: application to ball milling, *Physical Review Letters, 74,* 1819-1822.

Benjamin, J. S. (1970). Dispersion strengthened superalloys by mechanical alloying, *Metallurgical Transactions, 1,* 2943-2951.

Benjamin, J. S. (1992). Fundamentals of Mechanical Alloying: Mechanical Alloying. In P. H. Shingu (Ed.), *Proceedings of the International Symposium on Mechanical Allloying,* Vol. 88-90, (pp.2-17). Brookfield, VT: Trans Tech Publications, May 7-10.

Berchmans, L. J., Visuvasam, A., Angappan, S., Subramanian, C. and Suri, A. K. (2010). Electrosynthesis of samarium hexaboride using tetra borate melt, *Ionics, 16,* 833-838.

Bliznakov, G. and Peshev, P. (1964). The preparation of cerium, praseodymium, and neodymium hexaborides, *Journal of the Less Common Metals, 7,* 441-446.

Boldyrev, V. V. (1986). Mechanochemistry of inorganic solids, *Indian National Science Academy, 52,* 400-417.

Boldyrev, V. V. (2006). Mechanochemistry and mechanical activation of solids, *Russian Chemical Reviews, 75(3),* 177-189.

Boldyrev, V. V. and Tkacova, K. (2000). Mechanochemistry of solids: past, present and prospects, *Journal of Materials Synthesis and Processing, 8,* 121-132.

Botta, P. M., Aglietti, E. F. and Porto-Lopez, J. M. (2000). Thermal and phase evolution of mechanochemical reactions in the Al-Fe_3O_4 system, *Thermochimica Acta, 363,* 143-147.

Brewer, J. R., Deo, N., Wang, Y. M. and Cheung, C. L. (2007). Lanthanum hexaboride nanoobelisks, *Chemical Materials, 19,* 6379-6381.

Brewer, J. R., Jacobberger, R. M., Diercks, D. R. and Cheung, C. L. (2011). Rare earth hexaboride nanowires: general synthetic design and analysis using atom probe tomography, *Chemistry of Materials, 23,* 2606-2610.

Butyagin, P. Y. (1984). Structural disorder and mechanochemical reactions in solids, *Uspekhi Khimii, 53,* 1769-1789.

Calka, A. and Radlinski, A. P. (1991). Universal high performance ball-milling device and its application for mechanical alloying, *Material Science and Engineering, A134,* 1350-1353.

Carey Lea, M. (1893). On endothermic reactions effected by mechanical force: part first, *American Journal of Science: Third Series, XLVI,* 241-244.

Carlsson, M., Garcia-Garcia, F. J., Johnsson, M. and Gulian A. (2005). Synthesis of $La_xCe_{1-x}B_6$ whiskers, *Journal of Materials Science, 40,* 2991-2994.

Chen, Y., Hwang, T., Marsh, M. and Williams, J. S. (1997). Study on mechanism of mechanical activation, *Materials Science and Engineering, A226-228,* 95-98.

Chen, C. H., Xuan, Y. and Otani S. (2003). Temperature and loading time dependence of hardness of LaB_6, YB_6 and TiC single crystals, *Journal of Alloys and Compounds, 350,* L4-L6.

Chen, C., Aizawa, T., Iyi, N., Sato, A. and Otani, S. (2004). Structural refinement and thermal expansion of hexaborides, *Journal of Alloys and Compounds, 366,* L6-L8.

Chen, D. and Chen, Z. H. (2006). *Mechanical Alloying and Solid-Liquid Reaction Milling.* Beijing, China: Chemical Industry Press.

Chen, D., Yong, J., Jian-Guo, C., Zhen-Hua, C. and Pei-Yun, H. (2010). Production of intermetallic compound powders by a mechanochemical approach: solid-liquid reaction ball milling. In M. Sopicka-Lizer (Ed.), *High-energy Ball Milling: Mechanochemical Processing of Nanopowders* (pp.149-166). Cambridge, UK: Woodhead Publishing Limited, CRC.

Chen, B., Yang, L., Heng, H., Chen, J., Zhang, L. and Xu, L. (2012). Additive-assisted synthesis of boride, carbide, and nitride micro/nanocrystals, *Journal of Solid State Chemistry, 194,* 219-224.

Chen, C. and Chen, D. (2012). Preparation of LaB_6 nanoparticles as a novel and effective near-infrared photothermal conversion material, *Chemical Engineering Journal, 180,* 337-342.

Chin, Z. H. and Perng, T. P. (1997). Amorphization of Ni-Si-C ternary alloy powder by mechanical alloying, *Materials Science Forum, 235-238,* 121-126.

Cooley, C., Aronson, M. C., Fisk, Z. and Confield, P. C. (1995). SmB_6-kondo insulator or exotic metal, *Physical Review Letters, 74,* 1629-1632.

Curtis, B. J. and Graffenberger, H. (1966). The floating zone crystal growth of lanthanum hexaboride, *Material Research Bulletin, 1,* 27-31.

Delogu, F. and Mulas, G. (2010). Kinetic processes and mechanism of mechanical alloying, In M. Sopicka-Lizer *(*Ed.), *High-energy Ball Milling: Mechanochemical Processing of Nanopowders (*pp.92-100). Cambridge, UK: Woodhead Publishing Limited, CRC.

Dou, Z., Zhang, T. A. and He, J. C. (2011a). Preparation and characterization of cerium hexaboride nanometer powders by combustion synthesis, *Application of Ceramical Engineering, 236-238,* 1670-1674.

Dou, Z., Zhang, T., Liu, Y., Guo, Y. and Jicheng, H. (2011b). Preparation of CeB_6 nano-powders by self-propagating high-temperature synthesis (SHS), *Journal of Rare Earths, 29,* 986-990.

Dou, Z., Zhang, T., Zhang, Z., Zhang, H. and He, J. (2011c). Preparation and characterization of LaB_6 ultra fine powder by combustion synthesis, *Transactions of Nanoferrous Metals Society of China, 21,* 1790-1794.

Dou, Z., Zhang, T., Guo, Y. and Jicheng, H. (2012). Research on preparation optimization of nano CeB_6 powder and its high temperature stability, *Journal of Rare Earths, 30,* 1129-1133.

El-Eskandarany, M. S. (2001). *Mechanical Alloying for Fabrication of Advanced Engineering Materials.* Norwich, N.Y: Noyes Publications.

Erfani, M., Saion, E., Soltani, N., Hashim, M., Abdullah, W. S. B .W. and Navasery, M. (2012). Facile synthesis of calcium borate nanoparticles and the annealing effect on their structure and size, *International Journal of Molecular Sciences, 13,* 14434-14445.

Ermakov, A. E., Yurchikov, E. E. and Barinov, V. A. (1981). The magnetic properties of amorphous Y-Co alloy powders obtained by mechanical communition, *The Physics of Metals and Metallography, 52(6),* 50-58.

Fan, Q. H., Zhao, Y. M. and Li, D. D. (2013). Synthesis of single-crystalline lanthanum hexaboride nanowires by Au catalyst, *Ceramics International, 39,* 6271-6275.

Faraday, M. (1827). *Chemical Manipulations: Being Instructions to Students in Chemistry on the Methods of Performing Experiments of Demonstrations or of Research, with Accuracy and with Success.* London, UK: W. Phillips.

Fecht, H. J. (2002). Nanostructured materials and composites prepared by solid state processing, In C. C. Carl (Ed.), *Nanostructrured Materials: Processing, Properties and Potential Applications (*pp.73-107). New York: Noyes Publications.

Futamoto, M., Nakazawa, M. and Kawabe, U. (1980). Thermionic emission properties of hexaborides, *Surface Science, 100,* 470-480.

Gao, R., Min, G., Yu, H., Zheng, S., Lu, Q., Han, J. and Wang, J. (2005). Fabrication and oxidation behavior of LaB_6-ZrB_2 composites, *Ceramics International, 31,* 15-19.

German, R. M. (1994). *Powder Metallurgy Science.* Princeton, N.J.: Metal Powder Industries Federation.

German, R. M. (2005). *A-Z* of *Powder Metallurgy.* Oxford, UK: Elsevier Advanced Technology.

German, R. M. and Park, S. J. (2008). *Handbook of Mathematical Relations in Particulate Materials Processing.* United States of America: A John Willey & Sons, Inc.

Gilman, P. S. and Benjamin, J. S. (1983). Mechanical alloying, *Annual Review of Materials Science, 13,* 279-300.

Givargizov, E. I. and Obolenskaya, L. E. (1981). Controlled growth of LaB_6 whiskers by the vapour-liquid-solid mechanism, *Journal of Crystal Growth, 51,* 190-194.

Givargizov, E. I. and Obolenskaya, L. E. (1986). Regular arrays of LaB_6 whiskers grown on single crystal substrates by the vapour-liquid-solid method, *Journal of the Less Common Metals, 117,* 97-103.

Guo, W., **Iasonna, A., Magini, M., Martelli, F. and Padella, F.** (1994). Synthesis of amorphous and metastable $Ti_{40}Al_{60}$ alloys by mechanical alloying of elemental powders, *Journal of Material Science, 29,* 2436-2444.

Gutman, E. M. (1998). *Mechanochemistry of Materials.* Cambridge, UK: Cambridge International Publishing.

Hammerberg, J. E., Holian, B. L., Röder, J., Bishop, A. R. and Zhou, S. J. (1998). Nonlinear dynamics and the problem of slip at material interfaces, *Physica D, 123,* 330-340.

Hasan, M., Sugo, H. and Kisi, E. (2013). Low temperature carbothermal and boron carbide reduction synthesis of LaB_6, *Journal of Alloys and Compounds, 578,* 176-182.

Hatnean, M. C., Less, M. R., Paul, D. M^{c}K. and Balakrishnan, G. (2013). Large, high quality single-crystals of the new topological kondo insulator, SmB_6, *Scientific Reports, 3:3071,* 1-4.

Heegn, H. P. (1989). On the connection between ultrafine grinding and mechanical activation of minerals, *Chemie Ingenieur Technik, 62,* 458-464.

Heinicke, G., (1984). *Tribochemistry.* Munich, Germany: Carl Hanser Verlag.

Huot, J., Ravnsbaek, D. B., Zhang, J., Cuevas, F., Latroche, M. and Jensen, T. R. (2013). Mechanochemical synthesis of hydrogen storage materials, *Progress in Materials Science, 58,* 30-75.

Hüttig, G. (1943). Intermediate steps at solid-state reactions and their significance in catalysis, In G.M Schwab (Ed.), *Handbook of Catalysis* (Vol. 4, pp. 318-577). Wien, Austria: Springer Verlag.

Iltis, A. and Maestro, P. (1991). Preparation of rare earth borides, *United States Patent No. 4,999,176.* Retrieved from Scopus.

Iltis, A. and Maestro, P. (1993). Preparation of rare earth borides, *United States Patent No. US005176890A.* Retrieved from Scopus.

Ivanov, E. and Suryanarayana, C. (2000). Materials and process design through mechanochemical routes, *Journal of Materials Synthesis and Processing, 8,* 235-244.

Jha, M., Patra, R., Ghosh, S. and Ganguli, A. K. (2012a). Novel borothermal route for the synthesis of lanthanum cerium hexaborides and their field emission properties, *Journal of Solid State Chemistry, 194,* 173-178.

Jha, M., Patra, R., Ghosh, S. and Ganguli, A. K. (2012b). Vertically aligned cerium hexaboride nanorods with enhanced field emission properties, *Journal of Materials Chemistry, 22,* 6356-6366.

Ji, X. H., Zhang, Q. Y., Xu, J. Q. and Zhao, Y. M. (2011). Rare-earth hexaborides nanostructures: recent advances in materials, characterization and investigations of physical properties, *Progress in Solid State Chemistry, 39,* 52-69.

Juhasz, A. Z. and Kollath, B. (1993). Mechanochemical reactions of OH-containing crystals, *Acta Chimica Hungarica, 130,* 725-735.

Juhasz, Z. A. (1998). Colloid chemical aspects of mechanical activation, *Particulate Science and Technology, 16,* 145-161.

Kamaludeen, M., Selvaraj, I., Visuvasam, A. and Jayavel, R. (1998). LaB_6 crystals from fused salt electrolysis, *Journal of Materials Chemistry, 8,* 2205-2207.

Kanakala, R. (2008). *Exploring the synthesis of hexaborides: the basis of a newchemistry for the preparation of electro-optical materials*. (Doctoral dissertation). University of Nevada, Reno.

Kanakala, R., Rojas-George, G. and Graeve, O. A. (2010). Unique preparation of hexaboride nanocubes: a first example of boride formation by combustion synthesis, *Journal of American Ceramic Society, 93,* 3136-3141.

Karthikeyan, S., Agrawal, A. and Rigney D. A., (2009). Molecular dynamics simulations of sliding in a Fe-Cu tribopair system, *Wear, 267,* 1166-1176.

Kim, D. H., Park, H. S., Kim, S. J. and Lee, K. S. (2005). Characteristics of Ni 8 wt.%-doped titanium dioxide photocatalyst synthesized by mechanical alloying, *Catalysis Letters, 100,* 49-52.

Kim, H. J., Kim, W. K., Falk, M. L. and Rigney, D. A. (2007). MD simulations of microstructure evolution during high-velocity sliding between crystalline materials, *Tribology Letters, 28,* 299-306.

Kimura, H. and Kimura, M. (1990). Solid State Powder Processing. In A. H. Clauer, J. J. Debarbadillo (Eds.), *Proceedings of TMS Powder Metallurgy Committe,* (pp.365-377). Warrendale, PA: TMS-AIME.

Kis-Varga, M. and Beke, D. L. (1996). Phase transitions in Cu-Sb systems induced by ball milling, *Material Science Forum, 225-227,* 465-470.

Knoch, H., Bechler, E. and Lipp, A. (1987). Polycrystalline sintered bodies based on lanthanum hexaboride and a process for their manufacture, *United States Patent No. 4,661,740.* Retrieved from Scopus.

Koch, C. C., Cavin, O. B., Mckamey, C. G. and Scarbrough, J. O. (1983). Preparation of amorphous $Ni_{60}Nb_{40}$ by mechanical alloying, *Applied Physics Letters, 43,* 1017-1019.

Koch, C. C., Pathak, D. and Yamada, K. (1993). Mechanical Alloying for Structural Applications. In J. J. Debarbadillo et al. (Eds.), *Proceedings of the 2nd International Conference on Structural Applications of Mechanical Alloying,* (pp.205-212). Vancouver, Canada: ASM International.

Komarov, S. V., Romankov, S. E., Hayashi, N. and Kasai, E. (2010). Mechanochemical plating and surface modification using ultrasonic vibration, In M. Sopicka-Lizer (Ed.), *High-energy Ball Milling: Mechanochemical Processing of Nanopowders* (pp.251-274). Cambridge, UK: Woodhead Publishing Limited, CRC.

Landolt, B. (1984). *Numerical Data and Functional Relationships in Science and Technology: New series, Group III, Semiconductors* (Vol. 17). Berlin, Germany: Springer-Verlag.

Late, D. J., Date, K. S., More, M. A., Misra, P., Singh, B. N., Kukreja, L. M., Dharmadhikari, C. V. and Joag, D. S. (2008). Enhanced field emission from LaB_6 thin films with nanoprotrusions grown by pulsed laser deposition method on Zr foil, *Applied Surface Science, 254,* 3601-3605.

Late, D. J., Singh, V. R., Sinha, S., More, M. A., Dasgupta, K. and Joag, D. S. (2009). Synthesis of LaB_6 micro/nano structures using picosecond (Nd:YAG) laser and its field emission investigations, *Applied Physics A, 97,* 905-909.

Levitas, V. I. (2004). Continuum mechanical fundamentals of mechanochemistry, In V. Domnich, Y. Gogotsi (Eds.), *High Pressure Surface Science and Engineering* (pp. 161-292). Bristol, UK: Institue of Physics, IOP Publishing Ltd.

Li, P., Tian, W., Wang, D. and Liu X. (2012). Grain refining potency of LaB_6 on aluminum alloy, *Journal of Rare Earths, 30,* 1172-1176.

Lin, I. J. (1998). Implications of fine grinding in mineral processing: mechanochemical approach, *Journal of Thermal Analysis, 52,* 453-361.

Liu, Y., Zhang, T., He, J., Dou, Z., LV, G. and Guo, Y. (2010). Preparation of high-purity cerium hexaboride nanopowder by mixing cerium oxide, boron oxide and magnesium powder, ball milling, pressing, heating in air, leaching with diluted sulfuric acid, filtering, washing, and drying, *Chinese Patent No. CN 101891216-A,* Retrieved from Scopus.

Ljachov, N. (1993). Mechanical Activation from the Viewpoint of Kinetic Reaction Mechanism. In K. Tkacova (Ed.), *INCOME'93. Proceedings of the 1st International Conference on Mechanochemistry Fundamentals and Models of Mechanically Stimulated Processes* (Vol. 1., pp.59-65). Moscow, Russia: Cambridge International Science Publishing.

Loboda, P. I., Kysla, H. P., Dub, S. M. and Karasevs'ka, O. P. (2009). Mechanical properties of the monocrystals of lanthanum hexaboride, *Materials Science, 45,* 108-113.

Lundström, T. (1985). Structure, defects and properties of some refractory borides, *Pure and Applied Chemistry, 57,* 1383-1390.

Macedo, C. A. and Souza, A. M. C. (2002). Thermodynamic properties of samarium hexaboride, *IEEE Transactions on Magnetics, 38,* 2875-2876.

Machio, C., Chikwanda, H. K. and Chikosha, S. (2011). Effect of process control agent (PCA) on the characteristics of mechanically alloyed Ti-Mg powders, *The Journal of The Southern African Institute of Mining and Metallurgy, 111,* 149-153.

Maltseva, N. N., Golovanova, A. I., Dymova, T. N. and Aleksandrov D. P. (2001). Solid-phase formation of calcium hydridoaluminates $Ca(AlH_4)_2$ and $CaHAlH_4$ upon mechanochemical activation or heating of mixtures of calcium hydride with aluminum chloride, *Russian Journal of Inorganic Chemistry, 46,* 1793-1797.

Massalski, T. M., Okamoto, M., Subramanian, P. R. and Kacprzak, L. (1990). *Binary Alloy Phase Diagrams.* Materials Park, Ohio: ASM International.

Matteazzi, P. and Le Caer, G. (1992). Mechanically activated room-temperature reduction of sulphides, *Materials Science and Engineering, A156,* 229-37.

McCormick, P. G., Wharton, V. N. and Schaffer, G. B. (1989). *Physical Chemistry of Powder Metals Production and Processing.* Warrendale, PA: TMS.

McCormick, P. G., Wharton, V. N., Reyhani, M. M. and Schaffer, G. B. (1991). Synthesis of nanophase titanium alloys by chemical reduction during mechanical alloying. In D.C. Van Aken, G.S. Was, A.K. Ghosh (Eds.), *Microcomposites and Nanophase Materials* (pp. 65-79), Warrendale, PA.

McCormick, P. G. (1995). Application of mechanical alloying to chemical refining, *Materials Transactions The Japan Institute of Metals, 36,* 161-169.

McCormick, P. G. and Froes, F. H. (1998). The fundamentals of mechanochemical processing, *The Member of The Minerals, Metals and Materials Society, 50,* 61-65.

McKelvy, M. J., Eyring, L. and Storms, E. K. (1984). Analytical and structural analysis of the lanthanum-deficient lanthanum hexaboride, *Journal of Physics Chemistry, 88,* 1785-1790.

Menth, A., Buehler, E. and Gaballe, T. (1969). Magnetic and semiconducting properties of SmB_6, *Physical Review Letters, 22,* 295-297.

Meschel, S. V. and Kleppa, O. J. (1995). Standart enthalpies of formation of some borides of Ce, Pr, Nd and Gd by high-temperature reaction calorimerty, *Journal of Alloys and Compounds, 221,* 37-41.

Miani, F. and Fecht, H. J. (1999). Evaluating the mechanochemical power transfer in the mechanosynthesis of nanophase Fe-C and Fe-Cu powders, *International Journal of Refractory Metals and Hard Materials, 17,* 133-139.

Mitterer, C., Waldhauser, W., Beck, U. and Reiners, G. (1996). Structure and properties of decorative rare-earth hexaboride coatings, *Surface and Coatings Technology, 86-87,* 715-721.

Miyazaki, H., Hajiri, T., Ito, T., Kunii, S. and Kimura, S. (2012). Momentum-dependent hybridization gap and dispersive in-gap state of the kondo semiconductor SmB_6, *Physical Review, 86,* 075105-1-075105-4.

Motojima, S., Takahashi, Y. and Sugiyama, K. (1978). Chemical vapor growth of LaB_6 whiskers and crystals having a sharp tip, *Journal of Crystal Growth, 44,* 106-109.

Murty, B. S. and Ranganathan, S. (1998). Novel materials synthesis by mechanical alloying-milling, *International Materials Reviews, 43,* 101-141.

Nakagawa, H., Nishi, Y. and Kieda N. (2000). Floating zone growth and high temperature hardness of rare-earth hexaboride crystals: LaB_6, CeB_6, PrB_6, NdB_6, and SmB_6, *Journal of Solid State Chemistry, 154,* 238-241.

Niemyski, T. and Kierzek-Pecold, E. (1968). Crystallization of lanthanum hexaboride, *Journal of Crystal Growth, 3-4,* 162-165.

Ninga, L. J., Wua, Y. P., Fanga, S. B., Rahmb, E. and Holzeb, R. (2004). Materials prepared for lithium ion batteries by mechanochemical methods, *Journal of Power Sources, 133,* 229-242.

Nouri, A. and Wen, C. (2014). Surfactants in mechanical alloying/milling: a catch-22 situation, *Critical Reviews in Solid State and Materials Sciences, 39,* 81-108.

Odunuga, S., Li, Y., Krasnochtchekov, P., Bellon, P. and Averback, R. S. (2005). Forced chemical mixing in alloys driven by plastic deformation. *Physical Review Letters, 95,* 045901-1-045901-4.

Ogino, Y., Yamasaki, T., Atzumi, N. and Yoshioka, K. (1993). Nitriding of transition metal powders by ball milling in nitrogen gas, *Materials Transaction The Japan Institute of Metals and Materials, 34,* 1212-1216.

Ostwald, W. (1887). *Lehrbuch der Allgemeinen Chemie.* Leipzig, Germany: Verlag Von Wilhelm Engelmann.

Ostwald, W. (1909). *Grundriss der Kolloidchemie.* Dresden, Germany: Verlag von Theodor Steinkopff.

Otani, S., Honma, S. and Ishizawa, Y. (1993a). Preparation of LaB_6 single crystals by the floating zone method, *Journal of Alloys and Compounds, 193,* 286-288.

Otani, S., Honma, S., Yajima, Y. and Ishizawa, Y. (1993b). Preparation of LaB_6 single crystals from a boron-rich molten zone by the floating zone method, *Journal of Crystal Growth, 126,* 466-470.

Otani, S., Tanaka, T. and Ishizawa, Y. (1993c). Crystal quality and high temperature hardness of LaB_6 crystals prepared by the floating zone method, *Journal of Alloys and Compounds, 202,* L25-28.

Otani, S. and Ishizawa, Y. (1996). Thermionic emission properties of boron-rich LaB_6 and CeB_6 crystal cathodes, *Journal of Alloys and Compounds, 245,* L18-L20.

Otani, S., Nakagawa, H., Nishi, Y. and Kieda, N. (2000). Floating zone growth and high temperature hardness of rare-earth hexaboride crystals: LaB_6, CeB_6, PrB_6, NdB_6, and SmB_6, *Journal of Solid State Chemistry, 154,* 238-241.

Öveçoğlu, M. L. and Nix, W. D. (1986). Characterization of rapidly solidified and mechanically alloyed Al-Fe-Ce powders, *International Journal of Powder Metallurgy, 22,* 17-30.

Öveçoğlu, M. L. (1987). *Development of a dispersion strengthened Al-Fe-Ce alloy by mechanical alloying and related theoretical modeling of dislocations in composite materials*. (Doctoral dissertation). Stanford University, San Francisco.

Paderno, V. N., Paderno, Yu. B., Pilyankevich, A. N., Lazorenko, V. I. and Bulychev, S. I. (1979). The micromechanical properties of melted borides of rare earth metals, *Journal of the Less-Common Metals, 67,* 431-436.

Paderno, V., Paderno, Y. and Britun, V. (1995). Features of the real structure of lanthanum hexaboride single crystals, *Journal of Alloys and Compounds, 219,* 228-231.

Pardavi-Horvath, M. and Takacs, L. (1992). Iron-alumina nanocomposites prepared by ball milling, *IEEE Transactions on Magnetics, 28,* 3186-3188.

Perkins, C. L., Trenary, M., Tanaka, T. and Otani, S. (1999). X-ray photoelectron spectroscopy investigation of the initial oxygen adsorption sites on the LaB_6 (100) surface, *Surface Science Letters, 423,* L222-L228.

Petrosyan, V., Vardanyan, V., Kuzanyan, V., Konovalov, M., Gurin, V. and Kuzanyan, A. (2012). Thermoelectric properties and chemical composition of CeB_6 crystals obtained by various methods, *Solid State Sciences, 14,* 1653-1655.

Popov, P. A., Nonikov, V. V., Siderov, A. A. and Meksimenko E. V. (2006). Thermal conductivity of LaB_6 in the range 6-300 K., *Inorganic Materials, 43,* 1187-1191.

Popov, P. A., Novikov, V. V., Sidorov, A. A. and Maksimenko, E. V. (2007). Thermal conductivity of LaB_6 and SmB_6 in the range 6-300 K, *Inorganic Materials, 43,* 1187-1191.

Post, B., Moskowitz, D. and Glaser, F. W. (1956). Borides of rare earth metals, *American Chemical Society, 78,* 1800-1802.

Pourghahramani, P. (2007). *Mechanical activation of hematite using different grinding methods with special focus on structural changes and reactivity.* (Doctoral dissertation), Lulea University of Technology, Lulea, Sweden.

Qian, Y., Xu, L., Ma, X. and Wang, L. (2011). Preparation of rare-earth hexaboride nano powder involves reacting metal source raw material and boron source raw material, obtaining primary product, performing post treatment, adding hydrochloric acid, filtering, washing and drying. *Chinese Patent No. CN101948117-A.* Retrieved from Scopus.

Qin, L., Zhang, H., Zhang, Q. and Tang, J. (2010). Single-crystalline, rare-earth metal hexaboride nanowires used as electron emitter for electron emission cathode used for electron gun, contains rare-earth metals such as yttrium, lanthanum, cerium, samarium and gadolinium. *United State Patent No. US2010028235-A1*. Retrieved from Scopus.

Rhodes, M. (2008). *Introduction to Particle Technology.* Chichester, England: John Wiley&Sons.

Rigney, D. A. and Hammerberg, J. E. (1999). Advanced Materials for the 21st Century. In Y. W. Chung, D. C. Dunand, P. K. Liaw, G. B. Olson (Eds.), *The 1999 Julia R. Weertman Symposium*, (pp. 465-474). Cincinnati, Ohio: TMS.

Samsonov, G. V., Paderno, Yu. B. and Fomenko, V. S. (1963). Hexaborides of the rare-earth metals, *Soviet Powder Metallurgy and Metal Ceramics, 2(6),* 449-454.

Schaffer, G. B. and McCormick, P. G. (1990). Displacement reactions during mechanical alloying, *Metallurgical and Materials Transactions A,* **A21**, 2789-2794.

Schaffer, G. B. and McCormick, P. G. (1992). On the kinetics of mechanical alloying, *Metallurgical Transactions A: Physical Metallurgy and Materials Science, 23*, 1285-1290.

Schlesinger, M. E., Liao, P. K and Spear, K. E. (1999). The B-La (boron-lanthanum) system, *Journal of Phase Equilibria, 20,* 73-78.

Scholz, H., Bauhofer, W. and Ploog, K. (1976). Preparation of lanthanum hexaboride by electrolysis and measurement of the Raman-active phonons, *Solid State Communications, 18,* 1539-1542.

Selvan, R. K., Genish, I., Perelshtein, I., Moreno, M. C. and Gedanken, A. (2008). Single step, low-temperature synthesis of submicron-sized rare earth hexaborides, *Journal of Physical Chemistry C, 112,* 1795-1802.

Shen, T. D., Wang, K. Y., Wang, J. T. and Quan, M. X. (1992). Solid state displacement reaction of Fe and CuO induced by mechanical alloying, *Materials Science and Engineering, A151,* 189-195.

Shigeki, O., Honma, S. and Ishizawa, Y. (1993a). Preparation of LaB_6 single crystals by the floating zone method, *Journal of Alloys and Compounds, 193,* 286-288.

Shigeki, O., Honma, S., Yajima, Y. and Ishizawa, Y. (1993b). Preparation of LaB_6 single crystals from a boron-rich molten zone by the floating zone method, *Journal of Crystal Growth, 126,* 466-470.

Shigeki, O., Tanaka, T. and Ishizawa, Y. (1993c). Crystal quality and high temperature hardness of LaB_6 crystals prepared by the floating zone method, *Journal of Alloys and Compounds, 202,* L25-L28.

Shiota, M., Tsutsumi, M. and Uchida, K. (1980). Synthesis of LaB_6 from BN and lanthanum-citrate-hydrate, *Journal of Materials Science, 15,* 1987-1992.

Shmyt'ko, I. M., Kiryakin, I. N. and Strukova, G. K. (2013). Features of $LaBO_3$ phase formation during solid-phase synthesis from the amorphous precursor state, *Physics of the Solid State, 55(7),* 1468-1475.

Smolyakov, V. K., Lapshin, O. V. and Boldyrev, V. V. (2008). Mechanochemical synthesis of nanosize products in heterogeneous systems: macroscopic kinetics, *International Journal of Self-Propagating High-Temperature Synthesis, 17,* 20-29.

Soni, P. R. (2001). *Mechanical Alloying: Fundamentals and Applications.* Cambridge, UK: Cambridge International Science Publishing.

Sopicka-Lizer, M. (2010). Introduction to mechanochemical processing, In M. Sopicka-Lizer (Ed.), *High-energy Ball Milling: Mechanochemical Processing of Nanopowders* (pp.1-5). Cambridge, UK: Woodhead Publishing Limited, CRC.

Sturgeon, G. D. and Eick, H. A. (1965). Samarium borides: the tetraboride-hexaboride conversion, *The Journal of Physics Chemistry, 69,* 3705-3708.

Suryanarayana, C. (2001). Mechanical alloying and milling, *Progress in Materials and Science, 46,* 1-184.

Suryanarayana, C., Ivanov, E. and Boldyrev, V. V. (2001). The science and technology of mechanical alloying, *Materials Science and Engineering, A304-306,* 151-158.

Suryanarayana, C. and Norton, M. G. (1998). *X-Ray Diffraction: A Practical Approach.* New York, USA: Plenum Press.

Swanson, L. W. and McNeely, D. R. (1979). Work functions of the (001) face of the hexaborides of Ba, La, Ce and Sm, *Surface Science,* **83**, 11-28.

Szépvölgyi, J., Mohai, I., Károly, Z. and Gál, L. (2008). Synthesis of nanosized ceramic powders in a radiofrequency thermal plasma reactor, *Journal of the European Ceramic Society, 28,* 895-899.

Takacs, L. (1992). Reduction of magnetite by aluminum: a displacement reaction induced by mechanical alloying, *Materials Letters, 13,* 119-124.

Takacs, L. (1996). Nanocrystalline materials by mechanical alloying and their magnetic properties, In C. Suryanarayana, J. Singh, F.H. Froes (Eds.), *Processing and Properties of Nanocrystalline Materials* (pp.453-464), Warrendale, PA: TMS.

Takacs, L. (2002). Self-sustaining reactions induced by ball milling, *Progress in Materials Science, 47,* 355-414.

Takacs, L. (2007). The mechanochemical reduction of AgCl with metals: revisiting an experiment of M. Faraday, *Journal of Thermal Analysis and Calorimetry, 90,* 81-84.

Takagi, K. and Ishii, M. (1977). Growth of LaB_6 single crystals by a laser heated floating zone method, *Journal of Crystal Growth, 40,* 1-5.

Tanaka, T., Bannai, E., Kawai, S. and Yamane T. (1975). Growth of high purity LaB_6 single crystals by multi-float zone passage, *Journal of Crystal Growth, 30,* 193-197.

Tanaka, Y., Staub, U., Narumi, Y., Katsumata, K., Scagnoli, V., Shimomura, S., Tabata, Y. and Onuki, Y. (2004). Non-resonant X-ray Bragg diffraction by CeB_6, *Physica B: Condensed Matter, 345,* 78-81.

Tkacova, K., Balaz, P., Misura, B., Vigdergauz, V. E. and Chanturiya, V. A. (1993). Selective leaching of zinc from mechanically activated complex Cu-Pb-Zn concentrate, *Hydrometallurgy, 33,* 291-300.

Trunov, V. A., Malyshev, A. L., Chernyshov, D. Y., Kurbakov, A. I., Korsukova, M. M., Gurin, V. N., Aslanov, L. A. and Chernyshev, V. V. (1991). Isotopic engineering of "zero-matrix" samarium hexaboride: results of high-resolution powder neutron diffraction and X-ray single-crystal diffractometry studies, *Journal of Applied Crystallography, 24,* 888-892.

Trunov, V. A., Malyshev, A. L., Chernyshov, D. Y., Korsukova, M. M., Gurin, V. N., Aslanov, L. A. and Chernyshev, V. V. (1993). Temperature dependences of the parameters of atoms in the crystal structure of the intermediate-valance semiconductor SmB_6: investigation by high-resolution powder neutron diffraction, *Journal of Physics: Condensed Matter, 5,* 2479-2488.

Upadhyaya, G. S. (2002). *Powder Metallurgy Technology*. Cambridge, UK: Cambridge International Science.

Url-1 <http://techsunchina.com/product.asp?id=758>, erişim tarihi 28.11.2013.

Url-2 <http://techsunchina.com/product.asp?id=759>, erişim tarihi 28.11.2013.

Url-3 <http://www.a-p-tech.com/aptech_cebix_lab6_material_data.html>, erişim tarihi 29.11.2013.

Url-4 <http://www.emsdiasum.com/microscopy/technical/datasheet/80920.aspx>, erişim tarihi 03.12.2013.

Url-5 <http://www.chinararemetal.com/product/Lanthanum_hexaboride_LaB_6.htm>, erişim tarihi 02.12.2013.

Url-6 <http://techsunchina.com/list.asp?tcid=197&tsid=230>, erişim tarihi 03.12.2013.

Url-7 <http:// extras.springer.com/2000/.../3Las08d1.pdf>, erişim tarihi 02.12.2013.

Verhoeven, J. D., Gibson, E. D, Noack, M. A. and Conzemius, R. J. (1976). An arc floating zone technique for preparing single crystal lanthanum hexaboride, *Journal of Crystal Growth, 36,* 115-120.

Wang, L., Xu, L., Ju, Z. and Qian, Y. (2010). A versatile route for the convenient synthesis of rare-earth and alkaline-earth hexaborides at mild temperatures, *CrystEngComm, 12,* 3923-3928.

Wang, X., Jiang, Y., Lin, Z., Qi, K. and Wang, B. (2009). Field emission characteristics of single crystal LaB_6 field emitters fabricated by electrochemical etching method, *Journal of Physics D: Applied Physics, 42,* 055409.

Weimer, A. W. (1977). *Carbide, Nitride and Boride Materials Synthesis and Processing*. London, UK: Chapman & Hall.

Weimin, W., Zhengyi, F., Hao, W. and Runzhang, Y. (2002). Chemistry reaction processes during combustion synthesis of B_2O_3-TiO_2-Mg system, *Journal of Materials Processing Technology, 128,* 162-168.

Wen, C. H., Wu, T. M. and Wei, W. J. (2004). Oxidation kinetics of LaB_6 in oxygen rich conditions, *Journal of the European Ceramic Society, 24,* 3235-3243.

Wenyuan, W., Jingyu, X., Kewu, P. and Ganfeng, T. (2007). High temperature chemical reaction of La_2O_3 in H_3BO_3-C system, *Journal of Rare Earths, 25,* 282-285.

Wieczorek-Ciurowa, K., Oleszak, D. and Gamrat, K. (2007). Mechanosynthesis and process characterization of some nanostructured intermetallics-ceramics composites, *Journal of Alloys Compaunds, 434-435,* 501-504.

Wieczorek-Ciurowa, K. (2010). Mechanochemical synthesis of metallic-ceramic composite powders, In M. Sopicka-Lizer (Ed.), *High-energy Ball Milling: Mechanochemical Processing of Nanopowders* (pp. 193-223). Cambridge, UK: Woodhead Publishing Limited, CRC.

Xu, J. Q., Zhao, Y. M. and Zou, C. (2006). Self-catalyst growth of LaB_6 nanowires and nanotubes, *Chemical Phsysics Letters, 423,* 138-142.

Xu, J. Q., Zhao, Y. M., Shi, Z. D., Zou, C. Y. and Ding Q. W. (2008a). Single-crystalline SmB_6 nanowires, *Journal of Crystal Growth, 310,* 3443-3447.

Xu, J. Q., Zhao, Y. M. and Zhang, Q. Y. (2008b). Enhanced electron field emission from single-crystalline LaB_6 nanowires with ambient temperature, *Journal of Applied Physics, 104(12),* 124306-1-124306-4.

Xu, J. Q., Zhao, Y. M., Ji, X. H., Zhang, Q. and Lau, S. P. (2009). Growth of single-crystalline SmB_6 nanowires and their temperature-dependent electron field emission, *Journal of Physics D: Applied Physics, 42,* 135403-1-135403-6.

Xu, J. Q., Mori, T., Bando, Y., Golberg, D., Berthebaud, D. and Prytuliak, A. (2012). Synthesis of CeB_6 thin films by physical vapor deposition and their field emission investigations, *Material Science and Engineering B, 177,* 177-120.

Yang, H. and McCormick, P. G. (1993a). Combustion reaction of zinc oxide with magnesium during mechanical milling, *Journal of Solid State Chemistry, 107,* 258-263.

Yang, H. and McCormick, P. G. (1993b). Reduction of tantalum chloride by magnesium during reaction milling, *Journal of Materials Science Letters, 12,* 1088-1091.

Yang, L. C., Qu, Q. T., Shi, Y. and Wu, Y. P. (2010). Materials for lithium-ion batteries by mechanochemical methods, In M. Sopicka-Lizer (Ed.), *High-energy Ball Milling: Mechanochemical Processing of Nanopowders* (pp.361-408). Cambridge, UK: Woodhead Publishing Limited, CRC.

Yin, S., Zhang, Q., Satio, F. and Sato, T. (2010). Synthesis of titanium dioxide-based, visible-light induced photocatalysts by mechanochemical doping, In M. Sopicka-Lizer (Ed.), *High-energy Ball Milling: Mechanochemical Processing of Nanopowders* (pp.304-330). Cambridge, UK: Woodhead Publishing Limited, CRC.

Yuan, Y., Zhang, L., Liang, L., He, K., Liu, R. and Min, G. (2011). A solid-state reaction route to prepare LaB_6 nanocrystals in vacuum, *Ceramics International, 37,* 2891-2896.

Zelikman, A. H., Voldman, G. M. and Beljajevskaya, L. V. (1983). *Theory of Hydrometallurgical Processes.* Moscow, Russia: Metallurgia.

Zhang, H., Zhang, Q., Tang, J. and Qin, L. C. (2005). Single-crytalline CeB_6 nanowires, *Journal of American Chemical Society, 127,* 8002-8003.

Zhang, H., Tang, J., Zhang, Q., Zhao, G., Yang, G., Zhang, J., Zhou, O. and Qin, L. (2006). Field emission of electrons from single LaB_6 nanowires, *Advanced Materials, 18,* 87-91.

Zhang, H., Tang, B., Zhu, P. W., Zhang, Q., Zhou, O. and Qin, L. C. (2007). Fabrication of lanthanum hexaboride single nanowire field emitter and their field emission properties, *Transactions of the Materials Research Society of Japan, 32(3),* 747-750.

Zhang, H., Tang, J., Zhang L., An, B. and Qin, L. (2008a). Atomic force microscopy measurement of the Young's modulus and hardness of single LaB_6 nanowires, *Applied Physics Letters, 92,* 173121.

Zhang, M., Yuan, L., Wang, X., Fan, H., Wang, X., Wu, X., Wang, H. and Qian, Y. (2008b). A low-temperature route for the synthesis of nanocrystalline LaB_6, *Journal of Solid State Chemistry, 181,* 294-297.

Zhang, M., Wang, X., Zhang, X., Wang, P., Xiong, S., Shi, L. and Qian, Y. (2009). Direct low-temperature synthesis of RB_6 (R=Ce, Pr, Nd) nanocubes and nanoparticles, *Journal of Solid State Chemistry, 182,* 3098-3104.

Zhang, L., He, W., Tolochko, O., Polzik, L. and Min, G. (2010a). Morphology characterization and optical properties analysis for nanostructured lanthanum hexaboride powders, *Advanced Materials Research, 79-82,* 107-110.

Zhang, M., Jia, Y., Xu, G., Wang, P., Wang, P., Wang, X., Xiong, S., Wang, X. and Qian, Y. (2010b). Mg-assisted autoclave synthesis of RB_6 (R=Sm, Eu, Gd, and Tb) submicron cubes and SmB_6 submicron rods, *European Journal of Inorganic Chemistry, 8,* 1289-1294.

Zheng, S. Q., Min, G. H., Zou, Z. D., Wang X. Z. and Han, J. D. (2001). Synthesis of LaB_6 powder by reaction in La_2O_3-B_4C system, *Acta Metallurgica Sinica, 37,* 419-422.

Zhou, S., Zhang, J., Liu, D. and Bao, L. (2009). Properties of CeB_6 cathode fabricated by spark plasma reactive liquid phase sintering method, *Journal of Inorganic Materials, 24(4),* 793-797.

Zou, C. Y., Zhao, Y. M. and Xu, J. Q. (2006). Synthesis of single-crystalline CeB_6 nanowires, *Journal of Crystal Growth, 291,* 112-116.

Zubeck, I. V., Feigelson, R. S., Huggins, R. A. and Pettit, P. A. (1976). The growth of lanthanum hexaboride single crystals by molten salt electrolysis, *Journal of Crystal Growth, 34,* 85-91.

CURRICULUM VITAE

Name Surname:	Duygu AĞAOĞULLARI
Place and Date of Birth:	Istanbul, 29.09.1982
Address:	Mektep Sokak, İlhan Apartmanı, No:11, Kat:1, Daire:4, Florya/İstanbul
E-Mail:	bozkurtdu@itu.edu.tr
B.Sc.:	Istanbul Technical University, Department of Metallurgical and Materials Engineering, 2004.
	Istanbul Technical University, Department of Chemical Engineering, 2006.
M.Sc.:	Istanbul Technical University, Department of Materials Science and Engineering, 2007.

Professional Experience and Rewards:

- 15.07.2013-currently, Engineer, Istanbul Technical University, Faculty of Chemical and Metallurgical Engineering.
- 30.11.2005-15.07.2013, Research Assistant, Istanbul Technical University, Department of Metallurgical and Materials Engineering.
- Poster Award, 12th International Symposium on Novel and Nano Materials, Istanbul, Turkey, 2012
- Poster Award, 12th International Workshop on Nanoscience and Nanotechnology, Varna, Bulgaria, 2010
- Young Scientist Award, 14th International Metallurgy and Materials Congress, Istanbul, Turkey, 2008.
- Second Rank – Graduation, Istanbul Technical University, 2004.
- Success Scholarship, Turkish Educational Foundation, 2001-2004.
- First Rank – Graduation, Tercuman High School, 2000.

List of Publications and Patents:

International Articles

- Balcı, Ö., **Ağaoğulları, D.,** Gökçe, H., Duman, İ. and Öveçoğlu, M. L. (2014). Influence of TiB_2 particle size on the microstructure and properties of Al matrix composites prepared via mechanical alloying and pressureless sintering, *Journal of Alloys and Compounds, 586,* 578-584.
- **Ağaoğulları, D.,** Balcı, Ö., Demirkan, Ö.U., Gökçe, H., Genç, A., Öveçoğlu, M. L.and Duman, İ. (2013). Development of Mechanically Alloyed and Sintered W-1 wt.% Ni Matrix Composites Reinforced with TiB_2, *Solid State Phenomena, 194,* 194-198. *(cited in Web of Science)*
- **Ağaoğulları, D.,** Balcı, Ö., Gökçe, H., Öveçoğlu, M. L. and Duman, İ. (2013). Comparative Investigations of the Activated Sintered W-1 wt.% Ni Composites Reinforced with Various Boride and Oxide Particles, *International Journal of Refractory Metals and Hard Materials, 41,* 577-584.
- Balcı, Ö., Demirkan, Ö. U., **Ağaoğulları, D.,** Gökçe, H., Genç, A., Öveçoğlu, M. L. and Duman, İ. (2013). Effects of La_2O_3 Addition on the Microstructure and Properties of Activated Sintered W-Ni Compacts, *Solid State Phenomena, 194,* 217-221. *(cited in Web of Science)*
- Gökçe, H., Balcı, Ö., **Ağaoğulları, D.,** Demirkan, Ö. U., Genç, A., Öveçoğlu, M. L. and Duman, İ. (2013). Characterization Investigations of W-Ni Matrix Composites Reinforced with TiB_2 and La_2O_3, *Acta Physica Polonica A, 123 (2),* 309-311.
- Samur, R., Özyeğin, L. S., **Ağaoğulları, D.,** Oktar, F. N., Agathopoulos, S., Kalkandelen, C., Duman, I. and Ben Nissan, B. (2013). Calcium Phosphate Formation from Sea Urchin-(Brissus latecarinatus) via Modified Mechano-Chemical (Ultrasonic) Conversion Method, *Journal Metalurgija, 52 (3),* 375-378. *(cited in Web of Science)*
- **Ağaoğulları, D.,** Balcı, Ö., Gökçe, H., Duman, İ. and Öveçoğlu, M. L. (2012). Synthesis of Magnesium Borates by Mechanically Activated Annealing, *Metallurgical and Materials Transactions A-Physical Metallurgy and Materials Science, 43A (7),* 2520-2533.
- **Ağaoğulları, D.,** Gökçe, H., Duman, İ. and Öveçoğlu, M. L. (2012). Aluminum Diboride Synthesis from Elemental Powders by Mechanical Alloying and Annealing, *Journal of the European Ceramic Society, 32 (7),* 1457-1462.
- **Ağaoğulları, D.,** Gökçe, H., Duman, İ. and Öveçoğlu, M. L. (2012). Characterization Investigations of ZrB_2/ZrC Ceramic Powders Synthesized by Mechanical Alloying of Elemental Zr, B and C Blends, *Journal of the European Ceramic Society, 32 (7),* 1447-1455.
- **Ağaoğulları, D.,** Gökçe, H., Duman, İ. and Öveçoğlu, M. L. (2012). Influences of Metallic Co and Mechanical Alloying on the Microstructural and Mechanical Properties of TiB_2 Ceramics Prepared via Pressureless Sintering, *Journal of the European Ceramic Society, 32 (9),* 1949-1956.

- **Ağaoğulları, D.,** Kel, D., Gökçe, H., Duman, İ., Öveçoğlu, M. L., Akarsubaşı, A. T., Bilgiç, D. and Oktar, F. N. (2012). Bioceramic Production from Sea Urchins, *Acta Physica Polonica A, 121 (1),* 23-26.
- Balcı, Ö., **Ağaoğulları, D.,** Duman, İ. and Öveçoğlu, M. L. (2012). Carbothermal Production of ZrB_2-ZrO_2 Ceramic Powders from ZrO_2–B_2O_3/B System by High-Energy Ball Milling and Annealing Assisted Process, *Ceramics International, 38 (3),* 2201-2207.
- Balcı, Ö., **Ağaoğulları, D.,** Duman, İ. and Öveçoğlu, M. L. (2012). Synthesis of CaB_6 powders via mechanochemical reaction of Ca/B_2O_3 blends, Powder *Technology, 225,* 136-142.
- **Ağaoğulları, D.,** Balcı, Ö. and Duman, İ. (2011). Nanocrystalline Tungsten Powders Synthesized from Uludağ Scheelite Concentrates via Mechanochemical Route, *Nanoscience & Nanotechnology, 11,* 231-234.
- **Ağaoğulları, D.,** Balcı, Ö., Duman, İ. and Öveçoğlu, M. L. (2011). Synthesis of α- and β-Rhombohedral Boron Powders via Gas Phase Thermal Dissociation of Boron Trichloride by Hydrogen, *Metallurgical and Materials Transactions B, 42 (3),* 568-574.
- Balcı, Ö., **Ağaoğulları, D.,** and Duman, İ. (2011). Process Design for the Preparation of Micron-Scale Elemental Boron Powders by Chemical Vapor Deposition, *Nanoscience & Nanotechnology, 11,* 226-230.
- Gökçe, H., **Ağaoğulları, D.,** Öveçoğlu, M. L., Duman, I. and Boyraz, T. (2011). Characterization of Microstructural and Thermal Properties of Steatite/Cordierite Ceramics Prepared by Using Natural Raw Materials, *Journal of the European Ceramic Society, 31 (14),* 2741-2747.
- Kel, D., Gökçe, H., Bilgiç, D., **Ağaoğulları, D.,** Duman, İ., Öveçoğlu, M. L., Kayali, E. S., Kiyici, I. A., Agathopoulos, S. and Oktar, F. N. (2011). Production of Natural Bioceramic from Land Snails, *Key Engineering Materials, 493-494,* 287-292.
- Balci, Ö., **Ağaoğulları, D.** and Duman, İ. (2010). The Production of HfO_2-HfB_2 Composite Powder from HfO_2, B_2O_3 and Mg by Solid State Reaction and Subsequent Annealing, *Solid State Science and Technology, 18 (2),* 91-98.

International Conference Papers

- Ovalı, D., Balcı, Ö., **Ağaoğulları, D.,** Gökçe, H., Öveçoğlu, M. L., Duman, İ. (2013). Effects of La_2O_3 Addition on the Properties of Mechanically Alloys and Sintered W-1 wt.% Ni-2 wt.% WB Composites, AMWC 2013: Advanced Materials World Congress, İzmir, Türkiye, 16-19 October.
- **Ağaoğulları, D.,** Balcı, Ö., Duman, İ. and Öveçoğlu, M. L. (2013). Effects of Milling Duration and Annealing Temperature on the Microstructure and Properties of ZrB_2 Powders, *ICMAT 2013: 7th International Conference on Materials for Advanced Technologies,* Suntec, Singapore, 30 June-5 July.

- Balcı, Ö., **Ağaoğulları, D.,** Duman, İ., Öveçoğlu, M. L. (2013). Effect of Mechanical Milling on the Microstructure of Niobium Boride Powders Synthesized by Magnesiothermic and Carbothermic Reductions, *ICMAT 2013: 7th International Conference on Materials for Advanced Technologies,* Suntec, Singapore, 30 June-5 July.
- **Ağaoğulları, D.,** Balcı, Ö., Gökçe, H., Duman, İ., Öveçoğlu, M. L. (2013). Microstructural and Mechanical Evaluation of Al-xTiB_2 (x=5, 10, 15 wt.%) Composites Fabricated by Cryogenic Milling, METAL 2013: 22nd International Conference on Metallurgy and Materials, Poster Session E: Non-Ferrous Metals and Alloys, Brno, Czech Republic, EU, 15-17 May.
- Balcı, Ö., **Ağaoğulları, D.,** Duman, İ. and Öveçoğlu, M. L. (2013). Synthesis of Calcium Boride Powders via Mechanochemical Route, *IFW Winterschool 2013,* Oberwiesenthal, Germany, 20-23 January.
- Oktar, F. N., Kıyıcı, I. A., Gökçe, H., **Ağaoğulları, D.** and Kayalı E. S. (2013). Tropical Sea Snail Shells: Possible Exotic Sources for Ceramic Biomaterial Synthesis, *APMAS 2013: 3rd International Advances in Applied Physics & Materials Science Congress,* Antalya, Turkey, 24-28 April.
- **Ağaoğulları, D.,** Balcı, Ö., Demirkan, Ö. U., Gökçe, H., Genç, A., Öveçoğlu M. L. and Duman I. (2012). Development of Mechanically Alloyed and Sintered W-1 wt.% Ni Matrix Composites Reinforced with TiB_2, *SCTE 2012: 18th International Conference on Solid Compounds of Transition Elements,* Lisbon, Portugal, 31 March-5 April.
- **Ağaoğulları, D.,** Balcı, Ö., Duman, İ. and Öveçoğlu, M. L. (2012). Synthesis and Characterization of IVB Group Transition Metal Borides, *ISNNM-2012: 12th International Symposium on Novel and Nano Materials,* Istanbul, Turkey, 26-30 August. (Poster Award)
- Balcı, Ö., Demirkan Ö. U., **Ağaoğulları, D.,** Gökçe, H., Genç, A., Öveçoğlu M. L. and Duman, I. (2012). Effects of La_2O_3 Addition on the Microstructure and Properties of Activated Sintered W-Ni Compacts, *SCTE 2012: 18th International Conference on Solid Compounds of Transition Elements,* Lisbon, Portugal, 31 March-5 April.
- Balcı, Ö., **Ağaoğulları, D.,** Gökçe, H., Duman, İ., Öveçoğlu, M. L. (2012). Influence of TiB_2 Particle Size on the Microstructure and Properties of Al Matrix Composites Prepared via Mechanical Alloying and Sintering, *ISMANAM 2012: 19th International Symposium on Metastable, Amorphous and Nanostructured Materials,* Moscow, 18-22 June.
- Balcı, Ö., **Ağaoğulları, D.,** Gökçe, H., Öveçoğlu, M. L. and Duman, İ. (2012). Effects of Sequential Ball Milling at Ambient and Cryogenic Conditions on the Microstructure of W-1 wt.% Ni Compacts Reinforced with ZrC and Y_2O_3 Particles, *ISMANAM 2012: 19th International Symposium on Metastable, Amorphous and Nanostructured Materials,* Moscow, 18-22 June.
- Balcı, Ö., **Ağaoğulları, D.,** Gökçe, H., Öveçoğlu, M. L. and Duman, İ. (2012). Fabrication of W-1 wt.% Ni Matrix Composites Reinforced with TiB_2 and Y_2O_3 via Mechanical Alloying at Ambient/Cryogenic Conditions and Activated Sintering Methods, *ISNNM-2012: 12th International Symposium on Novel and Nano Materials,* Istanbul, Turkey, 26-30 August.

- Gökçe, H., Balcı, Ö., Demirkan, Ö. U., **Ağaoğulları, D.,** Genç, A., Öveçoğlu, M. L. and Duman, I. (2012). Characterization Investigations of W-Ni Matrix Composites Reinforced with La_2O_3 and TiB_2, *APMAS 2012: 2nd International Advances in Applied Physics and Materials Science Congress,* Antalya, Turkey, 26-29 April.
- Karacaylı, U., Aytekin, A., Erhan, O., Ozyegin, L. S., Duman, I., **Agaogulları, D.** and Oktar F. N. (2012). Characterization of Zeolite Enriched-Chitosan Based Wound Dressing Membrane, *APMAS 2012: 2nd International Advances in Applied Physics and Materials Science Congress,* Antalya, Turkey, 26-29 April.
- **Ağaoğulları, D.,** Duman, I. and Keleş, Ö. (2011). Evaluation of the Effect of Residual Silver in Copper on the Cementation Process by Factorial Design and Multiple Regression Analysis, *TMS 2011: 140th Annual Meeting and Exhibition,* San Diego, California, USA, 27 February-3 March.
- **Ağaoğulları, D.,** Balcı, Ö. and Duman, I. (2011). The Production of LaB_6 by Hot-Powder CVD Method, *Engineering Ceramics 2011 from Materials to Components,* Smolenice, Slovakia, 8-12 May.
- **Ağaoğulları, D.,** Balcı, Ö., Gökçe, H., Duman, I. and Öveçoğlu, M. L. (2011). A Sequential Process for Synthesizing Chromium Boride-Chromium Nitride Composite Powders, *ECERS XII: 12th Conference of the European Ceramic Society,* Stockholm, Sweden, 19-23 June.
- **Ağaoğulları, D.,** Gökçe, H., Duman, I. and Öveçoğlu, M. L. (2011). Influence of Co Metallic Additive on the Microstructural and Mechanical Properties of TiB_2 Ceramics Prepared via Mechanical Alloying and Pressureless Sintering, *Engineering Ceramics 2011 from Materials to Components,* Smolenice, Slovakia, 8-12 May.
- **Ağaoğulları, D.,** Gökçe, H., Duman, I. and Öveçoğlu, M. L. (2011). Microstructure Characterization and Mechanical Properties of Steatite/Cordierite Ceramics, *ECERS XII: 12th Conference of the European Ceramic Society,* Stockholm, Sweden, 19-23 June.
- **Ağaoğulları, D.,** Kel, D., Gökçe, H., Duman, I., Öveçoğlu, M. L., Akarsubaşı, A. T., Bilgiç, D. and Oktar, F. N. (2011). Hydroxyapatite Production from Sea Urchins, *APMAS 2011: Advances in Applied Physics & Materials Science Congress, Session: 65,* Antalya, Turkey, 12-15 May.
- Balcı, Ö., **Ağaoğulları, D.** and Duman, I. (2011). A Comparative Study on the Synthesis and Characterization of CaB_6 Powders, *ECERS XII: 12th Conference of the European Ceramic Society,* Stockholm, Sweden, 19-23 June.
- Balcı, Ö., **Ağaoğulları, D.** and Duman, I. (2011). Carbothermal Production of ZrB_2-ZrO_2 Ceramic Powders from ZrO_2-B_2O_3/B System by High-Energy Ball Milling and Annealing, *Engineering Ceramics 2011 from Materials to Components,* Smolenice, Slovakia, 8-12 May.
- Gökçe, H., **Ağaoğulları, D.,** Öveçoğlu, M. L. and Duman, I. (2011). Investigation on the Structural, Physical and Mechanical Properties of La_2O_3 Reinforced Cordierite Based Ceramics, *ECERS XII: 12th Conference of the European Ceramic Society,* Stockholm, Sweden, 19-23 June.

- **Ağaoğulları, D.,** Aynibal, F., Demirhan, O. C. and Duman, İ. (2010). Characterization of Mechanochemically Synthesized ZrO_2-B_2O_3-Mg System by Thermogravimetry/Differential Thermal Analyses and X-Ray Diffraction Studies, *TMS 2010: 139th Annual Meeting and Exhibition,* Seattle, Washington, USA, 14-18 February.
- **Ağaoğulları, D.,** Balcı, Ö. and Duman, I. (2010). Mechanisms and Effects of Various Reducing Agents on the Fabrication of Elemental Boron, *METAL 2010: 19th International Conference on Metallurgy and Materials,* Roznov pod Radhostem, Czech Republic, EU, 18-20 May.
- **Ağaoğulları, D.,** Balcı, Ö. and Duman, I. (2010). Nanocrystalline Tungsten Powders Synthesized from Uludağ Scheelite Concentrates via Mechanochemical Route, *12th International Workshop on Nanoscience and Nanotechnology,* Varna, Bulgaria, 26-28 November.
- **Ağaoğulları, D.,** Balcı, Ö. and Duman, İ. (2010). The Production of BCl_3 Gas from Mechanochemical Reaction Product Containing Elemental Boron and Magnesium Oxide, *TMS 2010: 139th Annual Meeting and Exhibition,* Seattle, Washington, USA, 14-18 February.
- **Ağaoğulları, D.** and Duman, I. (2010). Novel Routes for Production of Different Metal Borides, *The Fifth International Annual Meeting of Alb-Science Institute, Conference of Engineering Sciences and Information Technology,* Tirana, Albania, 2-5 September.
- **Ağaoğulları, D.,** Gökçe, H., Balcı, Ö., Duman, I. and Öveçoğlu, M. L. (2010). Synthesis of Magnesium Borates by Mechanically Activated Annealing, *ICCPS-11 2010: 11th International Conference on Ceramic Processing Science, Particle Synthesis IV,* Zurich, Switzerland, 29 August-1 September.
- **Ağaoğulları, D.,** Gökçe, H., Duman, I. and Öveçoğlu, M. L. (2010). Synthesis Mechanism and Characterization of ZrC-ZrB_2 Composite Powder Fabricated by Mechanical Alloying of Zr-C-B System, *ISSNOX 2010: 3rd International Symposium on SiAlONs and Non-Oxides,* Cappadocia, Turkey, 1-4 June.
- **Ağaoğulları, D.,** Gökçe, H., Duman, I. and Öveçoğlu, M. L. (2010). Preparation of ZrB_2 Particulate Reinforced Al Matrix Composite by Mechanical Alloying and Sintering, *13th International Materials Symposium,* Denizli, Turkey, 13-15 October.
- **Ağaoğulları, D.,** Gökçe, H., Genç, A., Duman, I. and Öveçoğlu, M. L., (2010). Characterization of Mechanically Alloyed and Sintered ZrC Particulate Reinforced Al Matrix Composites, *METAL 2010: 19th International Conference on Metallurgy and Materials,* Roznov pod Radhostem, Czech Republic, EU, 18-20 May.
- Balcı, Ö., **Ağaoğulları, D.** and Duman, İ. (2010). A Study on Crystallization Mechanism of Amorphous Boron, *METAL 2010: 19th International Conference on Metallurgy and Materials,* Roznov pod Radhostem, Czech Republic, EU, 18-20 May.

- Balcı, Ö., **Ağaoğulları, D.** and Duman, I. (2010). Process Design for the Preparation of Micron-Scale Elemental Boron Powders by Chemical Vapor Deposition, *12th International Workshop on Nanoscience and Nanotechnology*, Varna, Bulgaria, 26-28 November. (Poster Award)
- Gökçe, H., **Ağaoğulları, D.,** Duman, I. and Öveçoğlu, M. L. (2010). Synthesis of Aluminum Diboride from Elemental Powders by Mechanical Alloying and Annealing, *ISSNOX 2010: 3rd International Symposium on SiAlONs and Non-Oxides*, Cappadocia, Turkey, 1-4 June.
- Gökçe, H., **Ağaoğulları, D.,** Öveçoğlu, M. L., Duman, I. and Boyraz, T. (2010). Characterization of Microstructural and Thermal Properties of Cordierite/Steatite Ceramics Prepared by Using Natural Raw Materials, *ICCPS-11 2010: 11th International Conference on Ceramic Processing Science*, Zurich, Switzerland, 29 August-1 September.
- Gökçe, H., Küçük, İ., Boyraz, T., **Ağaoğulları, D.,** Duman, I. and Öveçoğlu, M. L, (2010). Characterization of Microstructural and Physical Properties of Y_2O_3 Reinforced Cordierite Based Ceramic Materials, *13th International Materials Symposium*, Denizli, Turkey, 13-15 October.
- Nilüfer, B., Gökçe, H., **Ağaoğulları, D.,** Çimenoğlu, H., Öveçoğlu, M. L. and Duman, I. (2010). The Effect of La_2O_3 Modification on the Microstructural and Mechanical Properties of YSZ Ceramics Prepared by Powder Metallurgy, *ICCPS-11 2010: 11th International Conference on Ceramic Processing Science, Microstructure and Properties III*, Zurich, Switzerland, 29 August-1 September.
- **Ağaoğulları, D.,** Aynibal, F., Demirhan, O. C. and Duman, İ. (2009). A Room-Temperature Route for the Synthesis of Zirconium Diboride by Mechanochemical Reactions, *ROCAM 2009: The Sixth International Edition of Romanian Conference on Advanced Materials*, Brasov, Romania, 25-28 August.
- **Ağaoğulları, D.,** Aynibal, F., Demirhan, O. C. and Duman, İ. (2009). An Optimization Study for Separation of TiB_2 from a Solid-State Reaction Product by HCl Leaching, *SERES'09 I. International Ceramic, Glass, Porcelain, Enamel, Glaze and Pigment Congress*, Eskişehir, Turkey, 12-14 October.
- **Ağaoğulları, D.,** Aynibal, F., Demirhan, O. C. and Duman, İ. (2009). Formation of TiB_2 from Ti and B_2O_3 by High-Energy Ball Milling in Magnesiothermic Reduction Medium, *ROCAM 2009: The Sixth International Edition of Romanian Conference on Advanced Materials*, Brasov, Romania, 25-28 August.
- **Ağaoğulları, D.,** Aynibal, F., Demirhan, O. C. and Duman, İ. (2009). Mechanochemical Synthesis and Characterization of Titanium Diboride Powder, *TMS 2009: 138th Annual Meeting and Exhibition*, San Francisco, California, USA, 15-19 February.
- **Ağaoğulları, D.,** Aynibal, F., Demirhan, O. C. and Duman, İ. (2009). Synthesis of Titanium Diboride by Solid-State Reaction Between TiO_2, B_2O_3 and Mg, *SERES'09: I. International Ceramic, Glass, Porcelain, Enamel, Glaze and Pigment Congress*, Eskişehir, Turkey, 12-14 October.

- Balcı, Ö., **Ağaoğulları, D.,** Aynibal, F., Demirhan, O. C. and Duman İ. (2009). Thermogravimetry / Differential Thermal Analyses and X-Ray Diffraction Studies on the Mechanochemical Reaction Mechanism of TiO_2-B_2O_3-Mg and Ti-B_2O_3-Mg Systems, *ROCAM 2009: The Sixth International Edition of Romanian Conference on Advanced Materials,* Brasov, Romania, 25-28 August.
- Balcı, Ö., **Ağaoğulları, D.** and Duman, İ. (2009). The Production of HfO_2-HfB_2 Composite Powder from HfO_2, B_2O_3 and Mg by Solid State Reaction and Subsequent Annealing, *RCSSST 2009: 25th Regional Conference on Solid State Science & Technology 2009,* Penang, Malaysia, 21-23 December.
- Duman, İ. and **Ağaoğulları, D.** (2009). Changes in Microstructure and Mechanical Properties of CIP-Processed Tungsten Rods during Rotary-Swaging and Stretching Operations, *TMS 2009: 138th Annual Meeting and Exhibition,* San Francisco, California, USA, 15-19 February.
- **Ağaoğulları, D.** and Duman, İ. (2008). Process Design and Production of Boron Trichloride from Native Boron Carbide in Lab-Scale, *MS&T'08: Materials Science and Technology 2008 Conference and Exhibition, Materials and Systems: International Symposium on Innovative Processing and Synthesis of Ceramics, Glasses and Composites,* Pittsburgh, Pennsylvania, USA, 5-9 October.
- **Ağaoğulları, D.** and Duman, İ. (2008). The Production of Boron Trichloride from Boron Carbide, *14th International Metallurgy and Materials Congress,* Istanbul, Turkey, 16-18 October. (Young Scientist Award)
- Duman, İ., **Ağaoğulları, D.,** Ertürk, S. and Eke, K. (2008). The Effect of Doping on Grain Size of Tungsten Powder under Thermal Impact, *14th International Metallurgy and Materials Congress,* Istanbul, Turkey, 16-18 October.
- Duman, İ., **Ağaoğulları, D.,** Ertürk, S. and Kunt, A. I. (2008). Electrolytical Cleaning and Diameter Reduction of Tungsten Filaments and Very Thin Wires in Continuous System, *14th International Metallurgy and Materials Congress,* Istanbul, Turkey, 16-18 October.
- Duman, İ., Ertürk, S., **Ağaoğulları, D.** and Ulus, A. (2008). Optimization of the Operation Conditions in Tungsten Wire Draft Production, *14th International Metallurgy and Materials Congress,* Istanbul, Turkey, 16-18 October.
- Duman, İ., Gürmen, S., Ertürk, S. and **Ağaoğulları, D.** (2008). The Production of Pure Tungstenoxide from Tungsten Scraps, *14th International Metallurgy and Materials Congress*, Istanbul, Turkey, 16-18 October.
- Duman, İ., Öngel, D. and **Ağaoğulları, D.** (2008). The Effect of Remaining Silver in Copper on the Cementation Process, *BiCongress 08: Science-Technology-Ecology, V Congress of Metallurgists of Macedonia,* Ohrid, Macedonia, 17-20 September.
- **Ağaoğulları, D.** and Duman, İ. (2008). Removal of Phosgene from Boron Trichloride by IR Laser Under Continuous Flow, *TMS 2008: 137th Annual Meeting and Exhibition*, Extraction and Processing Division (EPD) Student Poster Contest, New Orleans, LA, USA, 9-13 March.

National Articles

- Balcı, Ö. and **Ağaoğulları, D.** (2011). The Production of Some Metal Borides via Mechanochemical Synthesis and Mechanical Alloying, *Metallurgy, 160,* 26-30.

National Conference Papers

- Gökçe, H., **Ağaoğulları, D.,** Yetmez, M., Gündüz, O., Aktaş, C., Öveçoğlu, M. L., Duman, İ., Agathopoulos, S. and Oktar, F. N. (2011). Production and Characterization of Composites of Hydroxyapatite Reinforced with Nano-Yttrium-Oxide, *International Participated V. National Biomechanics Congress,* Çeşme, Izmir, Turkey, 23-25 September.
- **Ağaoğulları, D.** and Boyraz, T. (2010). Investigation of Thermal Stresses in Dental Zirconia Fullceram Restoration by Mathematical Method, *International Participated V. National Biomechanics Congress*, Çeşme, Izmir, Turkey, 23-25 September 2010.

Patents

- Duman, İ., **Ağaoğulları, D.,** Balcı, Ö. and Öveçoğlu, M. L. "A Reactor Designed for Chemical Vapor Deposition Method and Method of Producing Elemental Boron and Advanced Ceramic Powders with This Reactor", Pending International Patent Application.

PUBLICATIONS/PRESENTATIONS ON THE THESIS

- **Ağaoğulları, D.,** Balcı, Ö., Duman, İ. and Öveçoğlu, M. L. (2013). Microstructure and Properties of Nanocrystalline LaB_6 Powders Synthesized in a High-Energy Planetary Ball Mill, *METAL 2013: 22nd International Conference on Metallurgy and Materials, Symposium E: Non-Ferrous Metals and Alloys,* Brno, Czech Republic, EU, 15-17 May.
- **Ağaoğulları, D.,** Duman, İ. and Öveçoğlu, M. L. (2013). Effect of Ball-to-Powder Weight Ratio on the Microstructure and Properties of Mechanochemically Synthesized LaB_6 Powders, *ICMAT 2013: 7th International Conference on Materials for Advanced Technologies*, Suntec, Singapore, 30 June-5 July.
- **Ağaoğulları, D.,** Duman, İ. and Öveçoğlu, M. L. (2012). Synthesis of LaB_6 Powders from La_2O_3, B_2O_3 and Mg Blends via a Mechanochemical Route, *Ceramics International, 38 (8),* 6203-6214.
- **Ağaoğulları, D.** and Duman, İ. (2009). Synthesis of Submicron LaB_6 Powder from La_2O_3, B_2O_3 and Mg via a Mechanochemical Route, *RCSSST 2009: 25th Regional Conference on Solid State Science & Technology 2009,* Penang, Malaysia, 21-23 December.